MEMS Reference Shelf

Rajesh Duggirala
Amit Lal
Shankar Radhakrishnan

# Radioisotope Thin-Film Powered Microsystems

Springer

# Radioisotope Thin-Film Powered Microsystems

# MEMS Reference Shelf

For other titles in this series, go to:
www.springer.com/series/7724

Rajesh Duggirala • Amit Lal
Shankar Radhakrishnan

# Radioisotope Thin-Film Powered Microsystems

Springer

Rajesh Duggirala
Intel Corporation
Hillsboro, OR, USA
rajesh.duggi@gmail.com

Amit Lal
Cornell University
School of Electrical and Computer
Engineering
Ithaca, NY, USA
lal@ece.cornell.edu

Shankar Radhakrishnan
Cornell University
New York, NY, USA
shankarrad@gmail.com

ISBN 978-1-4419-6762-6 e-ISBN 978-1-4419-6763-3
DOI 10.1007/978-1-4419-6763-3
Springer New York Dordrecht Heidelberg London

Library of Congress Control Number: 2010933848

Printed on acid-free paper

Springer is part of Springer Science+Business Media (www.springer.com)

To my grandparents
Ammamma and Tatagaru
and my parents
Usha Rani and Vijaya Sekhar Duggirala

Rajesh

I am thankful to my family and grateful to my friends. I am thankful and grateful to my wife for being both.

Shankar

# Preface

This book presents the technical accomplishments of research that started with the intent of realizing radioisotope micro-power sources suitable for microelectromechanical systems, and subsequently broadened into exploring other micro-scale applications of the unique properties of radioactivity. The text primarily discusses the radioisotope powered electromechanical micro power generators developed as part of the research, and their applications in long lifetime wireless sensors. These electromechanical micro power generators utilize very low quantities of radioisotope fuels, to minimize radiation hazard and safety concerns, and use high efficiency pulsed release of energy to amplify the low power output of low activity radioisotopes by $10^3$–$10^5$ to power microsystems. The text also introduces other micro-scale applications of radioactivity by presenting radioactivity based counting clocks. The success in the demonstration of the above two applications have encouraged us in the SonicMEMS Laboratory at Cornell University to successfully explore new and exciting micro-scale applications of radioisotopes such as massively parallel nano-scale lithography, self-powered lamps, and self-powered ultra-high vacuum pumps and gauges.

This research started in year 2000 when we were investigating micro power generators suitable for long lifetime microsystems including wireless sensor networks. Reliable, compact, and long lifetime micro power sources are needed to successfully deploy wireless sensor networks for applications ranging from environmental monitoring to national security. Our investigations revealed that there were no commercial or even research stage micro power sources available that could satisfy the requirements of the wireless sensor networks. We identified that the main limitation of the available micro power sources was the low energy density of fuels being used, and started exploring the use of high energy density radioisotope fuels to micro power sources. Radioisotope fuels also have the advantage of being very reliable under a wide range of environmental conditions, as the rate of isotope disintegration does not change with ambient conditions. Initially guided by our nuclear engineering colleagues at University of Wisconsin-

Madison, we embarked on this exciting area of research, and to our surprise and delight, discovered new and exciting phenomenon in electrostatics, vacuum science, surface science, and materials science, that led to the research and development of novel applications of radioisotopes at the micro scale.

While we are successfully solving the technological problems currently limiting microsystems by applying the unique properties of radioisotopes, we are aware that the biggest hurdle to the widespread adoption of radioisotope technologies is the perception that radioisotopes are unsafe and should be avoided as much as possible. This is both because of a lack of general knowledge about radioisotopes, and a lack of awareness among the public about the widespread use of radioisotopes around us. In spite of radioisotopes and their applications ranging from nuclear power to nuclear arms playing an important role in all our lives, even engineering students rarely get exposed and educated in the basics of radioactivity. The physics and health-physics of radioisotopes are only taught on a need-to-know basis to people experimenting with radioisotopes in medical and biological sciences. The science and technology of producing and handling radioisotopes is even more elusive, due to the small number of companies that produce radioisotopes commercially. This lack of knowledge prevents a rational cost benefit analysis for every radioisotope application, as was done in the past, where several radioisotope based commercial devices were approved by the Nuclear Regulatory Commission and Food and Drug Administration, including:

1. Tritium powered light sources: These include self-powered exit signs, and watches. These sources use tritium with activities in the range from microCuries to 10–20 Curies. These light sources are regulated by the Nuclear Regulatory Commission and have been approved for use even in elementary schools and airplanes, where highly reliable function is needed to potentially save lives.
2. Gas ionizers: Nickel-63 is used in airport gas detectors to ionize the gas atoms, effusing off the wipes that are used to collect samples from luggage. Although other technologies for gas ionization are possible, the ultimate reliability and

decreased chances of false-negatives in testing provide the justification for the use of radioisotopes to potentially save lives.

3. Smoke detectors: Americium-241 (10 microCurie) is used in smoke detectors for its alpha radiation, which is directed toward an alpha particle detector placed across an air chamber. When smoke enters the air chamber, the smoke particles stop the alpha particles from the crossing the air chamber and being incident on the detector. The lack of alpha particle radiation at the detectors serves as a smoke signal. The stability of alpha particle emission by Americium-241, compared to other ion-emission technologies, enables a highly reliable smoke detector that can save lives.
4. Radioisotope power sources on space missions: NASA uses radioisotope sources (based on plutonium alpha emission), that provide power for several years to tens of years required for mission. Here, no other source would provide the reliability needed for such missions.
5. Radioisotopes in Medicine: Radioisotopes are used everyday in various medical procedures to save lives. These procedures include Positron Emission Tomography (PET) and radiation therapies for many types of cancer. In PET therapy, the specific positron generated by radioisotopes is detected by the resulting gamma particles. In cancer therapy, neutron–boron reaction is used to cause local damage to tissue. Additionally, radioisotopes are used in the discovery of biological phenomena. In many biological labs, radioisotope labeling is used to trace proteins and DNA by size and mass on X-ray film.

In all of the above cases, a risk-benefit analysis led to the commercial acceptance of the devices, because these devices were reliable, and had the potential to save lives. In the case of microsystems such as sensor networks, we face the same choice. Can we develop a technology that might provide high reliability and operation in harsh environments, such that the true benefit of sensor networks to mankind can be achieved? We answer this in the affirmative, with the material in this text. We also introduce the basics of the physics and the health physics of spontaneous disintegration, so the public can make a rational risk-benefit assessment of all the new applications.

We hope that this new area of radioisotope based micro-power sources and this text book will excite educators, policy makers, environmentalists, and the public at large to appreciate radioisotopes and their various applications that might make our lives safer in the future.

| | |
|---|---|
| USA | R. Duggirala |
| USA | A. Lal |
| USA | S. Radhakrishnan |

# Acknowledgement

We would greatly like to thank the tax-payers of the United States of America and the program managers at DOE and DARPA who funded this work. Without their support, this idea would have remained an interesting curiosity.

We would also to thank the team of Nuclear Engineers at University of Wisconsin-Madison, Prof. Michael Corradini, Prof. James Blanchard, and Prof. Douglas Henderson, who had the courage to support a MEMS group to start radioisotope based microsystem research. We would also like to thank Dr. Madan Dubey and Dr. Ron Polcawich who supported the fabrication of micro fabricated devices at the Army Research Labs. Numerous industrial engineers at Isotope Products Labs and NRD helped in realizing how much we needed to rediscover about radioisotope thin films.

The material presented in this book is a culmination of work and intellectual contributions from several current and previous students of the SonicMEMS Laboratory, including Dr. Hui Li, Prof. Hang Guo, Dr. Norimasa Yoshimizu, Dr. Shyi-Herng Kan, Steven Tin, and Yuerui Liu, in addition to the authors of this book.

## TABLE OF CONTENTS

# LIST OF FIGURES

# LIST OF TABLES

# Chapter 1
# Radioactivity and Radioisotopes

## 1.1 Introduction

Radioactivity was discovered in 1896 by Henri Becquerel, when he found that a mixture of uranium salts emitted a mysterious penetrating radiation that passed through thin sheets of metal. Since then, radioactivity has been applied in many diverse areas within the fields of industry, agriculture, medicine, and the military. In industry, sealed radioactive sources are used in industrial radiography, gauging applications, and mineral analysis. Short-lived radioactive material is used in flow tracing and mixing measurements. In agriculture, gamma sterilization is used for food preservation and sterilization of bulk commodities. In medicine, gamma sterilization is also used for sterilizing medical supplies, but more importantly, radioisotopes are indispensable in both diagnosing and treating some diseases including cancer. However, the most prevalent use of radioactivity is in the generation of electrical power. Applications benefiting from nuclear power generation range from industries and residences to submarines and deep space probes.

## 1.2 Radioactive Decay

Radioactive decay is the process in which an unstable nucleus spontaneously disintegrates to emit energy in the form of ionizing particles and electromagnetic radiation. The spontaneous decay may lead to changes in the charge (Z) and mass (M) of the unstable atomic nucleus. The difference between the rest energy of the parent nucleus and the rest energy of the daughter nucleus and the emitted particles is transformed into the kinetic energy of the daughter nucleus and the emitted particles. A radioisotope

R. Duggirala et al., *Radioisotope Thin-Film Powered Microsystems*,
MEMS Reference Shelf 6, DOI 10.1007/978-1-4419-6763-3_1,

is a radioactive isotope of an element. Radioisotopes can either be natural or artificial. Examples of natural radioisotopes include unstable isotopes arising from the decay of primordial uranium and thorium. Artificial radioisotopes are manufactured by producing a combination of neutrons and protons that does not exist in nature. The most common method uses neutron activation in a nuclear reactor. This involves the capture of a neutron by the nucleus of an atom resulting in an excess of neutrons (neutron rich). Some radioisotopes are manufactured in a cyclotron in which protons are introduced to the nucleus resulting in a deficiency of neutrons (proton rich).

## 1.3 Radioactive Decay Law

All radioisotopes decay at a rate obeying the universal law of radioactive decay. The radioactive decay law states that the number of radioisotope nuclei within a population of $N$ radioisotope nuclei decaying at any instant is proportional to $N$, or

$$\frac{dN}{dt} = -\lambda N, \tag{1.1}$$

where $\lambda$ is the radioactive decay constant that characterizes the probability of decay of any nucleus in unit time. A convenient way to express the decay probability of any radioisotope nucleus is the half-life $\tau_{1/2}$, which is the period in which half of the original number of nuclei in any population undergo decay. The half life can be calculated from $\lambda$ using (1.1). If a given radioisotope nuclei population started out with $N_0$ parent nuclei at time $t = 0$, then the number $N$ of parent nuclei in the population at any time $t$ is

$$N = N_0 e^{-\lambda t}. \tag{1.2}$$

To calculate $\tau_{1/2}$, $N(\tau_{1/2} = \frac{N_0}{2})$ is used in (1.2) to give

$$\tau_{1/2} = \frac{ln2}{\lambda}. \tag{1.3}$$

The rate at which a given mass of radioisotope decays is called the activity of the radioisotope $A_r$, and is defined as the number of nuclei of the radioisotope decaying in unit time, and given by

$$A_r = -\frac{dN}{dt} = \lambda N. \tag{1.4}$$

The SI unit of radioisotope activity is Becquerel ($Bq$), which stands for 1 decay/second. A commonly used unit is Curie ($Ci$), which is equal to $3.7 \times 10^{10}$ Bq.

## 1.4 Types of Radioactive Decay

Radioactivity can be of different types, depending on the types of emitted particles and radiation as follows [1, 2]:

### Alpha Decay

An alpha decay is characterized by the emission of alpha particles, i.e., a double-ionized helium atoms. The nuclear reaction can be represented as

$${}_{Z}^{A}N \rightarrow_{Z-2}^{A-4} N +_{2}^{4} \mathrm{He}. \tag{1.5}$$

The alpha particles emitted in decay of a given nucleus can have the same energy or a set of discrete energies. The alpha particles are typically emitted with a kinetic energy of 4–9 MeV depending on the radionuclide, and may be accompanied by electromagnetic radiation as the daughter nucleus transitions from excited states to its ground state. Alpha decay is characteristic of natural and artificial radioisotopes with large atomic numbers, such as $Po - 210$, $Am - 214$, and $Cm - 242$.

### Beta decay

A radioisotope decay that results in the emission of a beta particle, i.e., an electron $e^-$ or a positron $e^+$, is called a beta decay. The beta-minus decay, which results in the emission of an electron and an antineutrino $\nu^\sim$, can be represented as

$${}_{Z}^{A}N \rightarrow_{Z+1}^{A} N + e^- + \nu^\sim. \tag{1.6}$$

Because the distribution of decay energy between the two emitted particles is random, the energy spectrum of electronic beta-particles is continuous and covers the range from zero to the maximum energy of the beta particle. The maximum beta energy released ranges from 0.018 MeV for $^{3}$H–16.4 MeV for $^{12}$N. Beta-minus decay occurs in both natural and artificial radionuclides.

The beta-plus decay, which results in the emission of a positron and a neutrino $\nu$, can be represented as

$$ {}^{A}_{Z}N \rightarrow {}^{A}_{Z-1} N + e^{+} + \nu. \tag{1.7}$$

The energy spectrum of positronic beta-particles is also continuous. After escape from the nucleus, the positron unites with an electron to form two quanta of electromagnetic radiation. Beta-plus decay occurs in just artificial radionuclides.

## Gamma Decay

Gamma decay refers to any decay that produces gamma rays ($\gamma$), i.e., electromagnetic radiation. If any radioactive decay results in a daughter nucleus formed in an excited state, then the transition of the nucleus from the excited state to the ground state is followed by the emission of $\gamma$ rays with discrete energies, and can be represented as

$$ {}^{A}_{Z}N^{*} \rightarrow {}^{A}_{Z} N + \gamma. \tag{1.8}$$

Here, "*" means that the nucleus is in an excited state. Since $\gamma$ rays have no charge or mass, the nucleus does not change its atomic number ($Z$) or mass ($M$). The energy of $\gamma$ quanta accompanying an alpha decay can reach 0.5 MeV, and the energy of $\gamma$ quanta accompanying an beta decay can reach 2.5 MeV. Gamma radiation can also be stimulated by other means, such as neutron bombardment.

## Electron Capture

Electron capture is the phenomenon where a nucleus with too many protons, but not enough energy to emit a positron, captures one of the orbit electrons, usually from the K shell, to form a neutron and a neutrino. This process is followed by electronic transitions to fill the vacancy formed in the electronic shells, which result in the emission of X-rays and Auger electrons. The decay is represented as

$$^{A}_{Z}N + e^{-} \rightarrow^{A}_{Z-1} N + X - ray + \nu. \tag{1.9}$$

Here, $\nu$ is the neutrino emitted as a result of the electron capture. The energy associated with electron capture is low. An example of an isotope that decays by electron capture is $^{55}$Fe.

### Spontaneous Fission

Very heavy elements sometimes fission spontaneously without neutron bombardment. It can be represented as

$$^{A}_{Z}N \rightarrow x + y + n's, \tag{1.10}$$

where $x$ and $y$ are fission fragments and $n$ represents a neutron. The process is very much like a neutron induced fission. Spontaneous fission happens rarely, and most of the released energy is retained in the fission fragments.

### Neutron Emission

Neutron emission is a type of radioactive decay in which a neutron is simply ejected from a nucleus. It can be represented as

$$^{A}_{Z}N \rightarrow^{A-1}_{Z} N + n. \tag{1.11}$$

Very few radioisotopes emit neutrons. Some examples are $^{13}$Be and $^{14}$C.

### Proton Emission

A radioactive decay in which a proton is emitted from a nucleus is called proton emission. Proton emission can occur from excited states in a nucleus following a beta-decay, or can occur from the ground state of a very proton rich nucleus. It can be represented as

$$ {}_{Z}^{A}N \rightarrow {}_{Z-1}^{A-1}N + p. \tag{1.12} $$

Proton emission is not seen in naturally occurring isotopes. Proton emitters can be produced via nuclear reactions, usually with a particle accelerator. Some examples of proton emitters are $^{5}$Li and $^{11}$N.

## 1.5 Interaction of Ionizing Radiation with Matter

Ionizing radiation from radioactive decay, comprising of charged particles and electromagnetic waves, interacts with matter via elastic and nonelastic scattering events with the electrons and nucleus of the atoms of that substance [2]. In an elastic scattering, no new particles are created, no particles disappear, and particles involved do not change their internal energy states. Elastic scattering events result in the total kinetic energy of the interacting particles being preserved, redistribution of the total kinetic energy among the interacting particles, and often a change in the direction of motion of the interacting particles. In contrast, nonelastic scattering events could result in the creation of new particles and change in the internal energy states of the resulting nuclei. The kinetic energy of the moving particle is converted into either the excitation energy of the nucleus, radiation energy, or the rest energy of newly created particles. The type of interaction any incident radiation undergoes depends both on the type of radiation and the material it is passing through.

### Alpha Radiation

Alpha radiation interacts with matter through nonelastic and elastic scattering with electrons and elastic scattering with the nuclei in the material. The alpha particles gradually lose their energy to nonelastic scattering with the electrons until their energy becomes comparable to the average energy of thermal motion of the medium particles. The primary energy loss mechanism is the nonelastic Coulombic interaction with substrate electrons, which either causes ionization or excitation of the atoms of the substance (ionization stopping). The alpha particles typically travel straight because the probability of elastic collision with nuclei is very low, owing to the low ratio of the nucleus diameter to the atom diameter ($\approx 10^{-4}$), and the path length $R'$ depends on the initial energy $E_{0\alpha}$. Empirical tables and formulas for $R'$ in various materials are given in physical handbooks. For example, $R'$ of $^{226}$Ra alpha particles ($E_{0\alpha} = 4.78\,\text{MeV}$) is about 3.3 cm in air and 33 μm in water.

### Beta Radiation

Beta particles interact with particles in the matter they are passing and lose their kinetic energy via two dominant mechanisms, ionization loss and radiation loss. Electrons with low kinetic energy (<0.5 MeV) lose their energy primarily through ionization loss, where the beta electrons undergo elastic and nonelastic collisions with the atoms in the irradiated substance. Electrons with high kinetic energy can also lose a significant portion of their energy through radiation loss, where the deceleration of the beta electron in the Coulombic field of a nucleus in the matter results in the generation of Bremsstrahlung, or soft electromagnetic radiation. In both types of interactions, the change in the kinetic energy of the incident electrons can be significant, and the deviations in the direction of motion quite large. As a result, the motion of incident beta electrons in matter can be chaotic, and especially for energies <100 keV, the motion resembles diffusion rather than forward motion in the initial direction. The penetration range of the beta electrons increases with the increasing initial energy of the beta electrons. A detailed discussion of penetrating ranges of beta electrons in matter is carried out in subsequent chapters.

### Gamma Radiation

In contrast with the interaction of charged particles with matter, the interaction of gamma radiation with matter is primarily through the photoelectric effect, Compton scattering, and formation of electron–positron pairs. Because the electromagnetic quanta have zero rest mass, travel at the velocity of light, and being chargeless are not subject to the long range Coulombic forces, the probability of their interaction with the particles in the matter is quite low. Therefore, their penetrating range in matter tends to be quite high, and they are very difficult to shield against.

### Dose and Dose Rate

The energy transfer process between any type of radiation incident on any material is captured through two parameters, dose and dose rate. The energy transferred to a material by ionizing radiation is quantitatively characterized by the absorbed radiation dose $D_{abs}$, which is defined as the ratio of the ionizing radiation energy $E$ transferred to the material with mass $m$, or

$$D_{abs} = \frac{E}{m}. \tag{1.13}$$

The SI unit of $D_{abs}$ is Gray ($Gy$), which is equal to 1 $J$ of energy absorbed per Kg of the material. The unit for dose used in the context of radiation incident on humans is *rad* (Radiation Absorbed Dose), where 1 rad=0.01 Gy. The biological effect of the absorption of radiation energy by humans is captured using the unit *rem* (Roentgen Equivalent Man). To relate the absorbed dose of specific types of radiation to their biological effect, a "quality factor" must be multiplied by the dose in rad, which then shows the dose in rems. For gamma rays and beta particles, 1 rad of exposure results in 1 rem of dose. The SI unit which may be used in place of rem is sievert (Sv), where 1 Sv=100 rem.

The absorbed dose rate $P_D$ is the dose absorbed in unit time, or

$$P_D = \frac{D_{abs}}{t}. \tag{1.14}$$

The SI unit of absorbed dose rate is gray per second (Gy/s = 1 W/Kg).

## 1.6 Radiation Safety

All forms of ionizing radiation have sufficient energy to ionize atoms that may destabilize molecules within cells and lead to tissue damage. Excessive exposures to even non-ionizing radiation will cause tissue damage. Therefore, it is important to consider radiation safety when considering any application of radioisotopes. While the maximum radiation exposure humans can safely tolerate depends on the type of radiation, the type of radioactive material, and the part of the human body, most safety regulations recommend limits shown in Table 1.1. Any application of radioisotopes has to be designed with the exposure limits in mind.

For microsystems, the safety of radioisotopes can be evaluated using the following criteria: (1) penetration range of primary radiation; (2) generation of Bremsstrahlung secondary radiation during the stopping of primary radiation; (3) effusivity of the

Table 1.1: Maximum radiation exposure limits (rem/year) for radiation workers, as prescribed by US Nuclear Regulatory Commission (NRC) and US Occupational Safety and Health Assessment (OSHA). Source: Office of Research Services, National Institute of Health, USA

| Exposed parts | NRC | OSHA |
|---|---|---|
| Whole body | 5 | 5 |
| Lens of the eye | 15 | 5 |
| Skin | 50 | 30 |
| Extremeties | 50 | 70 |
| General public | .01 | NA |

radioisotope source, if gaseous; (4) chemical toxicity, in case of release and ingestion or inhalation; and (5) security and non-proliferation risk.

### Safe Radioisotope Fuels Suitable for Terrestrial Applications

Radioisotopes employed in terrestrial microsystems should ideally satisfy the following criteria: (1) minimal shielding should be required for stopping both the primary radiation and the resulting Bremsstrahlung; (2) radioisotope sources should not be prone to dispersal through effusion; and (3) they should not be chemically toxic. Given these requirements, radioisotopes emitting low energy ($E_{rad,avg} < 100\,\text{keV}$) $\beta$-radiation are particularly suitable for terrestrial microsystems. Low-energy $\beta$-radiation can be shielded easily by thin ($<100\,\mu\text{m}$) sheets of most metals, and the resulting Bremsstrahlung is very weak, as just $<0.1\%$ of $E_{rad}$ is converted into photons [3]. In contrast, $\beta$-radiation with average energies $E_{rad,avg} > 500\,\text{keV}$ is difficult to shield due to its considerable penetrating power arising from the low mass of electrons, and generates significant Bremsstrahlung [4]. Additionally, even though $\alpha$-radiation is easily shielded due to the large mass and ionized state of helium ions, most $\alpha$-radioisotopes also emit high penetration range $\gamma$ radiation from the decay chain, are highly toxic chemically [3], and are typically unsafe from proliferation standpoint. This makes large activities of $\alpha$-radioisotopes unsuitable for widespread deployment in terrestrial applications. Furthermore, $\gamma$-radiation requires heavy shielding because of its high penetration power [3], and is unsuitable for most terrestrial applications.

### Safe Radioisotope Fuels Suitable for Long Lifetime Microbatteries in Terrestrial Applications

Long half-lifetime radioisotopes emitting low energy $\beta$-radiation include tritium ($^{3}$H), nickel-63 ($^{63}$Ni) and promethium-147 ($^{147}$Pm) (Table 1.2), which are typically employed in thin film form to minimize $\beta$-radiation self-absorption [5].

Table 1.2: Comparison of radiation properties of $^{3}$H, $^{63}$Ni, and $^{147}$Pm thin films

| Parameters | $^{3}$H | $^{63}$Ni | $^{147}$Pm |
|---|---|---|---|
| Half-life (years) | 12.4 | 100.3 | 2.64 |
| Radiation type | $\beta$ | $\beta$ | $\beta$, weak $\gamma$ |
| $E_{rad,avg}$ (keV) | 5.7 | 17.3 | 63.5 |
| $E_{rad,max}$ (keV) | 18.6 | 63 | 220 |

## 1.7 Availability of Radioisotopes

### 1.7.1 Tritium

Tritium is widely used in its gaseous form in self-luminescent signs [6]. However, most practical uses of $^{3}$H use its metal tritides, especially titanium tritide, which can have a specific activity of up to 1,000 Ci/g [2]. It is stable in air, and is water resistant up to 100 C. However, under normal temperature and pressure, $^{3}$H effuses out of titanium tritide at a rate of $2.5 \times 10^{-6}$ Ci/h per *curie* of adsorbed $^{3}$H (Ref). Recently, tritiating silicon, both porous crystalline and amorphous, is gaining popularity because of renewed interest in $^{3}$H powered silicon betavoltaics [7], where the beta source can be deposited right next to the betavoltaic junction in silicon. Tritium is a by product of nuclear fission reaction, and Canada is the largest producer (3.5 kg/year) of $^{3}$H today owing to its large number of nuclear fission based power plants [8].

### 1.7.2 Nickel-63

Nickel-63 is readily electroplated and is used widely in industrial applications including electron capture devices [9] and measuring thickness of metal films. Nickel-63 is produced in the

United States by the Oak Ridge National Laboratories (ORNL) by irradiating highly enriched $^{62}$Ni targets with high neutron fluxes in a high flux isotope reactor (HFIR), and processing the resulting material to remove undesired by products and impurities. Production of large quantities of high specific activity ($> 10\,\mathrm{Ci/g}$) $^{63}$Ni is possible using this method [10].

### 1.7.3 Promethium-147

Promethium-147 deposited on the surfaces to be irradiated as promethium oxide $Pm_2O_3$ was widely used in the past in low power betavoltaic microbatteries [11] for applications including cardiac pacemakers. High activity levels of $^{147}$Pm were traditionally obtained by the processing of uranium fission products, and until the early 1980s, inventories as high as 20,000 *curies* had been available for distribution through the Oak Ridge National Laboratories (ORNL) Isotope Distribution Office. Unfortunately, because the required large-scale fission product processing capabilities are no longer available in the United States, $^{147}$Pm has to be imported from Russia today. However, because of the broadening interest in $^{147}$Pm for US homeland security and industrial applications, the ORNL Nuclear Medicine Program is currently developing reactor production of neodymium-147 from enriched neodymium-146 in the High Flux Isotope Reactor (HFIR) and has demonstrated the efficient separation of $^{147}$Pm from neodymium [12].

# Chapter 2
# Radioisotope Thin Films for Microsystems

## 2.1 Introduction

Radioisotopes can be employed in microsystems in a variety of ways to exploit the many unique properties of radioactivity:

1. The kinetic energy of the emitted radiation can be converted into electrical energy for micropower generation
2. The energetic charged particles emitted can be directly collected and charge-separation based electrostatic actuation of cantilevers can be enabled for autonomous sensors
3. The near constant probability of decay of nuclei could be utilized for realizing frequency standards.

This chapter serves as an introduction to the aforementioned applications of radioisotopes in microsystems, and the subsequent chapters provide the details.

## 2.2 Radioisotope Micropower Generation

Autonomous microsystems deployed in remote locations need to have long lifetimes to avoid prohibitively expensive periodic replacement. Additionally, some autonomous microsystems need to be very compact ($< 1\,\mathrm{cc}$), so they can be deployed in small spaces. Applications requiring such compact long-lifetime autonomous microsystems include the low power wireless sensors that promise to revolutionize applications ranging from environmental monitoring [13, 14] to civil infrastructure health monitoring [15], and implantable medical devices such as pacemakers [11] and intracranial implants [16].

R. Duggirala et al., *Radioisotope Thin-Film Powered Microsystems*,
MEMS Reference Shelf 6, DOI 10.1007/978-1-4419-6763-3_2,

Compact microsystems with long-lifetimes can be realized by employing low power sensor and wireless communication subcomponents [17] powered by compact high energy capacity microbatteries. Low power sensors can be realized by taking advantage of the recent advances in microelectromechanical systems (MEMS) based transducer and packaging technology, and low power wireless signal generators can be realized using advanced CMOS integrated circuits. Compact high energy capacity microbatteries can be realized either by using high energy density fuels.

In particular, high energy density (≈1–100 MJ/cc) radioisotope fuels with long half-lifetimes (1–100 years) are employed in this book to realize high energy capacity microbatteries. In comparison, conventional electrochemical and hydrocarbon fuels offer energy densities of 1–5 kJ/cc [18] and 10–20 kJ/cc [19] respectively. Radioisotope fuels are also reliable under severe ambient conditions, as they emit radiation from spontaneously decaying at a rate that is almost invariant with ambient conditions.

### 2.2.1 Radioisotope Thin Film Fuels

In this book, the radiation kinetic energy emitted from thin films of radioisotopes is harvested to generate electrical energy. The radiation energy emitted from radioisotopes can be in the form of: doubly charged helium ions emitted with average energy $E_{rad,avg} > 5\,\mathrm{MeV}$, called $\alpha$ radiation; electrons ($\beta^-$) and positrons ($\beta^+$) emitted with $E_{rad,avg}$ ranging from 5.3 keV to 2 MeV, called $\beta$ radiation; and highly energetic electromagnetic radiation or photons emitted with $E_{rad,avg}$ in the range of MeV's, called $\gamma$ radiation. The selection of radioisotope fuel for any application is determined by the microbattery requirements of output power density, energy density, cost, and lifetime, and safety limitations (Table 2.1).

### 2.2.2 Power Density, Energy Density, and Lifetime of Radioisotope Fuels

The radiation power density $P_{g,dens}$ generated within a radioisotope fuel can be written as

$$P_{g,dens} = 3.7 \times 10^{10} \times SA_r \times \rho_r \times E_{rad,avg}, \tag{2.1}$$

Table 2.1: Comparison of radiation properties of $^{3}$H, $^{63}$Ni, and $^{147}$Pm thin films

| Parameters | $^{3}$H | $^{63}$Ni | $^{147}$Pm |
|---|---|---|---|
| Half-life (years) | 12.4 | 100.3 | 2.64 |
| Radiation type | $\beta-$ | $\beta-$ | $\beta-$, weak $\gamma$ |
| $E_{rad,avg}$ (keV) | 5.7 | 17.3 | 63.5 |
| $E_{rad,max}$ (keV) | 18.6 | 63 | 220 |
| Highest available specific activity (curie/cc) | 500 | 133 | 4300 |
| Optimal layer thickness for $\eta_r$ >75% (µm) | 0.1 | 0.8 | 6 |
| Power density ($\frac{\mu W}{cm^2}$) | 0.7 | 0.45 | 827 |

where $SA_r$ and $\rho_r$ are the specific activity (curies/g) and density (g/cc) of the radioisotope source respectively, and $E_{rad,avg}$ is the average energy of the particles or radiation emitted. For maximizing $P_{g,dens}$ in any material, it is desirable to maximize $SA_r$ by enriching the radioisotope fuel. Furthermore, since $P_{g,dens}$ decreases exponentially with time following the decrease in $SA_r$ as

$$SA_r(t) = SA_r(0)e^{0.3t/\tau_{1/2}}, \tag{2.2}$$

it is desirable to select radioisotopes with long half lifetimes $\tau_{1/2}$ for high energy capacity.

A portion of $P_{g,dens}$ is self-absorbed by the radioisotope fuel [3], and the rest is emitted to produce radioisotope fuel output energy density $P_{r,out}$ given by

$$P_{r,dens} = P_{g,dens} \times \eta_r. \tag{2.3}$$

Here, $\eta_r$ is the energy emission efficiency of the radioisotope fuel, and depends on the geometric form factor.

## 2.2.3 Review of Radioisotope Micropower Generation

Radioisotope energy can be converted to electrical energy at the micro-scale in any of the previously developed energy converters (Fig. 2.1): (1) thermoelectric engines; (2) direct charge nuclear batteries; (3) direct conversion batteries; or (4) indirect conversion batteries.

Thermoelectric engines first convert the kinetic energy of the particles into heat via collisions against target particles, and then transform the heat into electricity either by dynamic heat engines or by direct conversion devices such as thermoelectrics [1, 2] (Fig. 2.2). Thermoelectric conversion schemes tend to be inefficient at the micro-scale because it is difficult to realize high temperatures or large heat gradients at the micro-scale. The surface to volume ratios tend to be high at the micro-scale, and heat losses

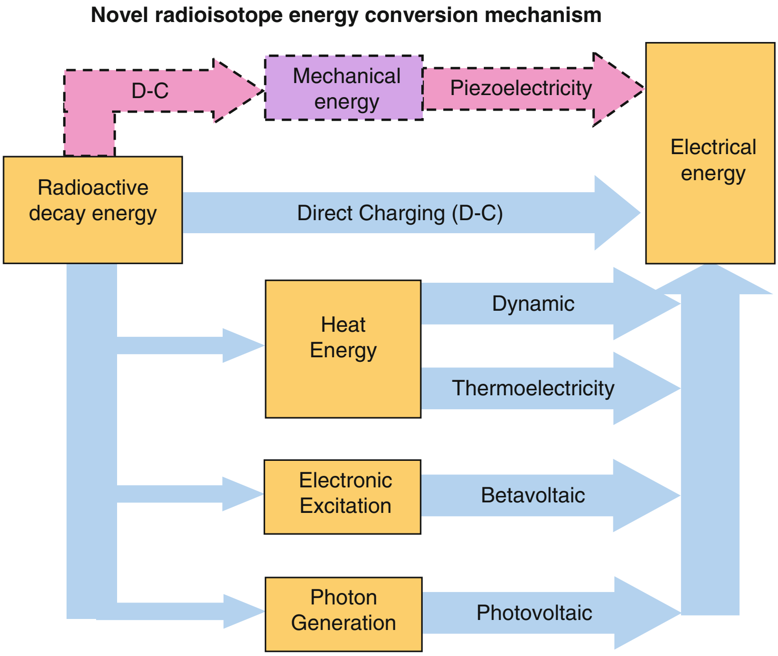

Figure 2.1: Schematic illustrating the various radioisotope energy conversions, including the newly developed radioisotope electro mechanical power generation presented in this book

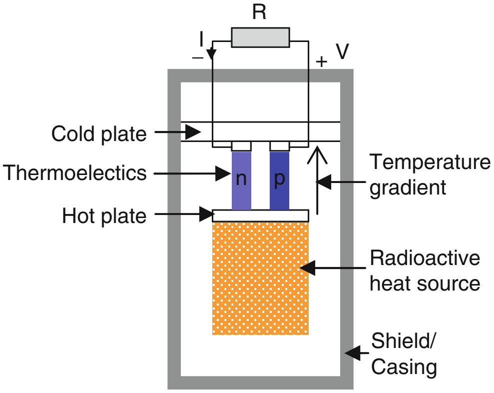

Figure 2.2: Schematic illustrating a radioisotope powered thermoelectric generator

can be significant. Additionally, realization of high temperatures can require large activities of the radioisotope, and that limits their utility in microsystems use where radiation safety is important. Therefore, nuclear batteries, radioisotope energy converters that do not use heat cycles, are more applicable at the micro-scale. Nuclear batteries here refer to the radioisotopic power generators that do not use heat engines in the energy conversion process.

### Direct Charge Nuclear Battery

A direct charge nuclear battery generates electricity by collecting the charged particles emitted by radioisotopes across an air-gap or dielectric capacitor, and supplying any electrical load with that charge at a voltage that builds up across the capacitor because of the charge separation (Fig. 2.3). Generally, a direct charging nuclear battery is made up of two electrically isolated concentric spheres or coaxial tubes or parallel plates acting as two electrodes, and the space in between filled with vacuum or a dielectric material that does not absorb the radiation. One electrode is coated with the radioisotope thin-film, and the other electrode acts as the charge collector. Electrical loads are connected across the two electrodes. This type of battery was first demonstrated by Moseley in 1913 [20].

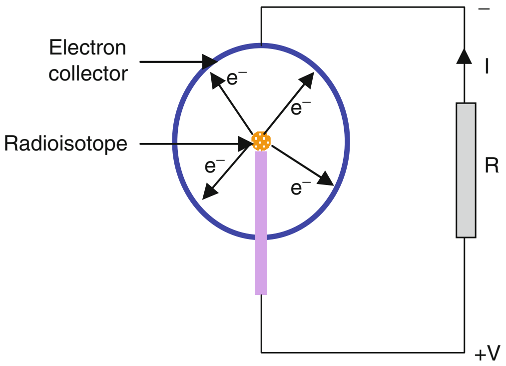

Figure 2.3: Schematic illustrating a radioisotope direct charging generator

Direct charged nuclear batteries typically supply low current (≈nAs) at very high voltages (up to hundreds of kVs). The current is determined by the activity of the radioisotope. For example, the current outputs of 1 millicurie $\alpha$ and $\beta$ radioisotopes is just 5.9 pA and 11.8 pA respectively. The operating voltage of the battery depends on the maximum energy of the emitted charged particles, charge leakages in the air gap, and the electrical load. The efficiency of energy conversion depends on the ratio of the battery voltage to the average kinetic energy of emitted particles, as that is the energy each emitted charge particles transfers to the electrostatic system while overcoming the built up voltage. Therefore, high energy conversion efficiency requires voltages to be built up across the capacitor, which greatly limits the application of this battery.

### Direct Conversion Nuclear Battery

Direct conversion nuclear batteries operate by utilizing the radiation output of a radioisotope to ionize atoms in a medium between two electrodes, and use a voltage gradient set-up between the two electrodes to separate and collect the ionized charges and supply to any electrical load connected across the two electrodes. Each ionizing particle or quanta in the radiation can ionize many atoms, depending on the ratio of the average kinetic energy of the ionizing particle and the average ionization energy for the atoms. Since the average ionization energy for most atoms tends to be in the range of 1–100 eV, and most radioisotopes emit radiation with average kinetic energy ranging from keV to MeV, a much larger current can be realized using direct conversion nuclear batteries compared to direct charged nuclear batteries. The voltage gradient can be realized using one of two ways. The two electrodes in the battery can be constructed from two different metals, and the contact potential difference between the two can be used for producing the voltage gradient. Such batteries are called contact potential difference (CPD) battery (Fig. 2.4). Alternatively, the two electrodes could be across p-n junctions, and the electric fields set-up across the depletion region could be used to separate the charged particles (Fig. 2.5).

In a CPD battery, the open circuit voltage, defined as the voltage that builds up across the battery when there is no load connected across its terminals, equals the contact potential difference between the two metals, which is generally equal to or

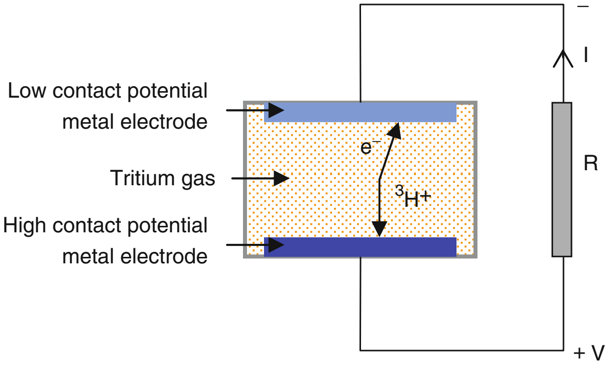

Figure 2.4: Schematic illustrating a radioisotope powered contact potential difference generator

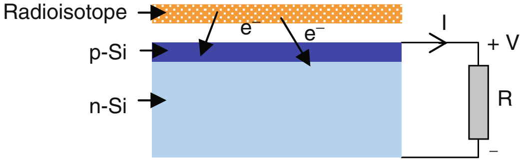

Figure 2.5: Schematic illustrating a radioisotope powered electronvoltaic generator

less than one volt [21]. While a CPD battery can be constructed by depositing the radioisotope on one of the electrodes and filling up the gap between the electrodes with a gas, an alternative is to fill the gap between the two electrodes using a gaseous mixture containing a gaseous radioisotope source. In such a battery, a large part of the beta particle energy can be transformed into useful current, as there are no losses of kinetic energy due to self-absorption inherent in solid sources. An example of a gaseous radioisotope is $^3$H, which can be mixed uniformly with some other gas. The CPD battery using tritium gives about 100 times the current from the beta source itself [22]. However, even though the current is higher for a CPD nuclear battery compared to a direct conversion type nuclear battery, it is still small in absolute value. And for the ionization of the working gas to be efficient, the size of the CPD nuclear battery has to be large. Furthermore, the battery itself has a very high electrical impedance since the two electrodes form a capacitor. This limits the utility of CPD nuclear batteries in microsystems.

In an electronvoltaic battery, the open circuit voltage depends on the energy band-gap of the semiconductors used in the junction. For silicon electronvoltaics, it can be up to a few 100 mV. Larger voltages can be realized by connecting several cells in series. Since each electron-hole pair generation requires $\approx$3 eV, large current multiplication factors can be realized. For example, one $\beta$-particle from strontium-90 produces about 200,000 electron–hole pairs. However, one important drawback of junction-type nuclear batteries is that the lattice structure in the p–n junctions is susceptible to radiation damage, and subsequently, degradation in performance. This typically starts becoming important when the energy of charged particles exceeds a certain threshold, about 200 keV for Si [22]. Since for most radioisotopes the average energy of the emitted charged particles tends to be larger than 200 keV, electronvoltaic based nuclear batteries tend to have short lifetimes. Since $\alpha$-particles are much bigger and their kinetic energies are generally greater than 1 MeV, silicon alpha voltaic batteries have very limited lifetimes. In contrast, low power $\beta$-particle powered silicon electronvoltaic based nuclear batteries can have long lifetimes [11].

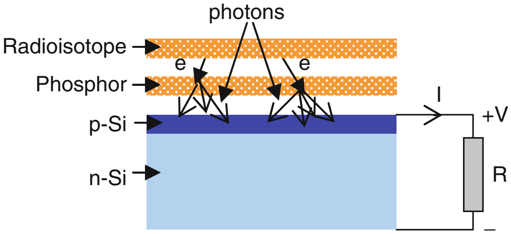

Figure 2.6: Schematic illustrating a radioisotope powered indirect conversion generator

### Indirect Conversion Nuclear Battery

Indirect conversion nuclear batteries operate by first converting the kinetic energy of charged particles into light by irradiating radioluminescent materials, and then converting the generated light into electrical energy using photovoltaics [1] (Fig. 2.6). By introducing the intermediate energy conversion step, the radiation sensitive photovoltaic elements are partially shielded from radiation damage. However, since it takes two processes to generate electricity, the efficiency of each process has to be relatively high for a good overall energy conversion efficiency. The efficiency of the first step can be improved by realizing high absorption of emitted particles in the phosphor, improving the conversion from nuclear energy to light, and by minimizing the light absorption in the phosphor. The efficiency of the second step depends on the fraction of the light that can be absorbed in the depletion region of the solar light, and on the energy band gap of the semiconductor used in the solar cell. While reasonable energy conversion efficiencies can be realized, the partial exposure of the solar cell may still result in damage and cause performance degradation.

## 2.2.4 $^{63}$Ni Micropower Generation

Thin film $^{63}$Ni is well suited for long lifetime safe microsystems because of its 100 year half-lifetime and its relatively low radiation and chemical risk. Thin films of $^{63}$Ni can be handled with minimal shielding requirements, because the $E_{^{63}\mathrm{Ni},avg} = 17.3\,\mathrm{keV}$

$\beta$-electrons cannot penetrate the dead layer of human skin [3], and the resulting Bremsstrahlung is insignificant. Additionally, $^{63}$Ni is not known to effuse out of thin films at temperatures as high as 400 C. Consequently, it is employed in a variety of industrial applications including electron capture devices [9]. However, $^{63}$Ni thin films suffer from very low power densities (0.1–1 $\mu$W/cm$^2$), and lead to microbatteries with low power densities ($< 50\,$nW/cm$^3$) [23]. Therefore, $^{63}$Ni microbatteries have found limited use in microsystems, which typically require 0.1–100 mW/cc.

In this book, the low power output limitation of $^{63}$Ni thin films is overcome by employing them to fuel pulsed power microbatteries (Chaps. 3 and 4), so their 0.1–1 $\mu$W/cm$^2$ power output can be integrated to produce 0.1–1% duty cycle 0.01–1 mW/cc electrical power pulses (Fig. 2.7) useful for periodically sampling wireless sensor microsystems (Fig. 2.8) [17].

Furthermore, pulsed electrical power can be generated from $^{63}$Ni thin films by employing any of the above energy converters to convert the low <1 $\mu$W/cm$^2$ radioisotope power to electrical power, integrating the electrical power using energy storage elements such as capacitors, and using low-duty cycle switching for pulsed discharge of the stored electrical energy across loads (Fig. 2.9). However, practical switches for isolating the storage capacitors from loads during the integration phase typically have leakages that result in inefficient integration of $< 1\,\mu$W electrical power for pulsed electrical power generation. This problem is overcome using a novel electromechanical energy converter that efficiently integrates the low 0.1–1 $\mu$W/cm$^2$ $^{63}$Ni power output to generate: (a) continuous power output of 10–100 nW/cc; (b) 0.1–1% duty cycle 0.01–1 mW/cc power pulse; and (c) 0.1–1% duty cycle discharge generated wireless RF pulses detectable up to 3.6 m, with an overall energy conversion efficiency of 4.13%.

The electro-mechanical converter consists of a radioisotope actuated reciprocating piezoelectric unimorph cantilever with integrated betavoltaics [24], and is an extension of the radioisotope-powered self-reciprocating cantilever demonstrated previously [25, 26]. Figure 2.10 illustrates the operating principle of the self-reciprocating cantilever, where a radioisotope thin film emitting

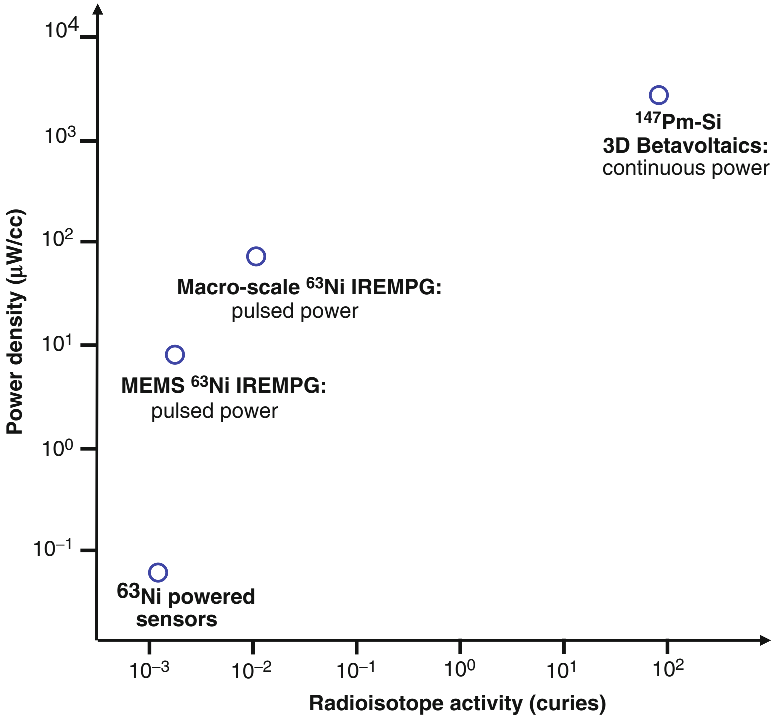

Figure 2.7: Schematic illustrating the performance space of the radioisotope powered microbatteries and zero-power sensors developed in this book. The $^{147}\mathrm{Pm}-\mathrm{Si}$ betavoltaic microbattery performance is estimated based on the design and performance of realized 3D silicon betavoltaics

energetic charged particles is used to electrostatically actuate a cantilever. The actuation charges increase with time, resulting in the cantilever deformation increasing with time. Thus, the cantilever acts a mechanical energy integrator. For suitable initial gap separations, the tip of the cantilever eventually makes contact with the radioactive thin film, and the accumulated charges get neutralized via charge transfer. As the electrostatic force is nulled, the cantilever is released and set into vibrations. Thus, the integrated stored mechanical energy is released as a pulsed mechanical energy output. This pulsed mechanical energy can be converted into a pulsed electrical energy output by attaching a piezoelectric element to the cantilever. The piezoelectric element

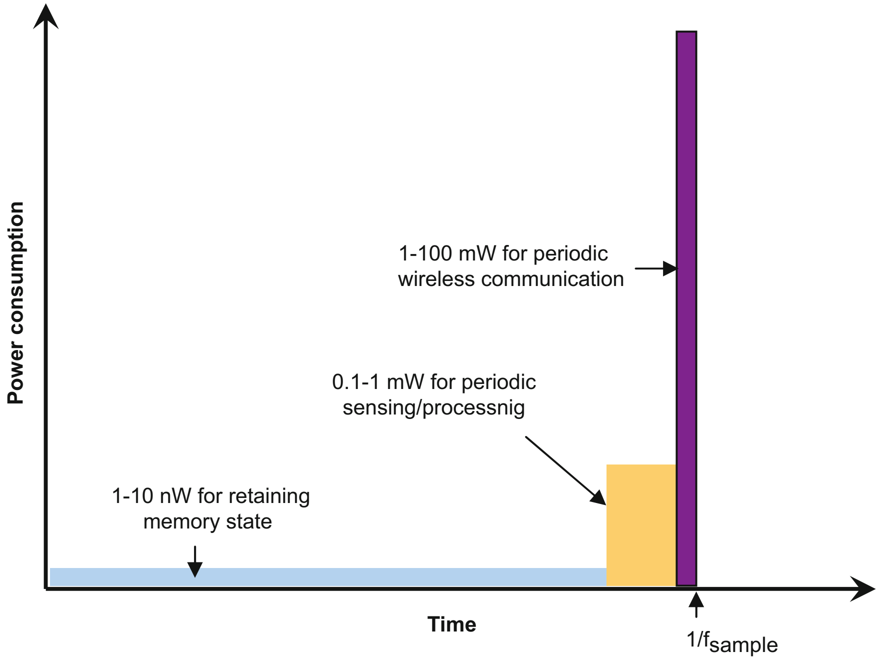

Figure 2.8: Schematic illustrating the power requirements of typical periodically sampling low power wireless sensor microsystems. The axes are not to scale

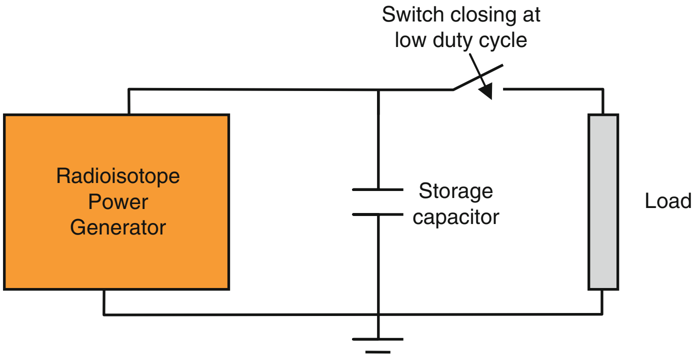

Figure 2.9: Schematic of a pulsed electrical power generator that integrates the continuous power output of a radioisotope power generator across a storage capacitor, and uses low duty cycle switching for pulsed discharge of the stored electrical energy across the load

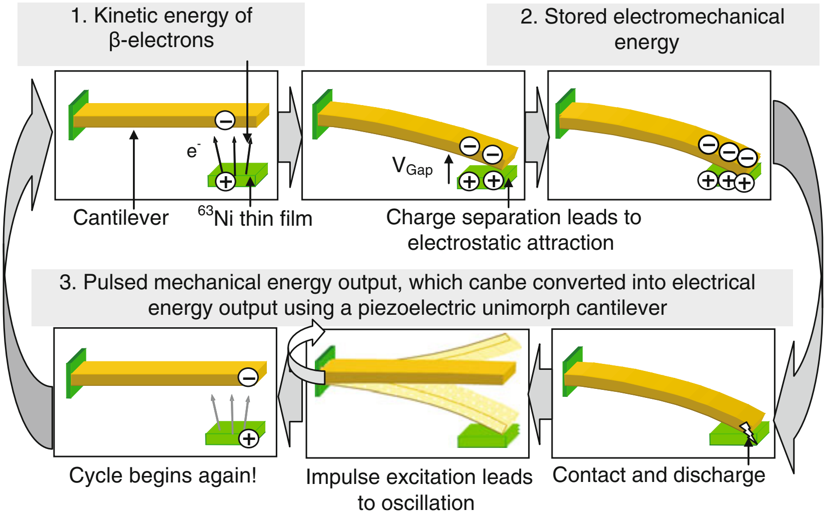

Figure 2.10: Schematic illustrating the radioisotope actuation of self-reciprocating cantilevers, and the generation of electrical energy when the cantilever is a piezoelectric unimorph

produces electrical charges in response to the mechanical deformations during cantilever vibrations, and converts the stored mechanical energy into electrical energy (Fig. 2.1). The piezoelectric unimorph also acts as a transformer, generating a directly usable voltage signal (≈1 V) from the high air-gap voltages (few kVs) generated due to direct charging from the radioisotope film. Hand assembled macro power generators were tested with four 3 millicurie $^{63}$Ni sources to yield a maximum power output of 750 µW and a maximum energy conversion efficiency of 3.94% efficiency (Appendix B).

### MEMS Reciprocating Electro-Mechanical Power Generators

Previously demonstrated hand-assembled radioisotope powered electro-mechanical power generators (REMPG's) [24] comprised of piezoelectric unimorph cantilevers fabricated by adhesively bonding bulk piezoelectric (lead zirconate titanate, PZT) plates (125 µm thick) to copper sheets (125 µm). The resulting beams were $> 4$ cm long, because the unimorph cantilever stiffness had to be low enough (1–10 N/m) for radioisotope actuation to result in pull-in and discharge. This limited the radioisotope fuel fill factor ($FFF$), or the ratio of the volume of the fuel to the total volume of the generator, which in turn limited the REMPG energy and power output density $P_{out,rempg,dens}$, because

$$P_{out,rempg,dens} = P_{r,dens} \times FFF \times \eta_{rempg}, \tag{2.4}$$

where $\eta_{rempg}$ is the REMPG energy conversion efficiency. Additionally, the lossy adhesive and bulk materials limited the REMPG energy conversion efficiency of stored electromechanical energy to electrical energy to $< 60\%$.

To overcome these limitations, microfabricated radioisotope-actuated reciprocating electro-mechanical generators that achieve higher fuel fill factors at milli-scale have been developed. The unimorph cantilevers are fabricated by deep reactive ion etching (DRIE) silicon cantilevers coated with either sol-gel deposited PZT thin films or RF sputtered aluminum nitride (AlN) thin films. The resulting high quality interfaces and low loss silicon cantilevers also lead to higher stored electromechanical energy to electrical energy conversion efficiency. Furthermore, the microfabricated REMPGs can be readily integrated with on-chip microsystems.

### Multiple Power-Output Integrated Radioisotope Electro-Mechanical Power Generators (IREMPG)

The energy conversion efficiency of the REMPG is proportional to the gap voltage $V_{gap}$ built up across the direct charging electrostatic gap, because the radioisotope energy to electromechanical energy conversion occurs when the $\beta$-electrons spend energy $qV_{gap}$ in overcoming the impeding electric field to cross the gap. The gap voltage should ideally be 17.3 kV, so the $E_{^{63}\mathrm{Ni},avg} = 17.3\,\mathrm{keV}$ electrons can transfer all of their kinetic energy in overcoming the impeding electric field across the gap. However, charge leakages through the vacuum in the gap limit the maximum realizable $V_{gap}$ to <5–10 kV. Furthermore, the $V_{gap}$ versus time profile resulting from the gradual charging up of the air-gap results in even lower $V_{gap,avg}$. Therefore, only a fraction of the 17.3 keV is

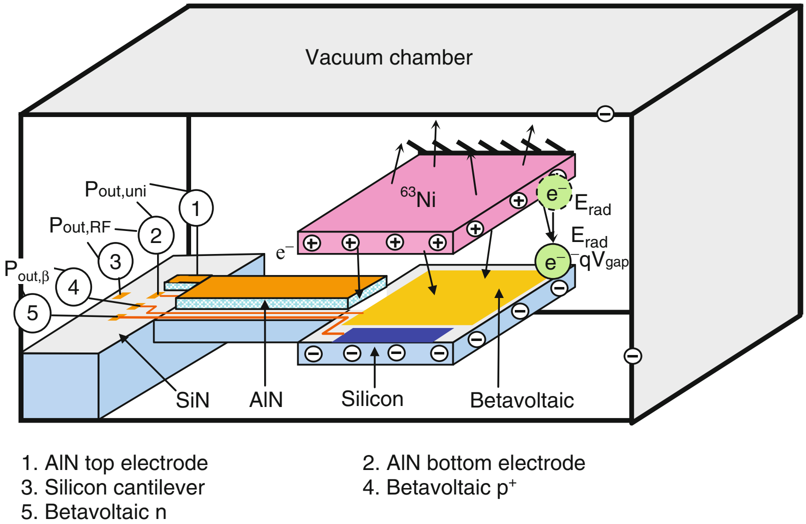

Figure 2.11: Schematic illustrating IREMPG construction, and snapshot of operation during the charging phase. The $^{63}$Ni thin film is charged to voltage $V_{gap}$, and the $\beta$-electrons expend energy $qV_{gap}$ in overcoming the impeding electric field before reaching the collector on the piezoelectric unimorph

transferred to the electromechanical system, and the rest is dissipated as heat in the collector. A portion of the remaining kinetic energy can be used to generate electron-hole-pairs (EHPs) in a betavoltaic integrated at the collector (Fig. 2.11), and the energy conversion efficiency increased. The integration of betavoltaics in the microfabricated micropower generators results in a *continuous* 0.3–0.7 nW power output from the micropower generator ($P_{out,\beta}$ in Fig. 2.12), in addition to the 12.95 $\mu$W pulsed electrical power output from the piezoelectric thin film ($P_{out,uni}$ in Fig. 2.12).

Additionally, the basic REMPG fails to take advantage of the radioisotope discharge event to generate wireless RF signals, which has been previously demonstrated in radioisotope actuated dielectric cantilever systems [27] (Fig. 2.13). The discharge event can be harnessed to produce wireless RF signals ($P_{out,RF}$ in Fig. 2.12) by exciting the LC resonance of the circuit formed by the piezoelectric unimorph cantilever and the electrical components connected across the dielectric insulating the piezoelectric

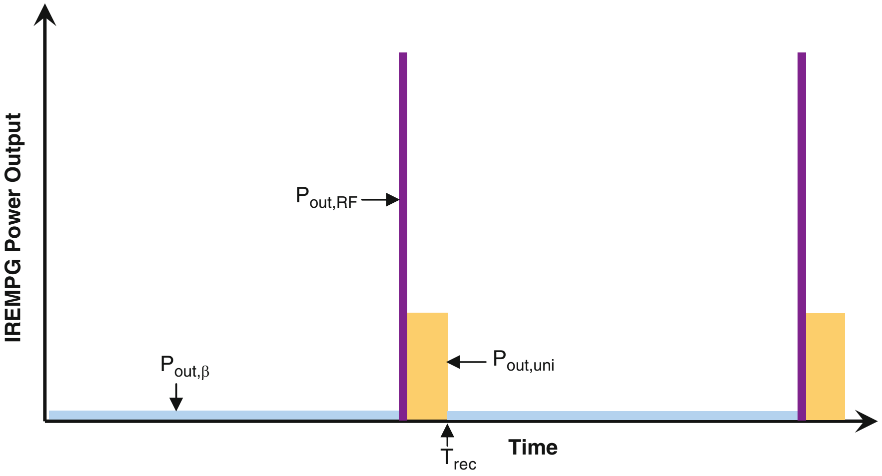

Figure 2.12: Schematic illustrating the power output profile of the IREMPG

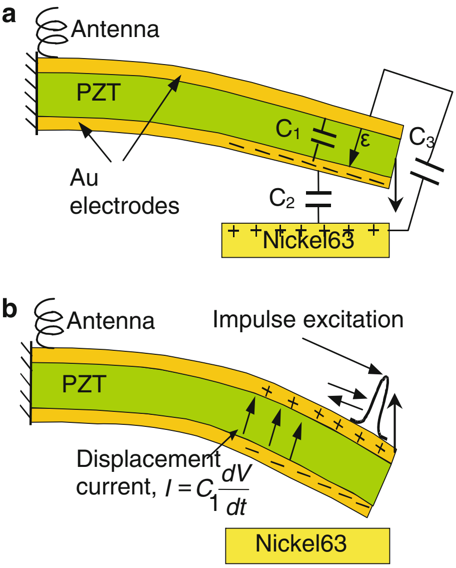

Figure 2.13: Schematic illustrating the generation of wireless RF signals in radioisotope actuated reciprocating dielectric cantilevers, due to (**a**) build-up of an electric field in the dielectric with charges accumulating on either electrode during the charging phase, and (**b**) excitation of RF modes in the dielectric waveguide by the displacement current caused by the sudden shorting during discharge

stack from the silicon cantilever body. Furthermore, the wireless RF signal frequency can be tuned by applying voltage biases across the piezoelectric thin film. This frequency tunability can be used to realize self-powered wireless RF sensors beacons to convey information between wireless sensor and RFID nodes.

## 2.2.5 $^{147}$Pm Micropower Generation

A majority of autonomous microsystems require 100 μW–100 mW continuous power output from their microbatteries. Therefore, they cannot function with the pulsed electrical power generators fueled by $^{63}$Ni. Microbatteries for such applications require high power density and high energy capacity radioisotope fuels. Thin film $^{147}$Pm is a very suitable fuel for such microbatteries because of its high $P_{g,dens}$ ($\approx 2.05$ W/cc at 830 curie/g) [28] and long $\tau_{1/2}$ (2.6 years). Even though the $^{147}$Pm maximum radiation energy of 200 keV poses a slightly increased radiation safety risk, $^{147}$Pm powered betavoltaic microbatteries have been proven safe enough to be deployed widely in implantable cardiac pacemakers. Previously developed cardiac pacemaker batteries employing as much as 66 curies of $^{147}$Pm realized low radiation dose rates of 6.1 millirem/h at 2.5 cm [11].

In this book, high efficiency 3D silicon electronvoltaics are developed (Chap. 5) to realize $> 5$ mW/cc, 5 year lifetime betavoltaic microbatteries using $\approx 100$ curies of $^{147}$Pm (Fig. 2.7).

### $^{147}$Pm-Silicon Betavoltaic Microbatteries

A variety of radioisotope energy conversion mechanisms can be employed for $^{147}$Pm energy conversion. However, betavoltaic energy conversion has proven most efficient for $^{147}$Pm. Primary energy conversion is not suitable because it requires generation and sustenance of impeding voltages equivalent to the average energy of the radiation, and it is difficult to sustain 63 keV across microscale gaps. Heat based engines are not as suitable because they require radioisotope fuels with $P_{g,dens} \approx$10–100 W/cc [1] to sustain the large temperature gradients required for efficient energy conversion.

Radioisotope powered betavoltaic microbatteries operate by irradiating semiconductor p–n junctions with low energy $\beta$-radiation to generate electron–hole pairs (EHPs), and collecting the EHPs across the junction to generate electrical power. Betavoltaics are analogous to photovoltaics, where photons are used to generate EHPs near a semiconductor junction. Previous $^{147}$Pm betavoltaic microbatteries employed planar silicon betavoltaics, and realized 100 μW/cc output power densities and 6–8 year lifetimes [11]. Their power densities, given by

$$P_{out,\beta,dens} = P_{r,dens} \times FFF \times \eta_{\beta}, \tag{2.5}$$

were low both because of low radioisotope fuel fill factors $FFF$ (2%) and low energy conversion efficiency $\eta_{\beta}$ (2%). The fuel fill factor was low because the $\beta$-electron self-absorption in the $^{147}$Pm thin film limits the maximum thin film thickness to 6 μm for $\eta_r > 85\%$. Since the silicon betavoltaics were fabricated on 300 μm thick wafers, $FFF$ was $6/300 \approx 2\%$. The $FFF$ can be raised by increasing the radioisotope-betavoltaic interface surface area, and past attempts have included employing KOH etched pyramidal texturing [23], and porous silicon 3D nano-texturing [29] of the betavoltaic surface. However, while KOH etched pyramids give a fuel fill factor enhancement of just $1.85X$, porous silicon approaches are not efficiently applicable to $^{147}$Pm powered silicon betavoltaics, because silicon microstructures need to be $> 50$ μm thick to absorb $> 90\%$ of the 63 keV $\beta$-electrons.

### 3D Silicon electronvoltaics for $^{147}$Pm Microbatteries

The aforementioned limitations can be overcome by employing DRIE textured 3D betavoltaics that are interleaved and stacked for maximum $FFF$ (Fig. 2.14). The novel 3D design promises to realize a net power density increase of 14–20X over previous planar betavoltaics, through a 8–10X increase in the fuel fill factor realized by increasing the radioisotope-betavoltaic interface surface area, and a 1.5–2X increase in the conversion efficiency realized by efficiently utilizing the $\beta$-electron radiation emitted from both sides of the radioisotope thin film. The resulting betavoltaics can enable smaller microbatteries with useful power output levels, using smaller quantities of radioisotope fuel for lower cost and radia-

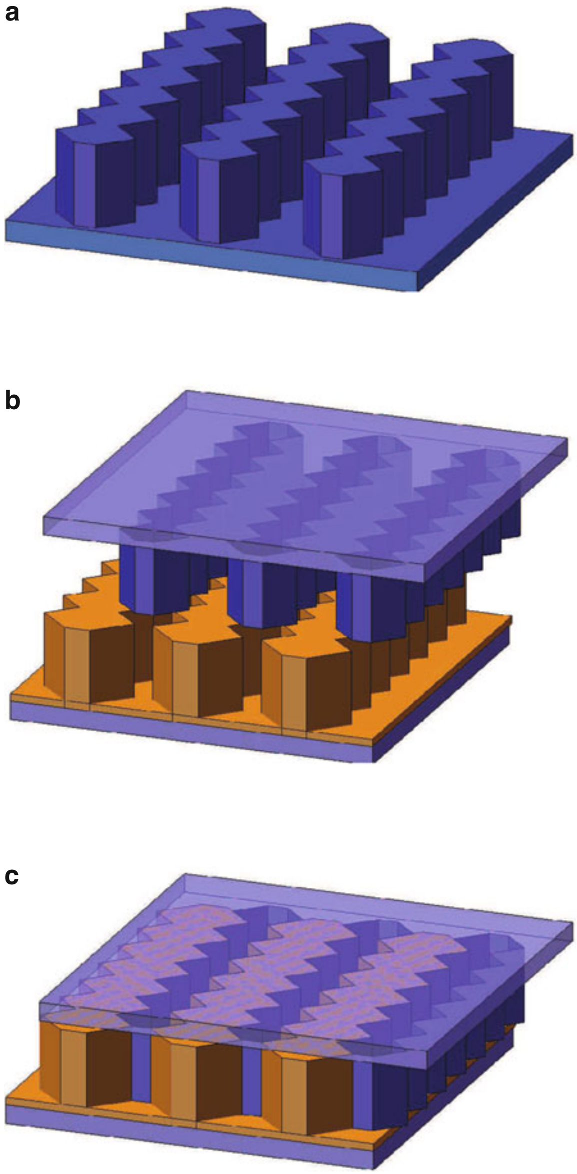

Figure 2.14: 3D dimetric view schematics of (**a**) 3D silicon diodes, (**b**) two interleaved betavoltaic wafers to be stacked, and (**c**) assembled 3D betavoltaics

tion dose rate. Furthermore, the 3D design can be readily applied to betavoltaics fabricated using higher band-gap semiconductors such as silicon carbide (SiC), gallium nitride (GaN), and Diamond for even higher conversion efficiencies.

## 2.3 Radioisotope Direct Charged Voltage Biases for Autonomous Sensors

Radioisotopes can be used as high energy density fuels in high energy capacity microbatteries for long lifetime microsystems. However, high power output microbatteries require high activities of radioisotope fuels. This undesirably raises safety concerns, and often limits the use of such microbatteries to specialized applications that can tolerate the lower radiation safety.

Alternatively, radioisotopes can also enable long-lifetime microsystems through their radiation effects. For example, $^{63}$Ni and americium-241 ($^{241}$Am) enable low-power electron capture detectors [9] and smoke detectors respectively by acting as zero-power ionization sources. Such applications can function with very small activities ($< 1$ millicurie) of radioisotopes. Consequently, such applications may be safe enough to be deployed widely. In this book, another such application for $^{63}$Ni thin films is proposed.

### 2.3.1 $^{63}$Ni Thin Film Generated Voltage Bias for Self-powered Sensors

The $\beta$-radiation from $< 5$ millicurie of $^{63}$Ni is used to enable a zero-power wireless sensor microsystem which can transmit a pulsed RF signal coded with the sensed environmental information [30]. The $^{63}$Ni source is used to electrostatically actuate a gold cantilever, and the pull-in triggered discharge is used to generate wireless transmission signals [27]. The frequency of this wireless signal generated is modulated by a humidity sensitive capacitor sensor connected to the cantilever. The humidity sensitive capacitor can be replaced by a capacitor sensitive to any other physical measurand to realize a wireless sensor microsystem. The resulting self-powered wireless sensors can function autonomously for decades enabling long-term monitoring of structural and environmental health in remote places.

## 2.4 Radioisotope Decay Rate based Counting Clock

The rate of radioactive disintegrations (activity) is a constant for a given amount of radioisotope material. The radioisotopes do not age as there are no inherent physical effects that change the rate for a given amount of material. Thus a radioactive source can potentially be used to construct atomic clocks and provide the necessary long-term stability for the clock. This book presents such clocks, called radioactive counting clocks, or simply, counting clocks.

# Chapter 3
# Radioisotope Micropower Generation: Microfabricated Reciprocating Electro-Mechanical Power Generators

## 3.1 Introduction

In this chapter, microfabricated radioisotope power generators that employ 100.3 year half-lifetime $^{63}$Ni radioisotope fuel for realizing long operational lifetime are presented. The generators utilize energetic electrons emitted from $^{63}$Ni thin films to electrostatically actuate reciprocating piezoelectric unimorph cantilevers, converting the emitted radioisotope energy to electromechanical energy stored in the deformed unimorph cantilever, and piezoelectricity to convert the resulting mechanical strain into electrical charges, converting the stored electromechanical energy to extractable electrical energy. The reciprocating piezoelectric unimorph cantilevers go through charge-discharge-vibrate cycles, and efficiently integrate the low ≈300 nW output from low activities (≈2.9 millicurie) of safe $^{63}$Ni thin films to generate 0.25% duty cycle 12.95 µW power pulses (across an optimal load impedance of 521 kΩ) potentially useful for pulsed sensor microsystems.

## 3.2 Design

Figures 3.1 and 3.2 illustrate the construction and equivalent 1D electromechanical representation of the REMPG. The REMPG employs radioisotope-charged electrostatic actuation to convert radioisotope energy to stored mechanical energy, and piezoelectricity to convert the stored mechanical energy into electrical

R. Duggirala et al., *Radioisotope Thin-Film Powered Microsystems*,
MEMS Reference Shelf 6, DOI 10.1007/978-1-4419-6763-3_3,

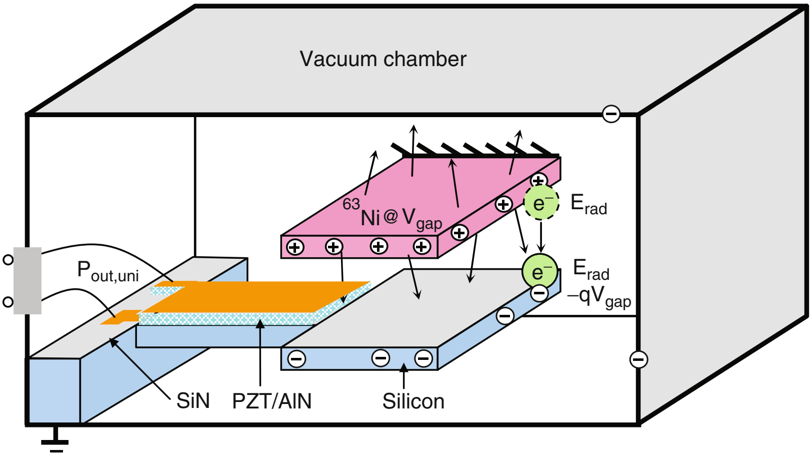

Figure 3.1: Schematic illustrating REMPG construction, and snapshot of operation during the charging phase. The $^{63}$Ni thin film is charged to voltage $V_{gap}$, and the $\beta$-electrons expend energy $qV_{gap}$ in overcoming the impeding electric field before reaching the collector on the piezoelectric unimorph. Also illustrated is the charge sharing between the piezoelectric unimorph and the vacuum chamber

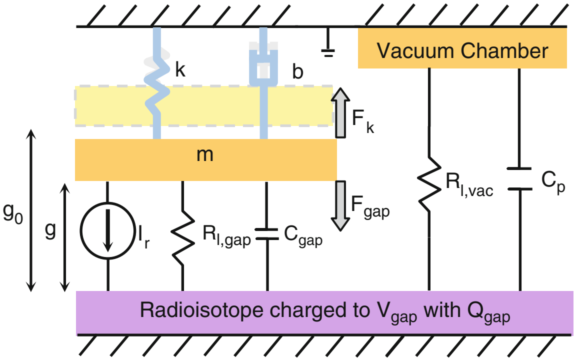

Figure 3.2: Schematic representation of REMPG equivalent 1D electromechanical circuit. Here, $Q_{gap}$ and $V_{gap}$ are the charge and voltage across air-gap $g$ at time $t$, $g_0$ is the initial gap, $k$ is the stiffness of the unimorph cantilever, $b$ is the damping coefficient, $I_r$ models the charge current and $R_{l,gap}$ the leakage resistance across the air-gap, and $C_{gap}$ and $C_p$ are the capacitances between the radioisotope thin film and the piezoelectric unimorph cantilever and the vacuum chamber respectively

energy. The two individual energy conversion mechanisms are described first, followed by an overview of the radioisotope energy to electrical energy conversion.

## 3.2.1 Radioisotope-Charged Electrostatic Actuation Dynamics

Radioisotope-charge actuation of the piezoelectric unimorph cantilever can be modeled as charge-controlled electrostatic actuation [31] of the air-gap capacitor formed by the moveable unimorph cantilever collector and the fixed radioisotope source (Fig. 3.2). The electrically isolated radioisotope source emits the $\beta$-electrons generated within the film through spontaneous decay, and steadily accumulates positively charged ions. The emitted $\beta$-electrons are collected either by the piezoelectric unimorph collector or by the vacuum chamber, both of which are connected to ground. This leads to separation of electrical charges, which in turn leads to electrostatic attraction.

The quasi-static electromechanical system dynamics are modeled best in the state space, where the state equations can be written by first identifying the three independent state variables to be the charge on the radioisotope thin film $Q_{gap}$, gap $g$, and tip velocity $v$. The first state equation can be derived by applying KCL at the radioisotope thin film as

$$\frac{\partial Q_{gap}}{\partial t} = I_r - I_{l,gap} = I_r - \frac{V_{gap}}{R_{l,gap}}, \tag{3.1}$$

where $I_r$ is the net $\beta$-electron current emitted by the radioisotope source, and $I_{l,gap}$ is the leakage current in the air-gap. In reality, $I_r$ depends on $V_{gap}$, because the emitted $\beta$-electrons need kinetic energy $E_{rad} > qV_{gap}$ to overcome the impeding electric field caused by $V_{gap}$ and cross the air-gap. However, if we assume that all the $\beta$-electrons are emitted with $E_{rad} = E_{rad,avg}$, and that

$$V_{gap} < \frac{1}{2}\frac{E_{rad,avg}}{q} \tag{3.2}$$

during the charging phase, then we can assume $I_r$ to be constant over the charging period. For the REMPGs presented in this book,

$V_{gap}$ is always less than $0.5 \times E_{rad,avg}/q$. Therefore, $I_r$ can be assumed to be constant. The gap voltage $V_{gap}$ is given by

$$V_{gap} = \frac{Q_{gap}}{C_{gap} + C_p}, \tag{3.3}$$

where $C_{gap}$ is the capacitance between the radioisotope source and the electrically grounded piezoelectric unimorph cantilever, calculated including the fringing field capacitance [32] using

$$C_{gap} = \epsilon_0 w_{coll} \left( 1.15 \left( \frac{l_{coll}}{g} \right) + 5.6 \left( \frac{t_{coll}}{g} \right)^{0.22} \right), \tag{3.4}$$

and $C_p$ is the parasitic capacitance arising from the interaction between the radioisotope source and the vacuum chamber. Here, $w_{coll}$, $l_{coll}$ and $t_{coll}$ are the width, length and thickness of the piezoelectric unimorph cantilever collector respectively, and equal 5 mm, 5 mm, and 42.5 μm for the REMPGs presented in this book. The charge leakages in the air-gap are modeled using resistance $R_{l,gap}$ as

$$R_{l,gap} = \frac{\rho_{gap} g}{A_{coll}}. \tag{3.5}$$

The air-gap leakage between the radioisotope thin film and the vacuum chamber can be ignored for the REMPGs discussed in this book because of the large gap separation between them. Therefore, the first state equation can be derived from (3.1) and (3.3) to be

$$\frac{\partial Q_{gap}}{\partial t} = I_r - \frac{1}{R_{l,gap}} \frac{Q_{gap}}{(C_{gap} + C_p)}. \tag{3.6}$$

The second state equation is derived from the relationship between the gap and the unimorph cantilever collector velocity as follows

$$\frac{\partial g}{\partial t} = v. \tag{3.7}$$

The third state equation is derived by balancing the mechanical forces acting on the moveable unimorph cantilever collector as

$$m \frac{\partial v}{\partial t} + bv + k(g_0 - g) = F_{gap}, \tag{3.8}$$

where $F_{gap}$ is the electrostatic force acting on the unimorph cantilever collector, given by

$$F_{gap} = \frac{Q_{gap}^2}{2\left(C_{gap} + C_p\right)^2} \frac{\epsilon_0 w_{coll}}{g} \left(1.15 \left(\frac{l_{coll}}{g}\right) + 0.22 \times 5.6 \left(\frac{t_{coll}}{g}\right)^{0.22}\right), \tag{3.9}$$

and $k_{uni}$ is the stiffness of the piezoelectric unimorph cantilever, calculated assuming the application of a point electrostatic force equivalent to the actual distributed electrostatic force. The point of application changes from the center of the collector when $g = g_0$ and the collector is parallel to the radioisotope source, to the tip of the unimorph cantilever when $g = 0$ and the charges accumulate at the tip (Fig. 3.3). In the electromechanical model, $k_{uni}$ was approximated to vary linearly with $g$ as

$$k_{uni} = k_{uni,tip} + (k_{uni,center} - k_{uni,tip}) \times g/g_0, \tag{3.10}$$

where $k_{uni,tip}$ and $k_{uni,center}$ are the unimorph cantilever stiffnesses with the point electrostatic force applied at the tip and center of the collector respectively.

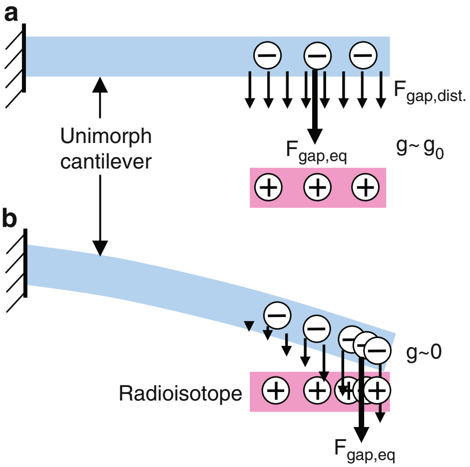

Figure 3.3: Schematic illustrating the variation in the equivalent point electrostatic force $F_{gap,eq}$, acting on the piezoelectric unimorph cantilever collector, with gap $g$, as the distributed electrostatic force $F_{gap,dist}$ changes

The third state equation can thus be written as

$$\frac{\partial v}{\partial t} = -\frac{1}{m}\left(bv + k(g_0 - g) + \frac{\partial}{\partial g}\left(\frac{Q^2}{2\left(C_{gap} + C_p\right)}\right)\right) \tag{3.11}$$

The set of non linear state equations described above can be solved using a Simulink model (Appendix C), and used to predict the variation of $Q_{gap}$, $g$, and $V_{gap}$ during the charging phase. Simulations were carried out for REMPGs with easily realizable dimensions of $l_{cant} = 10\,\text{mm}$, $l_{piezo} = 4.5\,\text{mm}$, $w_{cant} = w_{piezo} = 2\,\text{mm}$, $t_{cant} = 42.5\,\mu\text{m}$, and $t_{piezo} = 1\,\mu\text{m}$ to illustrate the radioisotope-charge actuation dynamics. As $I_r$ gradually charges up the air-gap capacitor, increase in $Q_{gap}$ results in an increase in $F_{gap}$, which in turn reduces the gap. The gap decreases slowly at first, and then rapidly falls down to zero as the unimorph cantilever gets pulled-in (Fig. 3.4(a)). It is important to note that charge controlled electrostatic actuation does not typically exhibit pull-in. However the presence of parasitic capacitance $C_p > C_{gap}|_{g=g_0}$ leads to pull-in the REMPG, at gaps [33]

$$g_{pi} = \frac{g_0}{3}\left(2 - \frac{C_{gap}}{C_p}\right). \tag{3.12}$$

The increase in $Q_{gap}$ also leads to $V_{gap}$ increasing initially, but $V_{gap}$ eventually peaks out, and starts decreasing because of $C_{gap}$ increasing due to the decreasing $g$ (Fig. 3.4(b)). The variation in the independent variables can also be used to calculate the variation in the electromechanical energy $E_{eme,rempg}$ stored in REMPG (Fig. 3.5), given by

$$E_{eme,rempg} = E_{es,rempg} + E_{me,rempg}. \tag{3.13}$$

Here, $E_{es,rempg}$ is the electrostatic energy stored in the air-gap, given by

$$E_{es,rempg} = \frac{1}{2}\frac{Q_{gap}^2}{C_{gap} + C_p}, \tag{3.14}$$

and $E_{me,rempg}$ is the mechanical energy stored in the deformed unimorph cantilever, given by

$$E_{me,rempg} = \frac{1}{2}k\left(g_0 - g\right)^2. \tag{3.15}$$

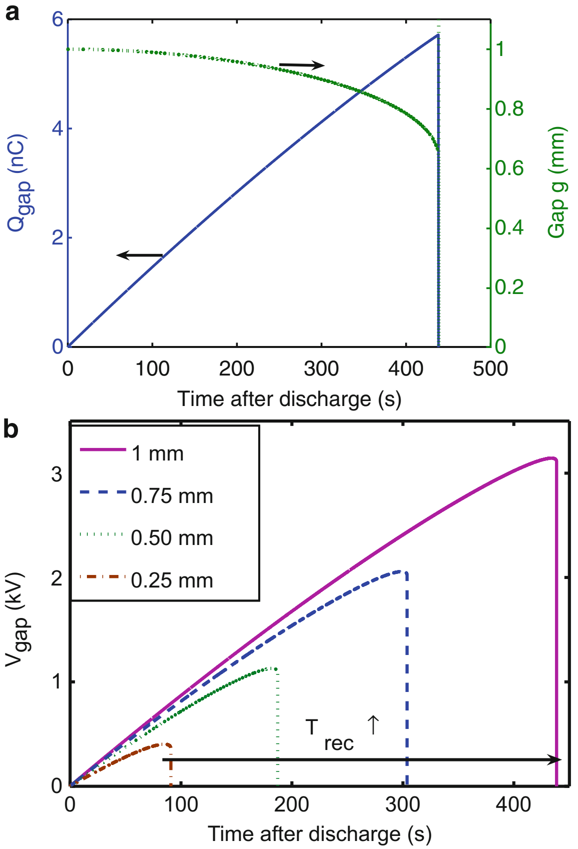

Figure 3.4: Plot of the calculated variation of REMPG (**a**) air-gap charge $Q_{gap}$ and gap $g$ with time for initial gap $g_0 = 1\,\text{mm}$, and (**b**) air-gap voltage $V_{gap}$ with time for various $g_0$. REMPG dimensions of $l_{cant} = 10\,\text{mm}$, $l_{piezo} = 4.5\,\text{mm}$, $w_{cant} = w_{piezo} = 2\,\text{mm}$, $t_{cant} = 42.5\,\mu\text{m}$, $t_{piezo} = 1\,\mu\text{m}$ were used in the simulations

$E_{es,rempg}$ increases initially with increasing $Q_{gap}$, reaches a peak just before pull-in, and goes to zero upon air-gap discharge. During pull-in, a portion of $E_{es,rempg}$ is converted to mechanical energy stored in the unimorph cantilever $E_{me,rempg}$ and electrostatic energy stored in the piezoelectric film $E_{es,piezo}$.

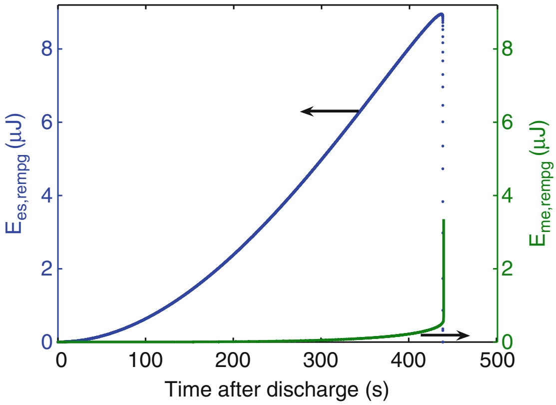

Figure 3.5: Plot of the calculated variation of stored REMPG electrostatic energy $E_{es,rempg}$ and mechanical energy $E_{me,rempg}$ with time during a reciprocation cycle, for initial gap $g_0 = 1\,\mathrm{mm}$

## 3.2.2 Piezoelectric Power Generation

The sudden release of the unimorph cantilever after pull-in and discharge sets it in vibration at its fundamental resonance frequency $f_{res,uni}$, when the piezoelectric element converts $E_{eme,rempg}$ to output electrical energy $E_{ee,rempg} = E_{out,uni}$. The power output characteristics of the piezoelectric unimorph can be derived by calculating the charge induced in the piezoelectric element due to the strain from the vibrations as [34]

$$Q_{out,piezo} = \int_A D_z dA = w_{piezo} \int_0^{l_{piezo}} \left( e_{31}\varepsilon_x + \epsilon_{33} E_z \right), \qquad (3.16)$$

where $e_{31}$ is the piezoelectric strain coupling coefficient, $\varepsilon_x$ is the strain along the length of the piezoelectric, $\epsilon_{33}$, $D_z$ and $E_z$ are the dielectric constant, electrical displacement and electric field perpendicular to the piezoelectric film thickness, and $w_{piezo}$ and $l_{piezo}$ are the width and length of the piezoelectric film respectively. The maximum current output of the piezoelectric unimorph $I_{out,uni,max}$ can be calculated from (3.16) by recognizing that

$$I_{out,uni,max} = \frac{\partial Q_{out,piezo}}{\partial t} = \omega_{res,uni} Q_{out,piezo,m} \qquad (3.17)$$

for sinusoidal vibrations with angular velocity $\omega_{res,uni}$. Furthermore, the maximum voltage output from the piezoelectric unimorph $V_{out,uni,max}$ across a load resistor $R_{l,uni}$ can be derived from (3.16) and (3.17) to be [12]

$$V_{out,uni,max} = \frac{\omega_{res,uni} w_{piezo} t_{cant} e_{31} \Phi R_{l,uni}}{2\left(1 + \omega_{res,uni} C_{piezo} R_{l,uni}\right)}, \tag{3.18}$$

where $t_{cant}$ is the thickness of the unimorph cantilever, $C_{piezo}$ the capacitance of the piezoelectric thin film, and $\Phi$ is a factor accounting for the modal shape of cantilever vibrations, written as

$$\Phi = \left(\phi'(0) - \phi'(l_{piezo})\right). \tag{3.19}$$

Here $\phi$ is the shape function along the unimorph cantilever beam for resonance at the fundamental frequency, given by

$$\begin{aligned} \phi = C_1 \Bigg( & [cosh(\beta x) - cos(\beta x)] - \frac{cosh(\beta l_c) + cos(\beta l_c)}{sinh(\beta l_c) + sin(\beta l_c)} \\ & \times [sinh(\beta x) - sin(\beta x)] \Bigg), \end{aligned} \tag{3.20}$$

where $\beta = \frac{1.875}{l_cant}$. The constant $C_1$ is calculated using the vibration amplitude of the tip $A_{tip}$ as

$$\phi(x)|_{x=l_{cant}} = A_{tip}. \tag{3.21}$$

From (3.17) and (3.20), the maximum power output of the piezoelectric $P_{out,uni}$ can be derived to be

$$\begin{aligned} P_{out,uni,max} &= V_{out,uni,max} I_{out,uni,max} \\ &= \frac{\omega_{res,uni}^2 w_{piezo}^2 t_{cant}^2 e_{31}^2 \Phi^2}{4\left(1 + \omega_{res,uni} C_{piezo} R_{l,uni}\right)^2} R_{l,uni}, \end{aligned} \tag{3.22}$$

From (3.22), the optimal REMPG load $R_{l,uni,opt}$ for maximum efficiency of conversion from mechanical to electrical energy can be calculated as [34]

$$R_{l,uni,opt} = \frac{1}{\omega_{res,uni} C_{piezo}}. \tag{3.23}$$

### 3.2.3 Energy Conversion Efficiency

The REMPG radioisotope energy to electrical energy conversion efficiency $\eta_{rempg}$ is defined as

$$\eta_{rempg} = \frac{E_{out,rempg}}{E_{in,rempg}}, \tag{3.24}$$

where $E_{in,rempg}$ is the input radiation kinetic energy over one reciprocation period $T_{rec}$, defined as

$$E_{in,rempg} = P_{in,rempg}T_{rec} = I_r \frac{E_{rad,avg}}{q} T_{rec}, \tag{3.25}$$

and $E_{out,rempg}$ is the piezoelectric output electrical energy over one reciprocation period, defined as

$$E_{out,rempg} = E_{out,uni} = \int_0^{T_{rec}} P_{out,uni} dt = \int_0^{T_{rec}} \frac{V_{out,uni}^2}{R_{l,uni,opt}}. \tag{3.26}$$

Furthermore, considering the two step energy conversion in the REMPG (Fig. 2.10), the input radioisotope kinetic energy to stored electromechanical energy conversion efficiency $\eta_{re-eme}$ can be written as

$$\eta_{re-eme} = \frac{E_{eme,rempg}|_{t=T_{rec}-\delta t}}{E_{in,rempg}}, \tag{3.27}$$

and stored electromechanical energy to output electrical energy conversion efficiency $\eta_{eme-ee}$ can be written as

$$\eta_{eme-ee} = \frac{E_{out,rempg}}{E_{eme,rempg}|_{t=T_{rec}-\delta t}}, \tag{3.28}$$

such that

$$\eta_{rempg} = \eta_{re-eme}\eta_{eme-ee} = \frac{E_{out,rempg}}{E_{in,rempg}} = \frac{\int_0^{T_{rec}} P_{out,rempg} dt}{I_r (E_{rad,avg}/q) T_{rec}}. \tag{3.29}$$

Here, $E_{eme,rempg}|_{t=T_{rec}} - \delta t$ is the electromechanical energy stored in the REMPG $t = \delta t$ before discharge.

The radioisotope kinetic energy to stored electromechanical energy conversion occurs when the radioisotope emitted $\beta$-electrons cross the air-gap to reach the collector, and expend energy $qV_{gap}$ to overcome the impeding electric field. The conversion efficiency $\eta_{re-eme}$ increases with average gap voltage $V_{gap,avg}$, and may equal 100% for $V_{gap,avg} = E_{rad,avg}/q$, when the $\beta$-electrons transfer all of their kinetic energy in overcoming the impeding field set-up by $V_{gap}$. However, the $V_{gap}$ versus time curve for a charge-actuated electrostatic actuator (Fig. 3.4(b)) limits the maximum $V_{gap,avg}$ to

$$V_{gap,avg} \approx 0.66 \times V_{gap,max}, \tag{3.30}$$

where $V_{gap,max}$ is the maximum gap voltage. Consequently, the maximum realizable $\eta_{re-eme}$ for the REMPG even with $V_{gap,max} = E_{rad,avg}/q$ is 66%. The above equation is based on the simplifying assumption that $V_{gap,max}$ is not limited by voltage breakdown in the gap, there is no leakage current in the air-gap, and all the emitted particles have kinetic energy $E_{rad,avg}$. Voltage breakdown in the air-gap restricts $V_{gap,max}$ to well below 17.3 keV, resulting in much lower values of $V_{gap,avg}$, and hence lower $\eta_{re-eme}$. The air-gap charge leakages result in longer integration times to accumulate the $Q_{gap,pi}$ required for pull-in, resulting in longer reciprocation periods, and hence lower $\eta_{re-eme}$. Spread in the energy emission spectrum results in loss of $\beta$-electrons with $E_{rad} << E_{rad,avg}$, because when $V_{gap,avg} > E_{rad,low}/q$, the $\beta$-electrons cannot overcome the impeding air-gap electric field to cross the air-gap and contribute to $F_{gap}$.

The stored electromechanical to output electrical energy efficiency is dependant upon the mechanical losses in the piezoelectric unimorph cantilever, and can be zero in the ideal case.

### 3.2.4 Radioisotope Fuel Source Design

Radioisotope fuel sources generate energy when their atoms disintegrate spontaneously to emit energetic particles or radiation. The net generated power density $P_{g,dens}$ can be written as

$$P_{g,dens} = 3.7 \times 10^{10} \times SA_r \times \rho_r \times E_{rad,avg}, \tag{3.31}$$

where $SA_r$ and $\rho_r$ are the specific activity (curie/g) and density (g/cc) of the radioisotope source respectively, and $E_{rad,avg}$ is the average energy of the particles or radiation emitted. These energetic particles travel through the volume of the radioisotope, before being emitted out of the surface with efficiency $\eta_r$ to produce output power density $P_{r,dens}$, given by

$$P_{r,dens} = \eta_r P_{g,dens} = \eta_r \times 3.7 \times 10^{10} \times SA_r \times \rho_r \times E_{rad,avg}. \quad (3.32)$$

Radioisotope fuel source design for any application consists of the selection of suitable radioisotope fuel material, to generate adequate $P_{g,dens}$ with suitable $E_{avg,rad}$, and design of the geometric form factor to maximize $\eta_r$.

### Material Selection

Radioisotopes for powering REMPGs can be selected on the basis of: (1) type of radiation emitted, ie., $\alpha$, $\beta$, or $\gamma$; (2) emission characteristics of the radioisotope, i.e., average energy ($E_{rad,avg}$) and maximum energy ($E_{rad,max}$) of radiation; (3) energy density ($E_{r,dens}$) and power density ($P_{r,dens}$); and (4) half-lifetime ($\tau_{1/2}$).

Only $\alpha$ and $\beta$ emitting radioisotopes are suitable for REMPGs, since energetic charged particles are required to electrostatically actuate piezoelectric unimorph cantilevers. Furthermore, only electrically conductive radioisotope thin films are suitable for powering REMPGs, because the unimorph cantilevers need to discharge upon contact for reciprocation to occur.

The emission characteristics affect energy conversion efficiency limits, REMPG radiation safety, and long-term degradation. Average energy $E_{rad,avg} < 100\,\text{keV}$ is desired, so the $V_{gap,avg} = E_{rad,avg}/q < 100\,\text{kV}$ required for $\eta_{re-eme} = 100\%$ can be sustained across milli-scale gaps. These low energy $\beta$-electrons also have low penetration lengths ($< 100\,\mu\text{m}$), and generate negligible Bremsstrahlung as $< 0.1\%$ of $E_{rad}$ is converted into photons [3]. Consequently, milli-scale microbatteries with thin radiation shields can be realized. Furthermore, low energy $\beta$-electrons lead to lower long term degradation of the collector, because $E_{rad,avg}$ for these radioisotopes is lower than the damage threshold of most materials (e.g., $E_{damage,th,Si} = 250\,\text{keV}$).

Among the low energy $\beta$-radioisotopes, it is desirable to select materials with adequate $SA_r$ to ensure suitable $P_{g,dens}$. Furthermore, since $SA_r$ decreases exponentially with time as

$$SA_r(t) = SA_r(0)e^{0.3t/\tau_{1/2}}, \tag{3.33}$$

$\beta$-radioisotopes with long half-lifetime $\tau_{1/2}$ is desirable. Table 1.2 [5] shows the three radioisotopes suitable for REMPGs, based on the criteria above. In this book, $^{63}$Ni is preferred over $^{147}$Pm because it is easier to sustain 17 kV across milli-scale gaps than 63 kV.

### Radioisotope Thin Film Design

Radioisotope fuel sources emitting low energy $\beta$-electrons ($E_{rad,avg} < 100\,\text{keV}$) need to be in thin film form to prevent significant energy loss to self-absorption, and $t_r$ needs to be chosen keeping in view both the $P_r$ and $\eta_r$ requirements. The power generated within a radioisotope thin film with area $A_r$ increases with $t_r$ as

$$P_g = P_{g,dens} \times A_r \times t_r = 3.7 \times 10^{10} \times SA_r \times \rho_r \times E_{rad,avg} \times A_r \times t_r. \tag{3.34}$$

However, $\eta_r$ decreases with $t_r$, since the generated $\beta$-electrons travel through a longer path in the radioisotope thin film source, while continuously losing energy to both inelastic collisions with the orbital electrons and radiative collisions with the nuclei of the radioisotope atoms [3], before emerging from the surface. The $\beta$-electron energy losses can be estimated using the theory of continuous slowing down approximation (CSDA), which assumes that charged particles traveling in any medium lose energy continuously along their tracks. The mean energy loss per unit path length is determined by both collision and radiative stopping powers [35]. Figure 3.6 plots the drop in the kinetic energy $E_{rad}$ of a $\beta$-electron ($E_{rad}|_{x=0} = 17.3\,\text{keV}$) with distance traveled in $^{63}$Ni. The energy loss is plotted until $E_{rad} = 10\,\text{keV}$ because CSDA theory is valid for only for $E_{electron} > 10\,\text{keV}$. Furthermore, the $\beta$-electron range was calculated by dividing the tabulated CSDA

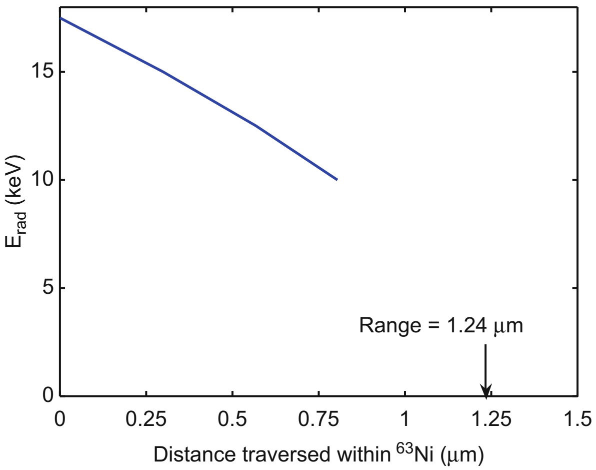

Figure 3.6: Plot illustrating the calculated drop in $\beta$-electron kinetic energy $E_{rad}$ with distance traversed in $^{63}$Ni for 17.3 keV $\beta$-electrons

range [35] by the density of $^{63}$Ni. Assuming a linear gradient of energy, calculated from the plot to be 12.4 keV/µm, the dependence of $\eta_r$ on $t_r$ can be calculated using

$$\eta_r = 1 - \frac{\partial E_{rad}}{\partial x}\frac{T}{2}\frac{1}{E_{rad,avg}}, \tag{3.35}$$

where $\frac{\partial E_{rad}}{\partial x}$ is the linear rate of energy loss due to self-absorption. The expression above assumes that all the $\beta$-electrons generated are emitted in a direction perpendicular to the film. However, since the $\beta$-electrons generated in the $^{63}$Ni film are emitted isotropically in reality, $\eta_r$ will be lower than the estimate from (3.35). Figure 3.7 illustrates the trade-off to be made between increasing $P_r$ and decreasing $\eta_r$ while increasing $t_r$. The maximum $^{63}$Ni thin film thickness for $\eta_r > 75\%$ can be calculated from (3.35) to be 0.8 µm. Table 1.2 shows the maximum values of $t_r$ for maintaining $\eta_r > 75\%$, and the resulting maximum power densities, for the three radioisotopes suitable for REMPGs.

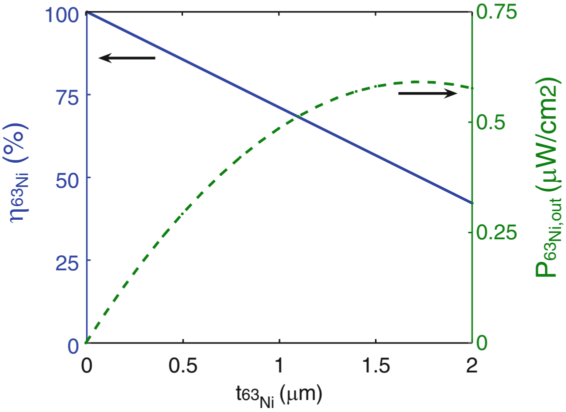

Figure 3.7: Plot of the calculated variation of radioisotope thin film emission efficiency $\eta_{^{63}\mathrm{Ni}}$ and power output $P_{^{63}\mathrm{Ni}}$ with thickness $t_{^{63}\mathrm{Ni}}$

### 3.2.5 Piezoelectric Material Selection

A variety of piezoelectric thin film materials can be employed in the REMPG, including lead zirconate titanate (PZT), aluminum nitride (AlN) and zinc oxide (ZnO). The selection of the piezoelectric material is based on: (1) piezoelectric strain coupling coefficient $e_{31}$ and dielectric constant $\varepsilon_{33}$; (2) ease of fabrication and integration with other microfabricated components; and (3) reliability and robustness.

The piezoelectric thin film properties $e_{31}$ and $\varepsilon_{33}$ affect the REMPG power generation characteristics such as $V_{out,uni}$, $P_{out,uni}$ and $R_{l,uni,opt}$ (3.18, 3.22, 3.23). Piezoelectric materials PZT and AlN are suitable for application in REMPGs because PZT possesses high $e_{31}$, and AlN has low $\varepsilon_{33}$ to compensate for its relatively low $e_{31}$ (Table 3.1).

Furthermore, both PZT and AlN can be integrated into MEMS REMPGs using well established microfabrication processes (sol gel based PZT deposition and RF sputtering of AlN). However, AlN thin films are preferred over PZT films when CMOS-compatibility is desired. Thin film PZT deposition and the subsequent annealing steps requires excessive thermal budget, and hence are CMOS incompatible. Moreover, multi-domain

Table 3.1: Comparison of REMPG power output characteristics with PZT and AlN thin films, for $l_{cant} = 10\,\text{mm}$, $l_{piezo} = 4.5\,\text{mm}$, $w_{cant} = w_{piezo} = 2\,\text{mm}$, $t_{cant} = 42.5\,\mu\text{m}$, $t_{piezo} = 1\,\mu\text{m}$, and $g_0 = 1\,\text{mm}$

| Parameters | Dependancy | PZT | AlN |
|---|---|---|---|
| $e_{31}(\frac{C}{m^2})$ | NA | 6.8 | 1 |
| $\varepsilon_{33}$ | NA | 1,190 | 10 |
| $V_{out,rempg}$ (V) | $\propto \frac{e_{31}}{\varepsilon_{33}}$ | 0.153 | 2.92 |
| $R_{l,rempg,opt}$ (kΩ) | $\propto \frac{1}{\varepsilon_{33}}$ | 4.4 | 526 |
| $P_{out,rempg,m}$ (μW) | $\propto \frac{e_{31}^2}{\varepsilon_{33}}$ | 5.9 | 16.38 |

PZT thin films undergo an aging process, which diminishes their piezoelectric coefficient over time. Single crystal AlN does not suffer from these drawbacks.

## 3.3 Fabrication

The REMPG is constructed by packaging a microfabricated piezoelectric unimorph cantilever on a dual inline package (DIP), and assembling it over a radioisotope thin film source. The piezoelectric unimorph cantilevers (Fig. 3.8) were microfabricated at the US Army Research Laboratory (Specialty Electronic Materials and Sensors Cleanroom) incorporating their thin film sol-gel PZT (53:47) and RF-sputtered AlN process (Fig. 3.9). The cantilevers were micromachined using two successive deep reactive ion etch (DRIE) steps, with the first DRIE performed on the front-side to define the shape and thickness of the unimorph cantilever, and the second DRIE on the back-side to release the unimorph cantilevers. The depth of the front-side DRIE was chosen to be

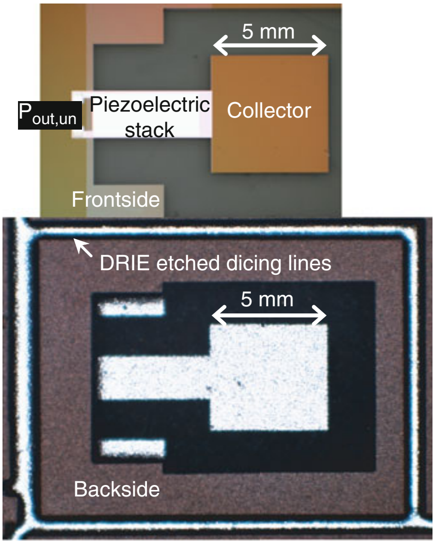

Figure 3.8: Photograph of the frontside and backside of the microfabricated piezoelectric unimorph cantilevers. The piezoelectric unimorph cantilever dimensions are: $l_{cant} = 10\,\mathrm{mm}$, $l_{piezo} = 4.5\,\mathrm{mm}$, $w_{cant} = w_{piezo} = 2\,\mathrm{mm}$, $t_{cant} = 42.5\,\mu\mathrm{m}$, $t_{piezo} = 1\,\mu\mathrm{m}$

slightly larger than the desired unimorph cantilever thickness, and the backside DRIE was performed until there was punch through in the areas etched with the frontside DRIE. The backside DRIE is also used to define the dicing pits, so the individual dice can be gently cleaved along the pits without breaking the released unimorph cantilevers. After separating individual dice, a $XeF_2$ etch was done on individual unimorph cantilevers to equalize the cantilever thicknesses. The cantilevers were thinned to $42.5\,\mu\mathrm{m}$, so the resulting 5–10 N/m cantilevers could be pulled down across large gaps using radioisotope actuation. Reciprocation at large gaps is required for generating high values of $V_{gap}$ during charging. The $XeF_2$ etching procedure can be avoided by using SOI wafers, where the bulk oxide can act as an etch stop, and result in unimorph cantilevers whose elastic layer thickness is equal to the top silicon body thickness.

The individual piezoelectric unimorph cantilevers were then packaged on a dual-inline package (DIP) (Fig. 3.10), so they could be conveniently positioned over the $^{63}$Ni thin film sources

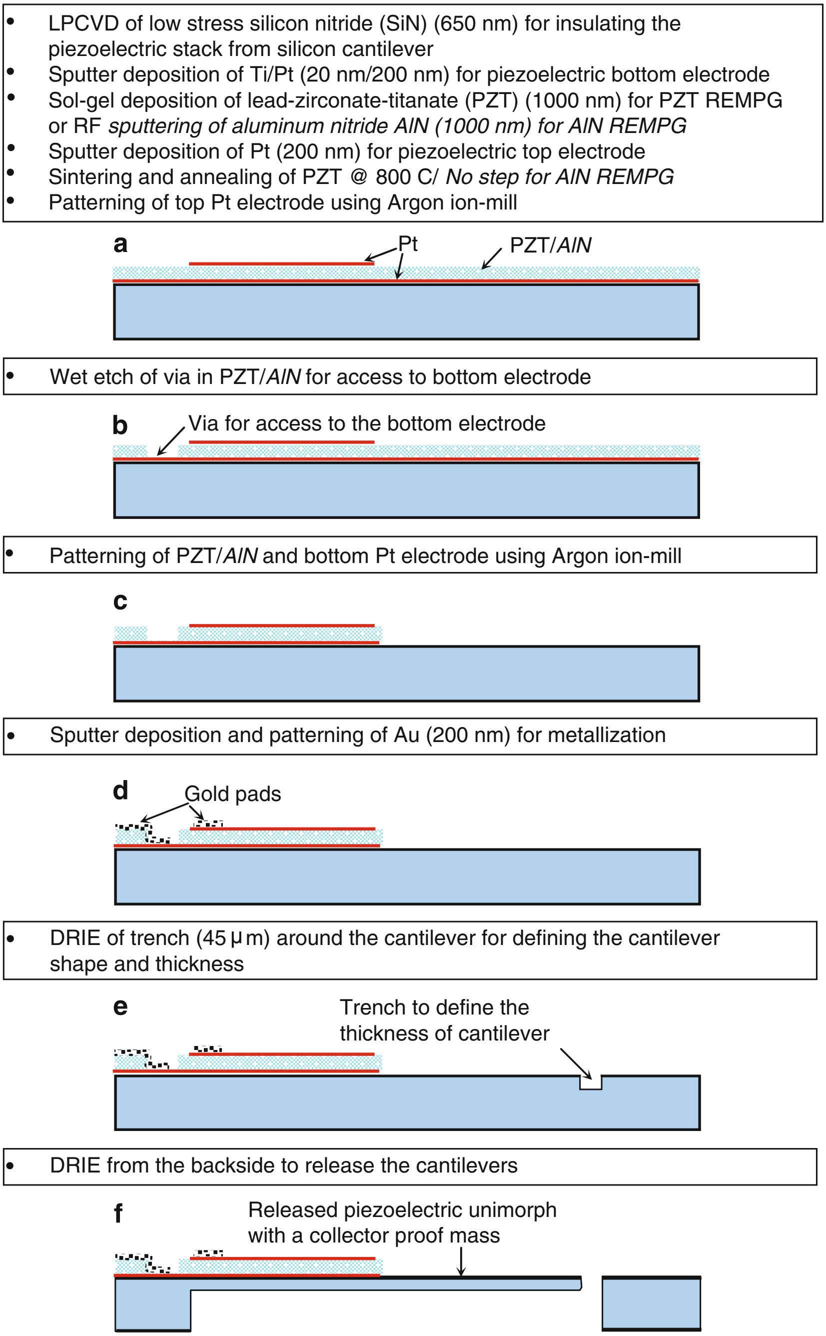

- LPCVD of low stress silicon nitride (SiN) (650 nm) for insulating the piezoelectric stack from silicon cantilever
- Sputter deposition of Ti/Pt (20 nm/200 nm) for piezoelectric bottom electrode
- Sol-gel deposition of lead-zirconate-titanate (PZT) (1000 nm) for PZT REMPG or RF *sputtering of aluminum nitride AlN (1000 nm) for AlN REMPG*
- Sputter deposition of Pt (200 nm) for piezoelectric top electrode
- Sintering and annealing of PZT @ 800 C/ *No step for AlN REMPG*
- Patterning of top Pt electrode using Argon ion-mill

- Wet etch of via in PZT/*AlN* for access to bottom electrode

- Patterning of PZT/*AlN* and bottom Pt electrode using Argon ion-mill

- Sputter deposition and patterning of Au (200 nm) for metallization

- DRIE of trench (45 μ m) around the cantilever for defining the cantilever shape and thickness

- DRIE from the backside to release the cantilevers

Figure 3.9: Schematic illustration of REMPG piezoelectric unimorph microfabrication process flow

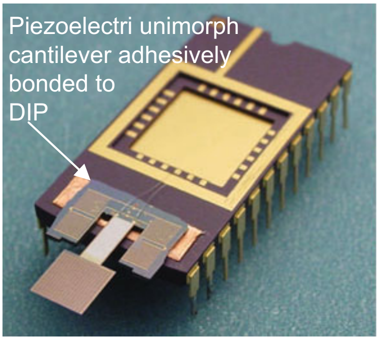

Figure 3.10: Photograph of the microfabricated piezoelectric unimorphs packaged on a dual inline package (DIP)

employed to characterize the REMPG. The $^{63}$Ni source comprised of a 1 cm×1 cm×100 µm nickel foils electro-less coated with 5–10% isotope purity $^{63}$Ni radioisotope (Isotope Products Laboratory, Los Angeles).

## 3.4 Testing and Results

The packaged AlN and PZT unimorph cantilevers were first tested for mechanical and piezoelectric dielectric properties to determine $R_{l,uni,opt}$ (3.23). The fundamental unimorph cantilever resonance frequency $f_{res,uni}$ was measured by applying a mechanical impulse excitation to the unimorph cantilever tips, and monitoring the ensuing natural vibrations via the piezoelectric leads. The measured $f_{res,uni}$ of 380.1 Hz and 379 Hz for AlN and PZT unimorph cantilevers respectively agreed well with the ANSYS calculated design value of 379.8 Hz for 42.5 µm thick beams. ANSYS simulations also showed $k_{uni}$ to vary from 10.3 N/m for $g = g_0$, when $F_{gap,eq}$ acts in the middle of the collector, to 6.74 N/m for $g = 0$, when the equivalent $F_{gap,eq}$ acts at the tip of the unimorph cantilever (Fig. 3.3). The mechanical properties of the piezoelectric unimorph cantilevers are the same irrespective of the piezoelectric film, because the thin (1 µm) piezoelectric films do not load the thick (42.5 µm) silicon cantilevers. The piezoelectric dielectric capacitances $C_{piezo,AlN}$ and $C_{piezo,PZT}$ for the 4.5 mm × 2 mm

× 1 µm piezoelectric stacks were then measured to be 0.83 nF and 94.7 nF, indicating $\epsilon_{33,AlN}$ and $\epsilon_{33,PZT}$ to be 10.5 and 1190 respectively. The values of $R_{l,uni,opt}$ were then calculated to be 521 kΩ and 4.4 kΩ for the AlN and PZT unimorph cantilevers respectively.

The $^{63}$Ni thin film source was then calibrated by measuring the net current output $I_r$ of the radioisotope source in vacuum to be 17.2 pA, indicating a radioisotope activity of 2.9 millicurie, and a power output $P_{out,^{63}\mathrm{Ni}}$ of 296 nW (3.25).

REMPG power generation was then characterized for both the AlN and PZT piezoelectric unimorph cantilevers by assembling them with radioisotope thin film sources inside a test vacuum chamber with a glass view port (Fig. 3.11). Both the piezoelectric unimorph cantilever and the radioisotope source were mounted on linear motion feedthroughs to characterize the REMPG at different values of $g_0$. The glass view port served to monitor the motion of the unimorph cantilever tip through a microscope connected to a CCD camera. The radioisotope source was positioned

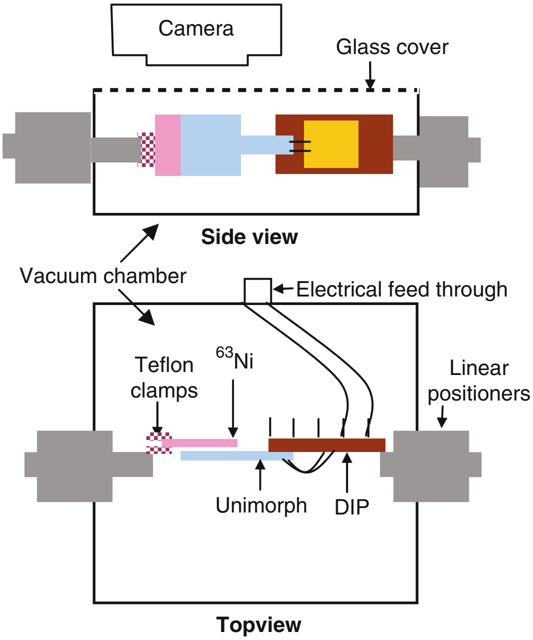

Figure 3.11: Schematic of the REMPG characterization set-up

at an initial gap $g_0$ from the tip of the unimorph cantilever, and the vacuum chamber was pumped down ($P \approx 10^{-3}$ millitorr) to minimize charge leakages in the air-gap due to build-up of high voltages. The unimorph cantilever tip position was monitored optically through the charge-discharge-oscillation cycle, and $V_{out,uni}$ was recorded at the end of every reciprocation cycle (Figs. 3.12(a), 3.13(a)) to further extract the maximum unimorph power output

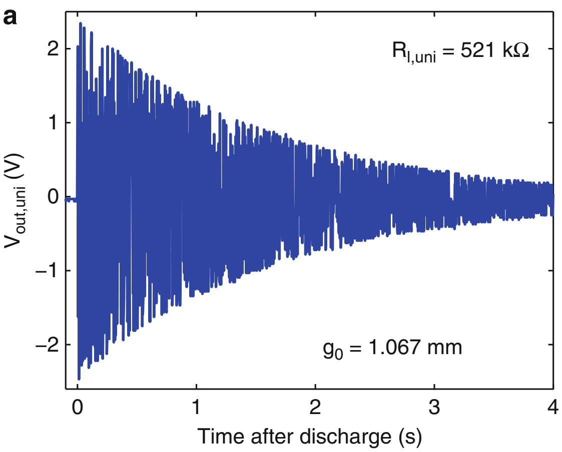

Complete waveform

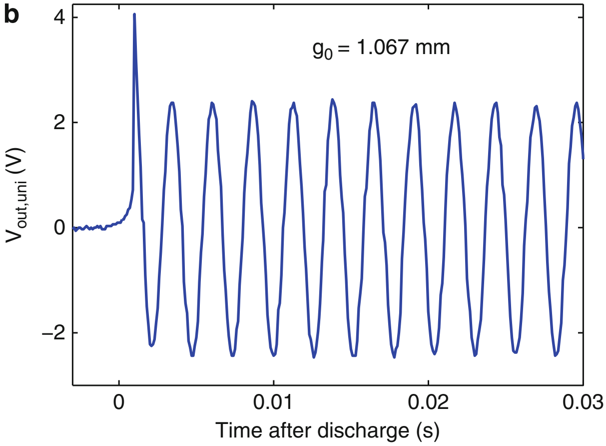

Inset at t=0 after discharge

Figure 3.12: Plot of measured AlN REMPG piezoelectric unimorph voltage output $V_{out,uni}$

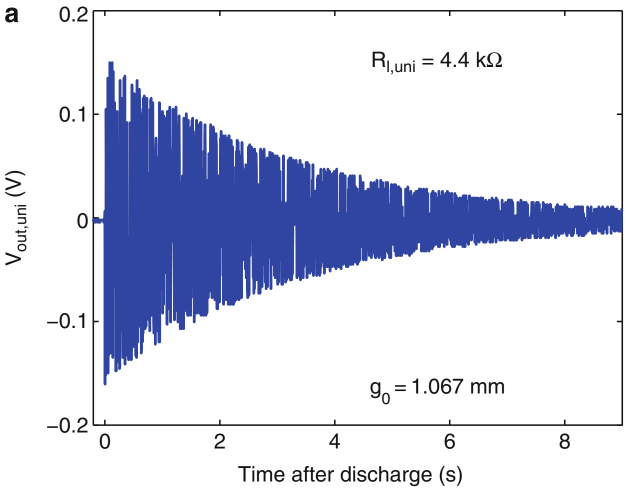

Complete waveform

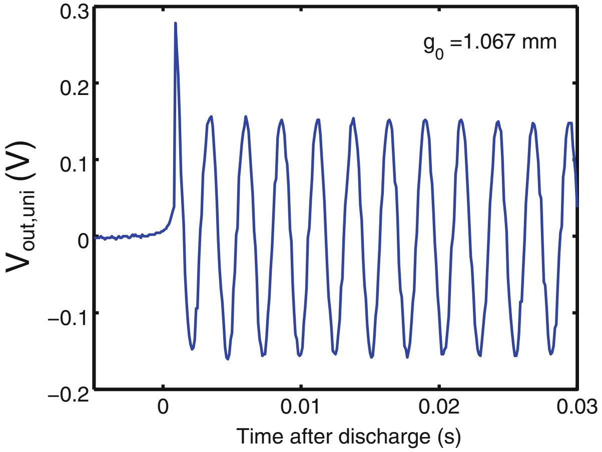

Inset at t=0 after discharge

Figure 3.13: Plot of measured PZT REMPG piezoelectric unimorph voltage output $V_{out,uni}$

$P_{out,uni,max}$, $E_{out,uni}$ and $\eta_{rempg}$. The reciprocation cycle was timed by calculating the interval between two consecutive $V_{out,uni}$ pulses. This was done for various values of $g_0$, until $g_0$ was too large for the unimorph cantilever to pull-in into the radioisotope and completely discharge.

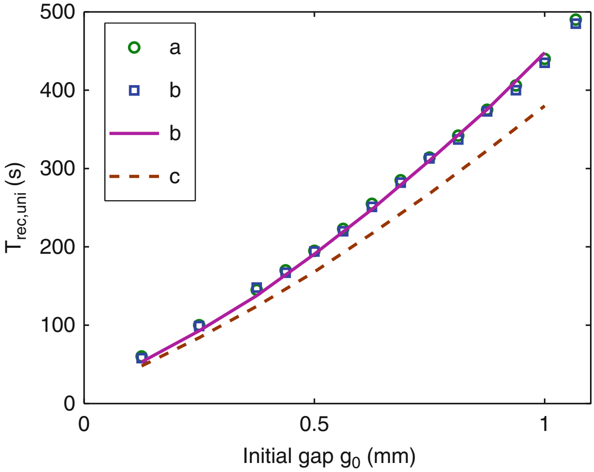

Figure 3.14: Plot of measured increase in (**a**) AlN REMPG and (**b**) PZT REMPG reciprocation period $T_{rec}$ with initial gap $g_0$ compared to simulated variation of REMPG reciprocation periods with (**c**) $\rho_{gap} = 2.5 \times 10^{13}\,\Omega$-cm and (**d**) $\rho_{gap} = \infty$. The REMPGs do not reciprocate for $g_0 > 1.067\,\text{mm}$

### 3.4.1 Radioisotope Actuation Dynamics

Since both AlN and PZT unimorph cantilevers had identical geometrical dimensions, the radioisotope actuation dynamics were almost identical. The reciprocation period $T_{rec}$ was measured to increase with $g_0$ (Fig. 3.14), as expected from radioisotope-charge driven electrostatic actuation theory (Fig. 3.4(b)). The measured values of $T_{rec}$ agreed well with the simulated values of $T_{rec}$ calculated assuming $C_p = 1.32\,\text{pF}$ and air-gap resistivity $\rho_{gap} = 2.5 \times 10^{13}\,\Omega$-cm. This quantifies both $C_p$ of the measurement set-up and resistivity of vacuum at $P \approx 10^{-3}$ millitorr. Additionally, the deduced value $C_p = 1.32\,\text{pF}$ is greater than $C_{gap|_{g=g_0}}$ for $g_0 > 225\,\mu\text{m}$, and pull-in was indeed observed to occur $g_0 > 375\,\mu\text{m}$.

### 3.4.2 Power Generation Characteristics

The maximum power output of the piezoelectric unimorph $P_{out,uni,max}$ after discharge was measured to increase with $g_0$ for both the AlN and PZT REMPGs (Fig. 3.15). The measured values

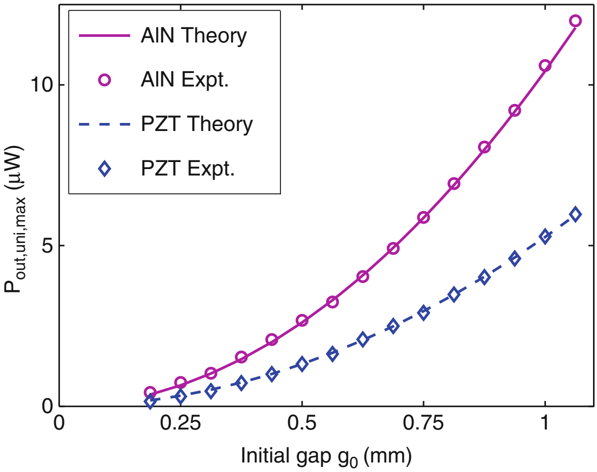

Figure 3.15: Plot of measured increase in maximum piezoelectric unimorph power output $P_{out,uni,max}$ with initial gap $g_0$ for both AlN and PZT REMPG

of $P_{out,uni,max}$ agreed well with the predictions by (3.22) when $e_{31,AlN}$ and $e_{31,PZT}$ were assumed to be $0.8\,\mathrm{C/m^2}$ and $6.2\,\mathrm{C/m^2}$ respectively, thus quantifying the $e_{31}$ for the thin films. The measured values of $e_{31}$ were also close to the typical $e_{31,AlN}$ and $e_{31,PZT}$ values of $1\,\mathrm{C/m^2}$ and $6.8\,\mathrm{C/m^2}$ respectively [36].

The REMPG energy conversion efficiency $\eta_{rempg}$ was then calculated from the measured values of $T_{rec}$ and $V_{out,uni}$ from (3.24), and found to increase with $g_0$ (Fig. 3.16). This is primarily due to the increase in $\eta_{re-eme}$ (Fig. 3.17), which rises due to increasing $V_{gap,avg}$ (Fig. 3.4(b)). Figure 3.18 shows the variation of $\eta_{eme-ee}$ with $g_0$ for both AlN and PZT unimorphs. The measured $\eta_{eme-ee} > 75\%$ for both AlN and PZT REMPGs was an improvement over the $\eta_{eme-ee} < 60\%$ realized in macro-scale REMPGs. However, the measured values of PZT REMPG $\eta_{eme-ee}$ were found to be lower than AlN REMPG $\eta_{eme-ee}$. This can be attributed to the higher mechanical losses during the vibration of the PZT unimorphs. This arises both because of the higher loss/cycle in the ceramic based multi-domain PZT thin film, compared to the relatively loss-less single crystal AlN thin films, and because of the larger number of oscillations in the PZT REMPG (Fig. 3.13). Additionally, measured values of $\eta_{eme-ee}$ were found to

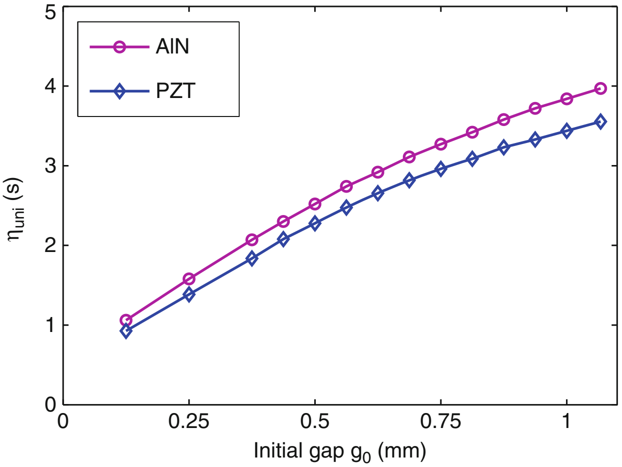

Figure 3.16: Plot of measured variation in energy conversion efficiency $\eta_{rempg}$ with initial gap $g_0$ for both AlN and PZT REMPG

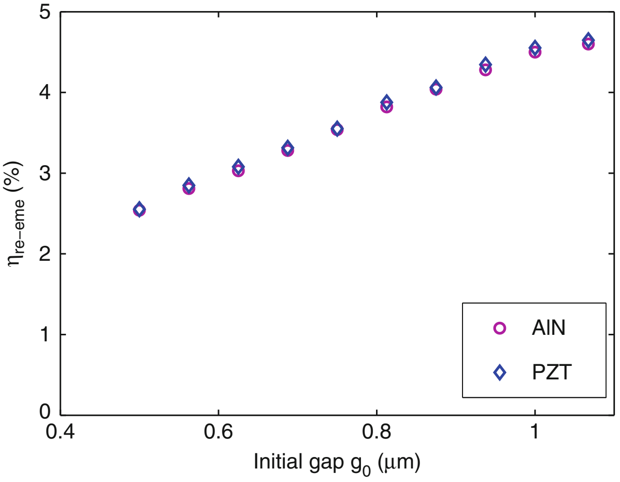

Figure 3.17: Plot of measured variation in radioisotope energy to electromechanical energy conversion efficiency $\eta_{re-eme}$ with initial gap $g_0$ for the AlN REMPG

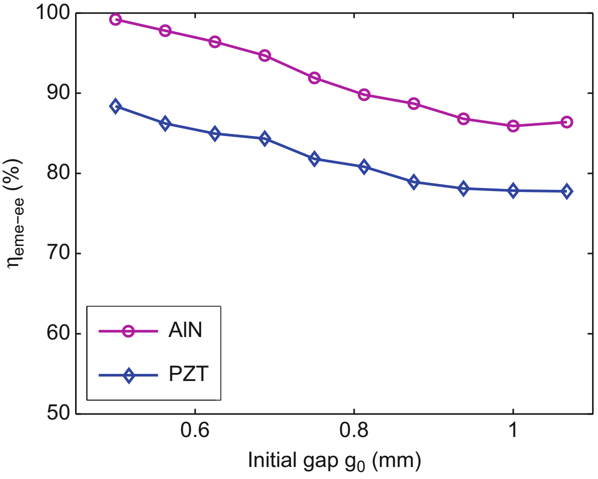

Figure 3.18: Plot of measured variation in electromechanical energy to electrical energy conversion efficiency $\eta_{eme-ee}$ with initial gap $g_0$ for both AlN and PZT REMPG. Optimal load impedances of 521 kΩ and 4.4 kΩ were employed for the AlN and PZT REMPGs respectively

drop with increasing values of $g_0$ for both AlN and PZT unimorph cantilevers. This can be attributed to the increase in the velocity dependant damping losses at higher values of $g_0$, caused by the higher velocity of vibration at higher values of $g_0$. Additionally, $\eta_{rempg}$ was measured at a fixed gap for a range of $R_{l,uni}$ (Fig. 3.19), and $R_{l,uni,m}$ confirmed to be 521 kΩ.

## 3.5 Discussion

### 3.5.1 Performance Variation with Vacuum Chamber Pressure

Ultra-low vacuum in the REMPG air-gap is necessary for high efficiency operation. Increasing pressure in the vacuum chamber results in lower air-gap leakage resistance $R_{l,gap}$, leading to larger charge leakage current $I_{l,gap}$. This results in longer reciprocation periods (Fig. 3.20), because it takes longer to accumulate the charge $Q_{gap,pi}$ required for pull-in, and leads to lower $\eta_{re-eme}$ (3.27). For any given $g_0$, $T_{rec}$ increases with pressure until the

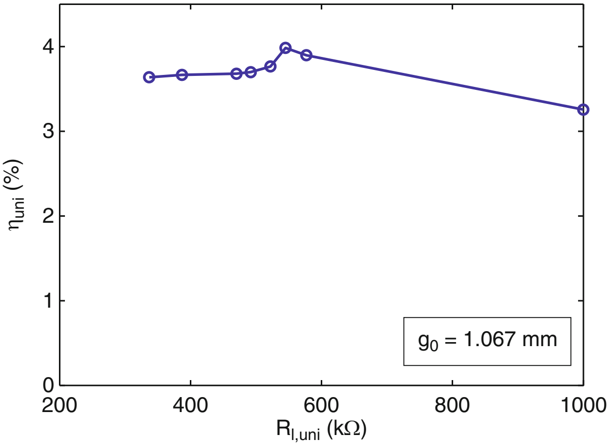

Figure 3.19: Plot of measured variation of AlN REMPG energy conversion efficiency $\eta_{rempg}$ with piezoelectric unimorph load impedance $R_{l,uni}$

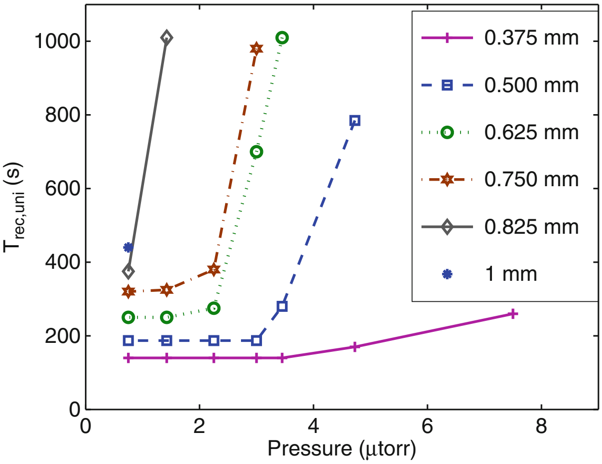

Figure 3.20: Plot of measured variation in REMPG reciprocation period $T_{rec}$ with pressure for different initial gap $g_0$

pressure dependant $R_{l,gap}$ decreases enough to result in a $I_{l,gap}$ that nullifies $I_r$, and hence reciprocation stops occurring. Additionally, at a given pressure, $T_{rec}$ increases with increasing $g_0$ because of the increase in $V_{gap,avg}$, which in turn raises $I_{l,gap}$ even when $R_{l,gap}$ remains the same. For example, at $P = 4.6\,\mu$torr, reciprocation occurs only for $g_0 < 500\,\mu$m.

### 3.5.2 Performance Variation with Radioisotope Specific Activity

Increasing radioisotope specific activity $SA_r$ can result in both larger $E_{out,rempg}$ (3.32 and 3.24), and shorter $T_{rec}$ for higher duty cycle pulsed power output $P_{out,rempg}$. The $SA_r$ for the $^{63}$Ni thin films used in this book was $< 5$ curie/g. This can be readily raised by employing $> 10$ curie/g ($\approx$15% isotope purity) $^{63}$Ni available from Oak Ridge National Laboratories [10], and possibly higher by employing $> 15\%$ isotope purity $^{63}$Ni. Figure 3.21 shows the simulated $g$ versus $t$ curves for different values of $SA_r$, and illustrates $T_{rec}$ decreasing with increasing $SA_r$. It is important to note that when $SA_r$ is increased $3X$ from 5 curie/g to 15 curie/g, the $T_{rec}$ decreases by more than $3X$, resulting in an increase in $\eta_{rempg}$ by almost 10%. This is expected, because when $SA_r = 5$ curie/g, the piezoelectric unimorph cantilever spends relatively longer time with the air gap charged to high voltages, and loses charges to leakages. The charge losses are reduced when $SA_r = 15$ curie/g results in shorter reciprocation periods, and hence the piezoelectric unimorph cantilever spends relatively shorter time with the air-gap charged to high voltages.

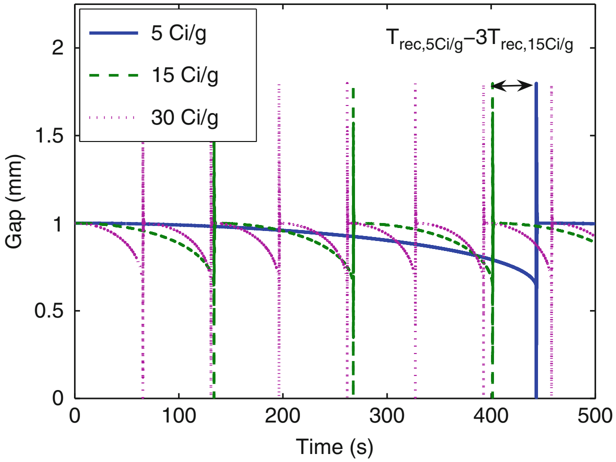

Figure 3.21: Plot of simulated variation in REMPG reciprocation period $T_{rec}$ with different radioisotope source specific activity $SA_r$ for initial gap $g_0 = 1\,\mathrm{mm}$

### 3.5.3 Performance Variation with Radioisotope Fuel Fill Factor

The REMPG power output density $P_{out,rempg,dens}$ can be written as

$$P_{out,rempg,dens} = P_{r,dens} \times FFF \times \eta_{rempg}, \tag{3.36}$$

where $FFF$ is the radioisotope source fuel fill factor, or the ratio of the volume of the radioisotope $V_r$ to the total packaged REMPG volume $V_{rempg}$ as

$$FFF = \frac{V_r}{V_{rempg}}. \tag{3.37}$$

For the REMPGs discussed in this book $V_r = 1\,\mathrm{cm} \times 1\,\mathrm{cm} \times 1\,\mathrm{mm} = 0.1\,\mathrm{cm}^3$, and $V_{rempg} = l_{rempg} \times w_{rempg} \times t_{rempg} = 2\,\mathrm{cm} \times 1.5\,\mathrm{cm} \times 5\,\mathrm{mm} = 1.5\,\mathrm{cm}^3$ when allowing 5 mm in all dimensions for the vacuum package. The resulting $FFF$ is 3.3%, which is an improvement over the $FFF = 0.8\%$ realized in previous macro hand assembled REMPGs, where $V_{rempg}$ was $l_{rempg} \times w_{rempg} \times t_{rempg} = 5.5\,\mathrm{cm} \times 1.5\,\mathrm{cm} \times 7.5\,\mathrm{mm} = 6.1875\,\mathrm{cm}^3$.

## 3.6 Conclusions

A radioisotope thin film powered microfabricated electromechanical generator was designed, fabricated, and tested with $^{63}$Ni thin films to yield 3.97% energy conversion efficiency. The generator comprises of reciprocating piezoelectric unimorph cantilevers electrostatically actuated using the energetic electrons emitted by $^{63}$Ni thin films. Microfabricated piezoelectric unimorph cantilevers employing both AlN and PZT thin films were successfully realized, and the resulting REMPGs were demonstrated to realize higher radioisotope fuel fill factor and mechanical energy to electrical energy conversion efficiency of 3.3% and $> 75\%$ respectively, compared to the 0.8% and $< 60\%$ realized in previous generators using macro-scale hand-assembled piezoelectric unimorph cantilevers. An experimentally verified model was developed to describe both radioisotope charge actuation, and power generation in the reciprocating piezoelectric unimorph cantilevers. This model can be used for future optimization of the generator design.

# Chapter 4
# Radioisotope Micropower Generation: Integrated Radioisotope Actuated Electro-Mechanical Power Generators

## 4.1 Introduction

The radioisotope actuated electro-mechanical power generators (REMPG) presented in the previous chapter convert radioisotope emitted kinetic energy to stored electromechanical energy using radioisotope actuation of piezoelectric unimorph cantilevers. The stored electromechanical energy is efficiently integrated over a reciprocation period, and discharged to generate pulsed electrical power through the piezoelectric with energy conversion efficiencies as high as 3.97%. The corresponding radioisotope kinetic to electromechanical energy conversion and electromechanical to electrical energy conversion efficiencies are $\approx 4.6\%$ and $\approx 85\%$ respectively.

The radioisotope to electromechanical energy conversion efficiency is a function of the air-gap voltages that build up during the radioisotope actuation of electro-mechanical structures. Radioisotope energy to electromechanical energy conversion occurs during radioisotope actuation when the $\beta$-electrons spend energy $qV_{gap}$ in overcoming the impeding electric field to cross the gap. The gap voltage should ideally be 17.3 kV, so the $E_{^{63}\mathrm{Ni},avg} = 17.3\,\mathrm{keV}$ electrons can transfer all of their kinetic energy in overcoming the impeding electric field across the gap. However, charge leakages through the air-gap limit the maximum realizable $V_{gap}$ to $<$5–10 kV. Furthermore, the $V_{gap}$ versus time profile resulting

R. Duggirala et al., *Radioisotope Thin-Film Powered Microsystems*,
MEMS Reference Shelf 6, DOI 10.1007/978-1-4419-6763-3_4,

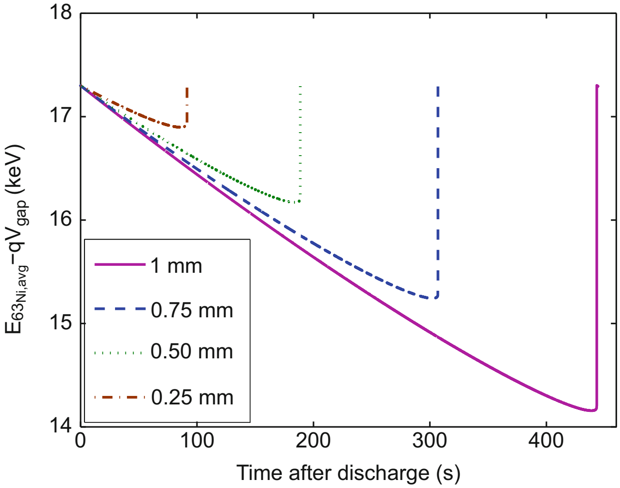

Figure 4.1: Plot of calculated $\beta$-electron kinetic energy unutilized during a reciprocation cycle of the REMPG. REMPG dimensions of $l_{cant} = 10\,\text{mm}$, $l_{piezo} = 4.5\,\text{mm}$, $w_{cant} = w_{piezo} = 2\,\text{mm}$, $t_{cant} = 42.5\,\mu\text{m}$, $t_{piezo} = 1\,\mu\text{m}$ were used in the simulations

from the gradual charging up of the air-gap (Fig. 3.4) results in even lower values of $V_{gap,avg}$. Hence, only a fraction of the 17.3 keV is transferred to the electromechanical system, and the rest is dissipated as heat in the piezoelectric unimorph collector (Fig. 4.1).

The portion of the $\beta$-electron kinetic energy not converted into electromechanical energy of the REMPG can be used generate electron–hole-pairs (EHPs) in a betavoltaic [11] integrated at the piezoelectric unimorph collector (Fig. 4.2), and increase the overall radioisotope to electrical energy conversion efficiency. Additionally, the REMPG can utilize the radioisotope discharge event to generate wireless RF signals. This has been previously demonstrated in radioisotope actuated dielectric cantilever systems [27] (Fig. 2.13). In the REMPG, the radioisotope discharge event can be harnessed to excite LC oscillations in any circuit connected across the dielectric that insulates the piezoelectric stack from the silicon cantilever body (Fig. 4.2). The resulting energy converter can utilize a portion of the kinetic energy of $\beta$-electrons

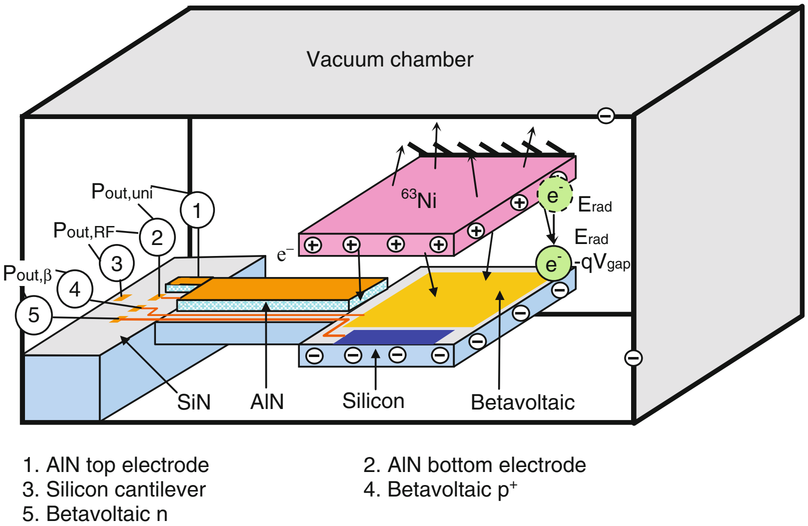

Figure 4.2: Schematic illustrating IREMPG construction, and snapshot of operation during the charging phase. The $^{63}$Ni thin film is charged to voltage $V_{gap}$, and the $\beta$-electrons expend energy $qV_{gap}$ in overcoming the impeding electric field before reaching the collector on the piezoelectric unimorph. Also illustrated is the charge sharing between the piezoelectric unimorph and the vacuum chamber

to generate pulsed electrical power via the piezoelectric unimorph cantilever, the remaining portion of the $\beta$-electron kinetic energy to generate continuous electrical power through the betavoltaics, and the charge of the $\beta$-electrons to generate wireless RF pulses (Fig. 4.3).

## 4.2 Principle of Operation

The operation and electrical power generation characteristics of the integrated radioisotope actuated electro-mechanical energy converters (IREMPG) can be understood better by individually considering the three different phases in the self-reciprocation cycle, i.e., charging, discharging, and vibration.

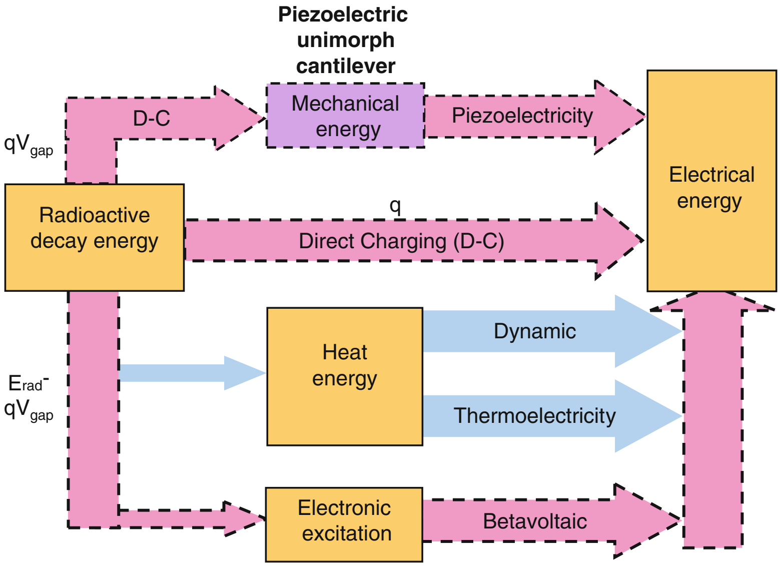

Figure 4.3: Schematic illustrating the IREMPG energy conversion mechanism

### 4.2.1 Charging Phase: Betavoltaic Power Output

The operation of the IREMPG at any point during the charging phase can be understood by considering the sequence of events following the emission of $\beta$-electrons from the radioisotope thin film. Assume that at time $t$, radioisotope actuation of the piezoelectric unimorph cantilever has resulted in the gradual accumulation of charges on the radioisotope thin film $Q_{gap}$, charging the air-gap to voltage $V_{gap}$. The resulting electrostatic force $F_{gap}$ on the piezoelectric unimorph has reduced the gap to $g$ (Fig. 4.4). The $\beta$-electrons emitted next with average kinetic energy $E_{rad,avg}$ will transfer energy $qV_{gap}$ to the electromechanical system while overcoming the impeding air-gap electric field, and arrive at the betavoltaic collector with energy $E_{in,\beta} = E_{rad,avg} - qV_{gap}$. This remaining kinetic energy will be spent in exciting electron-hole pairs (EHPs) and generating betavoltaic power output $P_{out,\beta}$ given by

$$P_{out,\beta} = \eta_\beta P_{in,\beta} = \eta_\beta \frac{I_c}{q}(E_{rad,avg} - qV_{gap}), \tag{4.1}$$

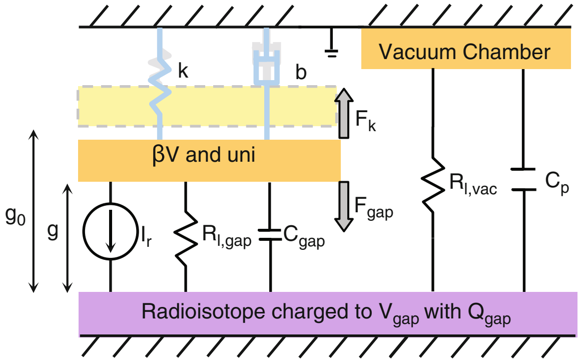

Figure 4.4: Schematic illustrating the 1D electromechanical equivalent representation of the IREMPG. Here, $Q_{gap}$ and $V_{gap}$ are the charge and voltage across air-gap $g$ at time $t$, $g_0$ is the initial gap, $k$ is the stiffness of the unimorph cantilever, $b$ is the damping coefficient, $I_r$ models the charge current and $R_{l,gap}$ the leakage resistance across the air-gap, and $C_{gap}$ and $C_p$ are the capacitances between the radioisotope thin film and the piezoelectric unimorph cantilever and the vacuum chamber respectively

where $\eta_\beta$ is the energy conversion efficiency of the betavoltaic, and $I_c$ is the current due to the collected $\beta$-electrons. The emitted $\beta$-electrons will also result in an increase in the charge accumulated at the radioisotope thin film by $\delta Q_{gap} = qI_c\Delta t$. This will result in an increase $\delta F_{gap}$ in the electrostatic force acting on the unimorph cantilever, moving the unimorph cantilever tip closer to the radioisotope by $\delta g$. The gap voltage $V_{gap}$ will change accordingly by $\delta V_{gap} = \delta(Q/(C_{gap} + C_p))$ (Fig. 3.4), resulting in the $\beta$-electron emitted next transferring $q\delta V$ more energy to the unimorph. This will in turn lead to a decrease in $E_{in,\beta}$ (Fig. 4.1). The trend is captured in the graphic below:

$$t \uparrow \Rightarrow Q_{gap} \uparrow \Rightarrow V_{gap} \uparrow \Rightarrow E_{in,\beta} \downarrow \Rightarrow P_{out,\beta} \downarrow \tag{4.2}$$

The $\beta$-electron kinetic energy $qV_{gap}$ transferred to the electromechanical system is stored as the mechanical energy in the deformed unimorph cantilever and electrostatic energy in the air-gap capacitor. However, there is no power output across the piezoelectric unimorph terminals, as the quasi-static movement of the beam is not fast enough to produce significant changes in the piezoelectric charges. Additionally, there is no power output across the dielectric separating the piezoelectric stack from the silicon cantilever body, as there are no significantly fast changes in the charges across the dielectric.

## 4.2.2 Discharge Phase: Wireless RF Signal Generation

Eventually, the charges accumulated across the gap exceed the pull-in charge $Q_{gap,pi}$, and the beam is pulled in. The piezoelectric unimorph cantilever makes contact with the radioisotope thin film, and the accumulated charges get neutralized via tunneling and direct conduction (Fig. 4.5b). This sudden change of charge distribution can produce a high amplitude and short duration current pulse, because the charge $Q_{gap}$ integrated over the reciprocation period is discharged in a short duration. This discharge can

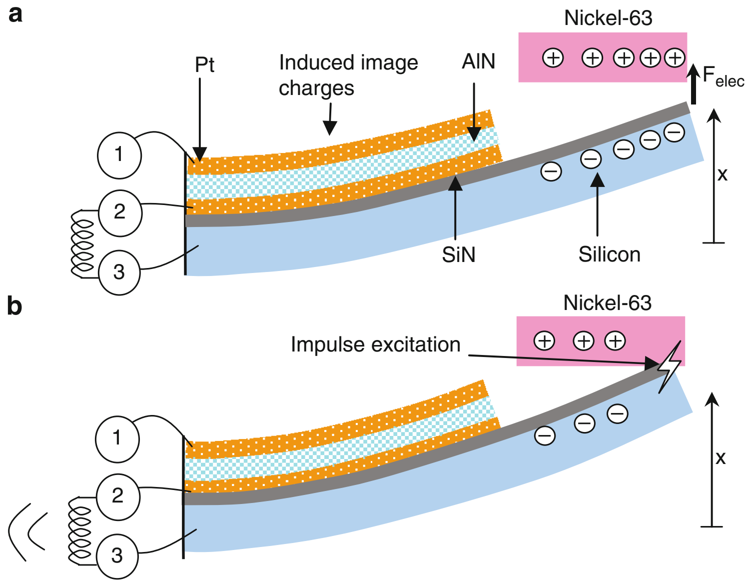

Figure 4.5: Schematic illustrating (**a**) the accumulation of charge across the dielectric during the charging phase, and (**b**) the impulse excitation of the thin film dielectric waveguide during air-gap discharge

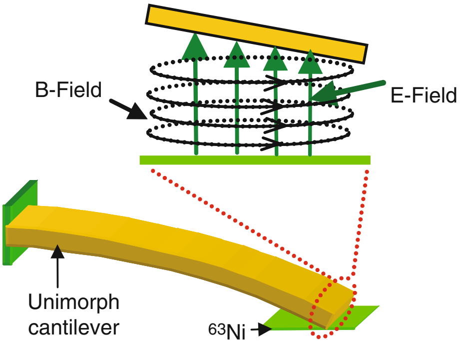

Figure 4.6: Schematic illustration of the electrical and magnetic fields generated in the discharge of the IREMPG. The unimorph cantilever is simplified for illustration

be modeled as an arc generation event [37] (Fig. 4.6), and the high current pulse modeled as a small dipole antenna transmitting a broadband magnetic pulse field isotropically in all directions. The generated RF pulse has a very broad spectrum, and excites the normal modes of any nearby electromagnetic resonator. A wireless transmitter can be realized by connecting a solenoid across the dielectric in the unimorph, and the resulting wireless RF signals can be utilized for communication in wireless sensor nodes. Frequency modulation of the wireless RF transmission for data communication can also be realized by varying the bias across the AlN thin film.

### 4.2.3 Vibration Phase: Piezoelectric Power Generation

The neutralization of $Q_{gap}$ on discharge results in a sudden nulling of $F_{gap}$, which is equivalent to a mechanical impulse excitation force on the piezoelectric unimorph. This excites natural vibrations in the piezoelectric unimorph cantilever, and the resulting mechanical strains lead to electrical charges induced in the piezoelectric. Thus, the stored electromechanical energy in the piezoelectric unimorph cantilever is converted into pulsed electrical power. Details of the piezoelectric power generation are explained in Chap. 3.

### 4.2.4 Energy Conversion Efficiency

The IREMPG energy conversion efficiency $\eta_{irempg}$ is defined as

$$\eta_{irempg} = \frac{E_{out,irempg}}{E_{in,irempg}}, \tag{4.3}$$

where $E_{in,irempg}$ is the input radiation kinetic energy over one reciprocation period $T_{rec}$, defined as

$$E_{in,irempg} = P_{in,irempg} T_{rec} = I_r \frac{E_{rad,avg}}{q} T_{rec}, \tag{4.4}$$

and $E_{out,irempg}$ is the output electrical energy over one reciprocation period, defined as

$$E_{out,irempg} = \int_0^{T_{rec}} P_{out,irempg} dt = \int_0^{T_{rec}} (P_{out,\beta} + P_{out,RF} + P_{out,uni})\, dt. \tag{4.5}$$

Here, $P_{out,\beta}$ is the betavoltaic power output across an optimal load resistance $R_{l,\beta,opt}$, given by

$$P_{out,\beta} = \frac{V_{out,\beta}^2}{R_{l,\beta,opt}}. \tag{4.6}$$

The optimal load resistance $R_{l,\beta,opt}$ is chosen to bias the betavoltaic at the maximum power point of its IV curve under radioisotope illumination. The efficiency of energy conversion in the betavoltaic $\eta_{\beta,irempg}$ can be calculated by integrating $P_{out,\beta}$ over a reciprocation cycle, and is defined as

$$\eta_{\beta,irempg} = \frac{\int_0^{T_{rec}} P_{out,\beta} dt}{I_r (E_{rad,avg}/q) T_{rec}}. \tag{4.7}$$

The RF energy output per reciprocation cycle $E_{out,RF}$ is $< 1\,\mu\text{J}$ for the IREMPGs discussed in this book. Therefore, $E_{out,RF}$ will be omitted from the energy conversion equations. The power output of the piezoelectric unimorph $P_{out,uni}$ across an optimal load resistor $R_{l,uni,opt}$ is given by

$$P_{out,uni} = \frac{V_{out,uni}^2}{R_{l,uni,opt}}, \tag{4.8}$$

where $R_{l,uni,opt}$ can be calculated from REMPG theory (Chap. 2, [34]) to be

$$R_{l,uni,opt} = \frac{1}{\omega_{res,uni} C_{piezo}}. \tag{4.9}$$

Here, $\omega_{res,uni}$ is the fundamental resonance frequency of the piezoelectric unimorph beam and $C_{piezo}$ is the dielectric capacitance of the piezoelectric thin film. The energy conversion efficiency of the piezoelectric unimorph $\eta_{uni,irempg}$ can then be calculated by summing the total power output of the unimorph over a reciprocation period, and is defined as

$$\eta_{uni,irempg} = \frac{\int_0^{T_{rec}} P_{out,uni} dt}{P_{in,irempg} T_{rec}}. \tag{4.10}$$

The total IREMPG energy conversion efficiency $\eta_{irempg}$ can be written from 4.3, 4.7 and 4.10 to be

$$\eta_{irempg} = \eta_{\beta,irempg} + \eta_{uni,irempg}. \tag{4.11}$$

## 4.3 Fabrication

The IREMPG is constructed by packaging a microfabricated AlN unimorph cantilever with integrated betavoltaics on a dual inline package (DIP), and assembling it over a radioisotope thin film source. The AlN unimorph cantilevers (Fig. 4.7) were microfabricated at the US Army Research Laboratory (Specialty Electronic Materials and Sensors Cleanroom) incorporating their RF-sputtered AlN process (Fig. 4.8). The microfabrication of IREMPG involves definition of the betavoltaic p–n junctions, deposition and patterning of the piezoelectric thin films, metallization, and micromachining of silicon cantilevers. The betavoltaic p–n junction deposition is done prior to the piezoelectric deposition because dopant activation and diffusion requires annealing at temperatures exceeding the high temperature limit of AlN thin films. Additionally, float-zone (FZ) silicon wafers (6–12 Ω-cm) are used to minimize bulk crystal defects that cause high reverse leakage current in diodes and reduce betavoltaic conversion efficiencies. The unimorph cantilevers were micromachined using

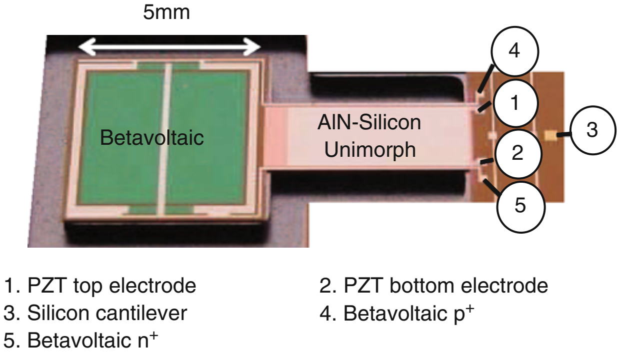

Figure 4.7: Photograph of the frontside and backside of the microfabricated piezoelectric unimorph cantilevers with integrated betavoltaics. The piezoelectric unimorph cantilever dimensions are: $l_{cant} = 10\,\text{mm}$, $l_{piezo} = 4.5\,\text{mm}$, $w_{cant} = w_{piezo} = 2\,\text{mm}$, $t_{cant} = 42.5\,\mu\text{m}$, $t_{piezo} = 1\,\mu\text{m}$, $l_{\beta} = 4\,\text{mm}$, and $w_{\beta} = 4\,\text{mm}$

two successive deep reactive ion etch (DRIE) steps, with the first DRIE performed on the front-side to define the shape and thickness of the cantilever, and the second DRIE on the back-side to release the unimorph cantilevers. The depth of the front-side DRIE was chosen to be slightly larger than the desired cantilever thickness, and the backside DRIE was performed until there was punch through in the areas etched with the frontside DRIE. The backside DRIE is also used to define the dicing pits, so the individual dice can be gently cleaved along the pits without breaking the released unimorph cantilevers. After separating individual dice, a $XeF_2$ etch was done on individual unimorph cantilevers to equalize the cantilever thicknesses. The unimorph cantilevers were thinned to $42.5\,\mu\text{m}$, so the resulting 5–10 N/m cantilevers could be pulled down across large gaps using radioisotope actuation. Reciprocation at large gaps is required for generating high values of $V_{gap}$ during charging. The $XeF_2$ etching procedure can be avoided by using SOI wafers, where the bulk oxide can act as an etch stop, and result in unimorph cantilevers whose thickness is equal to the top silicon body thickness.

The individual piezoelectric unimorph cantilevers were then packaged on a dual-inline package (DIP) (Fig. 4.9), so they could be conveniently positioned over the $^{63}$Ni thin film sources

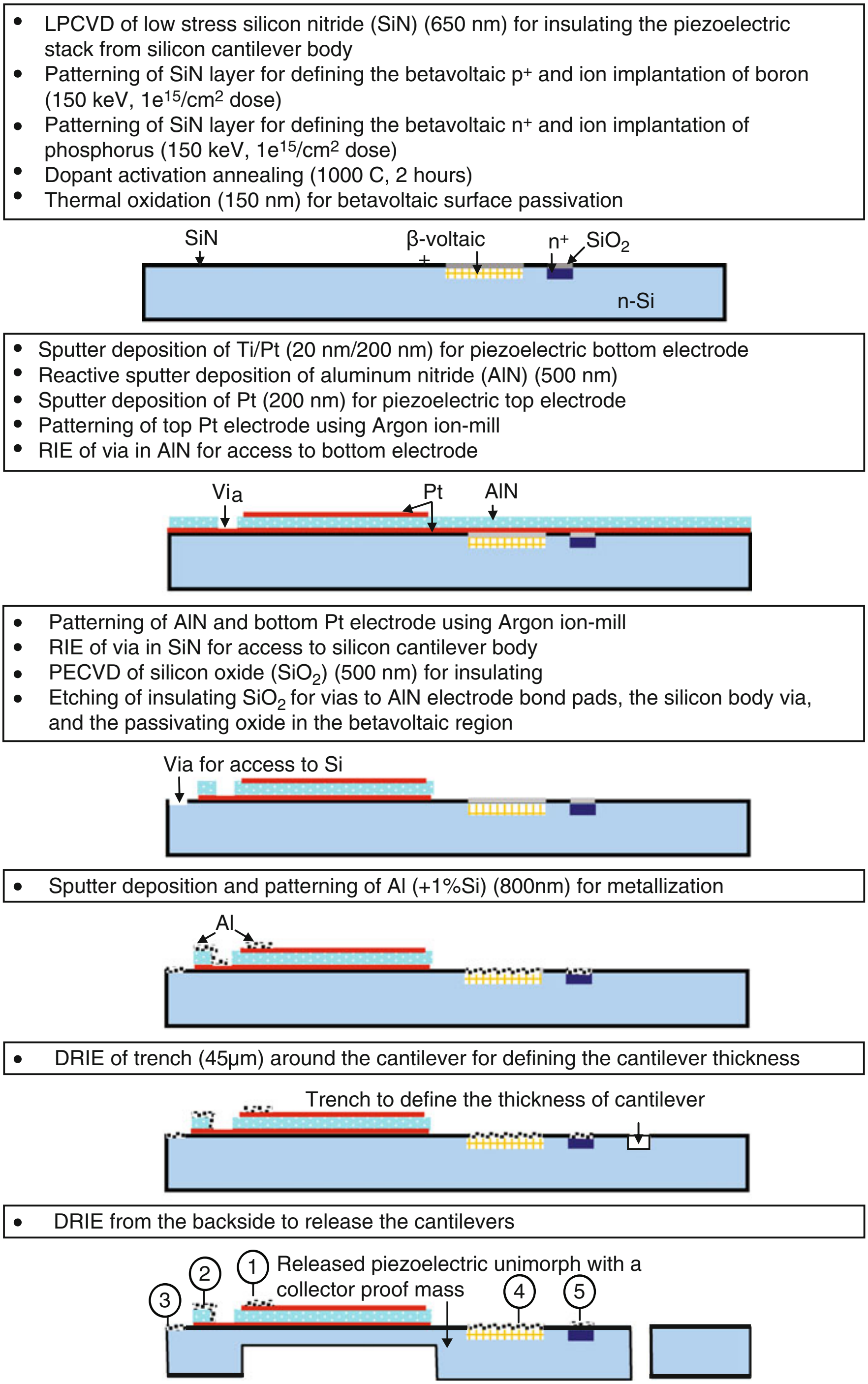

- LPCVD of low stress silicon nitride (SiN) (650 nm) for insulating the piezoelectric stack from silicon cantilever body
- Patterning of SiN layer for defining the betavoltaic p+ and ion implantation of boron (150 keV, 1e15/cm2 dose)
- Patterning of SiN layer for defining the betavoltaic n+ and ion implantation of phosphorus (150 keV, 1e15/cm2 dose)
- Dopant activation annealing (1000 C, 2 hours)
- Thermal oxidation (150 nm) for betavoltaic surface passivation

- Sputter deposition of Ti/Pt (20 nm/200 nm) for piezoelectric bottom electrode
- Reactive sputter deposition of aluminum nitride (AlN) (500 nm)
- Sputter deposition of Pt (200 nm) for piezoelectric top electrode
- Patterning of top Pt electrode using Argon ion-mill
- RIE of via in AlN for access to bottom electrode

- Patterning of AlN and bottom Pt electrode using Argon ion-mill
- RIE of via in SiN for access to silicon cantilever body
- PECVD of silicon oxide ($SiO_2$) (500 nm) for insulating
- Etching of insulating $SiO_2$ for vias to AlN electrode bond pads, the silicon body via, and the passivating oxide in the betavoltaic region

- Sputter deposition and patterning of Al (+1%Si) (800nm) for metallization

- DRIE of trench (45μm) around the cantilever for defining the cantilever thickness

- DRIE from the backside to release the cantilevers

Figure 4.8: Schematic illustration of microfabrication process flow for IREMPG piezoelectric unimorphs with integrated betavoltaics

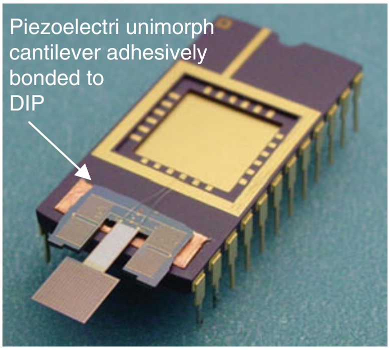

Figure 4.9: Photograph of the microfabricated IREMPG piezoelectric unimorph with integrated betavoltaics packaged on a dual inline package

employed to characterize the REMPG. The $^{63}$Ni source comprised of a 1 cm×1 cm×100 µm nickel foils electro-less coated with $\approx 5\%$ isotope purity $^{63}$Ni radioisotope (Isotope Products Laboratory, Los Angeles).

## 4.4 Testing and Results

The packaged AlN unimorph cantilevers were first tested for mechanical and piezoelectric dielectric properties to determine $R_{l,uni,opt}$. The IREMPG piezoelectric unimorph cantilevers were of the same dimensions as the REMPG AlN unimorph cantilevers presented in Chap. 2. Therefore, the unimorph mechanical and piezoelectric properties were similar. The $f_{res,uni}$ was measured to be 380.1 Hz, and $C_{piezo}$ was measured to be 0.83 nF. The resulting $R_{l,uni,opt}$ was calculated to be 521 kΩ. The ANSYS calculated $k_{uni}$ also varied from 10.3 N/m for $g = g_0$, when $F_{gap,eq}$ acts in the middle of the collector, to 6.74 N/m for $g = 0$, when $F_{gap,eq}$ acts at the tip of the unimorph cantilever (Fig. 3.3).

The $^{63}$Ni thin film source was then calibrated by measuring the net current output $I_r$ of the radioisotope source in vacuum to be 17.2 pA, indicating a radioisotope activity of 2.9 millicurie, and a continuous thermal power output $P_{out,^{63}\mathrm{Ni}}$ of 296 nW.

Subsequently, the 4 mm×4 mm betavoltaics integrated into the piezoelectric unimorph cantilever collector were characterized by

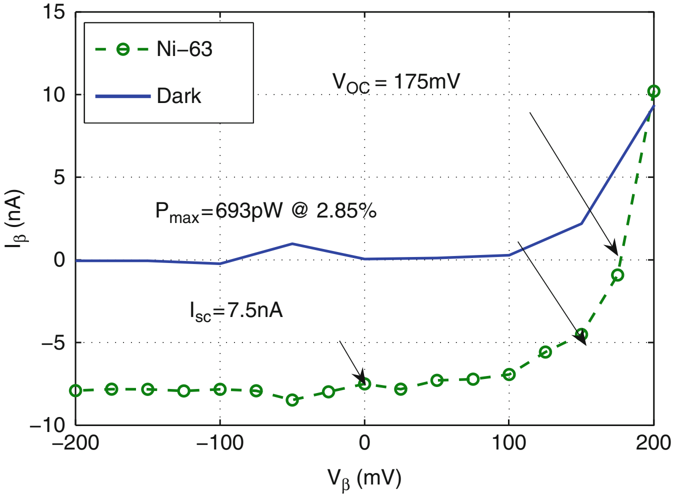

Figure 4.10: Plot of measured $I_\beta - V_\beta$ curves under dark and irradiated conditions for the 4 mm×4 mm silicon betavoltaic

placing the tip of the piezoelectric unimorph cantilever in contact with the $^{63}$Ni source, to avoid any voltage build-up on the radioisotope thin film, and measuring the $I_\beta - V_\beta$ curve (Fig. 4.10) using a semiconductor parametric analyzer (Keithley 4200). The maximum power output was calculated to be 690 pW at $\eta_\beta = 2.78\%$ efficiency, with the optimal operating point at $V_m = 150\,\text{mV}$ and $I_m = 4.6\,\text{nA}$, or $R_{l,\beta,opt} = 33\,\text{M}\Omega$. The high $\eta_\beta$ is enabled by the $<1\,\text{nA/cm}^2$ diode reverse leakage currents realized by optimizing the betavoltaic microfabrication process. The measured $R_{l,\beta,opt}$ and the calculated $R_{l,uni,opt}$ were used in the subsequent testing of the IREMPG.

IREMPG power generation was then characterized by assembling the packaged piezoelectric unimorph cantilevers with radioisotope thin film sources inside a test vacuum chamber with a glass view port (Fig. 3.11). Both the piezoelectric unimorph cantilever and the radioisotope source were mounted on linear motion feedthroughs to characterize the IREMPG at different values of $g_0$. The glass view port serves to monitor the motion of the unimorph cantilever tip through a microscope connected to a CCD camera. The radioisotope source was positioned at an initial gap $g_0$ from the tip of the unimorph cantilever, and the vacuum chamber was pumped down ($P \approx 10^{-3}$ millitorr) to minimize charge leakages in the air-gap due to build-up of high voltages. The unimorph cantilever tip position was monitored optically through the charge-discharge-oscillation cycles, and $V_{out,\beta}$, $V_{out,RF}$ and $V_{out,uni}$ were monitored during the reciprocation cycles to calculate $P_{out,\beta}$, $P_{out,RF}$, and $P_{out,uni}$, and further extract $\eta_{\beta,irempg}$, $\eta_{uni,irempg}$, and $\eta_{irempg}$. The reciprocation cycle was timed by calculating the interval between two consecutive $V_{out,uni}$ pulses. This was done for various values of $g_0$, until $g_0$ was too large for the unimorph cantilever to pull-in into the radioisotope and completely discharge.

The radioisotope actuation dynamics and the piezoelectric unimorph power generation characteristics were measured to be similar to those of REMPGs of similar dimensions presented in Chap. 2. Specifically, the measured values of $T_{rec}$ for the piezoelectric unimorph cantilevers at any $g_0$ were the same with and without the integrated betavoltaics, indicating that the inclusion of betavoltaics and the presence of extra electrodes does not affect radioisotope actuation. This can be attributed to the radioisotope actuation being driven by the charges accumulated on the electrically isolated radioisotope thin film, which are unaffected by the presence of extra electrodes on the piezoelectric unimorph cantilevers. Similarly, since the piezoelectric power generation is dependant only on the piezoelectric unimorph cantilever tip deflection and piezoelectric thin film dimensions and material properties, $P_{out,uni}$ characteristics were also measured to be similar. Hence, results from the radioisotope actuation dynamics and piezoelectric power generation of REMPGs presented in Chap. 2 are employed in the $P_{out,uni}$ and $\eta_{uni}$ calculations for the IREMPG.

## 4.4.1 Betavoltaic Power Generation

During the charging phase, $P_{out,\beta}$ was found to vary with time as shown in Fig. 4.11. Two trends can be observed from the data. First, the betavoltaic power output immediately after discharge $P_{out,\beta}|_{t=0}$ decreases with increasing $g_0$. Second, $P_{out,\beta}$ for any $g_0$ decreases with time during the reciprocation period. The measured

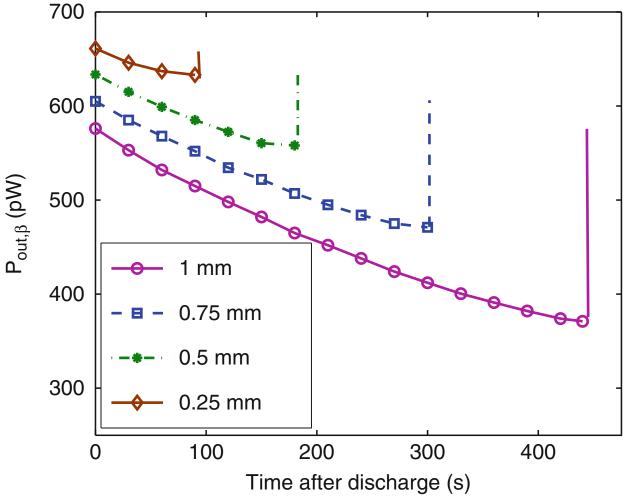

Figure 4.11: Plot of measured variation of the IREMPG betavoltaic power output $P_{out,\beta}$ with time at various initial gaps, with the 4 mm×4 mm silicon betavoltaic

$P_{out,\beta}|_{t=0}$ drops with increasing $g_0$ because $P_{in,\beta}$ decreases with $g_0$. This happens because the current due to the $\beta$-electrons collected by the betavoltaic collector $I_c$ decreases with increasing $g$. The $\beta$-electrons are emitted isotropically from the $^{63}$Ni thin films, and as the betavoltaic collector moves farther away from the radioisotope thin film, the solid angle it subtends at the radioisotope source decreases, and leads to lower $I_c$ (Fig. 4.12). However, the drop in measured $P_{out,\beta}$ with $g$ is steeper than the drop in $I_c$ with $g$ because $\eta_\beta$ also decreases with decreasing $I_c$ at larger gaps. This happens because $R_{l,\beta,opt}$ for $g > 0$, when $I_c \neq I_c|_{g=g_0}$, is different from $R_{l,\beta} = R_{l,\beta,opt}|_{g=g_0}$. Here, $I_c|_{g=g_0}$ is the $\beta$-electron current collected by a 4 mm×4 mm copper collector at $g = 0$.

The measured $P_{out,\beta}$ for any $g_0$ decreases with time during a reciprocation period because of the drop in $E_{in,\beta} = E_{rad,avg} - qV_{gap}$ with time (Fig. 4.1). However, the % drop in measured $P_{out,\beta}$ with time was higher than the calculated % drop in $E_{in,\beta}$. For example, at $g_0 = 1$ mm, the maximum drop in $E_{in,\beta}$ was calculated from Simulink simulations to be 18.1%, whereas the measured $P_{out,\beta}$ was found to drop by 34.9%. This is attributed to the drop in $\eta_\beta$ with time, both directly due to the variation of $E_{in,\beta}$

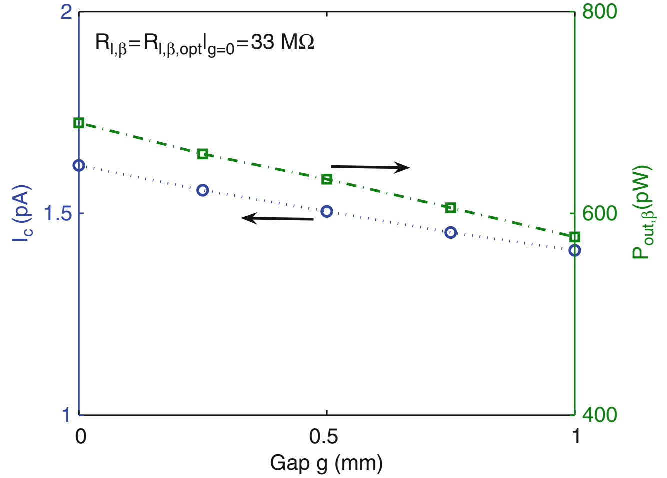

Figure 4.12: Plot of measured drop in the collected $\beta$-electron current $I_c$ with a 4 mm×4 mm copper collector, and the betavoltaic power output $P_{out,\beta}$ from a 4 mm×4 mm silicon betavoltaic with increasing gap $g$. The measurements were taken immediately after electrically shorting the collectors and the radioisotope thin films to avoid voltage build-up in the gap

with time during charging, and indirectly because $R_{l,\beta,opt}|_{g<g_0} \neq R_{l,\beta} = R_{l,\beta,opt}|_{g=g_0}$. The betavoltaic $\eta_\beta$ decreases with decreasing $E_{in,\beta}$ (Fig. 4.13) because of energy losses in the betavoltaic conversion mechanism. All $\beta$-electrons incident on the betavoltaic lose a fraction of their energy passing through inactive layers in the betavoltaic, before arriving near the junction to generate EHPs. Hence, a more accurate expression of $P_{out,\beta}$ is

$$P_{out,\beta} = \eta_\beta P_{in,\beta} = \eta'_\beta \frac{I_c}{q}(E_{rad,avg} - qV_{gap} - E_{loss,avg}), \qquad (4.12)$$

where $\eta'_\beta$ is a factor representing the betavoltaic EHP collection efficiency and $E_{loss,avg}$ is the average energy lost in the inactive layers of the betavoltaic. Such inactive layers include the passivation oxide layers on the diode, and the highly doped $p^+$ region of the diode if the junction is too deep. The losses result in $\eta_\beta$ dropping from 2.78% for $E_{in,\beta} = 17.3\,\text{keV}$ to 2.23% at $E_{in,\beta} = 14.2\,\text{keV}$. Furthermore, the resulting shift in $I_\beta - V_\beta$ characteristics changes $R_{l,\beta,opt}$. Hence, when $R_{l,\beta} = R_{l,\beta,opt}|_{g=0}$ is used, $\eta_\beta$ is further lowered, resulting in an even lower $P_{out,\beta}$.

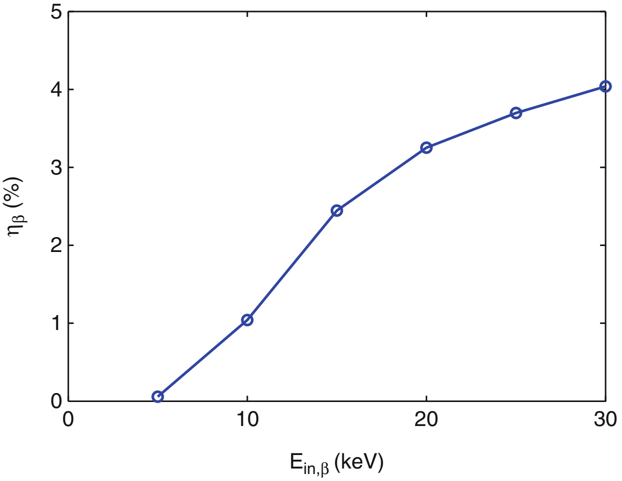

Figure 4.13: Plot of measured variation of betavoltaic energy conversion efficiency $\eta_\beta$ of 4 mm×4 mm silicon betavoltaics with incoming $\beta$-electron energy $E_{in,\beta}$. The measurements were done by irradiating the betavoltaic with SEM electron beams with varying accelerating voltages

As a consequence of the variation of $P_{out,\beta}$ during reciprocation at various values of $g_0$, the betavoltaic energy conversion efficiency, calculated as

$$\eta_{\beta,irempg}|_{I_{in}=I_c} = \frac{\int_0^{T_{rec}} P_{out,\beta} dt}{I_c|_{g=g_0}(E_{rad,avg}/q)T_{rec}}, \tag{4.13}$$

decreases with increasing $g_0$ (Fig. 4.14). Here, $I_c|_{g=g_0}$ equals $0.09 \times I_r$ for the IREMPGs discussed in this chapter, because the area of the radioisotope thin film source $A_r$ equals 1.75 cm$^2$.

### 4.4.2 Wireless RF Pulse Generation

The generation of wireless RF pulses from the radioisotope discharge was characterized using the experimental set-up shown in Fig. 4.15. Hand-wound air-core solenoid coils ($\approx$ 100 turns, $\phi$ = 10 mm, $\approx$ 27 $\mu$H, 0.8 $\Omega$) were used at both the transmission and receiving ends. The wirelessly received $V_{remote}$ was measured as a function of the distance $d$ between the coils, the initial gap $g_0$, and the voltage bias across the AlN thin film

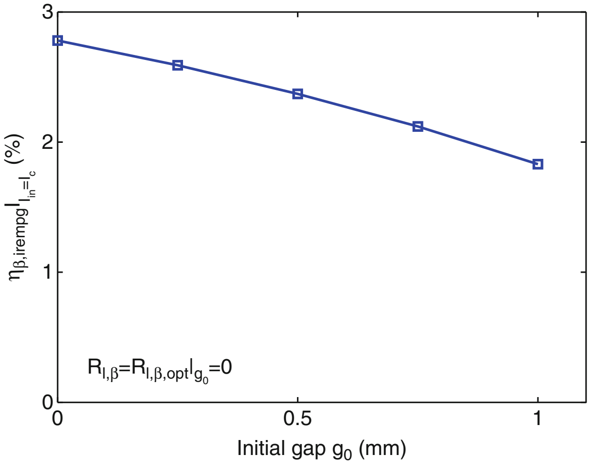

Figure 4.14: Measured variation of the 4 mm×4 mm silicon betavoltaic energy conversion efficiency $\eta_\beta|_{I_{in}=I_c}$, taking only the current collected by the betavoltaic as the input

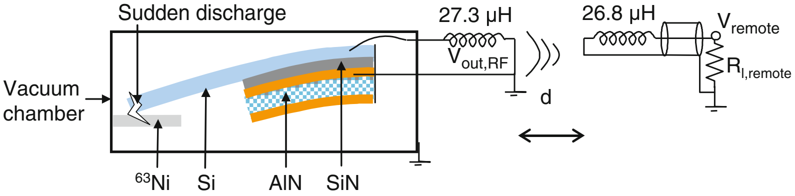

Figure 4.15: Schematic illustration of the IREMPG wireless transmission test set-up

$V_{AlN,bias}$. With $V_{AlN,bias} = 0\,\mathrm{V}$, $g_0 = 1\,\mathrm{mm}$, and $R_{l,remote} = 50\,\Omega$, $V_{remote}$ was measured for $d = 1\,\mathrm{m}$ to give a maximum peak-peak voltage of 0.8 V (Fig. 4.16), or a maximum RF power of $\approx$ 6 mW, which is more than $10^6$ times of the input power of 1.5 nW. This can be attributed to the long charging times and the short discharging times involved in the IREMPG. The RF signal can be detected as far as 3.6 m away from the transmitter (limited by the room size). The SNR of the signal within 2 m of the transmitter was estimated to be 39 dB given the noise level at the coil of 5 mV and a peak voltage of the signal of 0.4 volts. Next, with $V_{AlN,bias} = 0\,\mathrm{V}$, $d = 0.22\,\mathrm{m}$, and $R_{l,remote} = 50\,\Omega$, $V_{remote}$ was measured for various values of $g_0$

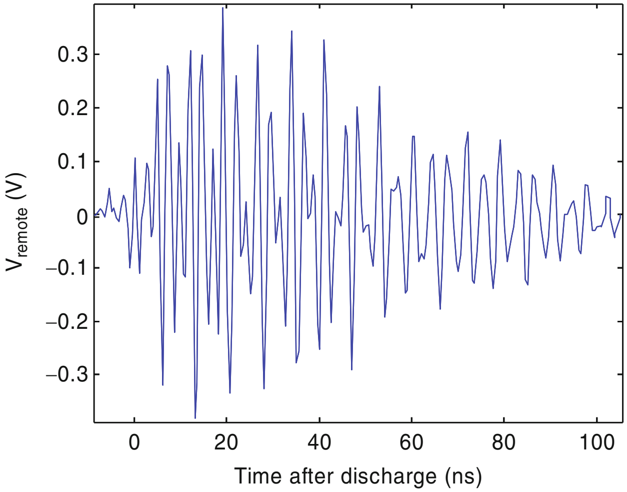

Figure 4.16: Plot of measured wireless RF signal $V_{remote}$ detected at $d = 1\,\mathrm{m}$ for $V_{AlN,bias} = 0\,\mathrm{V}$, $g_0 = 1\,\mathrm{mm}$, and $R_{l,remote} = 50\,\Omega$

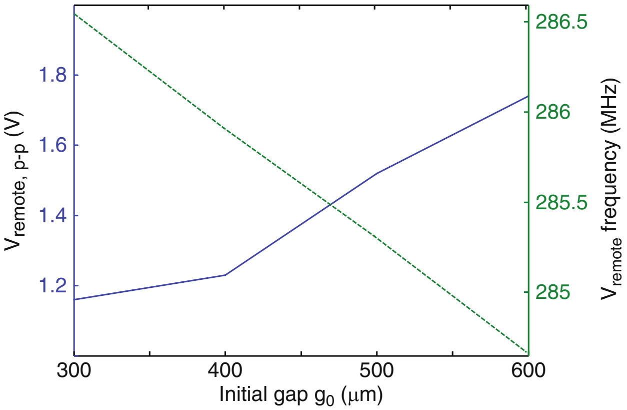

Figure 4.17: Plot of measured variation in $V_{remote}$ magnitude and frequency with $g_0$ for $V_{AlN,bias} = 0\,\mathrm{V}$, $d = 0.22\,\mathrm{m}$, and $R_{l,remote} = 50\,\Omega$

(Fig. 4.17). The amplitude of $V_{remote}$ was measured to increase with $g_0$ as expected, because larger $g_0$'s lead to larger $Q_{gap,pi}$, and therefore larger discharge currents. Moreover, the frequency of $V_{remote}$ was observed to decrease with $g_0$. This can be attributed to the higher voltages that build up across the dielectric and alter its effective dielectric constant, thereby changing the resonant frequency of the LC resonator formed by the dielectric

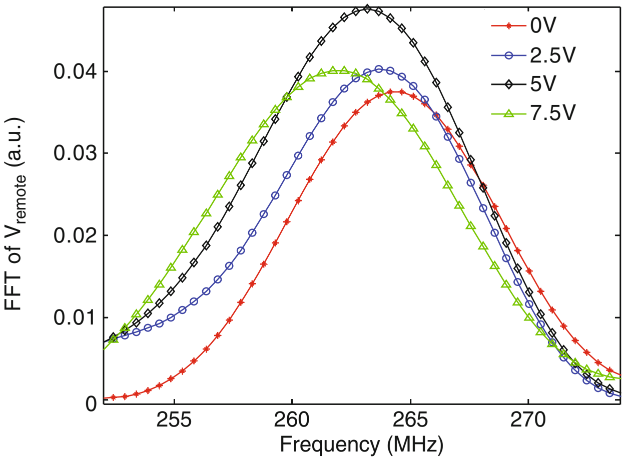

Figure 4.18: Plot of measured variation in $V_{remote}$ signal FFT with $V_{AlN,bias}$ for $g = 500\,\mu\text{m}$, $d = 0.22\,\text{m}$, and $R_{l,remote} = 50\,\Omega$

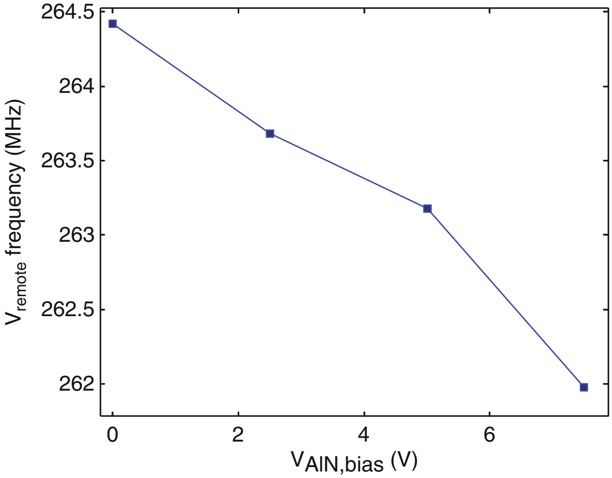

Figure 4.19: Plot of measured variation of $V_{remote}$ frequency with $V_{AlN,bias}$ for $g = 500\,\mu\text{m}$, $d = 0.22\,\text{m}$, and $R_{l,remote} = 50\,\Omega$

capacitor and the transmission solenoid outside. Subsequently, with $g = 500\,\mu\text{m}$, $d = 0.22\,\text{m}$, and $R_{l,remote} = 50\,\Omega$, $V_{remote}$ was measured for various values of $V_{AlN,bias}$ (Fig. 4.18). While the frequency of $V_{remote}$ was measured to decrease with increasing bias, the amplitude was measured to increase. Both these effects can be explained by the fact that the application of $V_{AlN,bias}$ results in the unimorph deforming, and decreasing $g_0$. As can be seen from Fig. 4.19, the frequency of $V_{remote}$ changes at 450 kHz/V with the application of $V_{AlN,bias}$. This frequency tunability can enable the IREMPG to convey sensor information wirelessly in a sensor network.

Furthermore, the total wireless RF energy transmitted from the IREMPG was estimated to be negligible ($<$ 1 nJ/reciprocation) compared to the input radioisotope power per reciprocation. Hence, $P_{out,RF}$ can be excluded from IREMPG energy conversion efficiency calculations.

### 4.4.3 IREMPG Energy Conversion Efficiency

The total measured IREMPG energy conversion efficiency can be calculated by adding the measured $\eta_{uni,irempg}$ (Fig. 3.16) and measured $\eta_{\beta,irempg}$. The measured $\eta_{\beta,irempg}$ can be calculated from the measured $\eta_{\beta,irempg}|_{I_{in}=I_c}$ (Fig. 4.14) by recognizing that $I_c = 0.09 \times I_r$, and hence $\eta_{\beta,irempg} = 0.09 \times \eta_{\beta,irempg}|_{I_{in}=I_c}$. Figure 4.20 plots the measured variation of $\eta_{irempg}$ with $g_0$ for the IREMPG, where the low $\eta_{\beta,irempg}$ results in a maximum $\eta_{irempg}$ of 4.13%.

## 4.5 Discussion

### 4.5.1 Betavoltaic Power Generation

The contribution of $\eta_{\beta,irempg}$ to $\eta_{irempg}$ can be raised by employing $^{63}$Ni thin films of higher $SA_r$, so the same $I_r$ can be realized in smaller area $^{63}$Ni thin films. If the same $I_r$ can be realized in a 4 mm×4 mm $^{63}$Ni thin film, $I_c$ collected by the betavoltaic will equal $I_r$, and hence $\eta_{\beta,irempg} = \eta_{\beta,irempg}|_{I_{in}=I_c}$. The resulting $\eta_{irempg}$ will vary with $g_0$ as shown in Fig. 4.21, where the maximum realizable $\eta_{irempg}$ is 5.75%.

## 4.6 Conclusions

An integrated radioisotope actuated electro-mechanical power generator (IREMPG), comprising of piezoelectric AlN unimorph cantilevers with integrated silicon betavoltaics, was designed,

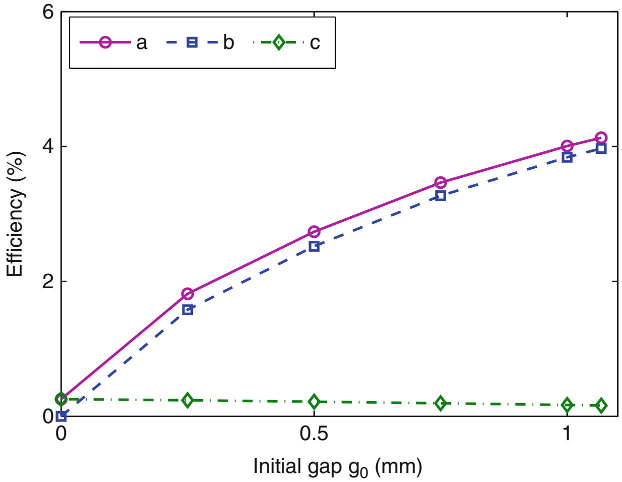

Figure 4.20: Plot of measured variation of IREMPG (**a**) $\eta_{irempg}$, (**b**) $\eta_{uni,irempg}$, and (**c**) $\eta_{\beta,irempg}$ with initial gap $g_0$. The 4 mm×4 mm silicon betavoltaic energy conversion efficiency $\eta_{\beta,irempg}$ is calculated using the net power input to the IREMPG

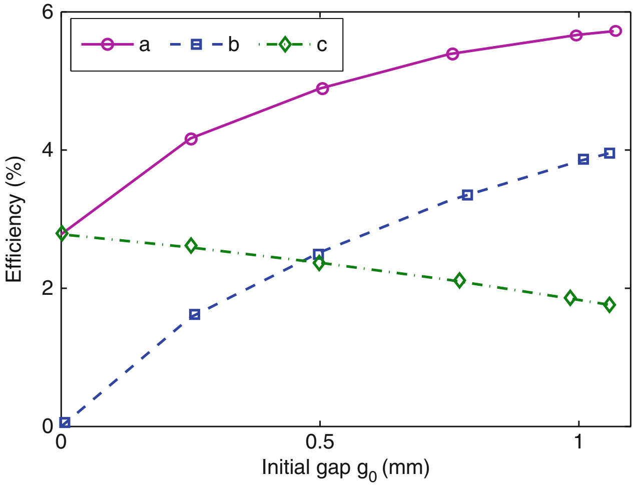

Figure 4.21: Plot of estimated variation of IREMPG (**a**) $\eta_{irempg}$, (**b**) $\eta_{uni,irempg}$, and (**c**) $\eta_{\beta,irempg}$ with initial gap $g_0$ when a 4 mm×4 mm $^{63}$Ni thin film $^{63}$Ni source with $9X\ SA_r$ is employed with 4 mm×4 mm silicon betavoltaic collectors

fabricated and experimentally characterized to yield a maximum an RF pulse remotely detectable up to 3.6 m, (2) a 12.95 $\mu$W low-frequency pulse across 521 k$\Omega$, for 1 s every 400 s, at 3.97% efficiency, and (3) 400-700 pW average continuous power across 33 M$\Omega$ at 2.78% maximum efficiency. The three power outputs can potentially be utilized in periodically sampling wireless sensor microsystems for retaining memory state during the dormant state, periodic sensing and computation, and periodic wireless communication respectively (Fig. 2.8).

## 4.7 Future Directions

Higher power integrated radioisotope micropower generators packaged in small portable vacuum packages are desired for deployment in terrestrial applications.

Higher power outputs can be realized by raising both the specific activity of $^{63}$Ni fuel and the energy conversion efficiency of the generator. The specific activity for the $^{63}$Ni thin films used in this book was $< 5$ curie/g. This can be readily raised by employing $> 10$ curie/g (15–20% isotope purity) available from Oak Ridge National Laboratories [10]. The higher specific activity will also lead to increased IREMPG energy conversion efficiency by increasing both the betavoltaic conversion efficiency, as higher $\beta$-electron current can be collected by smaller betavoltaics, and piezoelectric unimorph conversion efficiency, by enabling reciprocation at higher gaps. Betavoltaic energy conversion efficiency can also be raised by employing $\approx 20\%$ efficiency SiC betavoltaics. The SiC betavoltaics can be integrated with the microfabricated radioisotope power generators either directly by using epitaxially grown SiC junctions, or indirectly by adhesively bonding thin-layers of SiC diodes to the piezoelectric unimorph cantilever collectors. The energy conversion efficiency of the piezoelectric unimorph cantilevers can be raised by realizing higher air-gap voltages at larger initial gaps. The air-gap voltage is currently limited by the charge leakages in the air-gap, which result in leakage currents that eventually null the radioisotope output current. Higher specific activity radioisotope sources emitting larger radioisotope currents can sustain larger leakage currents, and hence can sustain higher voltages for higher energy conversion efficiency. The charge leakages can also be minimized by decreasing the vacuum level beyond the $10^{-6}$ millitorr employed in current systems. However, this may be difficult to attain and sustain in smaller vacuum packages without continuous pumping.

Furthermore, in order to employ the IREMPG on autonomous wireless sensor microsystem platforms, the transmission range of the wireless RF signals needs to be increased. This can be done by first gaining a thorough understanding of the radioisotope discharge triggered wireless signal generation and then optimizing the RF antenna transmitter and receiver design. Furthermore, wireless RF signal modulation schemes need to be developed to utilize the RF signals from IREMPGs as information carriers.

Simultaneously, efforts should focus on developing compact IREMPGs in vacuum packages that can sustain the ultra low vacuums ($\approx 1\,\mu$torr) required for high efficiency IREMPG operation. In particular, a study of the feasibility of maintaining $\approx 1\,\mu$torr pressure over long periods without continuous pumping needs to be carried out. Packages that can retain the ultra-high vacuum for longer periods need to be developed. This may be achieved by employing the recently developed MEMS hermetic packaging techniques that use conventional vacuum packaging technologies developed for integrated circuits. The thin film $^{63}$Ni radioisotope sources lend themselves well to conventional packaging techniques, both because of their thin film form and because of the low effusivity of $^{63}$Ni even at the elevated temperatures (300–400 C) [9] used for vacuum packaging. Getters may be incorporated into the package to sustain the ultra-low vacuum. Subsequently, the packaged IREMPGs can be evaluated for radiation safety.

# Chapter 5
# Radioisotope Micropower Generation: 3D Silicon Electronvoltaics

## 5.1 Introduction

In this chapter, the application of high power density (1–2 W/cc) and high energy density (100–200 MJ/cc) $^{147}$Pm fuel in 1–20 mW/cc, 5 year lifetime microbatteries is explored. The resulting $>220$ W-h/cc microbatteries could potentially replace the currently employed 1–10 W-h/cc electrochemical batteries [18] and enable longer lifetime autonomous microsystems.

In particular, novel high efficiency DRIE textured 3D silicon diodes (Fig. 5.1) are reported for potential use in the $^{147}$Pm betavoltaic microbatteries. Silicon electronvoltaics are chosen because they can be compact, produce readily usable currents (1–100 μW/cm$^2$) at practical output voltages (0.1–1 V), and can be fabricated easily in established silicon based microfabrication technology. The betavoltaics are 3D textured to realize a 14X–20X increase in the power density compared to previously demonstrated planar betavoltaic microbatteries [11].

## 5.2 Betavoltaics

### 5.2.1 Operation

Figure 5.2a illustrates the structure and operation of a radioisotope powered betavoltaic microbattery. Spontaneous decay of radioisotope atoms in the thin film source leads to the emission of $\beta$-electrons, which dissipate their energy primarily through inelastic collisions with the orbital electrons of atoms in the semiconductor [3]. The inelastic collisions result in the ionization of the atoms in the semiconductor, and lead to the generation of electron hole

R. Duggirala et al., *Radioisotope Thin-Film Powered Microsystems*,
MEMS Reference Shelf 6, DOI 10.1007/978-1-4419-6763-3_5,

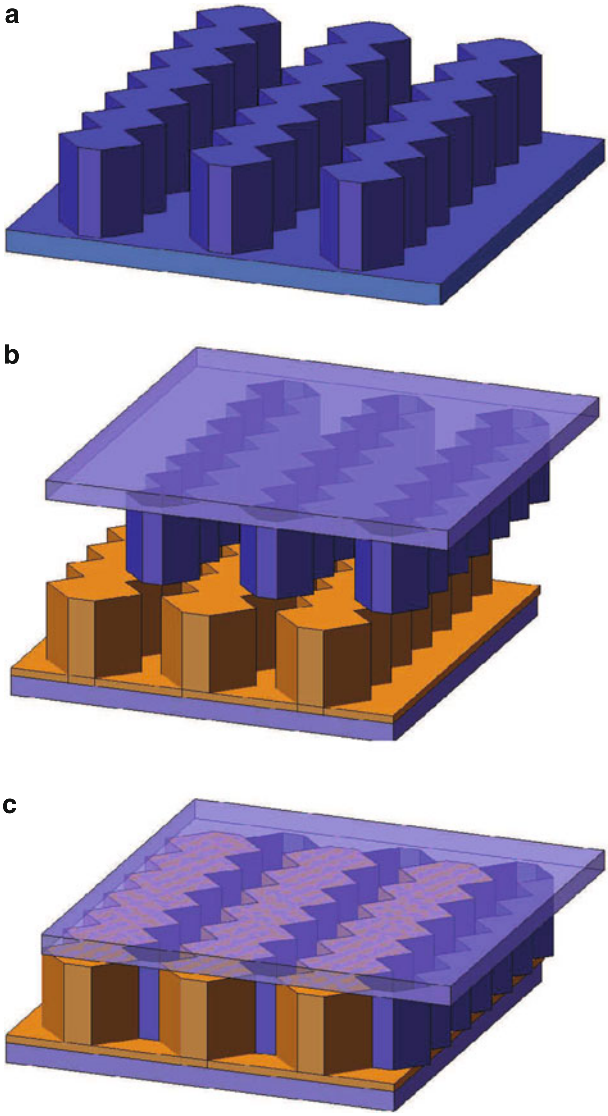

Figure 5.1: 3D dimetric view schematics of (**a**) 3D silicon diodes, (**b**) two interleaved betavoltaic wafers to be stacked, and (**c**) assembled 3D betavoltaics

pairs (EHPs). The EHPs generated within one minority carrier diffusion length of the depletion region diffuse to the edge of the depletion region, and along with the EHPs generated within the depletion region, are swept across the junction by the depletion region electric field to produce electrical power.

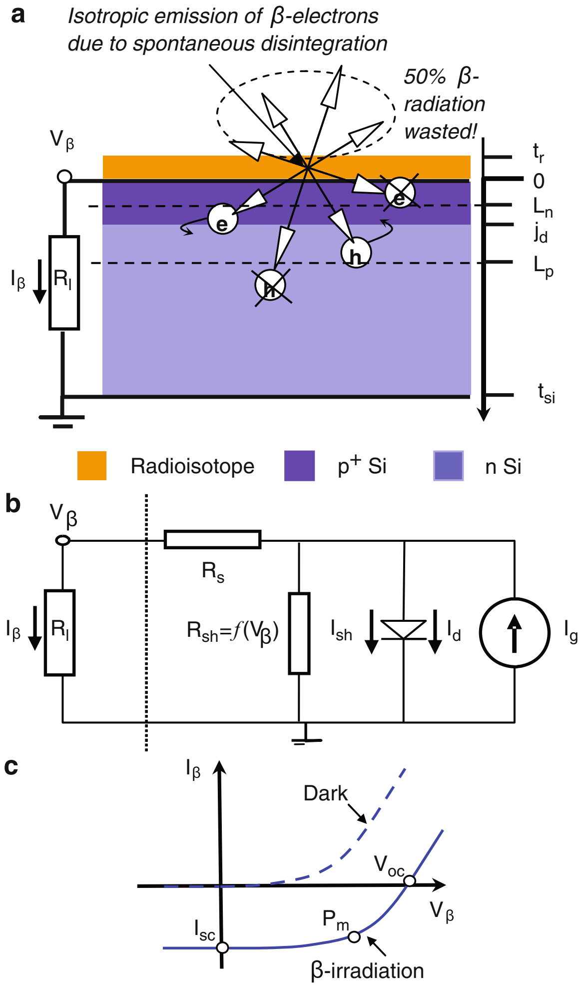

Figure 5.2: Schematics illustrating planar $p^+ - n$ betavoltaic (**a**) structure and principle of operation, (**b**) electrical equivalent circuit, and (**c**) output I-V characteristics. Here, $t_r$ and $t_{si}$ are the radioisotope thin film and silicon substrate thickness respectively, $j_d$ is the junction depth, and $L_n$ and $L_p$ are the minority carrier diffusion lengths

Figure 5.2b illustrates the electrical equivalent circuit of the betavoltaic microbattery. Current source $I_g$ models the current due to $\beta$-generated EHPs collected at the junction, and is usually 0.1–100 $\mu$A/cm$^2$ for betavoltaics (compared to 1–100 mW/cm$^2$ for photovoltaics). This is because of the much lower power outputs of $\beta$-radioisotope thin films ($\approx$1–100 μW/cm$^2$) compared to sunlight ($\approx$1–100 mW/cm$^2$). Resistor $R_{sh}$ models the shunt leakage in the diode due to carrier recombination-generation (R-G) in the depletion region [38], and has to be significantly larger than the load impedance $R_l$ to avoid current losses. While $R_{sh}$ has negligible effect on photovoltaics because of the high current injection levels, low $R_{sh}$ ($< G\Omega$) can lead to significant current losses in betavoltaics. Hence it is desirable to maximize $R_{sh}$ in betavoltaics. Resistor $R_s$ models the series resistance due to the diode neutral regions and contacts, and is typically 1–20 Ω. While $R_s$ is relatively important in photovoltaics due to the much higher current injection levels, it can usually be ignored in betavoltaics. This is because the betavoltaic output current $I_\beta$ is typically 1–10 μA/cm$^2$, and the resulting voltage drops of 1–100 μV are negligible compared to the betavoltaic output voltage $V_\beta$ of 100–400 mV common to betavoltaics. Hereafter, $R_s$ will be assumed to be zero.

Figure 5.2c illustrates the resulting output $I_\beta - V_\beta$ characteristics. The optimal betavoltaic operating point can be identified from the $I_\beta - V_\beta$ characteristics under irradiation by calculating the maximum power output $P_m$. The optimal load impedance $R_{l,m}$ can then be chosen as

$$R_{l,m} = \frac{V_m}{I_m}, \tag{5.1}$$

where $I_m$ and $V_m$ are the betavoltaic current and voltage at the maximum power operating points.

### 5.2.2 Theory

Figure 5.3 illustrates the various energy conversion processes in a betavoltaic microbattery. The spontaneous disintegrations within the radioisotope thin film produce $\beta$-electrons with average kinetic energy $E_{rad,avg}$, for a net power generation within the radioisotope $P_g$ given by

$$P_g = 3.7 \times 10^{10} \times SA_r \times \rho_r \times A_r \times t_r \times E_{rad,avg}, \tag{5.2}$$

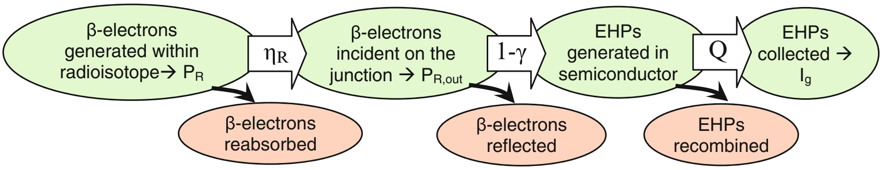

Figure 5.3: Schematic illustrating the various stages of energy conversion in a betavoltaic microbattery

where $SA_r$, $\rho_r$, $A_r$, and $t_r$ are the radioisotope thin film source specific activity in curie/g, density, area, and thickness respectively. The emitted $\beta$-electrons travel through the radioisotope thin film source, while continuously losing energy due to both the inelastic collisions with the orbital electrons in the thin film and radiative interactions with the nuclei [3], before emerging out of the thin film surface to irradiate the betavoltaic. The $\beta$-electron energy losses can be estimated using the continuous slowing down approximation (CSDA), with the mean energy loss per unit path length given by adding both collision and radiative stopping power [35]. The radioisotope emission efficiency $\eta_r$ can then be calculated as detailed in Sect. 5.2.1. Thus, the net power emitted by the radioisotope thin film is given by

$$P_{r,out} = \eta_r P_r = \eta_r \times 3.7 \times 10^{10} \times SA_r \times \rho_r \times A_r \times t_r \times E_{rad,avg}. \quad (5.3)$$

A portion of $P_{r,out}$ incident on the betavoltaic surface is reflected due to electron backscattering, and is lost in the thin film source. The transmitted portion of $P_{r,out}$ constitutes the betavoltaic input power $P_{in,\beta}$, and is given by

$$\begin{aligned} P_{in,\beta} &= (1-\gamma)\frac{1}{2}\eta_r \times 3.7 \times 10^{10} \times SA_r \times \rho_r \times A_r \times t_r \times E_{rad,avg} \\ &= \frac{I_{in,\beta}}{q} E_{rad,avg}. \end{aligned} \quad (5.4)$$

Here, $I_{in,\beta}$ is the net current input into the betavoltaic due to $\beta$-electron irradiation, and $\gamma$ is the electron reflection coefficient, which depends on the material properties of both the radioisotope thin film source and the betavoltaic. The factor of 1/2 is due to the loss of $\beta$-electrons emitted out of the upper surface. The incident $\beta$-electron kinetic energy is absorbed in the semiconductor to generate EHPs, and the number of EHPs generated $N_{EHP,g}$ can be computed by assuming that each EHP generation event consumes ionization energy $E_{ion}$. Therefore,

$$N_{EHP,g} = \frac{P_{in,\beta}}{E_{ion}} = \frac{I_{in,\beta} E_{rad,avg}}{q E_{ion}}. \tag{5.5}$$

The ionization energy $E_{ion}$ depends on the band gap of the semiconductor, and has been calculated to be $\approx 3.6\,\text{eV}$ for silicon [39]. The generated EHPs are collected by the betavoltaic with charge collection efficiency Q to generate $I_g$ as

$$I_g = qQN_{EHP,g} = Q\frac{I_{in,\beta} E_{rad,avg}}{E_{ion}}. \tag{5.6}$$

The betavoltaic charge collection efficiency $Q$ is $<100\%$ because of two non-idealities that exist in practical semiconductor junctions. First, since all the beta-electrons lose energy in passing through inactive layers in the betavoltaic structure where no EHPs are generated, the average energy spent on exciting EHPs is lower than $E_{avg}$. These layers include the metal electrode and the oxide passivation layer. Second, a fraction of the generated EHPs in the semiconductor recombine before being collected by the junction. The junction EHP collection coefficient $Q_j$ is determined by factors including the beta particle absorption characteristics, junction depth $j_d$, minority carrier diffusion lengths $L_n$ and $L_p$, and surface recombination velocities $S_n$ and $S_p$ at semiconductor interfaces. It is desirable to maximize $L_n$ and $L_p$, so EHPs generated farther away from the depletion region can still diffuse into the depletion region. It is also desirable to minimize $S_n$ and $S_p$, so that the loss of radiation generated EHPs due to recombination at the surface does not create minority carrier gradients that impede the diffusion of carriers into the depletion region [40]. Considering the two non-idealities, (5.6) can be rewritten as

$$I_g = qQ_j N_{EHP,g} = Q_j \frac{I_{in,\beta}(E_{rad,avg} - E_{loss,avg})}{E_{ion}}. \tag{5.7}$$

where $E_{loss,avg}$ is the average energy loss of $\beta$-electrons in traversing the inactive layers. Hence, the betavoltaic serves as a current multiplier, amplifying the current due to the $\beta$-electron emission by a factor $M$ to generate $I_g$. The betavoltaic current multiplication factor is given by

$$M = \frac{I_g}{I_{in,\beta}} = Q_j \frac{(E_{avg} - E_{loss,avg})}{E_{ion}}. \tag{5.8}$$

The betavoltaic generation current $I_g$ is shared by the diode, $R_{sh}$, and $R_l$ as

$$I_g = I_d + I_{sh} + I_\beta, \tag{5.9}$$

resulting in the I-V characteristics shown in Fig. 5.2c. Here, $I_d$ is the diode diffusion current, given by

$$I_d = I_0 \left( e^{V_\beta / V_t} - 1 \right), \tag{5.10}$$

and $I_{sh}$ is the current due to the recombination-generation (R-G) in the depletion region, given by [38]

$$I_{sh} = \frac{qAn_i}{2\tau_0} \frac{\left( e^{V_\beta / V_t} - 1 \right)}{\left( 1 + \frac{V_{bi} - V_\beta}{V_t} \frac{\sqrt{\tau_n \tau_p}}{2\tau_0} e^{(V_\beta / 2V_t)} \right)}. \tag{5.11}$$

Here, $I_0$ is the reverse bias saturation diffusion current of the ideal diode, given by

$$I_0 = qA \left( \frac{D_n}{L_n} \frac{n_i^2}{N_A} + \frac{D_p}{L_p} \frac{n_i^2}{N_D} \right), \tag{5.12}$$

and $V_t$ is the thermal voltage, $A$ is the area of the semiconductor junction, $n_i$ is the intrinsic carrier concentration, $V_{bi}$ is the built-in voltage, $\tau_n$ and $\tau_p$ are the minority carrier lifetimes of electrons and holes, and

$$\tau_0 = \frac{1}{2} \left( \tau_p e^{(E_T - E_i)/kT} + \tau_n e^{(E_i - E_T)/kT} \right), \tag{5.13}$$

where $E_T$ and $E_i$ are the semiconductor trap and intrinsic energies respectively. Additionally, $D_n$ and $D_p$ are the diffusion coefficients, $L_n$ and $L_p$ the minority carrier diffusion lengths of electrons and holes respectively, and $N_A$ and $N_D$ are the doping concentrations of the $n$ and the $p$ sides of the junction. The maximum power operating point can be extracted from measured I-V characteristics, and the maximum betavoltaic conversion efficiency $\eta_\beta$ calculated as

$$\eta_\beta = \frac{V_m I_m}{P_{r,out}}. \tag{5.14}$$

Hence, the overall betavoltaic microbattery conversion efficiency $\eta_{\mu B}$ can be written as

$$\begin{aligned} \eta_{\mu B} &= \frac{V_m I_m}{P_g} = \frac{V_m I_m}{3.7 \times 10^{10} \times SA_r \times \rho_r \times A_r \times t_r \times E_{rad,avg}} \\ &= \eta_r \frac{1}{2}(1-\gamma)\eta_\beta. \end{aligned} \tag{5.15}$$

## 5.3 Five Milliwatt per cubic centimeter, five Year Lifetime Microbattery Design

Betavoltaic microbattery power density $P_{\mu B,dens}$ can be written as

$$P_{\mu B,dens} = P_{g,dens} \times \eta_r \times (1-\gamma) \times FFF \times \eta_\beta, \tag{5.16}$$

where $P_{g,dens}$, $\eta_r$ and $FFF$ are the radioisotope thin film fuel power density, emission efficiency, and fuel fill factor ($FFF$) respectively, and $\eta_\beta$ is the betavoltaic energy conversion efficiency.

### 5.3.1 Radioisotope Thin Film Design

Radioisotope power density $P_{g,dens}$ is given by

$$P_{g,dens} = SA_r \rho_r, \tag{5.17}$$

and decreases exponentially with time as

$$P_{g,dens} = P_{g,dens}|_{t=0} \times e^{0.3t/\tau_{1/2}} \tag{5.18}$$

following the drop in the specific activity of the radioisotope. Here, $P_{g,dens}(\mathrm{t}=0)$ and $\tau_{1/2}$ are the radioisotope thin film initial output power density and half-life period (in years) respectively. In order to realize a safe microbattery with 5 mW/cc average

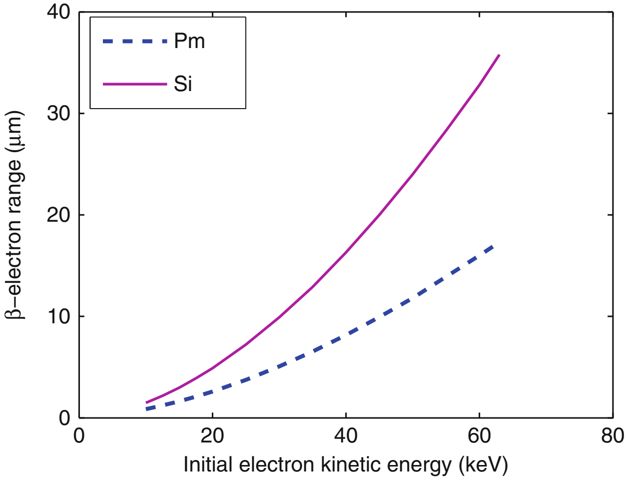

Figure 5.4: Plot of the calculated ranges of energetic electrons in $^{147}$Pm and silicon. The $\beta$-electron range was calculated by dividing the tabulated CSDA range by the density of $^{147}$Pm and silicon respectively

output and 5 year lifetime, a radioisotope fuel with adequate $P_{r,dens}$(t $=$ 0) and $\tau_{1/2}$ needs to be selected while considering the radiation safety requirements. Promethium-147 ($^{147}$Pm) is suitable for such a microbattery because $^{147}$Pm fuel, used in the form of $Pm_2O_3$ deposited over betavoltaics, has: (1) high energy density of 170 MJ/cc (5 year output); (2) high power density of 2.04 W/cc (at 830 curie/g); (3) half-life of 2.6 years; (4) low-energy $\beta$-electrons ($E_{^{147}\mathrm{Pm},avg} = 63$ keV) that are easily absorbed in thin layers of silicon ($t_{si} < 50\,\mu$m) (Fig. 5.4) [35]; and (5) negligible Bremsstrahlung emission when silicon in the stopping material (fraction of $^{147}$Pm $\beta$-electrons converted into photons <0.1% [3]), which results in low radiation dose rates for the microbatteries (6.1 mrem/hour at 2.5 cm when using 66 curies of $^{147}$Pm fuel and high density shielding [11]). The radioisotope fuel emission efficiency $\eta_r$ is limited by the $\beta$-electron energy loss within the fuel due to inelastic collisions with $^{147}$Pm orbital electrons. Figure 5.5 plots the drop in the kinetic energy of a 63 keV $\beta$-electron with distance traveled in $^{147}$Pm, calculated using the theory of continuous slowing down approach (CSDA) [3]. Assuming a linear

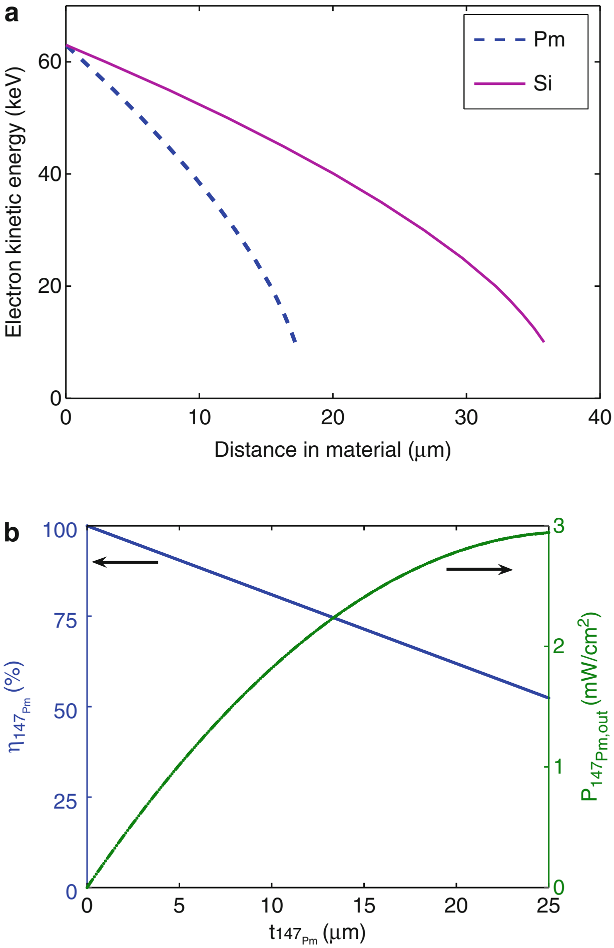

Figure 5.5: Plots of the calculated (**a**) decrease in the kinetic energy of 63 keV $\beta$-electrons when traveling through $^{147}$Pm and Si media, and (**b**) variation in $^{147}$Pm thin film power output $P_{^{147}\mathrm{Pm},out}$ and emission efficiency $\eta_{^{147}\mathrm{Pm}}$ with thickness $t_{^{147}\mathrm{Pm}}$

gradient of energy, calculated to be 2.4 keV/µm, the dependence of $\eta_r$ on $t_r$ can be calculated to be

$$\eta_r = 1 - \frac{\frac{\partial E_{rad}}{\partial x}\frac{t_r}{2}}{E_{rad,avg}} \tag{5.19}$$

where $\frac{\partial E_{rad}}{\partial x}$ is the linear rate of energy loss due to self-absorption. The expression above assumes that all the $\beta$-electrons generated are emitted in a direction perpendicular to the film. However, since the $\beta$-electrons are emitted isotropically, $\eta_r$ will be lower than the value estimated from (5.19). While low $t_r$ is desirable for high $\eta_r$, high $t_r$ is desirable for high $P_g$. Figure 5.5 illustrates this trade-off, and can be used to design the thickness of $^{147}$Pm thin film. The maximum $^{147}$Pm thin film thickness for $\eta_r > 85\%$ can be calculated from (5.19) to be 6 µm.

## 5.3.2 3D Silicon Betavoltaic Design

Since the radioisotope fuel is limited to thin film form for high $\eta_r$, $FFF$ depends on the surface area of the radioisotope-betavoltaic interface. The fuel fill factor $FFF$ can be maximized by optimizing the surface-to-volume ratio of the betavoltaic, as illustrated in Figs. 5.6 and 5.7 for a $^{147}$Pm-silicon microbattery. Silicon betavoltaics are suitable candidates for $^{147}$Pm powered microbatteries because: (1) the $^{147}$Pm $\beta$-electrons ($E_{^{147}\mathrm{Pm},avg} = 63\,\mathrm{keV}$) can be efficiently absorbed within 50–60 µm of silicon (Fig. 5.4), leading to the possibility of high $FFF$; (2) silicon offers minority carries diffusion lengths greater (>100 µm for <1 Ω-cm resistivity) than the range of $^{147}$Pm $\beta$-electrons (≈45 µm at 63 keV) in silicon, which leads to highly efficient collection of the $\beta$-electron generated EHPs; (3) silicon microfabrication technology is relatively mature; and (4) irradiation of the silicon lattice with $^{147}$Pm $\beta$-electrons ($E_{^{147}\mathrm{Pm},max} < 230\,\mathrm{keV}$) does not cause appreciable degradation even over 6–8 years [11], because the threshold for lattice damage in Silicon is 250 keV, and $< 1\%$ of the $\beta$-electrons emitted by $^{147}$Pm possess $E_{avg} > 250\,\mathrm{keV}$.

The DRIE textured 3D betavoltaics (Fig. 5.7b) can potentially increase $FFF$ by $9X$ over previously demonstrated planar betavoltaics [11]. The 3D betavoltaic can also lead to a 1.5X–2X improvement in $\eta_\beta$ by utilizing the electron emission from both sides of the radioisotope thin film source. The net result is a possible $P_{out} = 13.05\,\mathrm{mW/cc}$ power density (Table 5.1). However, since the power output of the radioisotope fuel decreases exponentially with time, the average output power density over 5 years equals $\approx 7.78\,\mathrm{mW/cc}$.

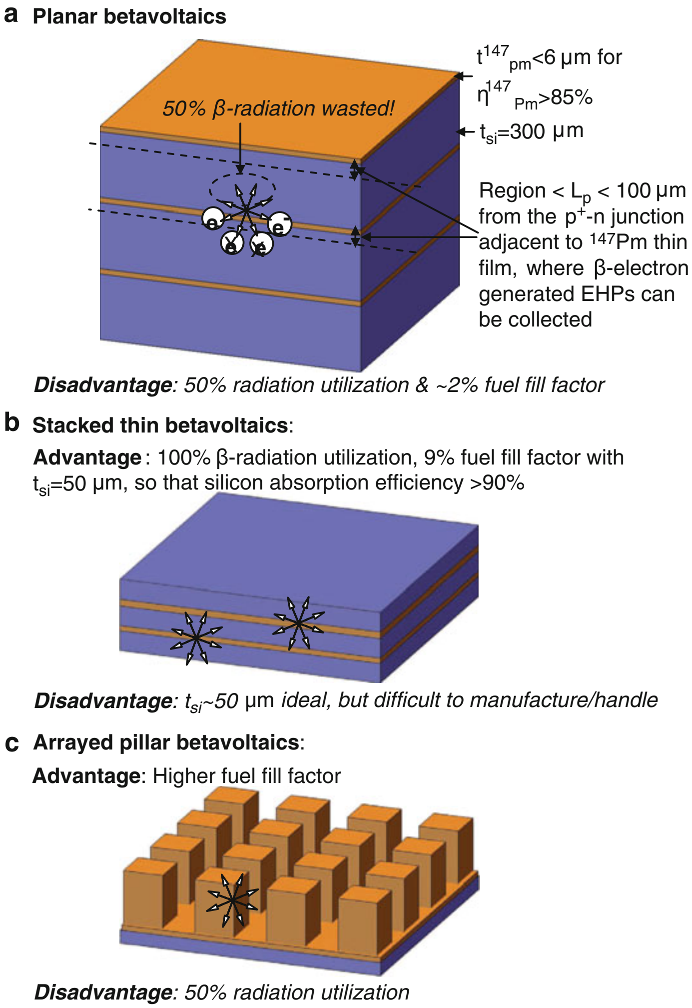

**a** **Planar betavoltaics**

***Disadvantage**: 50% radiation utilization & ~2% fuel fill factor*

**b** **Stacked thin betavoltaics**:

**Advantage**: 100% β-radiation utilization, 9% fuel fill factor with $t_{si}$=50 μm, so that silicon absorption efficiency >90%

***Disadvantage**: $t_{si}$~50* μm *ideal, but difficult to manufacture/handle*

**c** **Arrayed pillar betavoltaics**:

**Advantage**: Higher fuel fill factor

***Disadvantage**: 50% radiation utilization*

Figure 5.6: Schematics comparing the performance of various elementary betavoltaic designs

## 5.4 Fabrication

Prototype 3D silicon diodes were microfabricated using the 2-masks self-aligned process flow illustrated in Figs. 5.8 and 5.9. Float Zone (FZ) silicon wafers were employed because they offer lower bulk defects, and consequently the longer minority carrier lifetimes critical for higher betavoltaic collection efficiencies and

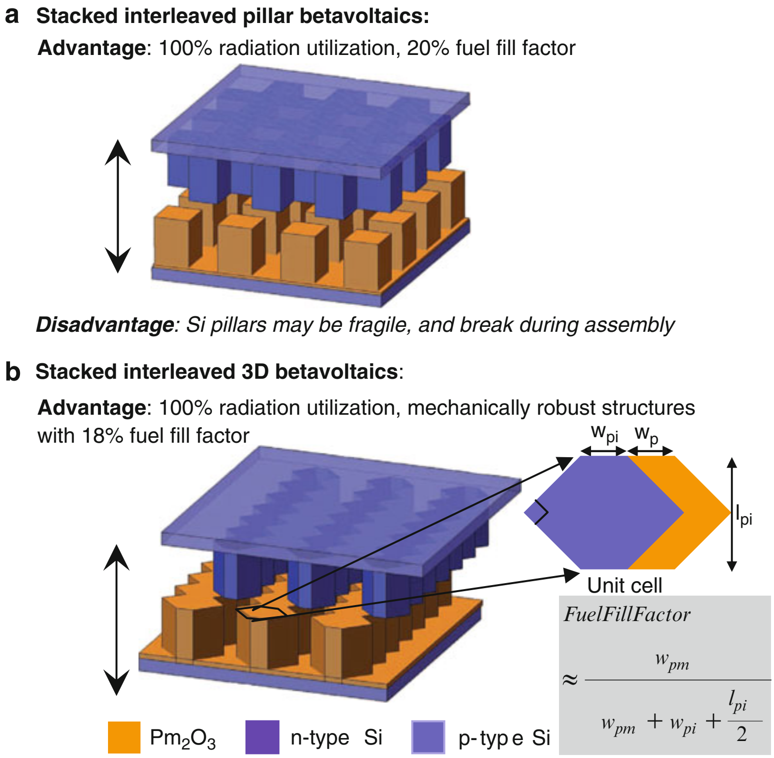

Figure 5.7: Schematics comparing the performance of interleaved 3D betavoltaic designs. These can be stacked for higher power output

lower R-G current in betavoltaics. Furthermore, while it is preferable to employ p-type wafers to take advantage of the higher minority carrier diffusion lengths of electrons, n-type wafers were employed for the prototypes due to the lack of immediate availability of p-type FZ wafers. Additionally, since low doping level substrates offer higher minority carrier lifetimes, 8–11 Ω-cm silicon wafers were used. The minority carrier diffusion length in the substrates used is expected to be >100 µm [41]. The microfabrication process flow was designed to confine the metal contact to the top surface of the pillars (Fig. 5.9), or 5–15% of total junction area. This serves to minimize the surface recombination at the silicon interface arising from silicon-aluminum contact [41], and results in higher betavoltaic current multiplication factor $M$ (5.8). The

Table 5.1: Comparison of initial power density of previous $^{147}$Pm planar betavoltaic battery (Fig. 5.6a) performance to projected performance of microbattery designs illustrated in Figs. 5.6b, 5.7a and 5.7b, assuming a 6 μm thick layer of 830 curie/g $^{147}$Pm fuel

| Design | $FFF$ (%) | $\eta_{\mu B}$ (%) | $P_{\mu B,dens}$ (mW/cc) |
|---|---|---|---|
| Figure 5.6a Planar ($t_{si} = 294\,\mu m$) | 2 | 2 | 0.69 |
| Figure 5.6b Stacked thin ($t_{si} = 50\,\mu m$) | 9 | 4 | 6.15 |
| Figure 5.7a Stacked interleaved pillar ($t_{si} = 50\,\mu m$) | 20 | 4 | 14.4 |
| Figure 5.7b Stacked interleaved 3D ($w_{pm} = 6\,\mu m$, $w_{pi} = 10\,\mu m$, $l_{pi} = 60\,\mu m$) | 18 | 4 | 13.05 |

contacts are defined using a self-aligned process to avoid lithography on a surface with 300–450 μm trenches. Betavoltaic microbatteries can be realized from the 3D diodes (Fig. 5.10) either by precipitating thin film $Pm_2O_3$ [28] in the trenches.

## 5.5 Testing and Results

The prototype 3D diodes were diced and tested under a probe station for diode characteristics, by measuring the I-V curve under dark conditions (Fig. 5.11). Diode series resistance $R_s$ was extracted from the diode forward bias I-V curve to be 22.1 Ω, justifying the exclusion of $R_s$ from the equivalent electrical circuit. The reverse bias current was found to be $\approx 7.5\,\mu A$ at 500 mV, and steadily increasing with reverse bias voltage. This reverse leakage current is high compared to the <1 nA reverse leakage

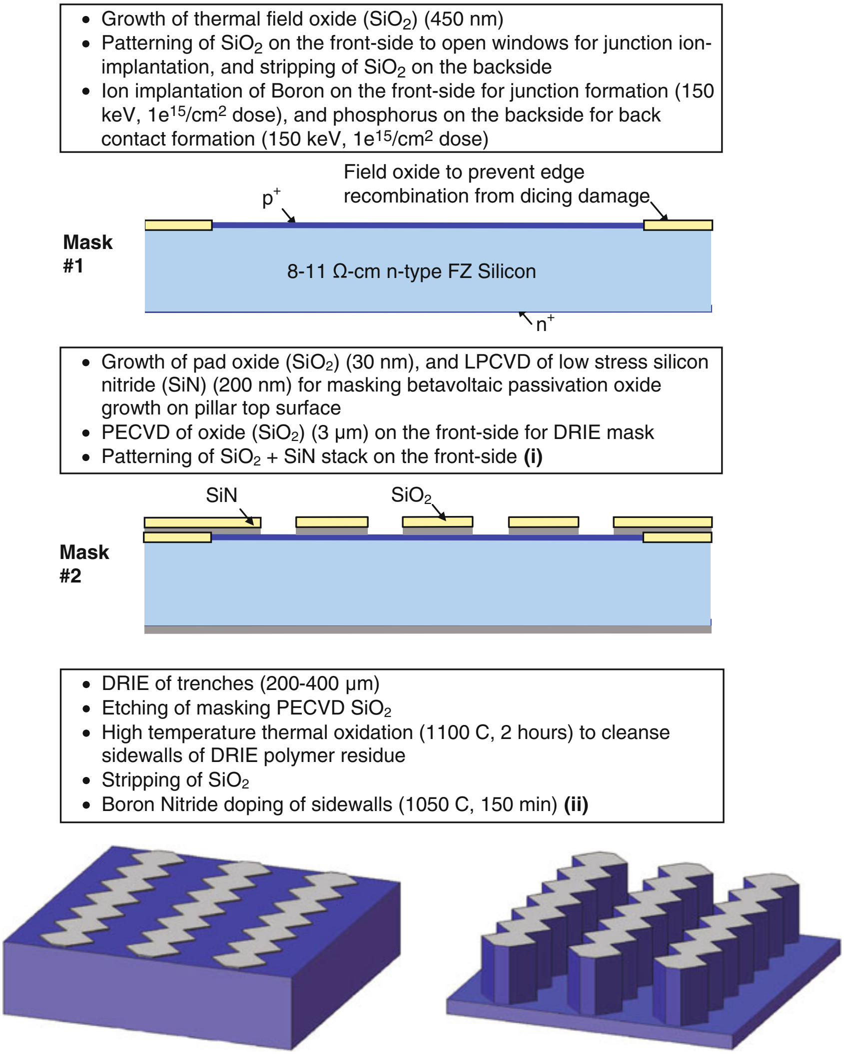

- Growth of thermal field oxide ($SiO_2$) (450 nm)
- Patterning of $SiO_2$ on the front-side to open windows for junction ion-implantation, and stripping of $SiO_2$ on the backside
- Ion implantation of Boron on the front-side for junction formation (150 keV, $1e^{15}/cm^2$ dose), and phosphorus on the backside for back contact formation (150 keV, $1e^{15}/cm^2$ dose)

- Growth of pad oxide ($SiO_2$) (30 nm), and LPCVD of low stress silicon nitride (SiN) (200 nm) for masking betavoltaic passivation oxide growth on pillar top surface
- PECVD of oxide ($SiO_2$) (3 μm) on the front-side for DRIE mask
- Patterning of $SiO_2$ + SiN stack on the front-side **(i)**

- DRIE of trenches (200-400 μm)
- Etching of masking PECVD $SiO_2$
- High temperature thermal oxidation (1100 C, 2 hours) to cleanse sidewalls of DRIE polymer residue
- Stripping of $SiO_2$
- Boron Nitride doping of sidewalls (1050 C, 150 min) **(ii)**

(i) After patterning of the $SiO_2$ + SiN stack on the front-side.

(ii) After Boron Nitride doping of sidewalls.

Figure 5.8: Schematic illustration of the lithography based microfabrication processing steps of 3D diodes. The cross-sectional views illustrate the processing of the whole die, and the 3D dimetric views further illustrate the processing of the textured ridges

current realized in planar diodes microfabricated from similar substrates, but different wafers. The non-saturating reverse bias current of the 3D diodes, arising from high recombination and generation (R-G) in the depletion region (5.11), results in an

- Growth of thermal oxide ($SiO_2$) (300 nm) for passivating the junction front surface, for low surface recombination **(iii)**

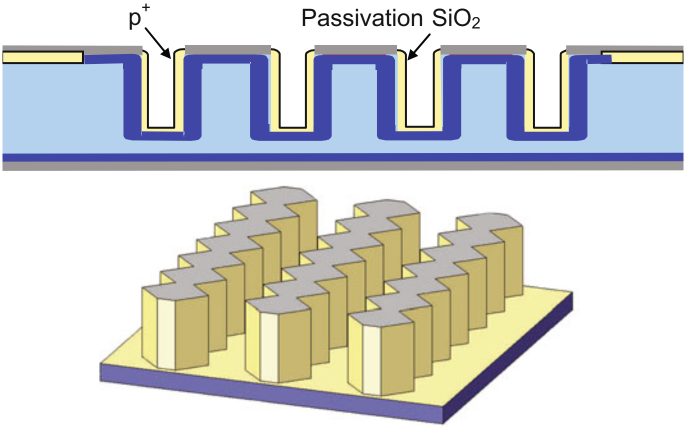

(iii) After growth of thermal oxide on the sidewalls. The top surface is protected by SiN.

- Etching of LPCVD SiN on both the front and back side, using RIE recipe selective to $SiO_2$
- Blanket evaporation of contact metal (Ti+Al) (20 nm+200 nm) on both sides **(iv)**

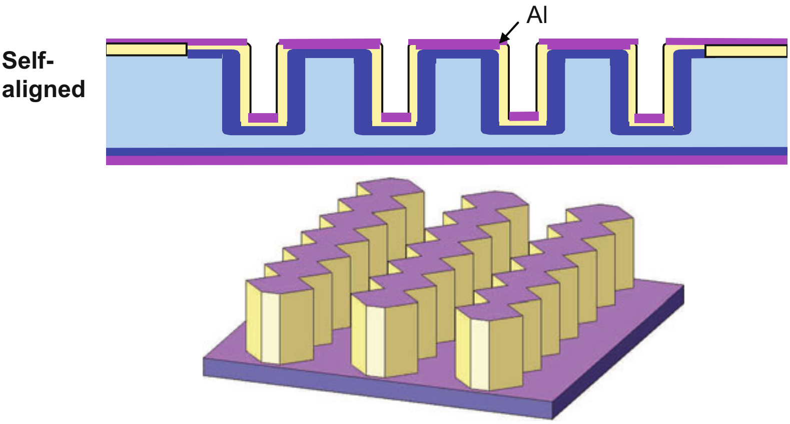

(iv) After blanket evaporation of Ti+Al, when the Al-Si contact is formed just on the pillat tops.

Figure 5.9: Schematic illustration of the self-aligned microfabrication processing steps of 3D diodes. The cross-sectional views illustrate the processing of the whole die, and the 3D dimetric views further illustrate the processing of the textured ridges

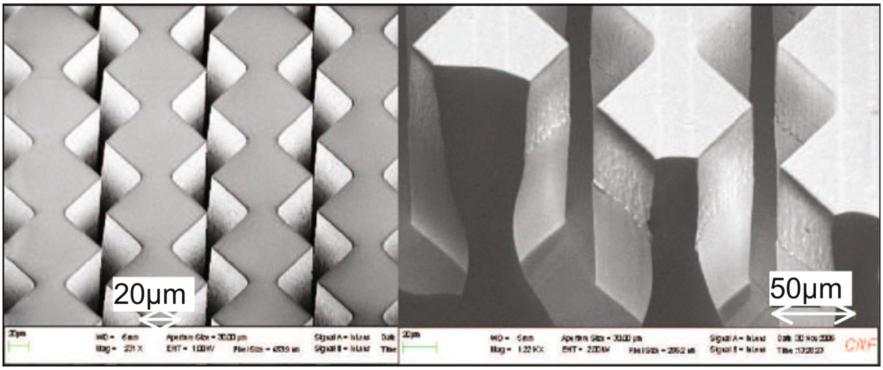

Figure 5.10: Isometric view SEM micrographs of 3D diode (**a**) top surface and (**b**) cleaved cross-section

undesirably low diode shunt resistance $R_{sh}$ of $50\,\mathrm{k\Omega}$ at $V_d = 0\,\mathrm{V}$ and $169\,\mathrm{k\Omega}$ at $V_d = -0.5\,\mathrm{V}$, compared to $>2\,\mathrm{G\Omega}$ realized in planar diodes.

The 3D diodes were then tested for betavoltaic response under electron irradiation. A readily available 1.5 millicurie/cm$^2$ $^{63}$Ni radioisotope source, generating an electron flux of 9 pA/cm$^2$, was first used to irradiate both the 3D and planar diodes to demonstrate betavoltaic response. Unfortunately, while the planar diode $I_\beta - V_\beta$ curves showed good response to the irradiation (Fig. 5.11), no observable shift was observed in the 3D diode $I_\beta - V_\beta$ curves. This can be attributed to the 1–10 μA/cm$^2$ R-G current in the depletion region overshadowing $I_g$ (=1–100 nA/cm$^2$) generated due to the 1–10 pA/cm$^2$ electron fluxes from $^{63}$Ni. The 1–10 μA/cm$^2$ R-G current is not expected to affect betavoltaic operation with the ≈500–800 curie/gm $^{147}$Pm fuel required for mW level power generation in micropower batteries, because the 5–20 nA/cm$^2$ electron fluxes are expected to result in $I_g$ =10–100 μA/cm$^2$. Unfortunately, this could not be verified immediately, as the high activity $^{147}$Pm fuel was not readily available. Hence, the 3D diodes were tested for betavoltaic energy conversion using electron beams from scanning electron microscopes (SEMs) (Cornell Nano-scale Facility).

First, the SEM electron beam was calibrated by measuring current output $I_{SEM}$ for various acceleration voltages $V_{SEM}$ and apertures openings (Fig. 5.12). The measurements were made by

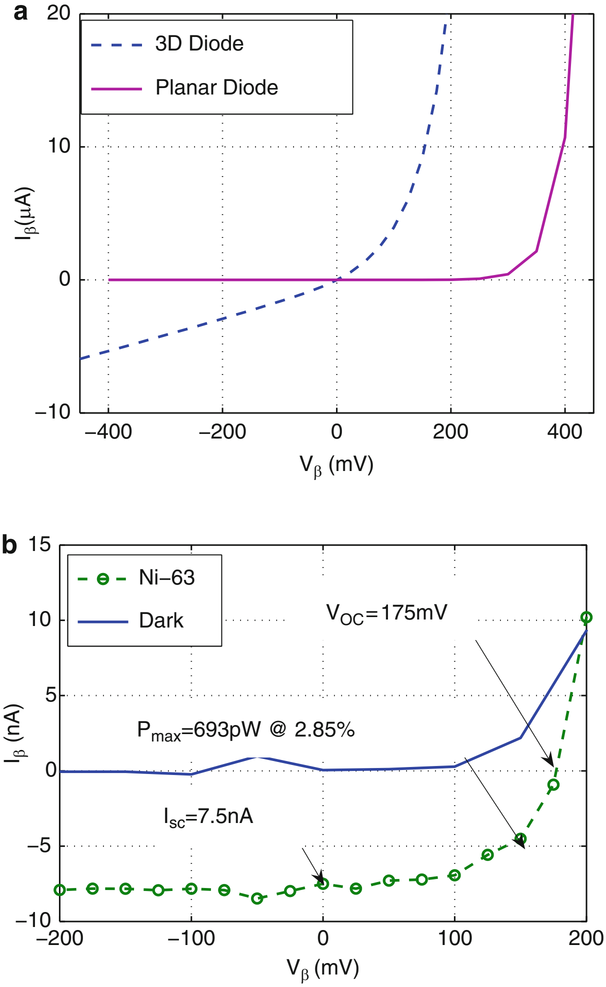

Figure 5.11: (**a**) Plot comparing measured I-V characteristics of 0.64 cm$^2$ 3D diodes and 0.16 cm$^2$ planar diodes under dark conditions. The plot shows the 3D diode reverse bias current increasing due to R-G current, and planar diode reverse bias current saturating. (**b**) Plot of measured I-V characteristics of the 0.16 cm$^2$ planar diode irradiated with 1.5 millicurie/cm$^2$ $^{63}$Ni source

focusing the electron beam inside a well in a metallic collector connected to a pico-ammeter. The well collects all the incident electrons and the resulting back-scattered and secondary electrons, and gives an accurate estimate of $I_{SEM}$. Betavoltaic $I_\beta - V_\beta$

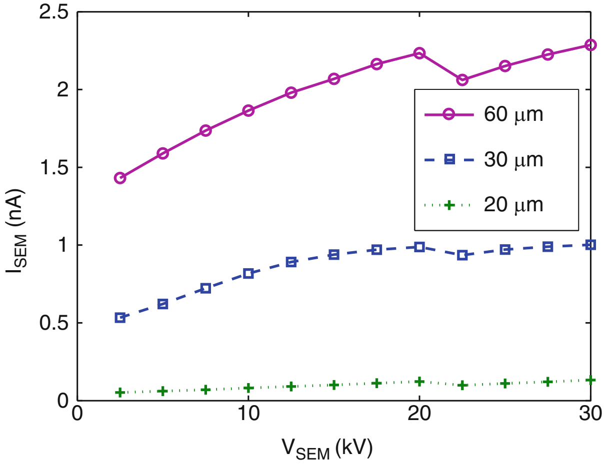

Figure 5.12: Plot of measured SEM calibration curve of electron beam current $I_{SEM}$ versus accelerating voltage $V_{SEM}$, for different aperture sizes in the SEM

curves were then measured (Fig. 5.13) for various values of $V_{SEM}$, with the electron beam focused on a 5 mm × 5 mm area on the diode, and were used to extract $V_{oc}$, $I_{sc}$, $P_m$, $V_m$, $I_m$, $R_{l,opt}$, and $\eta_\beta$. The betavoltaic conversion efficiency $\eta_\beta$, calculated using

$$\eta_\beta = \frac{P_m}{P_{in,\beta}} = \frac{V_m I_m}{V_{SEM} I_{SEM}} \tag{5.20}$$

was found to increase with $V_{SEM}$ (Fig. 5.13), reaching 1.61% at 30 kV. This dependence of $\eta_\beta$ on $V_{SEM}$ is primarily due to the increase in $M$ (Fig. 5.13) with $V_{SEM}$. The diode generates negligible amount of EHPs for $V_{SEM} < E_{loss,avg}/\mathrm{q}$, when the incoming electrons do not have sufficient energy to cross the inactive layers in the diode. The EHP generation starts when $V_{SEM}$ exceeds $E_{loss,avg}/\mathrm{q}$, and $M$ rises linearly with $V_{SEM}$. The betavoltaic $Q_j$ and $E_{loss,avg}$ can be extracted from the $M$ versus $V_{SEM}$ curve, which follows

$$M = \frac{I_g}{I_{SEM}} = qQ_j \frac{(V_{SEM} - E_{loss,avg}/q)}{E_{ion}}. \tag{5.21}$$

Assuming $E_{ion,Si} = 3.6\,\mathrm{eV}$, $Q_j$ was extracted from the slope to be 1.04, and $E_{loss,avg}$ was extracted from the x-axis intercept of the

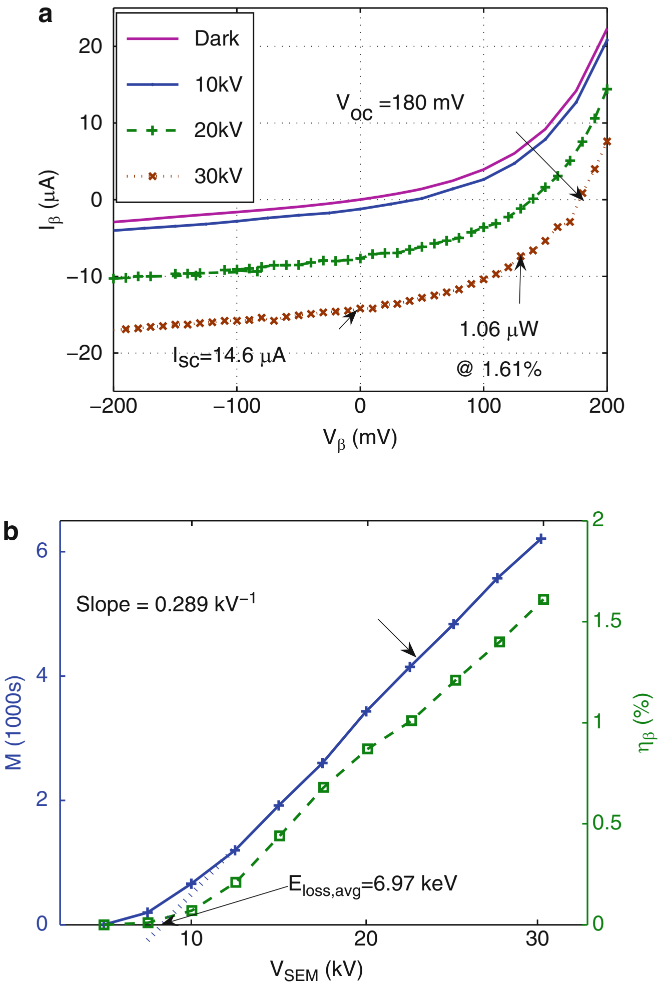

Figure 5.13: Plot of measured betavoltaic (**a**) I-V characteristics for different accelerating voltages $V_{SEM}$, and (**b**) current multiplication factor $M$ and conversion efficiency $\eta_\beta$ versus $V_{SEM}$, for a 0.64 cm$^2$ 3D diode irradiated with electron beam in a SEM

curve to be 6.97 keV. The extracted $Q_j$ being >1 suggests that the actual $E_{ion}$ for silicon could be less than 3.6 eV. However, the more significant observation is that $M$ is continuing its linearly increasing trend, which could mean that all the EHPs are being generated within a minority carrier diffusion length $L_p$ of the junction. If $M$ were to continue increasing linearly with $E_{avg}$, which

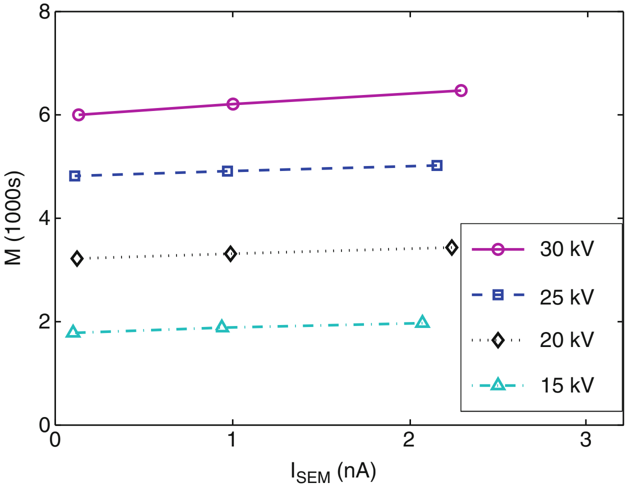

Figure 5.14: Plot of measured betavoltaic current multiplication factor $M$ versus electron beam current $I_{SEM}$ for different accelerating voltages $V_{SEM}$, for a $0.64\,\mathrm{cm}^2$ 3D diode irradiated with electron beam in a SEM. $I_{SEM}$ is varied from 0.132 to 2.287 nA (corresponding to radioisotope activities of 22–387 millicurie)

would happen if $L_p$ were >60–70 µm, $\eta_\beta$ could increase to ≈4% at $E_{avg} = 63\,\mathrm{keV}$. The betavoltaic current multiplication factor $M$ was also found to be relatively constant over a range of current injection levels (Fig. 5.14).

## 5.6 Discussion

The 3D diode betavoltaic energy conversion efficiency can be further increased by reducing the high R-G current leakage through $R_{sh}$, which degrades both $V_{oc}$ (180 mV) and fill factor (≈43%) (Fig. 5.15). Equation (5.11) suggests that the high leakage could arise from low minority carrier lifetimes, which depend on factors including substrate doping and defect levels, and processing conditions. Since planar diodes, using ion-implanted junctions in the same type of substrates yielded $R_{sh} > 2\,\mathrm{G}\Omega$ and $\eta_\beta > 5\%$ at 30 kV (Fig. 5.15), it is hypothesized that the processing steps particular to the 3D diodes lowered the lifetimes by introducing trap levels in the semiconductor band gap. These steps include DRIE of the

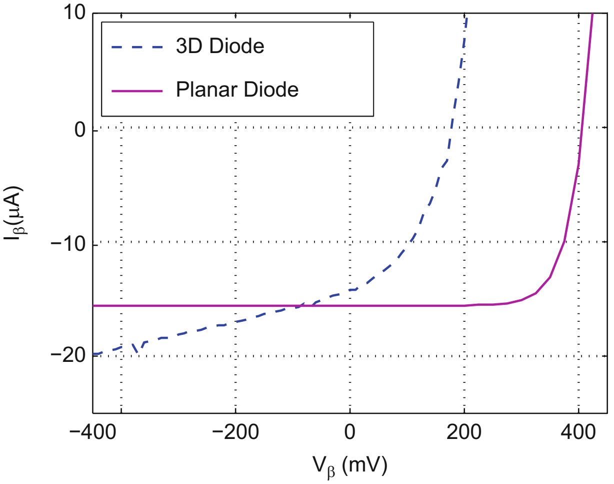

Figure 5.15: Plot comparing measured $I_\beta - V_\beta$ characteristics of $0.64\,\mathrm{cm}^2$ 3D diode and $0.16\,\mathrm{cm}^2$ planar diode under 30 kV, 2 nA electron beam irradiation. The high R-G current in the 3D diode results in $V_{oc}$ and $FF$ of 180 mV and 43% respectively, compared to planar diode $V_{oc}$ and $FF$ of 410 mV and 74% respectively under similar irradiation levels

trenches, the high temperature (1,100 C) thermal oxidation after the DRIE to smoothen out the trenches, and gas phase Boron doping (Fig. 5.8). The betavoltaic energy conversion efficiency can be increased by optimizing the microfabrication process for retaining high minority carrier lifetimes.

## 5.7 Conclusions

Novel DRIE textured 3D silicon diodes for potential application in 5 year lifetime 5 mW/cc (average) $^{147}$Pm radioisotope powered betavoltaic microbatteries were designed, fabricated using a 2-mask self-aligned process, and characterized using electron beams in a scanning electron microscope to yield 1.61% conversion efficiency @30 kV acceleration. High recombination-generation current in the diode depletion region was identified as the main efficiency limiter, and lowered minority carrier lifetimes due to the process flow was suggested as a possible reason.

## 5.8 Future Directions

Future work will involve: (a) increasing the betavoltaic energy efficiency of the 3D silicon diodes; and (b) realization of $^{147}$Pm powered 3D silicon betavoltaic microbatteries using the improved silicon diodes.

The energy conversion efficiency of the 3D silicon diodes can be improved, from the current 1.61% at 30 keV to ≈5% at 30 keV realized in planar silicon diodes, by optimizing the microfabrication process for maintaining longer minority carrier lifetimes in the silicon substrates. Minority carrier lifetime measurements can be carried out after every high temperature step in the microfabrication process, and the processing step lowering the lifetimes identified for optimization.

Subsequently, $^{147}$Pm powered 3D silicon betavoltaic microbatteries can be realized by depositing $^{147}$Pm thin films in the 3D diode trenches, and assembling the 3D diodes in the interleaved and stacked configuration. The $^{147}$Pm electro-less deposition or precipitation processes will have to be developed to attain conformal deposition of thin films in the high aspect ratio trenches. Previous work on $^{147}$Pm precipitation [28] can be optimized for realizing the uniform deposition. Furthermore, the interleaving and stacking assembly process will have to be developed to precisely align and fit the two complementary diode chips. Care will have to be taken in designing the periphery of the chips, and release pathways will have to be provided for the trapped air in the trenches to escape during assembly. Additionally, low weight low volume radiation shields will have to be designed, and an extensive study carried out to determine the radiation safety of the microbatteries.

Future research can also pursue further increases in the energy conversion efficiency of betavoltaic microbatteries for further increases in the power density. Higher efficiency betavoltaics can be developed using high band gap semiconductors such as SiC. Energy conversion efficiencies as high as 20% have been demonstrated with SiC planar betavoltaics, which can be thinned to realize stacked thin-planar betavoltaic microbatteries. Efforts can also focus on developing SiC DRIE technology capable of etching

450 μm deep trenches with 10 : 1 aspect ratios, so 3D interleaved and stacked microbatteries can be realized.

The energy conversion efficiency of the betavoltaic microbatteries can also be raised by employing thermoelectric panels as radiation shielding packages. The thermoelectric panels can harvest the $^{147}$Pm thermal energy unutilized by betavoltaics to generate electricity. Thus, they can both increase the energy conversion efficiency of the betavoltaic microbatteries, and decrease the inactive volume of the microbattery to result in microbatteries with higher power densities.

# Chapter 6
# Radioisotope Direct Charging: Autonomous Wireless Sensors

## 6.1 Introduction

The lifetime of autonomous wireless sensor microsystems can be increased either by increasing the energy capacity of microbatteries, or by decreasing the power consumption of on-board sensors and wireless transmitters. However, while radioisotope microbatteries do provide higher energy capacity energy sources compared to conventional electrochemical microbatteries, increasing the energy capacity of radioisotope microbatteries requires higher activities of radioisotope fuels. This undesirably raises safety concerns, and often limits the use of such microbatteries to specialized applications that can tolerate the lower radiation safety. Therefore, the application of radioisotopes to realizing zero-power wireless sensors was explored. Previously demonstrated applications utilizing radiation from radioisotopes for low-power sensing include the smoke detectors and electron capture detectors that employ the radiation for ionization of gas molecules. Such applications can function even with <1millicurie of radioisotope, and consequently are safe enough for widespread deployment.

In this chapter, the utilization of $^{63}$Ni $\beta$-radiation to enable a zero-power wireless sensor microsystem that can transmit a pulsed RF signal coded with the sensed environmental information is presented [30]. A prototype zero-power humidity sensing wireless node that transmits $500\,mW$ of remotely ($\approx$1 m) detected pulsed RF power even while using a benign $4\,millicurie$ source of $^{63}$Ni emitting $10\,nW$ is demonstrated. The frequency of the $\approx 150\,MHz$ RF pulse shifts by $4.27\,MHz$ when the humidity changes from 22% to 97%.

R. Duggirala et al., *Radioisotope Thin-Film Powered Microsystems*,
MEMS Reference Shelf 6, DOI 10.1007/978-1-4419-6763-3_6,

## 6.2 $^{63}$Ni Powered Autonomous Wireless Humidity Sensor

The $^{63}$Ni powered wireless sensors utilize the discharge event in a $^{63}$Ni actuated reciprocating cantilever to generate the wireless signal, and a passive humidity sensitive capacitor connected across the cantilever and the $^{63}$Ni thin film source to modulate the frequency of transmission.

### 6.2.1 $^{63}$Ni Actuated Reciprocating Cantilever Wireless Transmitter

Figure 6.1 illustrates a prototype $^{63}$Ni based wireless transmitter [42]. A gold cantilever (5 cm × 0.8 cm × 300 μm) placed alongside a 1.5 millicurie $^{63}$Ni radioactive thin film source (1 cm × 1 cm × 100 μm) constitutes the self-reciprocating cantilever system. Both the cantilever and the radioisotope thin film source are electrically isolated using teflon mounting blocks, and assembled inside a vacuum chamber ($10^{-3}$ mTorr). The constant emission of $\beta$-particles by the $^{63}$Ni thin-film source and the collection of a portion of those $\beta$-particles by the cantilever leads to electrostatic charge separation, which results in an electrostatic force that pulls the cantilever toward the fixed radioisotope source. As the charge separation increases with time, the electrostatic force increases until the cantilever eventually pulls into the radioisotope thin-film. For an initial gap between the cantilever and radioactive source of 500 μm, the cantilever takes 3 m to pull-in. Upon contact, the remaining charges are discharged through tunneling and direct conduction. The resulting electrical discharge pulses last for a very short time (<1ns). Since the energy integrated over the reciprocation period is released in a very short time, the pulse is very high power. As the electrostatic force is eliminated, the beam oscillates, comes to rest at its original position, and the cycle repeats, resulting in a self reciprocating cantilever system.

The discharge current pulse passes through the RF circuit formed by the device (Fig. 6.1c) and excites its electrical impulse response, which manifests itself as a RF transmission.

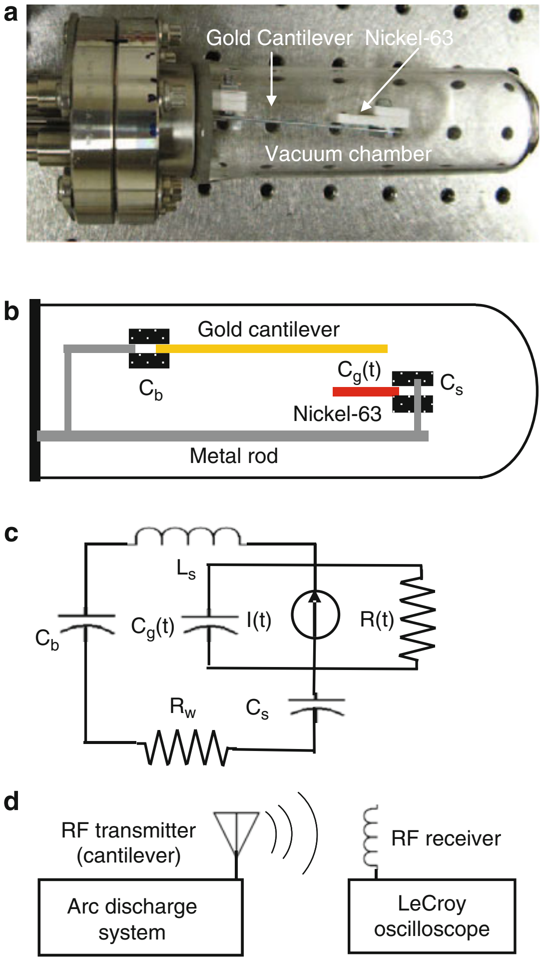

Figure 6.1: Radioisotope actuated reciprocating cantilever discharge based wireless transmitter (**a**) photograph, (**b**) schematic, and (**c**) equivalent LC circuit, and (**d**) schematic of wireless transceiver system

The RF transmission $V_{remote}$ was detected and recorded by a receiver (air-core coils with 21 turns and 1.5 cm inner diameter) connected to a high bandwidth oscilloscope (LeCroy WaveMast 8500). A 1.52 GHz signal lasting for around 10 ns was remotely detected upon cantilever discharge (Fig. 6.2).

The discharge based wireless RF transmitter can be better understood using an LC circuit model (Fig. 6.1c and Table 6.1).

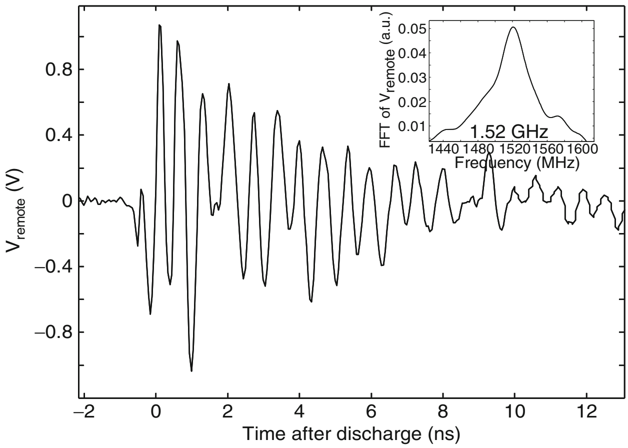

Figure 6.2: Plot of RF signal transmitted by the cantilever discharge based wireless transmitter, remotely detected at 1 m

Table 6.1: Representation and measured values of $R$, $L$, and $C$ components in circuit model in Fig. 6.1c

| Component | Representation | Value |
|---|---|---|
| $C_s$ | Source holder capacitance | 8.3 pF |
| $C_b$ | Beam holder capacitance | 8.3 pF |
| $R_w$ | Resistance of metal beams and rod | 0.1 Ω |
| $L_s$ | Equivalent inductance of the arc discharge system | 2.4 nH |
| $C_g(t)$ | Air gap capacitance | Time dependant |
| $I(t)$ | Air gap current | Discharge pulse |
| $R(t)$ | Equivalent resistance across the air gap | Arc resistance |

Simulations of the LC circuit carried out in SPICE are used to validate the model. Circuit elements $C_g$, $I(t)$, and $R(t)$ represent the air gap between the cantilever and the radioisotope source. During the discharge event, $C_g >> C_s$, and acts as a short compared to other impedances in the circuit. The air gap resistance $R(t)$ is ignored in this simulation as it is shorted out by $C_g$ at the time scales involved. The measured values of other capacitors and inductors used in the simulation are listed in Table 6.1. The discharge current $I(t)$ is roughly estimated by calculating the charge accumulated during the charging phase, and dividing it by the estimated duration of the discharge. The charge accumulated just before discharge can be calculated by multiplying the estimated rate of $\beta$-electron collection by the cantilever with the duration of the charging phase. The 1 cm$^2$ $\approx$1.5 millicurie source emits $\approx 9\,pA$. Given that 0.8 cm$^2$ of that source overlaps with the cantilever, the total charge across the air gap at the time of arc discharge can be estimated to be 1 nC. Assuming the discharge lasts 1 ns, the average discharge current can be calculated to be 1 A. A current pulse of amplitude 1 A and duration 1 ns with rise and fall times of 0.1 ns (time estimated from experimental values) are chosen to excite the LC circuit in the simulation (resonance frequency of the circuit is independent of pulse magnitude and duration). The simulated resonance frequency of the LC circuit is plotted in Fig. 6.3, together with the frequency of remotely measured RF signal from device shown in Fig. 6.2. The simulation predicts a resonance frequency of 1.53 GHz, which is close to the experimentally measured value of 1.52 GHz, thus validating the LC model representation of the self-reciprocating cantilever discharge based wireless transmitter.

The high power pulses from the arc discharge system can be utilized to generate wireless RF signals detectable over long distances. However, for the RF transmission to be useful for an autonomous wireless sensor system, RF output needs to be modulated with the sensed signal. In the system shown in Fig. 6.1, all the parameters inside the glass chamber have fixed values. The RF frequency can only be modulated with components outside the chamber. To modulate the frequency of the RF signal, an external capacitor $C_{ext} = 20\,\text{pF}$) was connected to the arc discharge system (Fig. 6.4 to alter the resonance frequency of the LC circuit

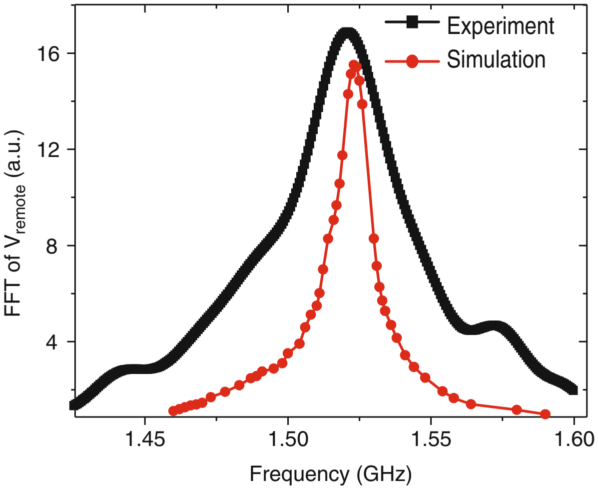

Figure 6.3: Plots of simulated and measured RF resonance response of the cantilever discharge based wireless transmitter

connected to the cantilever. This also introduces inductance $L_w$ and resistance $R_e$ due to the wire connections to the external capacitor. These parasitics were measured to be 61 nH and 0.8 Ω respectively using LCR meter (HP 4275A). Upon cantilever discharge, the RF transmission was measured at 20 cm to contain two components (Fig. 6.5). In addition to the 1.52 GHz signal that appeared for the 1st 10 ns, the RF transmission also contained a ≈214 MHz RF signal that lasted for more than 300 ns with a maximum of power output of 500 mW. The electrical equivalent circuit of the cantilever discharge based wireless transmitter with an external capacitor simulated in SPICE also yielded a resonance frequency of ≈214.5 MHz (Fig. 6.6), further validating the LC circuit model. Subsequently, the variation is the remotely detected wireless signal with different values of $C_{ext}$ was characterized (Fig. 6.7). The frequency of transmission was found to decrease with increasing external capacitance. An increase in the external capacitance from 12 pF to 75 pF resulted in a frequency shift of 63 MHz from 239 to 176 MHz. Simulation of the electrical equivalent circuit with different values of $C_{ext}$ yielded resonant frequencies that were close to the experimentally measured values. Figure 6.7 also plots relative power of detected RF signals with different external capacitor values. The relative power changes significantly with the

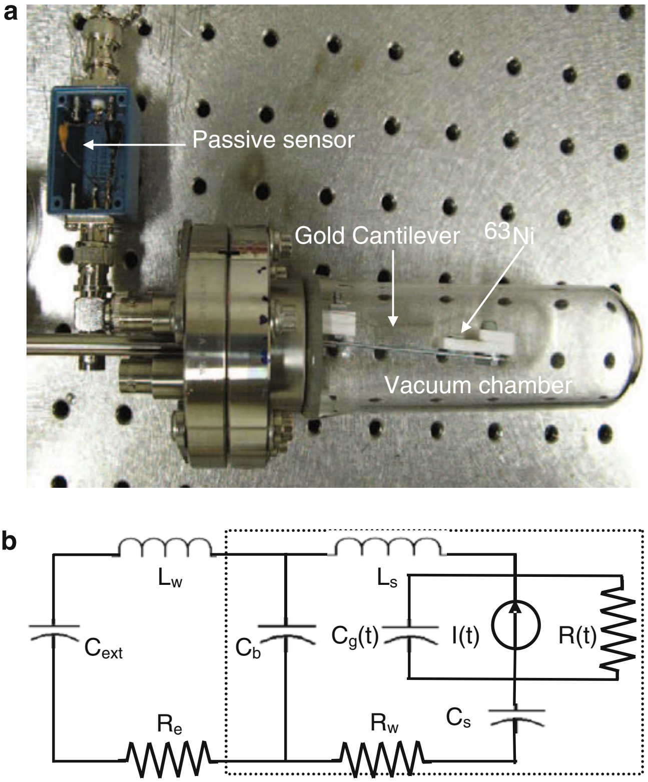

Figure 6.4: (**a**) Photograph and (**b**) equivalent LC circuit of the radioisotope actuated reciprocating cantilever discharge based wireless transmitter with an external capacitor for frequency modulation

external capacitor. This can be attributed to the different gains of the RF transceivers at different frequencies, as the RF power generated by the electrostatic system remains the same due to the reciprocation period remaining the same.

## 6.2.2 Humidity Sensitive Polymer Capacitor

The humidity sensitive polymer capacitor used in the experiments described in this chapter comprises of a porous polymer thin film sandwiched between a bottom metal electrode and a meshed top metal electrode. The humidity sensitivity of capacitance and leakage resistance of a polymer capacitor arises because of the ability

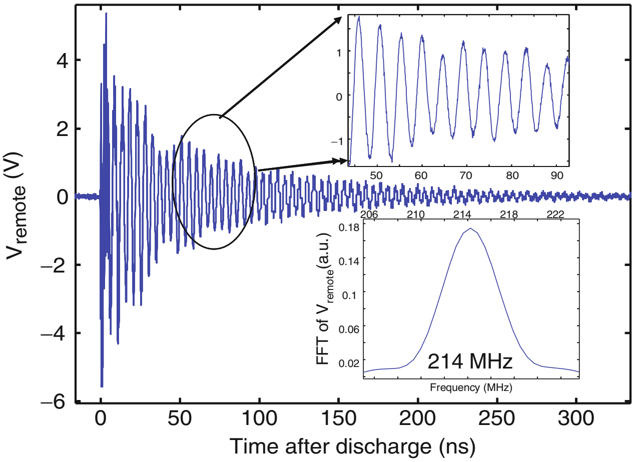

Figure 6.5: Plot of RF signal transmitted by the cantilever discharge based wireless transmitter with an external capacitance of 20 pF, remotely detected at 0.2 m

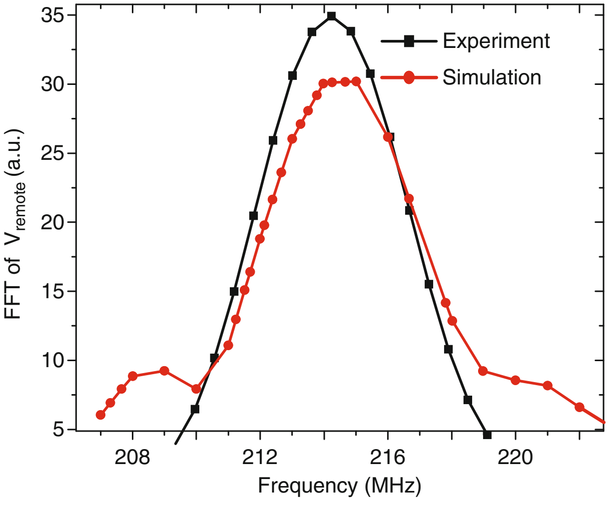

Figure 6.6: Plots of simulated and measured RF resonance response of the cantilever discharge based wireless transmitter with an external capacitance of 20 pF

of the porous polymer to absorb water molecules. The large polarizability of the water molecules alters the capacitance, and the ability of the water molecules to dissociate conducting ionic

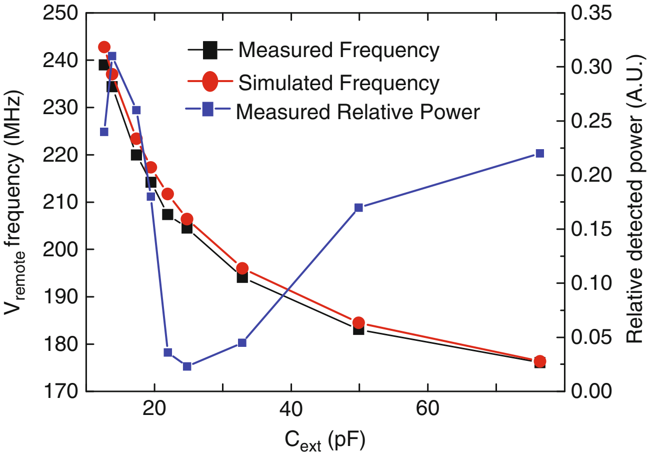

Figure 6.7: Plots of simulated and measured frequency, and measured relative power of RF signal transmitted by the cantilever discharge based wireless transmitter with different external capacitances. Remote measurements were made at a distance of 0.2 m

species from the polymer alters the leakage resistance. If $f_w$ is the volume fraction of water present in the polymer, then the polymer capacitance $C_{pc}$ is given by

$$C_{pc} = \frac{\epsilon_0 A_{pc}}{t_{pc}}(\epsilon_p + f_w(\epsilon_w - \epsilon_p)), \tag{6.1}$$

where $\epsilon_0$ is the permittivity of vacuum, $A_{pc}$ and $t_{pc}$ are the area and thickness of the polymer capacitor, and $\epsilon_p$ and $\epsilon_w$ are the relative dielectric constants of the polymer and water respectively. Similarly, the polymer capacitor leakage resistance $R_{pc}$ can be calculated as

$$\frac{1}{R_{pc}} = \frac{A_{pc}}{\rho_p t_{pc}} + \frac{A_{pc}}{f_w \rho_w t_{pc}}, \tag{6.2}$$

where $\rho_p$ and $\rho_w$ are the electrical resistivities of polymer and water respectively. The polymer capacitor can have low $R_{pc}$ even in the absence of absorbed water molecules due to impurities, and depending on the material processing conditions, $R_{pc}$ can

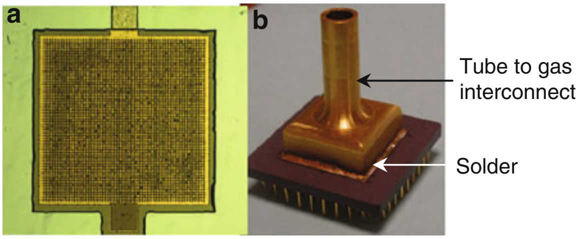

Figure 6.8: Photograph of (**a**) the top-view of the humidity sensitive polymer capacitor, and (**b**) the humidity sensitive polymer capacitor package

vary from 10 GΩ to >10 TΩ. The meshing of the top electrode determines the transient response of the polymer capacitor in response to changes in humidity. Larger mesh openings result in faster absorption of water molecules, and hence faster transient response.

The humidity sensitive polymer capacitor, comprising of a thin film of spin cast HD Microsystems $PI2723$ polyamide sandwiched between aluminum electrodes, was microfabricated and packaged at Morgan Research Corporation, Huntsville, AL.

The polymer capacitors were first characterized at the die level, and capacitors with $R_{pc} >> 1\,\text{T}\Omega$ were packaged in a ceramic pin grid array package. A copper lid with a 1/4" pipe fitting was then soldered onto the package (Fig. 6.8). The pipe fitting served to expose the polymer capacitor to ambient. The packaged polymer capacitor was then placed inside a controlled environmental chamber for testing the polymer capacitor characteristics at various levels of humidity. For polymer capacitors with $R_{pc} >> 1\,\text{T}\Omega$, $C_{pc}$ was measured at various levels of humidity (Fig. 6.9) by exciting the polymer capacitor top electrode with a $1\,V_{p-p}$ sinusoidal voltage at 0.2 Hz, and measuring the current passing through the polymer capacitor using a transimpedance amplifier ($10^9$ gain) connected to the bottom electrode. The 2 mm×2 mm polymer capacitors with 20% of the top electrode exposed to the atmosphere were tested to have a $C_{pc}$ humidity sensitivity of 0.33 pF/%RH, and time delay constant of approximately 50 s (Fig. 6.10).

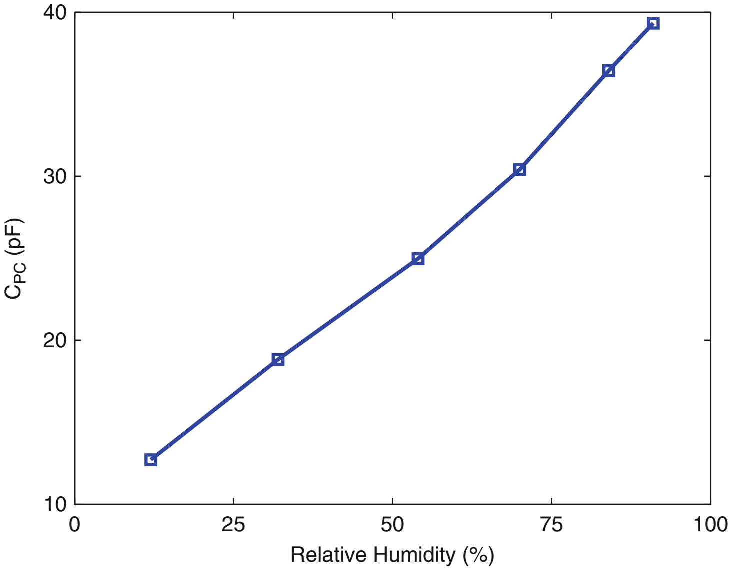

Figure 6.9: Plot of measured humidity sensitive polymer capacitor capacitance versus relative humidity RH for a polymer capacitor with a capacitance of 22 pF at 45% RH

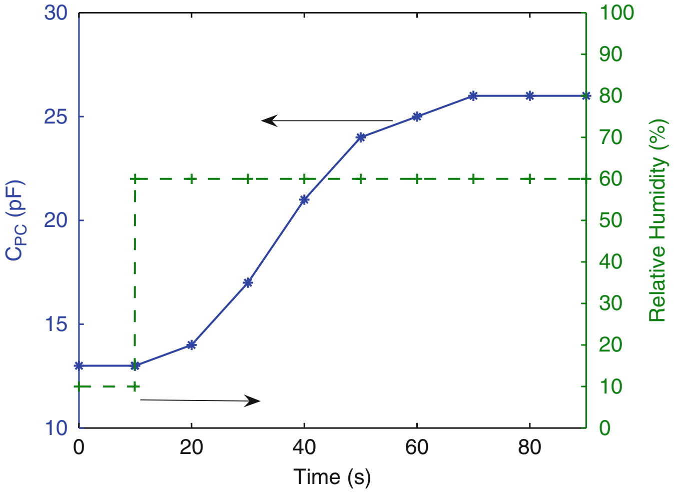

Figure 6.10: Plot of measured transient response of the polymer capacitor when subjected to a step increase in relative humidity from 0% RH to 60% RH in an environmental chamber

### 6.2.3 Autonomous Wireless Humidity Sensor

An autonomous wireless humidity sensor was realized by connecting the humidity sensitive polymer capacitor to the radioisotope actuated self-reciprocating cantilever, so the change in the capacitance in response to a change in the ambient humidity leads to a change in the frequency of the RF wireless transmission (Fig. 6.4). In order to characterize the response of the wireless humidity sensor, the capacitance of the sensor was first measured at different humidity levels (Fig. 6.11). The different levels of relative humidity were generated by exposing the humidity sensor to different saturated salt solutions (with known relative humidity values) in a closed chamber. The capacitance of the sensor was measured to increase with the relative humidity, as expected from the characterization tests that used the humidity chamber. Subsequently, the capacitor was connected to the radioisotope actuated cantilever and the discharge generated RF signals were remotely measured while exposing the humidity sensor to different humidity levels. The frequency of the signal was measured to shift by 4.27 MHz when the humidity changed from 22% to 97% (Fig. 6.12).

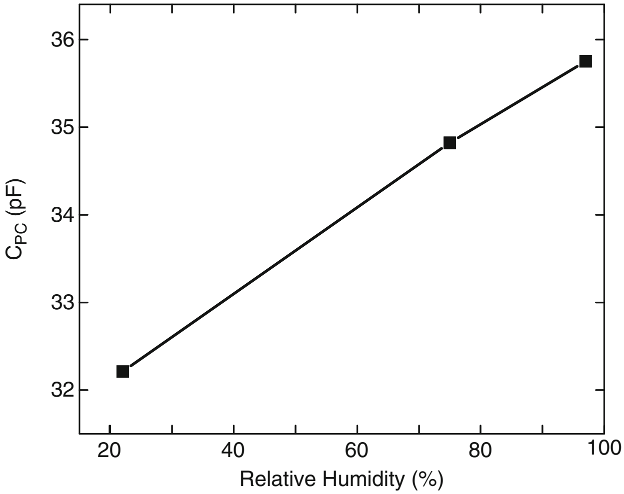

Figure 6.11: Plot of measured variation in capacitance with relative humidity levels for the humidity sensor used in the prototype wireless humidity sensor

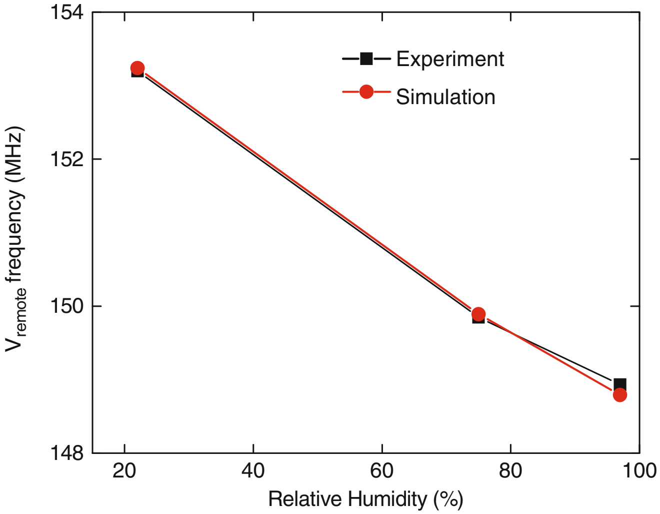

Figure 6.12: Plot of measured variation in RF signal frequency with relative humidity for the prototype wireless humidity sensor

## 6.3 Conclusions

In this chapter, a completely self-powered wireless sensor node which can transmit an RF signal coded with the environmental information gathered by a passive capacitive sensor was demonstrated. Such wireless sensor nodes that can operate for several decades and transmit data over RF-links at power of 100–1,000 milliWatts can potentially enable reliable long-term monitoring of structures where harvesting vibration or electromagnetic energy is not a reliable option for powering wireless sensor nodes. Such applications include monitoring water content in building foundations or detection of leached chemicals in chemical processing plants. In the near future, efforts in developing microscale vacuum packages will be undertaken to reduce volume. Furthermore, transmission line equivalent models are also being developed to engineer desired frequency output from the all-self-powered RF sensor node.

# Chapter 7
# Radioisotope Decay Rate Based Counting Clock

## 7.1 Introduction

Precise timing and frequency sources are vital in a wide range electronic-based systems such as communication networks and global positioning systems. These applications constantly demand reductions in size, weight and power (SWaP) while improving the precision of time or frequency references. Historically, clocks based on electromagnetic oscillations of atoms have provided the most precise method of timing events lasting longer than a few minutes. These oscillations are so precise that in 1967 the unit of time – the second – was redefined to be the time taken for a $Cs$ atom in a particular quantum state to undergo exactly $9,192,631,770$ oscillations. While the long-term precision of atomic clocks is unsurpassed, the size and power required to run these devices has prevented their use in a variety of areas, particularly in those applications requiring portability or battery operation. The NIST F-1 primary standard, for example, occupies a large optical table and requires many hundreds of watts to operate. The state-of-the-art in compact commercial atomic frequency references are Rb vapor-cell devices with volumes near $100\,\mathrm{cm}^3$ that operate on a few tens of watts of power and cost about 1–3 thousand dollars.

The long-term stability of atomic clocks including is based on the ability to interrogate a fundamental time constant – the hyperfine resonance frequency of ground level transitions[1]. It is thus natural to extend this idea of interrogating other time constants to realize clocks with good long-term stabilities.

We can identify three important characteristics necessary to realize a "good" time base or clock. These are

---

[1] For example, $\simeq 6.84\,\mathrm{GHz}$ in the case of rubidium atomic clocks

R. Duggirala et al., *Radioisotope Thin-Film Powered Microsystems*,
MEMS Reference Shelf 6, DOI 10.1007/978-1-4419-6763-3_7,

1. Long and short-term frequency stability, usually measured in Allan variance and phase noise of the frequency source
2. The physical size of the clock, and
3. The power consumed by the clock

Recent trends in miniaturization of atomic clocks – most notably, the chip-scale atomic clocks (CSACs) [43] – are based on Micro-electromechanical systems (MEMS) which offers advantages such as smaller size, an improvement in the device power dissipation (as the heat lost to the environment via the device surface is smaller) and enable high-volume, wafer-based production of atomic clocks, which would substantially reduce cost. In spite of the advantages offered such reduced power due to parasitic heat dissipation, the power consumed by such an envisioned MEMS-based atomic clocks hasn't shown reductions to orders in which these systems would be portable battery operated systems for long-term operations (such a week-long missions for the military, a few months-long working of communication based units or even year- or decade-long operations for sensor node applications).

## 7.2 Background

The key to realizing a short-and long-term stable clock is thus to lock-on a LO to an oscillator whose frequency is determined by a constant of nature. Solid-state resonators (such as RF resonators based on quartz, and silicon) do not fall under this category as they have non-systematic and random yet observable aging effects which cause their frequencies to shift in an unpredictable manner.

The emissions from a radioactive source, however, are a constant of nature, as the rate of radioactive disintegrations (activity or simply rate) is a constant for a given amount of material. They do not age as there are no inherent physical effects that change the rate for a given amount of material. Thus a radioactive source can potentially replace the physics package of an atomic clock to provide the necessary long-term stability for the clock – the radioactive counting clock or simply counting clock.

Potentially, a radioactive clock would have several advantages over a conventional atomic clock.

1. The radioactive decay is a spontaneous process and does not consume any active power. In contrast, the bulk of the power consumed by a typical atomic clock is to effect and interrogate a resonance (such as using a plasma or a laser source). The radioactive clock needs power only to interrogate its self-powered 'resonance' – this would be true of any system as it needs to be locked on to a short-term stable LO. This reduced power requirement would make this clock suitable particularly for battery-operable portable systems and for extremely long-term applications (weeks to decades).
2. The rate of a radioactive source is a constant and is independent of the environment (such as temperature, pressure, magnetic field and electric fields (latter two to a limited extent, and relative to atomic clocks), making this clock stable for long-term missions without parasitic effects such as unpredictable drifts observable even in atomic clock physics packages. In contrast, the rate of the radioactive clock also suffers from a drift due to the half life of the radioisotope but this effect is a well-defined and predictable effect that can be systematically corrected.

Much like the physics package of atomic clocks, the radioactive clock is short-term instable, requiring the clock to 'lock' on to a short-term stable LO. The following sections describe ways of locking a short-term stable LO to two types of physics package – resulting in the simple radioactive clock (simple RCC) or a dead-time-modified radioactive counting clocks (DTM RCC).

## 7.3 Simple Radioactive Counting Clocks

Radioactive decay process offers a fundamental time constant in the stability of rate of decay. If we ignore real effects such as self absorption and secondary electron generation, the radioactive decay is a Poisson process.

### 7.3.1 Radioactive Decay: A Poisson Process

We denote the rate of the radioactive source by $\lambda$. In any time interval $t$ that is much smaller than the half life of the radioisotope

($t \ll T_{1/2}$), $\lambda$ can be considered to be constant as the relative change in is $\lambda$ of the order of $1 - e^{-t/T_{1/2}}$ or $\simeq t/T_{1/2}$ [44]. In the case of nickel-63 ($Ni^{63}$), a beta ($\beta$) emitter with a half life $T_{1/2} = 100.2$ years), the rate can thus be considered invariant for time of up to a few months of operation with an accuracy of better than $10^{-5}$, or it can be systematically corrected.

With this notation, the radioactive decay process can be ideally modeled as a Poisson process with parameter $\lambda$. If we denote each instance of a radioactive beta decay as an event, the probability of $X = 1$ event occurring in any time interval $dt$ is given by

$$P(X = 1, dt) = \lambda dt \tag{7.1}$$

$$P(X = 0, dt) = 1 - \lambda dt \tag{7.2}$$

$$P(X = k, t) = \frac{(\lambda t)^k e^{\lambda t}}{k!} \tag{7.3}$$

Consider the case where a detector of radioactive beta particles is placed in close proximity to a $Ni^{63}$ radioactive source (Fig. 7.1)

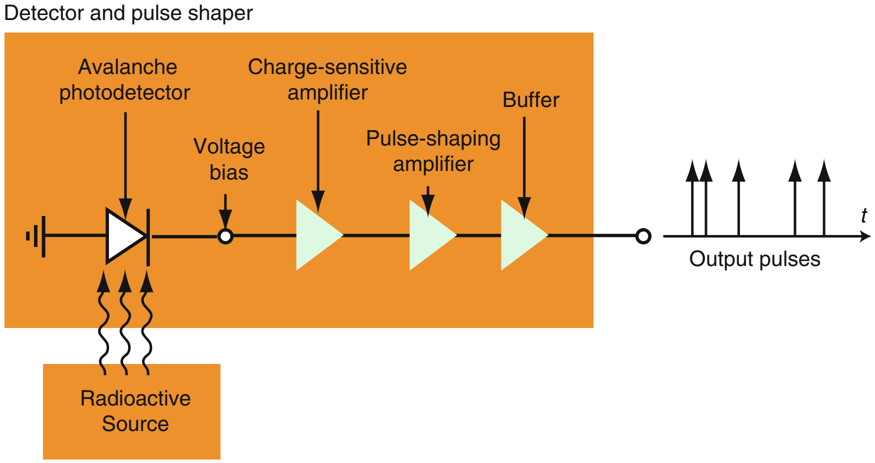

Figure 7.1: A radioactive detector and pulse shaper is placed in close proximity to a radioactive source generating output pulses of voltage $V_0$ at instances when radioactive decay events occur

of rate $\lambda$. In a time interval $[t, t+\tau]$, the average number of counts $\overline{k}$ and the standard deviation in counts $\sigma_k$ is given by

$$\overline{k} = \lambda\tau \tag{7.4}$$

$$\sigma_k = \sqrt{\lambda\tau} \tag{7.5}$$

Since $\overline{k}$ and $\sigma_k$ are independent of the time of measurement $t$, the two-point Allan deviation of fractional variation in counts can be expressed as $\sigma_k/\overline{k}$ (from [44])

$$\sigma_y(\tau) = \frac{1}{\sqrt{\lambda\tau}} \tag{7.6}$$

Figure 7.2 shows the Allan deviation of the radioactive source as a functions of time for different values of rate $\lambda$. The Allan deviation decreases as $1/\sqrt{\tau}$, similar to conventional atomic clocks.

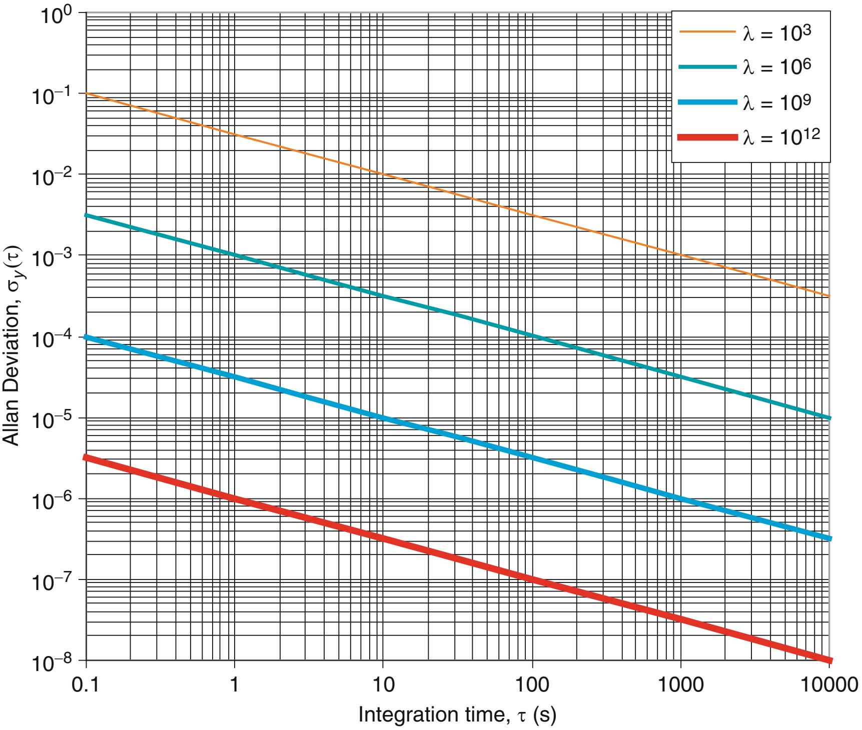

Figure 7.2: Allan deviation of counts from a radioactive source of different values of rate $\lambda$, as a function of time interval of measurement $\tau$. The figure shows Allan deviations for $\lambda = 10^3$ ($\simeq$25 nCi), $10^6$ ($\simeq$25 μCi), $10^9$ ($\simeq$25 mCi), and $10^{12}$ ($\simeq$25 Ci)

The Allan deviation of fractional frequency fluctuations at small times is large (short-term unstable) requiring it to be locked to a short-term stable LO.

## 7.3.2 Clock Architecture

Figure 7.3 shows the schematic diagram for locking a LO to the rate of emissions of a radioactive source, to form a simple radioactive counting clock (simple RCC). For very short times ($\tau \ll T_{loop}$, the loop time constant), the error signal out of the control loop is small and therefore the stability of the output frequency $f$ depends of the LO frequency stability. For long times ($\tau \gg T_{loop}$) the error signal generated is the difference between the frequency of the LO and that of the atomic clock. Thus the long-term stability of the clock is determined by that of the radioactive source. The control loop generates an error signal with appropriate gain to correct the frequency output of the LO reducing its long-term frequency variations or drifts. Thus the counting clock is realized by locking the short-term stable LO to a long-term stable radioactive source. Here the terms short term and long term are defined with respect to the loop time constant, $T_{loop}$.

In this architecture, we only need one radioactive source which will be counted by the radioactive detector/counter. The first

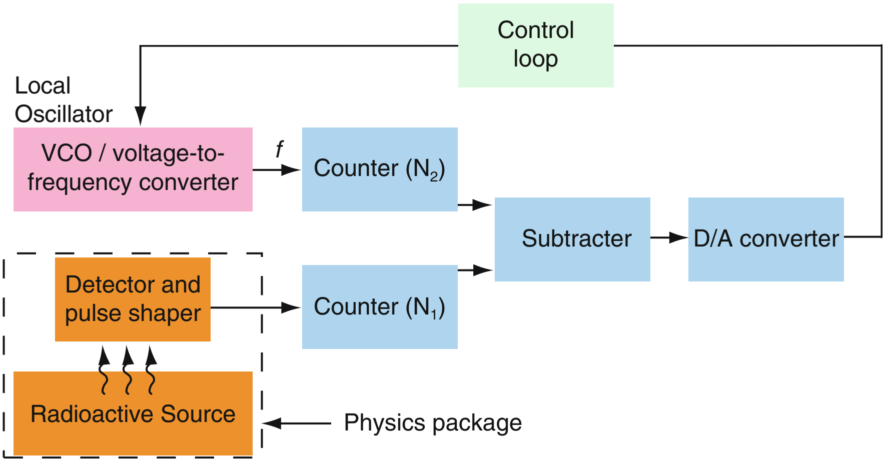

Figure 7.3: Schematic diagram of a simple radioactive counting clock showing the physics package locked on a local oscillator

counter will output a number $N_1$ that will be compared to the output of the second counter $N_2$. The second counter gets input from the LO/VCO. The subtracter's output will always adjust the VCO to give a frequency that will track the rate of radioactive emission [45].

### 7.3.3 Clock Analysis

#### Frequency Locking: Output Frequency *f*

We will first formulate the differential equation governing the output frequency $f$ of the simple RCC in the absence of the control loop. The VCO has a base (or center) frequency $f_0$ and has an output frequency $f$ given by

$$f = f_0 + k_1(N_1 - N_2), \tag{7.7}$$

where $k_1$ is the overall sensitivity of LO.

The frequency counter of the LO has a value $N_2$ given by the recursive relation

$$N_2 = \int_0^t (f_0 + k_1(\lambda t - N_2))dt \tag{7.8}$$

$$\frac{\partial N_2}{\partial t} = f_0 + k_1(\lambda t - N_2) \tag{7.9}$$

Rearranging, we arrive at the following differential equation.

$$\frac{\partial N_2}{\partial t} + k_1 N_2 = f_0 + k_1 \lambda t \tag{7.10}$$

This is a linear equation whose solution is given by

$$N_2 e^{k_1 t} = \int (f_0 + k_1 \lambda t) e^{k_1 t} dt \tag{7.11}$$

or

$$N_2 = \frac{(f_0 - \lambda)(1 - e^{-k_1 t})}{k_1} + \lambda t \tag{7.12}$$

Substituting in (7.7), we write $f$ as

$$f = f_0 - (f_0 - \lambda)(1 - e^{-k_1 t}) \tag{7.13}$$

Thus, for values of $t \gg 1/k_1$, (7.13) gives the value of $f = \lambda$. Thus the output frequency $f$ tracks the rate of emission of the radioactive source, or the LO is "locked" to the physics package.

### Phase Noise

We now analyze the phase noise of the clock with output frequency $f$. For the output frequency $f$, we $c$ If we denote $N$ as the number of counts, then from our definition the average value of $N$ over a time $\tau$ is

$$\overline{N} = \sum_{k=0}^{\infty} \frac{k(\lambda\tau)^k}{k!} e^{-\lambda\tau} \tag{7.14}$$

The average value of $f$ is given by

$$\overline{f} = \frac{1}{\tau} \sum_{k=0}^{\infty} \frac{k(\lambda\tau)^k}{k!} e^{-\lambda\tau} \tag{7.15}$$

$$\overline{f} = \lambda \sum_{k=0}^{\infty} \frac{(\lambda\tau)^k}{k!} e^{-\lambda\tau} \tag{7.16}$$

Thus $\lambda$ is the center frequency of the oscillator. ($\lambda$ is the instantaneous rate and $\lambda$ is the average rate – a constant).

To estimate the power spectral density, we find the probability that the frequency is off by a value $f_{\mathit{off}}$.

$$f = \lambda + f_{\mathit{off}} \tag{7.17}$$

$$N = (\lambda + f_{\mathit{off}})\tau \tag{7.18}$$

The probability that the number of $N$ being the value above is

$$P(f_{\mathit{off}}) = \frac{(\lambda)^{(\lambda+f_{\mathit{off}})\tau} e^{-\lambda\tau}}{(\lambda\tau + f_{\mathit{off}}\tau)!} \tag{7.19}$$

The square of the probability defined above is the power spectral density of the oscillator spectrum at $f_{\mathit{off}}$. The phase noise at the frequency $f_{\mathit{off}}$ is then

$$L(f_{\mathit{off}}) = \frac{1}{\lambda} \frac{P^2(f_{\mathit{off}})}{P^2(\lambda)} \tag{7.20}$$

$$L(f_{\mathit{off}}) = \frac{1}{\lambda} \left( \frac{\frac{(\lambda\tau)^{(\lambda+f_{\mathit{off}})\tau} e^{-\lambda\tau}}{(\lambda\tau+f_{\mathit{off}}\tau)!}}{\frac{(\lambda\tau)^{\lambda\tau} e^{-\lambda\tau}}{(\lambda\tau)!}} \right)^2 \tag{7.21}$$

$$L(f_{off}) = \frac{1}{\lambda}(\frac{\frac{(\lambda\tau)^{\lambda\tau}(\lambda\tau)^{f_{off}\tau}}{(\lambda\tau+f_{off}\tau)!}}{\frac{(\lambda\tau)^{\lambda\tau}}{(\lambda\tau)!}})^2 \tag{7.22}$$

$$L(f_{off}) = \frac{1}{\lambda}(\frac{\frac{(\lambda\tau)^{f_{off}\tau}}{(\lambda\tau+f_{off}\tau)!}}{\frac{1}{(\lambda\tau)!}})^2 \tag{7.23}$$

$$L(f_{off}) = \frac{1}{\lambda}(\frac{(\lambda\tau)!(\lambda\tau)^{f_{off}\tau}}{(\lambda\tau+f_{off}\tau)!})^2 \tag{7.24}$$

$$L(f_{off}) = \frac{1}{\lambda}(\frac{(\lambda\tau)!(\lambda\tau)^{f_{off}\tau}}{((\lambda\tau+f_{off}\tau)(\lambda\tau+f_{off}\tau-1)...(\lambda\tau+2)(\lambda\tau+1))(\lambda\tau)!})^2 \tag{7.25}$$

$$L(f_{off}) = \frac{1}{\lambda}(\frac{(\lambda\tau)^{f_{off}\tau}}{(\lambda\tau+f_{off}\tau)(\lambda\tau+f_{off}\tau-1)...(\lambda\tau+2)(\lambda\tau+1)})^2 \tag{7.26}$$

$$L(f_{off}) = \frac{1}{\lambda}(\frac{(\lambda\tau)^{f_{off}\tau}}{(\lambda\tau)^{f_{off}\tau}((1+\frac{f_{off}\tau}{\lambda\tau})(1+\frac{f_{off}\tau-1}{\lambda\tau})...(\lambda\tau+\frac{2}{\lambda\tau})(\lambda\tau+\frac{1}{\lambda\tau}))})^2 \tag{7.27}$$

$$L(f_{off}) = \frac{1}{\lambda}(\frac{1}{(1+\frac{f_{off}\tau}{\lambda\tau})(1+\frac{f_{off}\tau-1}{\lambda\tau})...(\lambda\tau+\frac{2}{\lambda\tau})(\lambda\tau+\frac{1}{\lambda\tau})})^2 \tag{7.28}$$

For a 1 mCi radioactive source (e.g., $\mathrm{Ni}^{63}$), then, $\lambda = 3.7\times10^7$. Thus for $\tau > 1\mu s$, $\lambda\tau \gg 1$.

Thus we simplify the expression for phase noise further by supposing that $\lambda\tau \gg 1$

$$L(f_{off}) = \frac{1}{\lambda}(\frac{1}{1+\frac{f_{off}\tau(1+f_{off}\tau)}{2\lambda\tau}})^2 \tag{7.29}$$

$$L(f_{off}) = \frac{1}{\lambda}(\frac{2\lambda}{2\lambda+f_{off}(1+f_{off}\tau)})^2 \tag{7.30}$$

$$L(f_{off}) = \frac{4\lambda}{(2\lambda+f_{off}(1+f_{off}\tau))^2} \tag{7.31}$$

We finally express the single-sided phase noise of the oscillator as twice the double-sided phase noise derived above. Thus

$$L(f) = \frac{8\lambda}{(2\lambda+f_{off}(1+f_{off}\tau))^2} \tag{7.32}$$

## Allan Deviation

The Allan variance of an oscillator with single side phase noise $L(f)$ is given by the equation [46]

$$\sigma_y^2(\tau) = 2\int_0^\infty L(f)\frac{1}{1+\frac{f^2}{f_c^2}}\frac{\sin^4(\pi f\tau)}{(\pi f\tau)^2}df \tag{7.33}$$

Here, $f_c$ is the cutoff frequency of the measurement device that measures the phase noise. We assume a large value of $f_c$ (i.e., $f_c \to \infty$), then the expression for Allan variance reduces to

$$\sigma_y^2(\tau) = 2\int_0^\infty L(f)\frac{\sin^4(\pi f\tau)}{(\pi f\tau)^2}df \tag{7.34}$$

This function was numerically integrated using Mathematica™ and is plotted in Fig. 7.4. We compare this with our expected value of Allan Deviation of fractional variation in counts given by (7.6).

So far we considered the case where the control loop is absent. In the presence of a control loop $H(s)$, the Allan deviation for the clock can be derived as follows.

In Fig. 7.5, let us assume that the absolute frequency variations of the free running oscillator (LO), the physics package, and the overall clock be denote respectively as $\Delta\Omega_{LO}$, $\Delta\Omega_{RS}$, and $\Delta\Omega_f$ respectively. From (7.7), we can write the Laplace domain loop equation for frequency variations as

$$\Delta\Omega_f(s) = \Delta\Omega_{LO}(s) + k_{LO}V'(s) \tag{7.35}$$

where $V'$ is the error signal generated by the control loop. Since the error signal $V$ is generated by the difference of the values of the counter, we write the equation

$$\begin{aligned} V'(s) &= H(s)V(s) = H(s)k_{DAC}\Delta(N_1 - N_2)(s) \\ &= k_{DAC}H(s)\frac{\Delta\Omega_{RS}(s) - \Delta\Omega_f(s)}{s} \end{aligned} \tag{7.36}$$

Combining (7.35) and (7.36), we write

$$\Delta\Omega_f(s) = \Delta\Omega_{LO}(s) + \frac{k_{LO}k_{DAC}H(s)}{s}(\Delta\Omega_{RS}(s) - \Delta\Omega_f(s)) \tag{7.37}$$

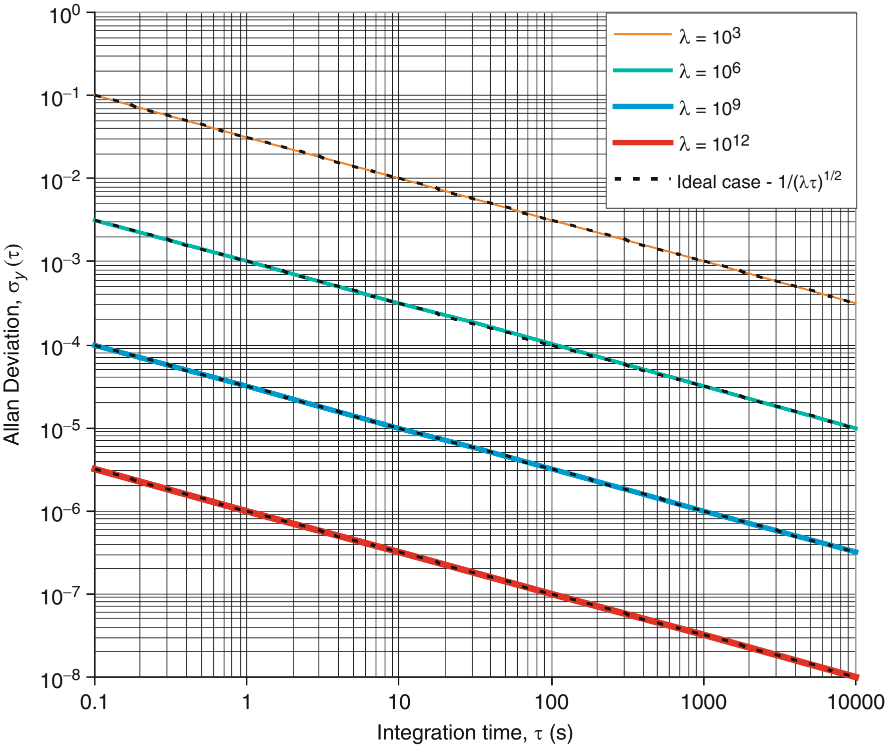

Figure 7.4: Allan deviation of the fractional frequency fluctuations of the simple RCC is compared with the Allan Deviation of fractional variation in counts from a radioactive source

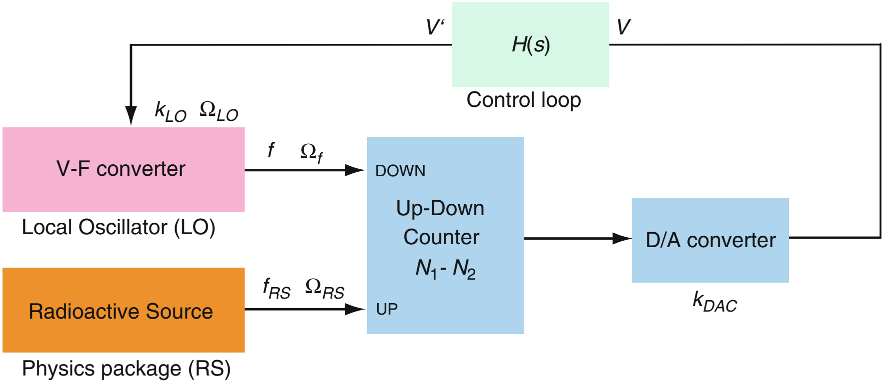

Figure 7.5: The schematic diagram of the implemented simple RCC shows a V-F converter locked to the radioactive source through a control loop $H(s)$

We write $k_1 = k_{LO}k_{DAC}$ and $G(s) = k_1 H(s)/s$ and rearrange (7.37) to obtain

$$\Delta\Omega_f(s) = \frac{1}{1+G(s)}\Delta\Omega_{LO}(s) + \frac{G(s)}{1+G(s)}\Delta\Omega_{RS} \tag{7.38}$$

In the case where $H(s) = 1$, i.e., the case with no control loop, (7.38) reduces to

$$\Delta\Omega_f(s) = \frac{sT_{loop}}{1+sT_{loop}}\Delta\Omega_{LO}(s) + \frac{1}{1+sT_{loop}}\Omega_{RS} \tag{7.39}$$

where $T_{loop} = 1/k_1$. For values of $t \gg T_{loop}$, the frequency stability is primarily determined by the physics package (RS) and for $t \ll T_{loop}$, the frequency stability is determined by that of the LO. This is the same insight we obtain from (7.13).

The fractional frequency fluctuations is related to frequency fluctuations by the relation $y = \frac{\Delta\omega}{\omega}$. In this case, the power spectral density of the fractional frequency fluctuations is given by the relation

$$S_{y,f}(\omega) = \frac{(\omega T_{loop})^2}{1+(\omega T_{loop})^2}S_{y,LO}(\omega) + \frac{1}{1+(\omega T_{loop})^2}S_{y,RS}(\omega) \tag{7.40}$$

In the case where the control loop has a function $H(s)$ given by a low pass filter function, the loop (7.38) can be written as

$$\Delta\Omega_f(s) = \frac{\frac{s}{k_1}+\frac{s^2T}{k_1}}{1+\frac{s}{k_1}+\frac{s^2T}{k_1}}\Delta\Omega_{LO}(s) + \frac{1}{1+\frac{s}{k_1}+\frac{s^2T}{k_1}}\Omega_{RS} \tag{7.41}$$

resulting in a second order loop filter, with times constants $T_{loop1}$ and $T_{loop2}$. In the case where the filter is critically damped, $T_{loop1}$ and $T_{loop2}$ each become $= T_{loop} = 1/(4k_1)$.

Finally, we write the expression for the power spectral density of fractional frequency fluctuations as

$$S_{y,f}(\omega) = \frac{(\omega T_{loop})^4}{(1+(\omega T_{loop})^2)^2}S_{y,LO}(\omega) + \frac{1+(2\omega T_{loop})^2}{(1+(\omega T_{loop})^2)^2}S_{y,RS}(\omega) \tag{7.42}$$

The Allan variance of fractional frequency fluctuations of the clock $\sigma^2_{y,f}(\tau)$ can be found by multiplying (7.40) or (7.42) by $2\sin^4(\pi f\tau)/(\pi f\tau)^2$ and integrating between 0 and $\infty$.

## 7.3.4 Simulations

The simple RCC can be simulated by using a random number generator program. We used MatLab$^{\text{TM}}$ to simulate the Poisson process. The code generates the arrival times of pulses by first generating the time intervals of the Poisson process. The time intervals of a Poisson process with parameter $\lambda$ has an exponential probability density function given by

$$P(t) = \lambda e^{-\lambda t} \tag{7.43}$$

By using the function "rand" that generates uniform random numbers (uniform distribution in the interval $[0, 1]$, we can generate time intervals for a Poisson process by making the transformation

$$E(\lambda) = -\frac{1}{\lambda} log(U) \tag{7.44}$$

where $U$ represents uniform random numbers $E(\lambda)$ represents exponentially distributed random numbers with parameter $\lambda$.

The arrival times of the process is then calculated by adding the time intervals. For a given integration time $\tau$, the number of pulses is given counted by finding the latest pulse whose arrival time $t_N < \tau$. A plot of Allan deviation $\sigma_y(\tau)$ as a function of integration time $\tau$ is identical to Fig. 7.2.

## 7.3.5 Experiments

### Construction of the Simple RCC

We implemented a simple RCC on a breadboard as described below. The radioactive source consists of a thin film of $\text{Ni}^{63}$ beta emitter. Although we have used $\text{Ni}^{63}$, it may be substituted with other beta emitters such as Tritium. The difference between the use of different radioactive sources is the difference in average electron energy emitted and the half life of the radioactive species. $\text{Ni}^{63}$ is most conveniently electroplated on a substrate to have activities of $\simeq 25$ mCi/cm$^2$ of area.

The function of the detector is to detect each radioactive beta emission from the radioactive source. The schematic diagram of the detector is described in Fig. 7.1. It consists of a reversed bias

PN diode which acts as an avalanche photodetector. An incoming high energy electron creates several electron hole pairs in the depletion region of the reverse-biased PN diode (a number dependent on the material and the diode design). It is important to maximize the depletion region width so as to be able to maximize the area over which the electrons can be detected. A detected electron will thus result in a current or a sudden burst of charge at the cathode of the PN diode. The charge can be sensed using a charge sensitive amplifier, which converts the normally low amount of charge generated per beta emission into a detectable range of voltage. The waveform generated at the output of the charge sensitive amplifier is shaped to a square wave output form with 0–10 V high and low levels to enable reliable operation of the counter. The buffer at the output is used to prevent loading of the pulse shaping amplifier. We used an evaluation board of from Amptek$^{\text{TM}}$ consisting of an ultra-low noise preamplifier A225 and a pulse shaping amplifier A206. An avalanche photodetector was used with a reversed bias voltage $V_{bias}$ to give output pulses from 0 to 10 V. Different values of $V_{bias}$ changes the threshold energy that is detectable by the charge-sensitive amplifier, hence giving different output rates. Figure 7.6 gives the value of the output rate of pulses from the radioactive sources as a function of reverse bias voltage $V_{bias}$.

We implemented the counters $N_1$ and $N_2$ using three 74LS193 4-bit binary up-down counters in cascade, generating a modulo $2^12$ counter. An output pulse from the radioactive clock generates a count up whereas the output from the LO generates a count down. Only 8 most significant bits of the 12-bit counter were used to convert the counts into an analog value. We used DAC0808 8-bit parallel load asynchronous digital-to-analog converter (DAC). The DAC converted the 8-bit number into a voltage from 50 mV to 6.1 V. Thus the sensitivity of the DAC $k_{DAC}$ was measured to be $6.05/256 = 0.0236$ V.

The analog voltage generated by the DAC was input to a voltage-to-frequency converter (V-F converter) through a control circuit. The control circuit consisted of a first order passive low pass filter with time constant $T$ generated by a resistor and a capacitor ($T = RC$), creating a second order loop filter as shown in

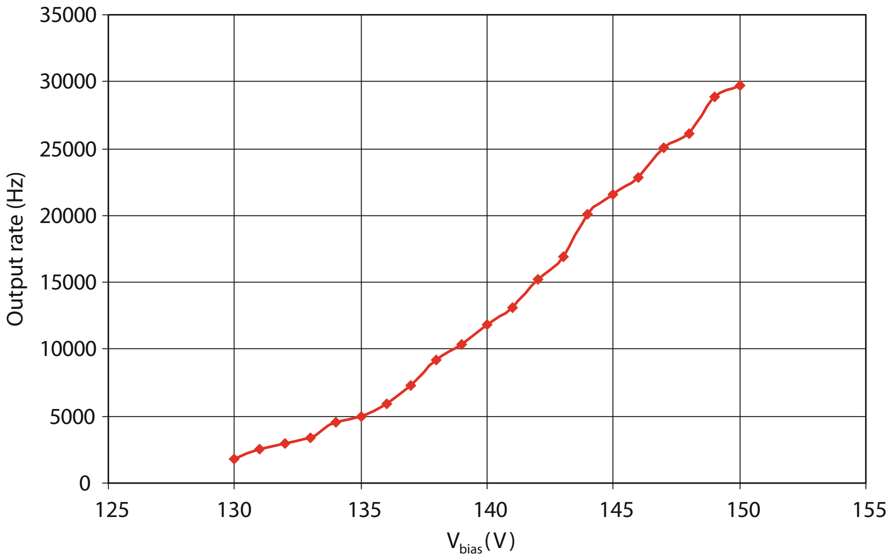

Figure 7.6: The output rate of pulses from the radioactive source is a function of the applied reverse bias to the avalanche photodetector

(7.42). The error signal generated by the control circuit tunes the V-F converter (LO) to correct for long-term variations or drift in the LO using the signal from the radioactive source. In the simplest implementation of the control circuit, i.e., the use of a single pole $RC$ filter, where the time constant $T_{loop}$ determines the time frame over which the radioactive clock corrects the LO frequency. This value was optimized depending on the short term stabilities for the LO and the radioactive source. This type of control circuit is similar to those used in Atomic clocks [47]. The V-F converter was realized using an asynchronous V-F converter chip AD654. The values of resistor and the capacitor used controls the frequency range of operation of the V-F converter. Figure 7.7 shows the output frequency of the V-F converter for as a function of its input gate voltage. The measured sensitivity of the V-F converter $k_{LO}$ was 2254.3 Hz/V for a values of resistor $R_{LO} = 4.7$ kΩ and capacitor $C_{LO} = 10$ nF.

The overall loop gain $k_1$ can then be calculated as $k_{LO}k_{DAC} = 0.0236 \times 2254.3 = 53.26$ Hz. From (7.13), the value of $k_1$ can also be measured by measuring the settling time when the

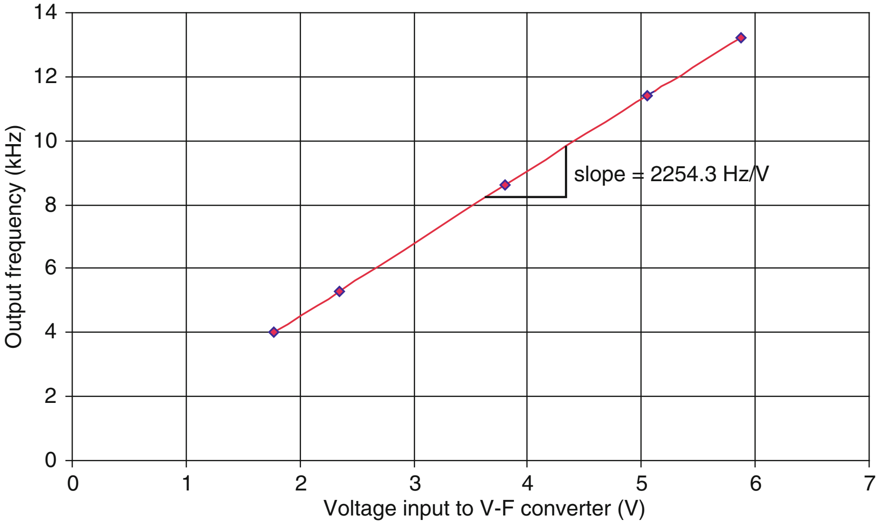

Figure 7.7: The output frequency of the V-F converter as a function of input gate voltage for resistor $R_{LO} = 4.7\,\mathrm{k\Omega}$ and capacitor $C_{LO} = 10\,\mathrm{nF}$

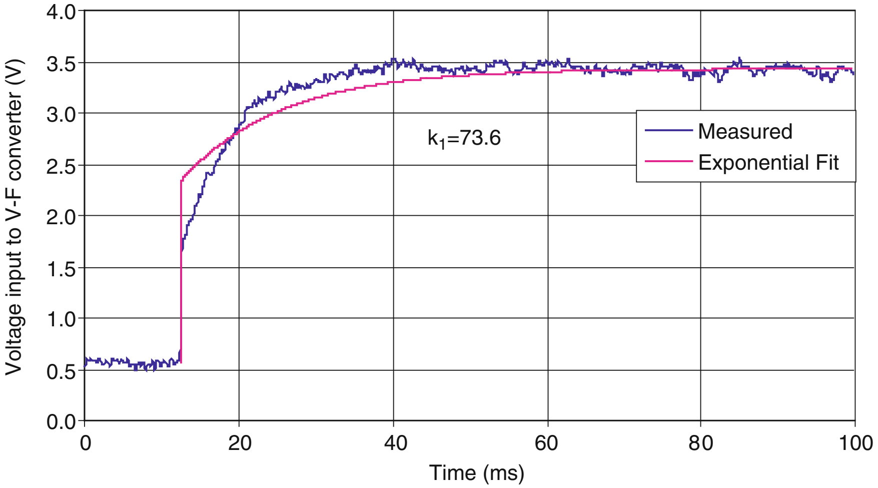

Figure 7.8: The graph shows the voltage at the input of the LO when it is locked to the radioactive source

loop is closed and the free-running oscillator is locked to the radioactive source. Figure 7.8 shows the voltage waveform of the gate voltage to the V-F converter when it is locked from its free-running frequency to that of the atomic clock. The gate voltage exponentially increases to settle down at the value corresponding to the frequency of the radioactive emission. The graph shows a best fit curve to the measured waveform (from (7.13)). This gives a measured value of $k_1 = 73.6$ Hz.

### Measurement Setup

The Allan deviation of fractional frequency fluctuations of the simple RCC described above was measured in the following manner.

The output frequency $f$ of the simple RCC was analyzed using a universal counter SRS620. The number of pulses of the output frequency source $f$ was counted over different values of integration time $\tau$. SRS620 allows for a number of values of gate time from $\tau = 1\,\text{ms}$ to $\tau = 500\,\text{s}$. To make sure that the measurement of counts happens between successive intervals of time, SRS620 uses two independent counters. For each value of $\tau$, two samples were measured, $C_1(\tau)$ and $C_2(\tau)$. The Allan variance of fractional frequency fluctuations can then be calculated using the relation

$$\sigma_y^2(\tau) = \frac{1}{2}[(C_1(\tau))^2 - (C_2(\tau))^2] \tag{7.45}$$

The SRS620 has an internal crystal oscillator that has a worst case Allan Deviation of $10^{-7}$ at 1 ms and decreases is $<10^{-9}$ for integration times of larger than 1 s for all the gate times over which the experiments were performed. Although the frequency stability of the internal oscillator is sufficient for all the measurements, these were verified by measuring the frequency stabilities of the simple RCC against the reference frequency of a Rb atomic clock from Frequency electronics. The counter has an option of measuring counts at one of its inputs (Source A) as a fraction of the counts measured at the other input (Source B). The Rb atomic clock is calibrated to have a frequency stability of $<10^{-9}$ at 1 ms and $<10^{-12}$ for all values of integration times $\tau$ greater than 1 s till the times used in the experiments.

### Stability Measurements

All the analysis and simulations done thus far have assumed that the radioactive decay process is a Poisson process. This is

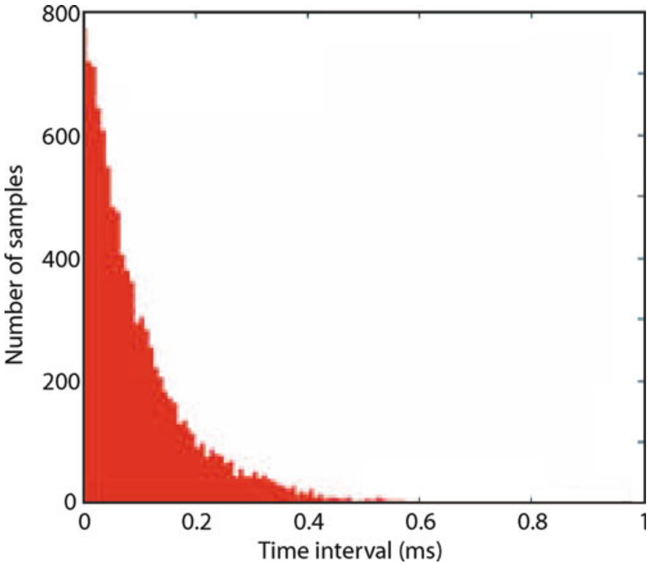

Figure 7.9: Histogram of time intervals for 10,000 samples for a radioactive source of average rate 27,000 Hz

verified experimentally by measuring a histogram of time intervals. Figure 7.9 shows the histogram of 10,000 samples of time intervals for a radioactive source with average rate of 27,000 Hz. The histogram is normalized and fit to the equation for the probability density function of the time intervals given by (7.43). The histogram was normalized and the value of lambda was extracted to be 28,000 using a best fit.

The values of counts as a function of integration time $\tau$ were acquired using Labview$^{\mathrm{TM}}$. The values reported are values averaged over ten data points.

Figure 7.10 shows the measured Allan deviation of the radioactive source as a function of integration time $\tau$. The measured Allan deviation shows good agreement with theory $(1/\sqrt{\lambda\tau})$. The value of $\lambda$ used in this measurement is 7,500 Hz. Figure 7.11 shows the measured Allan deviation for the simple RCC with $\lambda$ =7,500 Hz and four different values of loop filter $T_{loop}$. The graph also compares this with the Allan deviation from the physics package (RS) and that of the free-running oscillator (LO). As predicted by (7.42) the short term stability in frequency is determined primarily by the LO and the long term stability is governed by that

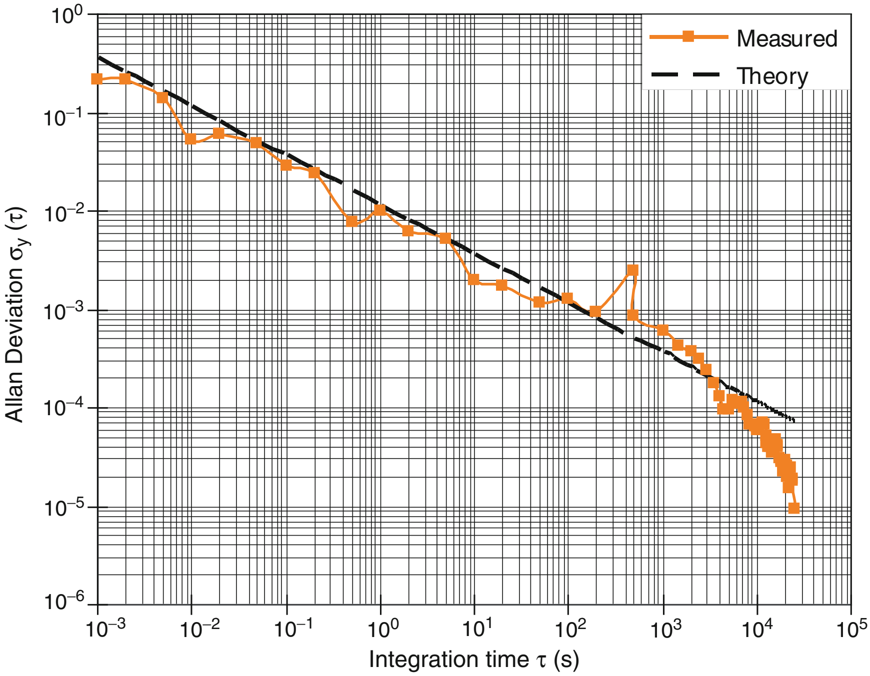

Figure 7.10: Allan deviation of the counts directly at the output of the radioactive source (physics package) compared with theoretical value for Allan deviation

of the RS. The four different values of loop constants determine the regions of integration time $\tau$ where each of the stability of the overall clock is primarily dependent on the RS.

Figure 7.12 shows the long-term stability of the simple RCC (primarily governed by the frequency stability of the RS), compared with the ideal value and the Allan deviation of the free-running LO. The measured result follows the ideal curve till integration time $\tau$ =25,000 s or $\simeq$ 7 h. The Allan deviation for larger $\tau$ increases from the predicted values. This is due to random drifts occurring either in the detector, the amplifier or other electronic devices.

Figure 7.13 shows the data values taken in subsequent intervals of integration time $\tau$ = 500 s. As evident form the long-term stability of the RS in Fig. 7.12, we see a random drift in the data.

The graph also shows a drift-corrected data set used to compute drift-corrected frequency stability for long-term, as shown in

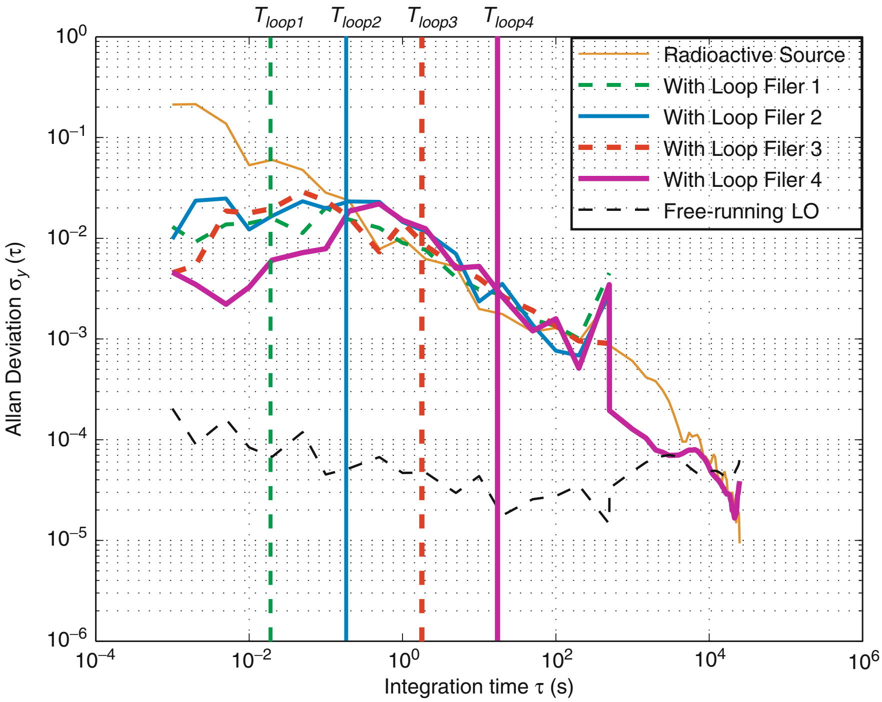

Figure 7.11: Allan deviation of the simple RCC for four different values of loop time constants, $T_{loop1} = 20$ ms, $T_{loop2} = 200$ ms, $T_{loop3} = 2$ s, and $T_{loop4} = 20$ s respectively. The graph also shows the Allan deviation from the RS and the free-running oscillator (LO)

Fig. 7.14. The long-term stability in this case closely follows the predicted value (shown in dotted line).

### Power Requirements

Although the implemented RCC was not optimized with respect to the power consumption, the power requirements for a simple RCC mainly consists of the power consumed by the loop electronics and the detector. Table 7.1 shows the measured power consumption of the various modules of the simple RCC. The loop electronics used for the bread board implementation employ a mixed CMOS-TTL chips that don't have the optimal speed-power performance. The main power advantage of the simple RCC comes from the low power consumption from the Physics package (<11 mW).

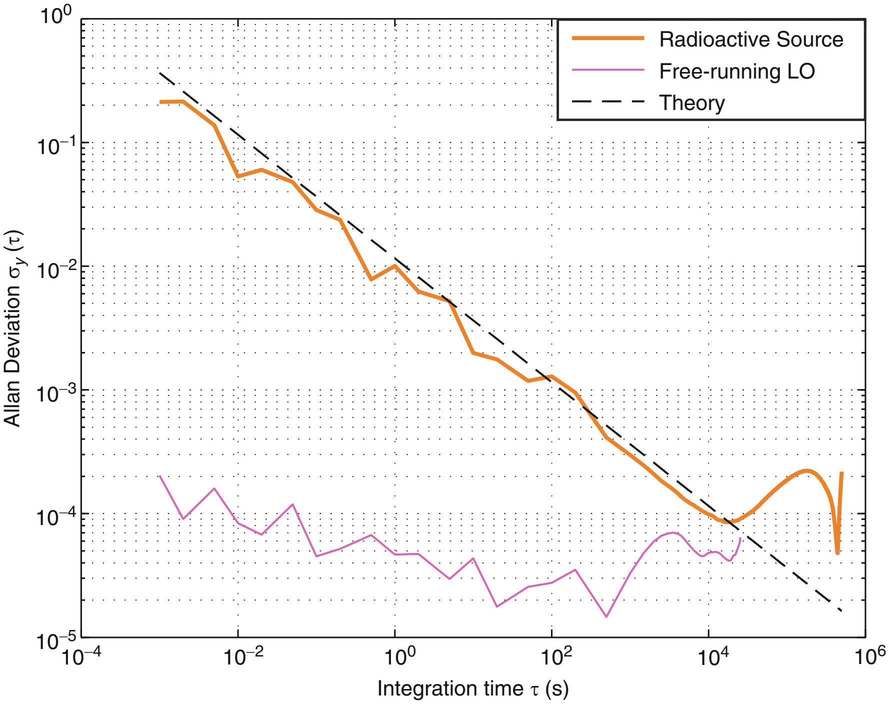

Figure 7.12: Allan deviation of the simple RCC for long integration times shows random drifts in frequency for $\tau > 25{,}000\,\text{s}$

### 7.3.6 Limitations of Simple RCCs

Although in principle, we can achieve Allan deviations comparable to state-of-the-art chip-scale atomic clocks [48], there are several practical problems which will make this system tough, if not impossible to implement.

1. Detector speed: From Fig. 7.2, we can achieve an Allan deviation of $<10^{-8}$ for radioactive rate $\lambda$ of $10^{12}$ at an integration time $\tau = 1\,\text{h}$. However, this means that the detector and the counter would have to work at frequencies of over $10^{12}$ Hz or over 1 THz which is simply not possible. At lower activities, we would have to wait much longer in order to achieve the same Allan deviation as those from radioactive sources of larger activities.

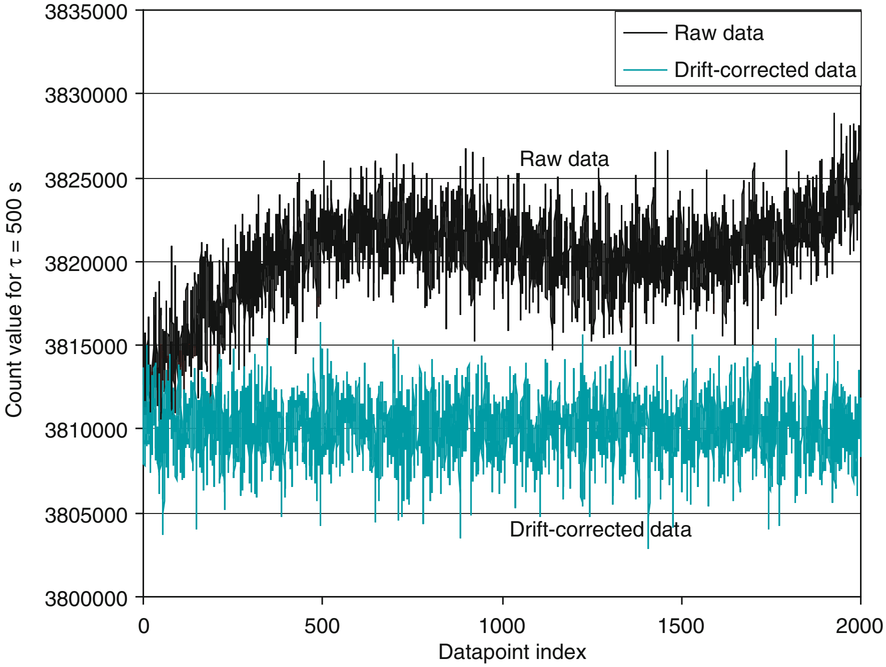

Figure 7.13: Figure shows 2,000 consecutive data points used to measure the long term stability of the simple RCC. Each data point is the count value for $\tau = 500$ s. The graph also shows a drift-corrected data set

2. Detector power: An alternative to circumventing the detector speed limitation is to break down the detection into multiple detectors. For example, for $\lambda = 10^{12}$, we could use 1000 detectors, each working at a frequency of around 1 GHz. Simple detector implementations from state-of-the-art electronics would enable detector speeds over 1 GHz. However, these would be relatively high power consuming devices possibly obviating the need for low power radioactive source-based clocks.
3. Radiation levels: This is currently not a limitation as the detector speed and power requirements are dominating problems compared to those causes by safety from the radiation level. Further, these devices can potentially detect all radioactive emissions, hence causing no external radiation such as to the operator and/or the surroundings.

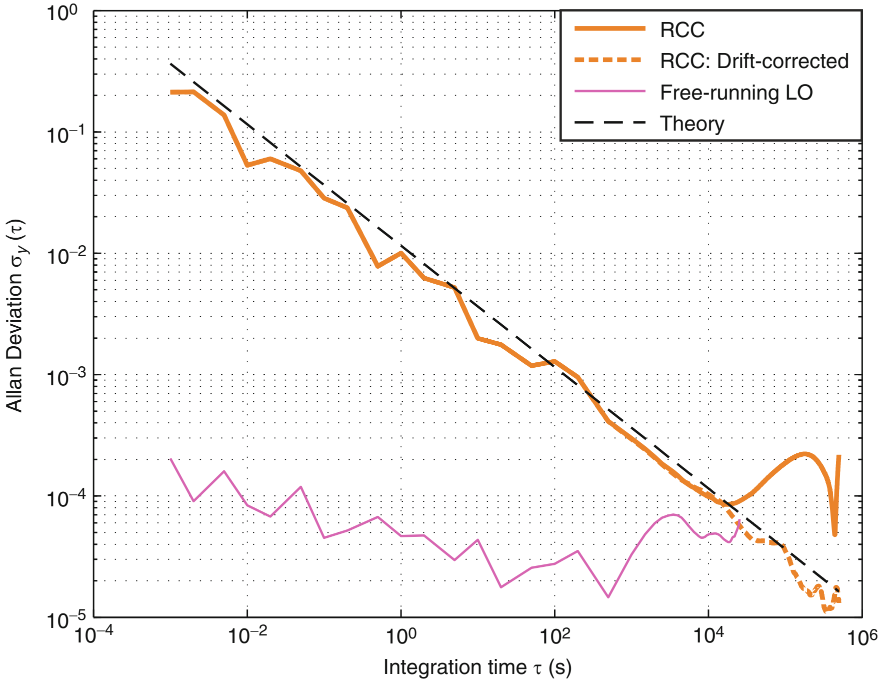

Figure 7.14: Allan deviation of the simple RCC for long integration times after drift correcting the obtained data as shown in Fig. 7.13

## 7.4 Stochastic Resonators

### 7.4.1 Introduction

The Poisson nature of the radioactive decay process can be exploited to give insights into ways of decreasing the activity and time required to achieve a required Allan deviation of frequency of the clock. An important characteristic of the Poisson process is that the time interval between successive decay events has an exponential distribution with parameter $\lambda$. Thus the probability density function of the time-intervals between successive events is given by the equation

$$P(t) = \lambda e^{-\lambda t} \tag{7.46}$$

Table 7.1: Measured power consumption of the simple RCC

| Module | Power consumed (mW) |
|---|---|
| *Physics package* | <11 |
| Radioactive source | 0 |
| Avalanche photodetector | <1 |
| Amplifier and buffer | 10 |
| *Loop electronics* | 680 |
| V-F converter | 30 |
| Up-down counter | 300 |
| D/A converter | 350 |
| Control loop | 0 |
| *Total clock power* | 691 |

Figure 7.9 shows an experimental verification of the exponential time interval distribution confirming the validity of Poisson process model of radioactive decay process. For the Poisson process, tt can be shown and expected that the average time interval for the Poisson process of parameter $\lambda$ is,

$$\overline{TI} = \frac{1}{\lambda} \tag{7.47}$$

This variation in the time intervals between successive pulses is what causes the standard deviation in the counts of the counting clock. This is equivalent to having a pure frequency source of frequency $\lambda$ with a Poisson noise as derived in (7.45).

As noted previously, detectors of radioactive sources (or any electronic detector) suffer from a finite dead-time in measurement. This means that if two pulses differ in their arrival times at the detector by less than the value of the dead-time, the detector will not be able to distinguish the two pulses and will register only one pulse. In this section, we analyze the use of a dead-time to our advantage in order to reduce the Poisson noise limitation of the simple RCC.

## 7.4.2 Dead-Time-Modified Poisson Process

A dead-time inserter is a device that causes each radioactive event to disable the detector for a constant time, called the dead-time, $T_{dead}$. There are two types of dead-time that differ in their response to pulses arriving during a dead-time, which 1. for a non-extended dead time; have no effect at all 2. for an extended dead time; extend the dead time by $T_{dead}$, measured from the last arrival time.

The effects of dead times on the counts of radioactive detectors have been extensively researched before [49, 50, 51]. Due to the exponential distribution of the time intervals of the radioactive decay process, most of the events occur within very short intervals of one-another. This requires very fast detectors (with response times $\ll 1/\lambda$, or operational speeds $\gg \lambda$) to record events without missing any. In the absence of such a detector, there would be unpredictable counting losses which can lead to errors in the device or experiment one intends. One way of overcoming the unpredictability of the counting losses is to insert an artificial dead-time in the detector.

Figure 7.15 shows a schematic diagram of a radioactive detector with a non-extendable dead time, $T_{dead}$. There are several effects of introducing a dead-time inserter. The average count rate decreases as several pulses are deleted by the dead-time inserted. The average count rate at the output of SR as $\lambda_{SR}$ is given by

$$\lambda_{SR} = \frac{\lambda}{1 + \lambda T_{dead}} \tag{7.48}$$

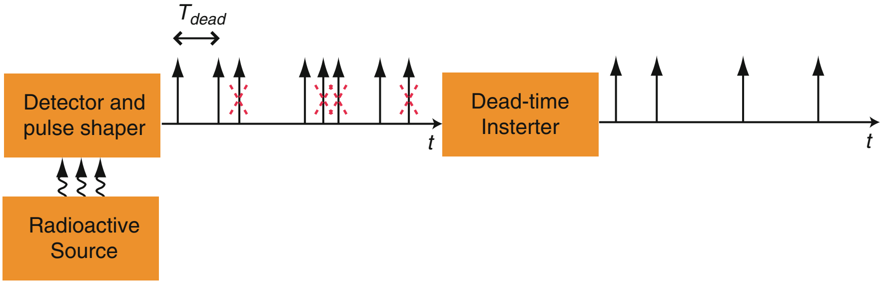

Figure 7.15: Illustration of a Poisson process modified by a non-extendable dead-time $T_{dead}$

The output pulses tend occur more periodically (compared to the original radioactive decay process) with a period close to $T_{dead}$ (for $T_{dead} \gg 1/\lambda$).

$$\lambda_{SR} = \frac{1}{\frac{1}{\lambda} + T_{dead}} \simeq \frac{1}{T_{dead}} \quad \forall T_{dead} \gg 1/\lambda \tag{7.49}$$

The probability density function of time intervals changes from an exponential distribution to that of a truncated exponential distribution.

$$P_{SR}(t) = \lambda e^{-\lambda(t - T_{dead})} \tag{7.50}$$

The dead time $T_{dead}$ can be expressed in terms of $\lambda$ such that

$$T_{dead} = \frac{a}{\lambda} \tag{7.51}$$

Figure 7.16 shows the histogram of time intervals before and after SR for $\lambda = 10^4$, for different values of $a$ (and hence $T_{dead}$). The dead-time for the detector can either be implemented within the detector itself or can be implemented as a separate block after the detector.

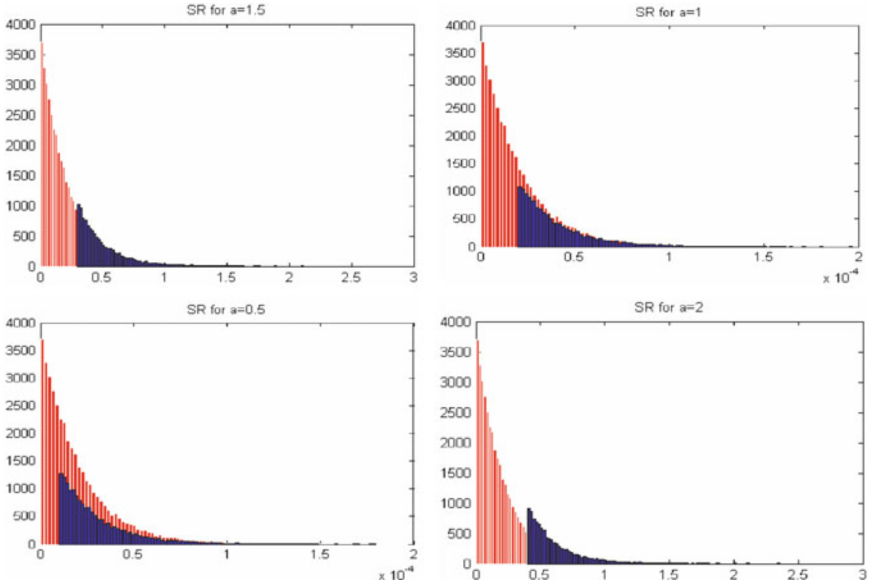

Figure 7.16: Illustration of a Poisson process modified by a non-extendable dead-time $T_{dead}$

### 7.4.3 Output Frequency of Dead-Time-Modified Poisson Process

#### Power Spectral Density

The power spectral density of a square wave output frequency of an original Poisson process modified by a dead-time $T_{dead}$ can be obtained by Muselli [52]. The power spectral density is given by the equation

$$S_{T_{dead}}(\omega) = \frac{4\lambda}{(\lambda T_{dead} + 1)(2\lambda^2 + \omega^2 + 2\lambda^2 \cos(\omega T_{dead}) - 2\lambda\omega \sin(\omega T_{dead}))} \tag{7.52}$$

By substituting $T_{dead} = 0$, the above equation reduces to the power spectral density of the original Poisson process, given by

$$S_{Poisson}(\omega) = \frac{4\lambda}{4\lambda^2 + \omega^2} \tag{7.53}$$

Figure 7.17 shows the normalized power spectral density of the square wave frequency output of the dead-time-modified Poisson process. As expected from (7.49), it can be seen that as $a$ (and hence $T_{dead}$) increases, the frequency source has a higher quality factor at its resonance. The resonance is effected using a dead-time forced by a stochastic process (the original Poisson process), hence the name stochastic resonator (SR).

#### Allan Deviation

From (7.49), for a given time $t$, the average value of count rate at the output of the SR $\overline{k_{SR}}$ can be is given by

$$\overline{k_{SR}} = \frac{\lambda t}{1 + \lambda T_{dead}} = \frac{\lambda t}{1 + a} \tag{7.54}$$

The variance of counts $\sigma_{SR}^2$ is given by [53]

$$\sigma_{SR}^2 = \frac{1}{(1+a)^3}(\lambda t + \frac{a^2(6 + 4a + a^2)}{6(1+a)}) \tag{7.55}$$

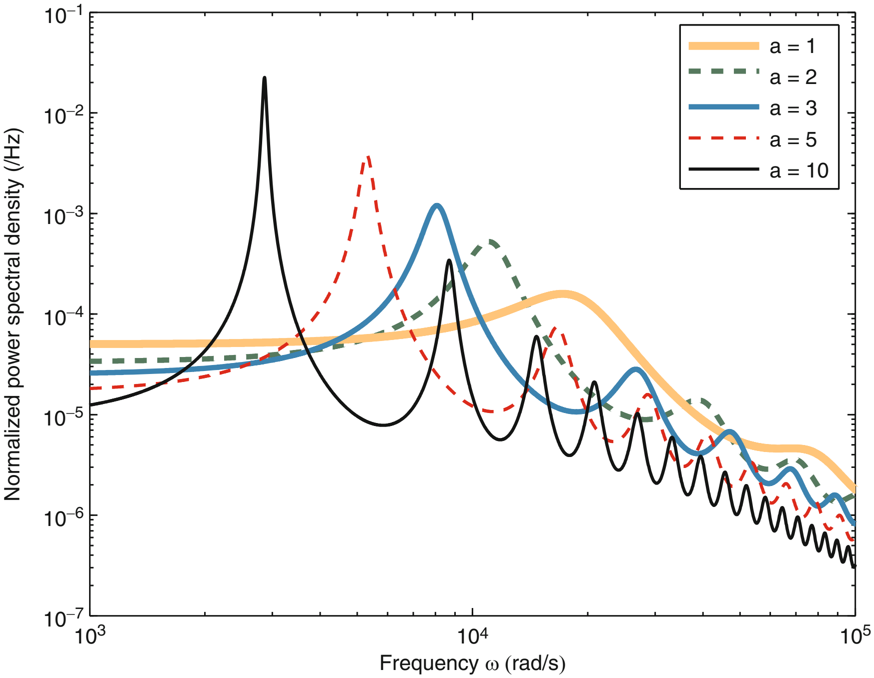

Figure 7.17: The power spectral density of the square wave output of a stochastic resonator for different values of $T_{dead} = 1/a$

If we assume no external source of noise, the Allan deviation of fractional frequency fluctuations of the SR can be calculated from (7.54) and (7.55).

$$\sigma_y(\tau) = \sqrt{\frac{1}{\lambda\tau(1+a)} + \frac{a^2(6+4a+a^2)}{6(\lambda\tau)^2(1+a)^2}} \tag{7.56}$$

We plot the Allan deviation as a function of $T_{dead}$ as shown in Figs. 7.18 and 7.19. The equations and the figures reveal that there exists a minimum in the Allan deviation for a given value of counter gate time (how long the counter counts – $\tau$). Figure 7.18 shows the values of $T_{dead}$ that gives the minimum values of Allan deviation for different values of $\tau$ (different colors), for two different rates $\lambda$. For example, we can see that for $\lambda = 10^{12}$, we obtain an Allan deviation of $10^{-11}$ at an integration time of 1 h ($\tau = 3600$ s) using a value of $T_{dead} = 2 \times 10^{-7}$ s or 200 ns. Again,

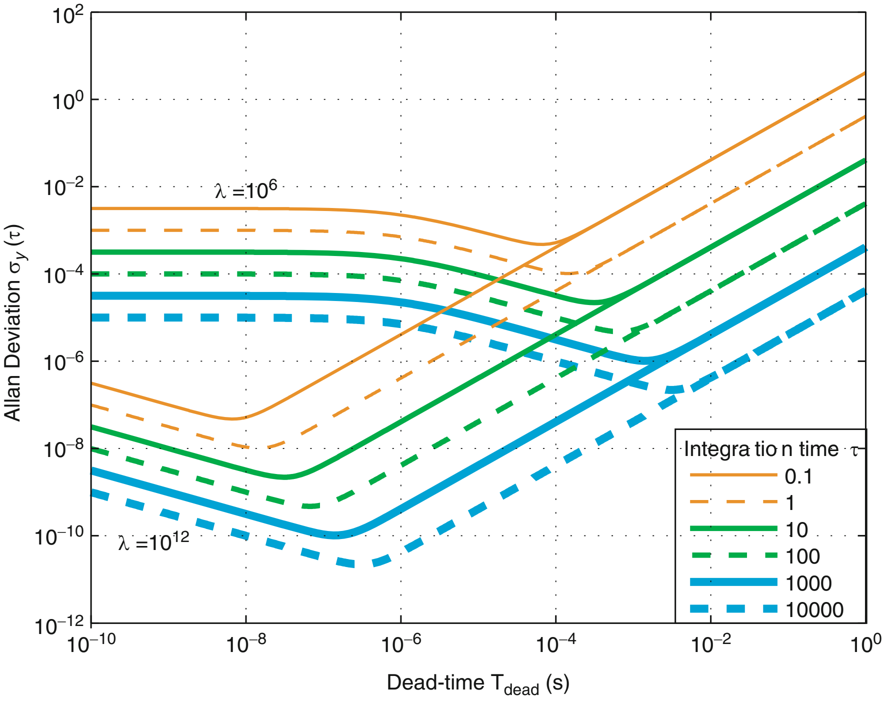

Figure 7.18: The Allan deviation of fractional frequency fluctuations for two values of $\lambda = 10^6$ and $10^{12}$ as a function of dead-time $T_{dead}$ for different values of integration time $\tau$

as in the case of the simple RCC, the detector needs to work at a speed of 1 THz, which is not possible. Figure 7.19 shows the same for and compares the Allan deviation of the clock with (solid lines) and without SR (dotted lines). Here we can achieve an Allan deviation of $<10^{-8}$ at an integration time $\tau$ of 1 h for $\lambda = 10^9$ with a dead-time $T_{dead} \simeq 1\mu$s. The required detector speed in this case is $\simeq$1 GHz (as against 1 THz in the case of simple RCC) to obtain the same stability at the same integration time.

### 7.4.4 Simulations

Based on the simulation model developed for the simple RCC in Sect. 7.3, a model to simulate the effect of dead-time $T_{dead}$ was developed in Matlab. The code first generates the time intervals for the original Poisson process and finds the corresponding arrival

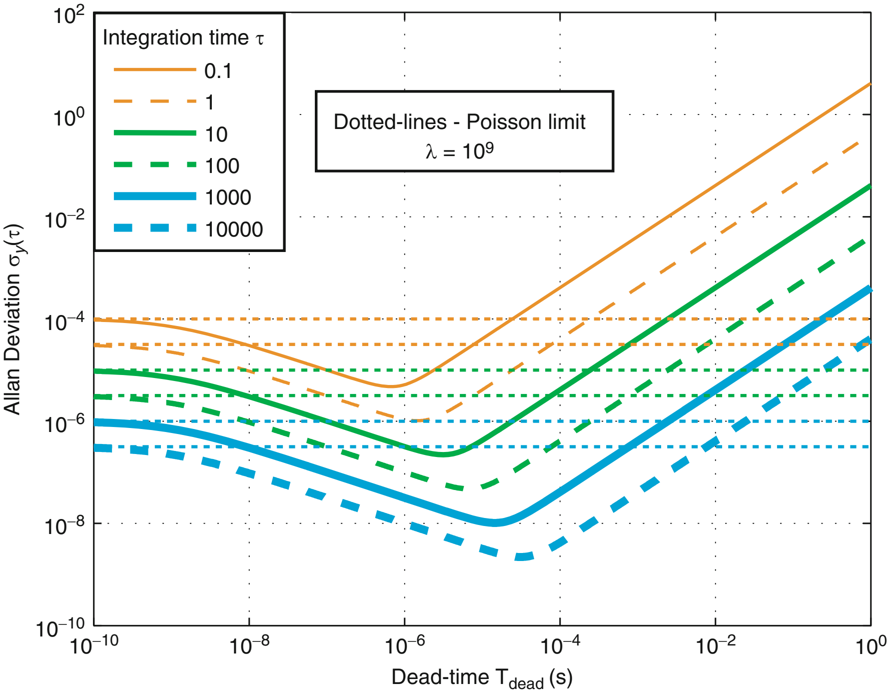

Figure 7.19: The Allan deviation of fractional frequency fluctuations for $\lambda = 10^9$ as a function of dead-time $T_{dead}$ for different values of integration time $\tau$. This compared with the Allan deviation of the original Poisson process (*dotted-lines*)

times of the pulses by summing up subsequent time-intervals. An algorithm to calculate the effect of dead-time was developed based on the illustration in Fig. 7.15. Appendix D.2 shows a code that outputs the counts for specified values of integration time.

### Real Effects in DTM-RCC

In the development of the theoretical model for both the simple and the DTM RCC, a number if real effects was ignored. In reality, these real effects (apart from power and speed limitations) limit the useful applicability of the RCCs. The code in Appendix D.2 incorporates all of these effects to understand the current limitations of the RCCs and suggests insights into further improvements to be made.

### Stability of Timing Elements

The realization of dead-time $T_{dead}$ uses passive or active electronic components (usually at least capacitor an a resistor) thus not based on a fundamental time constant. In the case when $T_{dead} > 1/\lambda$ (i.e., $a > 1$) the stability of the RCC is limited by the stability of $T_{dead}$.

One can expect this from the theory, as a variation in $T_{dead}$ directly results in a modulation of the output rate (7.54). For a fractional variation of $f$ in the value of $T_{dead}$, the modified rate $\lambda'_{SR}$ can be written as

$$\lambda'_{SR} = \frac{\lambda}{1 + \lambda T_{dead}(1+f)} = \frac{\lambda}{1 + a(1+f)} \tag{7.57}$$

The Allan deviation of fractional frequency fluctuations limited by drift is then given by

$$\sigma_{y,drift} = \frac{\lambda_{SR} - \lambda'_{SR}}{\lambda_{SR}} = \frac{\lambda}{1 + \lambda T_{dead}(1+f)} = \frac{\lambda}{1 + a(1+f)} \tag{7.58}$$

which can be written as

$$\sigma_{y,drift} = \frac{\frac{\lambda}{1+a} - \frac{\lambda}{1+a(1+f)}}{\frac{\lambda}{1+a}} = \frac{af}{1 + a(1+f)} \simeq \frac{af}{1+a} \tag{7.59}$$

For values of $a \ll 1$, the stability limit of the RCC is $af$. Thus the long-term stability is practically determined by the Poisson-limited noise. For values of $a \gg 1$, the stability limit becomes $f$. Thus the long-term stability is limited by the drift in the value of $T_{dead}$. Figure 7.20 shows the simulated value of Allan deviation of fractional frequency fluctuations as a function of integration time $\tau$ for three different values of $a$. The dotted lines indicate the Allan deviation due to drift, the dashed lines indicate the Allan deviation limited by the Poisson noise, and the solid lines indicate the limit Allan deviation for a drift-limited DTM RCC. The simulation also takes into account variations in the value of $T_{dead}$ due to noise (for example, thermal noise in the resistor and finite $Q$ of the capacitor). Since the contributions to the variations in these values always average to zero, the long-term stabilities are independent of these variations.

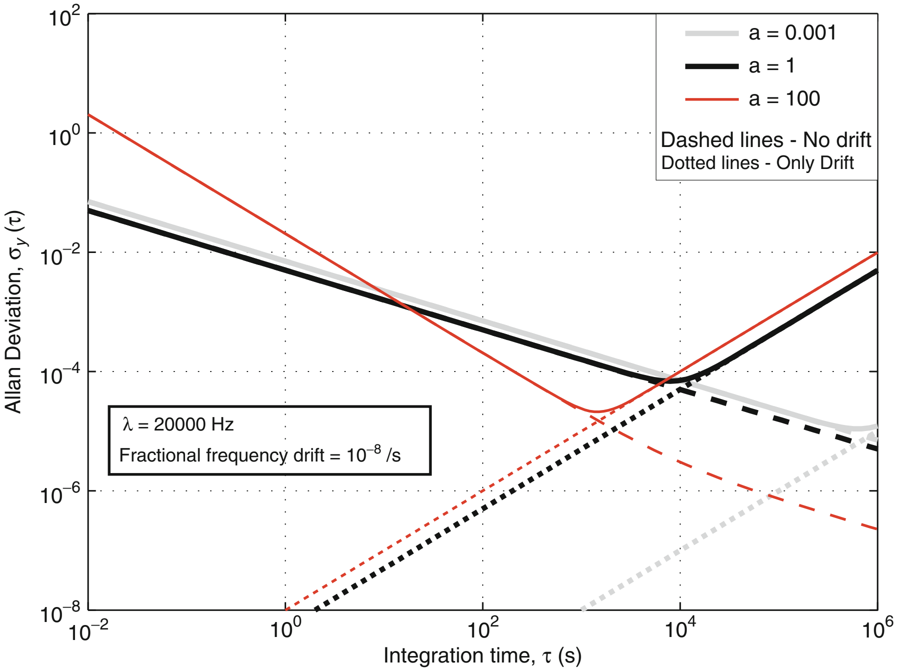

Figure 7.20: Simulated stability of DTM RCC for $a = 0.001$, 1, and 100. Here $\lambda = 20{,}000\,\text{Hz}$ and the fraction drift of $T_{dead}$ is $10^{-8}/\text{s}$

## Finite Detector Speed

Even in the case of the simple RCC, the original Poisson process is modified by the non-zero response time of the detector. This results in a dead-time $T_{dead}$. In the case of the evaluation board used in all the experiments performed, the value of the detector dead-time was $\simeq 5\,\mu\text{s}$. However, for all current experiments, the value of $a$ ($=\lambda T_{dead}$) was $<0.1$.

## Drift in Amplifier

As discussed in Sect. 7.3.6, the drift in the amplifier threshold of energy detection is the primary limiting factor in the measured stability of RCC. This drift effectively changes the average count rate of the radioactive source. This effect can thus be modeled a drift in the value of Poisson parameter $\lambda$. This model will be important in estimating the limits in the long-term stability of RCCs in future designs.

### 7.4.5 Experimental

#### Implementation of Dead-Time

Figure 7.21 shows the clock architecture that was implemented on a bread board. There are several ways to implement a dead-time inserter or the SR block. A simple way is the use of a monostable multivibrator and a bistable multivibrator in series. The monostable multivibrator implements a non-extendable dead-time $T_{dead}$ and bistable multivibrator toggles the output of the monostable each time a pulse is registered, hence generating a square wave output at the output of the dead-time inserter. Each of these multivibrators was realized using the commercially available IC555. In the case of the monostable, the $T_{dead}$ of the dead time inserter is equal to the product RC of the external timing components of IC555.

#### Stability Measurements

The frequency stability of the DTM RCC output was measured. Figures 7.22 and 7.23 show the measured Allan deviation of fractional frequency fluctuations for $\lambda = 2{,}000$ Hz and 20,000 Hz respectively. The figure shows drift-corrected values of counts due

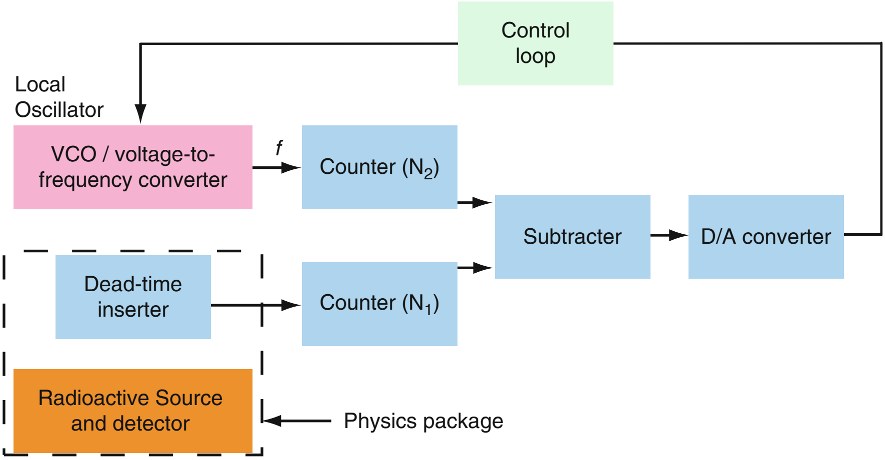

Figure 7.21: Clock architecture showing a dead-time inserter after the detector to realize a DTM RCC

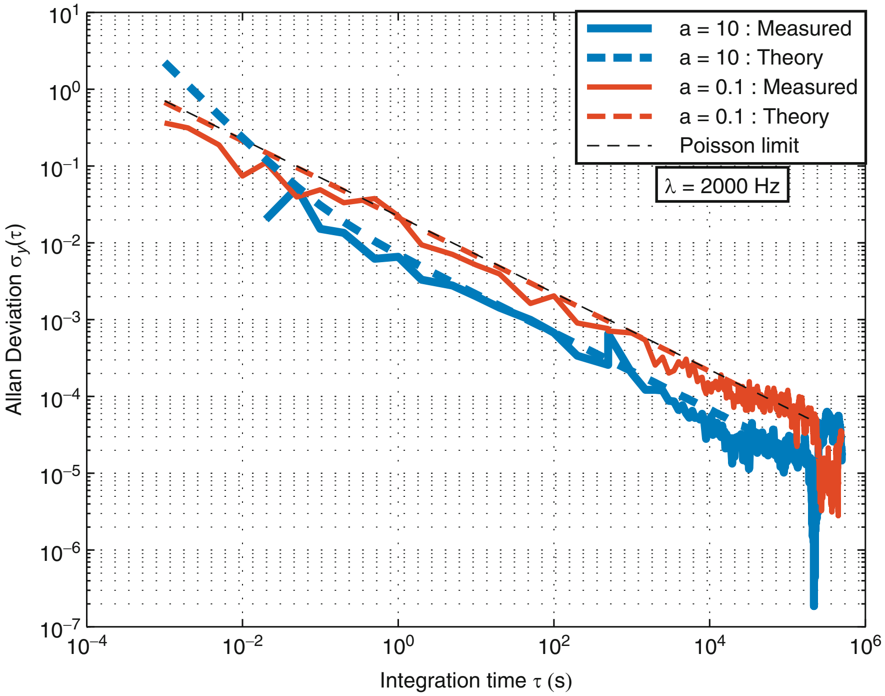

Figure 7.22: The measured drift-corrected Allan deviation of fractional frequency fluctuations compared with simple RCC and with theory for $\lambda = 2{,}000\,\mathrm{Hz}$

to variations in temperature. The measured values are also compared with the predicted values from (7.56) and with the Poisson limited value. Using a detector with a dead-time we obtain an Allan deviation of fractional frequency fluctuations of $3 \times 10^{-6}$ at an integration time of $10^5$ s for $\lambda$ =20,000 Hz. In the case of a simple RCC of the same $\lambda$ and integration time $\tau$, this value was $2.2 \times 10^{-5}$.

### Power Requirements

The additional power requirement for the DTM RCC compared to the simple RCC (Sect. 7.3.5) is that of the dead-time inserter, which consumes around 15 mW. this can be substantially improved by designing a single chip implementation of DRM RCC.

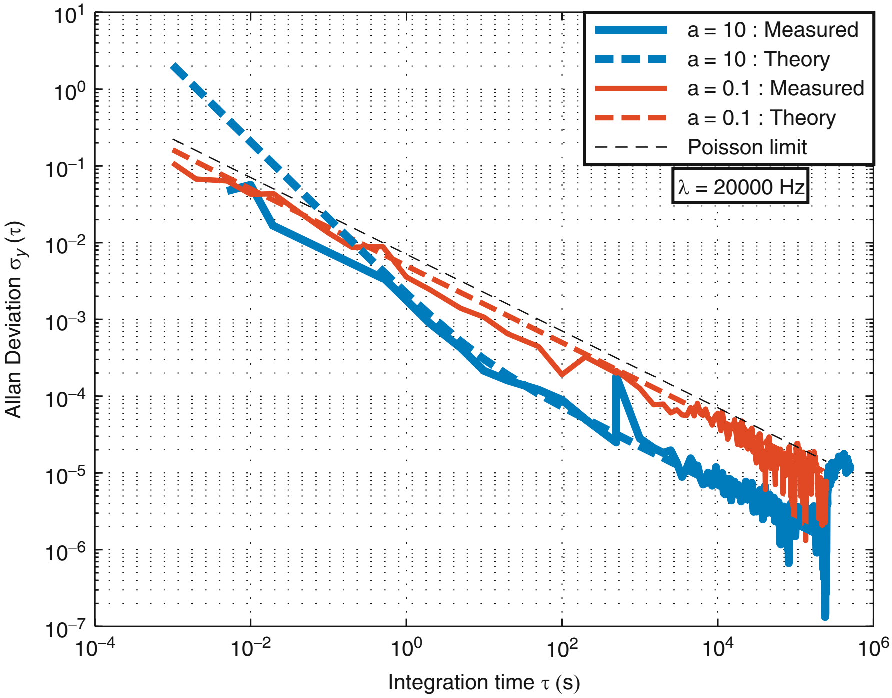

Figure 7.23: The measured drift-corrected Allan deviation of fractional frequency fluctuations compared with simple RCC and with theory for $\lambda = 20{,}000\,\mathrm{Hz}$

## 7.4.6 Limitations of DTM RCC

The short and long-term stabilities of the DTM RCC are limited by noise and drift in the electronic timing elements, detectors and amplifiers.

1. Noise-limited short-term stability: The dead-time-modified suffers from a worse short term stability than that of simple RCC. However, this is not a serious problem as this can be overcome by locking a LO with good short-term stability and designing an appropriate loop time constant.
2. Drift-limited long-term stability: The long-term stability of the DTM RCC will be primarily governed by the drift in the value of $T_{dead}$, especially for values of $a \gg 1$. For smaller values of $a$, the long-term stability of the dead-time

modified clock would be similar to the RCC. Thus, there is a fundamental trade-off between the achievable stabilities over the short-term (Poisson-limited regime) and over the long-term (drift-limited regime). Since the long-term stability of the DTM RCC depends on the drift of in $T_{dead}$, this is no longer a fundamental frequency reference. The long-term stability of the timing elements of $T_{dead}$ are usually sensitive to environmental changes such as temperature. The corresponding non-drift-corrected stability measurements shown in Figs. 7.22 and 7.23, the long-term Allan deviation of fractional frequency fluctuations would be $10^{-3}$ for temperature variations of a few °C. However, one could potentially make high-frequency and stable oscillators that consume relatively low power compared to quartz or MEMS oscillators.

## 7.5 Other Methods

The goal of radioactive counting clocks is to generate a stable frequency source out of the stable emissions of radioactive emissions. One way to generate a clock is to use the properties of the Poisson process and perform computation to generate a stable clock. For example, one could use a microcontroller to generate a frequency given the average time interval (in terms of clock cycles) between pulses, measured using an $N$-bit counter. Alternatively, the microcontroller can measure the number of pulses in a given amount of clock cycles, and calibrate its clock with respect to the acquired count rate. It is possible to prove in each of these cases that the best achievable frequency stability is given by that of the simple RCC, i.e.,

$$\sigma_y(\tau) = \frac{1}{\sqrt{\lambda\tau}}. \tag{7.60}$$

Thus the long-term frequency stability of a clock that utilizes radioactive emissions is indeed limited by the Poisson variation in the rate of emission.

## 7.6 An Aside: True Random Number Generators

### 7.6.1 Introduction

In the sections in this chapter so far, several important properties of the Poisson process were analyzed to both design and understand the limitations of RCCs. Since the Poisson process is a truly random process, it is natural to use this to generate random numbers.

One must distinguish between hardware and software random number generators (RNGs) and, among the algorithms, between deterministic and non-deterministic algorithms. Deterministic RNGs are usually called pseudo-random number generators (p-RNGs), and not appropriate for cryptographical applications, as they produce predictable output streams. Algorithms that produce nearly true random number are, on the other hand, cryptographic RNGs and are usually too slow for doing Monte Carlo simulations.

The Poisson process of radioactive decay events have three equivalent distributions, which are 1. the Poisson distribution of counts, 2. the exponential distribution of inter-arrival times, and 3. uniform distribution of arrival times. Any one or more of these three distributions can be used for the generation of truly random numbers. The following describe each of these properties and how they have be used in the past to generate truly random numbers and introduces two of our implementations to generate TRNs.

#### Poisson Distribution of Counts

In a given interval of time $\tau$, the total number of events that occur (counts) is Poisson distributed. This property was made use of by Vincent [54] and Gude [55] in the 1970s and 1980s. The time window $\tau$ should be chosen at least 10 times larger than the mean decay rate $\lambda$ of the radioactive substance to minimize the influence of autocorrelation and hence, minimize the error in the equal distribution. This method is therefore in random bit stream output rate (the number of random bits generated per decay event).

### Exponential Distribution of Inter-Arrival Times

The inter-arrival times between pulses are exponentially distributed. This has been illustrated in (7.43). Walker [56] made use of this property to generate random numbers by comparing two adjacent inter-arrival times. In this implementation, Krypton-85 with a half-life of 10.73 years was used to generate an output random bit stream at 200 bps. Alkassar et al. [57] improved over this implementation with the use of a constant time source to measure the inter-arrival time to generate one random bit per event. Using Americium-241, a data rate of 1,600 bps was reported in the work. In both of these implementations, inter-arrival times are compared to generate the random number – the properties of exponential distribution were not made use of fully.

In our first implementation called TRNG-E, we use the property of the exponential distribution of inter-arrival times to generate TRN (E stands for the use of exponential distribution of inter-arrival times). Since it is required for most applications to generate uniformly distributed random numbers, it is difficult to use exponential distribution directly to generate multi-bit random numbers. However, if a uniform distribution is available, multi-bit random numbers can be easily generated by using a comparator array. We obtain a uniform distributed random numbers for the exponential distributed random numbers using the transformation,

$$U = e^{-\lambda E}. \tag{7.61}$$

(1) where $U$ is uniform distribution, and $E$ is exponential distribution, $\lambda$ being the parameter of the exponential distribution. We make use of a hardware transformation to implement (7.61) using a RC circuit.

### Uniform Distribution of Arrival Times

The last property of a Poisson process that we will use to generate TRNs is the uniform distribution of arrival times. In any interval of time $[0, \tau]$, the unordered set of arrival times of events of a Poisson process is uniformly distributed. Figure 7.24 illustrates this property of a Poisson process. Since the average time interval between the pulses for a rate of $\lambda$ is $1/\lambda$, and we can only make

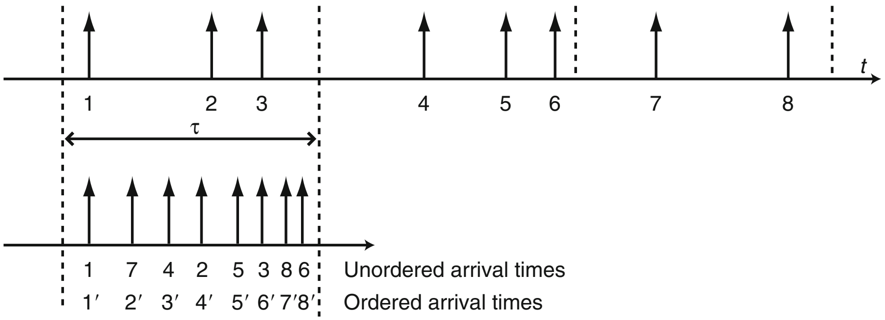

Figure 7.24: Illustration of the property that the set of unordered arrival times of events of a Poisson process is uniformly distributed

ordered measurements (for real-time TRNGs), one must design the TRNG such that $\tau < 1/\lambda$. This implementation uses the uniform distribution property of the Poisson process and is called TRNG-U.

### 7.6.2 True Random Number Generator TRNG-E

The implementation of TRNG-E can be done by use of a hardware transformation of the exponentially distributed inter-arrival times. This can be implemented by use of an RC circuit, as shown in Fig. 7.25.

The radioactive detector has a nominal output of 0 V and outputs a pulse of voltage $V_0$ every time it detects an event. The TRNG-E consists of an inverter which inverts the voltage levels (i.e., normally $V_0$ and outputs a pulse of 0 V when there is an event). This charges the capacitor $C$, through a resistor $R$. When there is a pulse, the capacitor $C$ discharges quickly through the diode and starts charging again till the next pulse occurs. The RC circuit shown creates the required exponential transformation as the capacitance charging is governed by the equation

$$V = V_0 e^{-t/RC}, \tag{7.62}$$

where $t$ is the exponential distributed inter-arrival time between two consecutive events. Combining (7.61) and (7.62), we arrive at a uniform distributed number by making the transformation

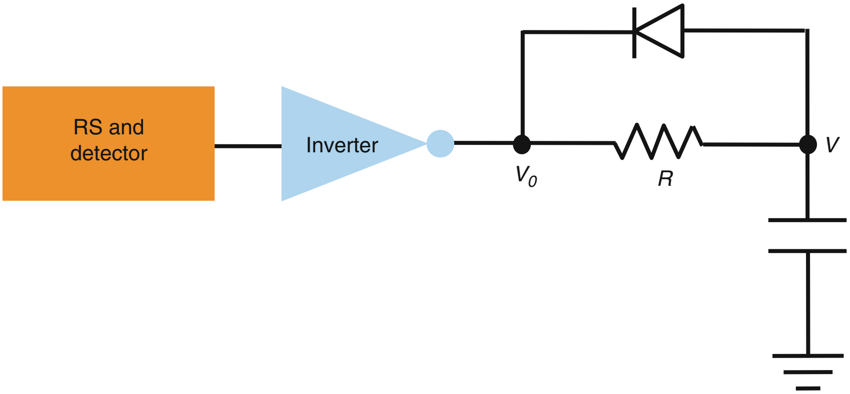

Figure 7.25: Schematic diagram showing the implementation of TRNG-E where the charging of a capacitor $C$ through a resistor $R$ implements the transformation in (7.61)

$$U = \left(1 - \frac{V}{V_0} e^{-\lambda RC}\right). \tag{7.63}$$

This transformation can be implemented using another hardware, or maybe altogether eliminated by choosing the values of $R$ and $C$ such that

$$\lambda RC = 1. \tag{7.64}$$

For example, if $\lambda = 10^6$, $R = 1$ k$\Omega$ and $C = 1$ nF, (7.64) is satisfied. In this case, since $1 - V/V_0$ is a uniform random number, $V/V_0$ is also a uniform random number. Thus V can be directly applied to the input of an $N$-bit analog-to-digital converter generate an $N$-bit uniform random number per radioactive pulse.

Figure 7.26 shows a histogram of binary numbers obtained from a TRNG-E with values $R = 1$ k$\Omega$, $C = 1$ nF, and $\lambda =$ 20,000 Hz. The binary numbers in the two ends (close to 0 and 1 are missing due to the measurement limitations and noises in the conversion process. For example, the binary number with values 0 correspond to time intervals of very small values. The presence of a dead-time $T_{dead} = 5\,\mu$s precludes the output of binary numbers with values corresponding to $t < 5\,\mu$s. In the case of large time-intervals, the exponential transformation corresponds to the charging of the capacitor, which asymptotically reaches the value of $V_0$. In this case, the resolution of time becomes limited by the noise in the value of $V$ across the capacitor.

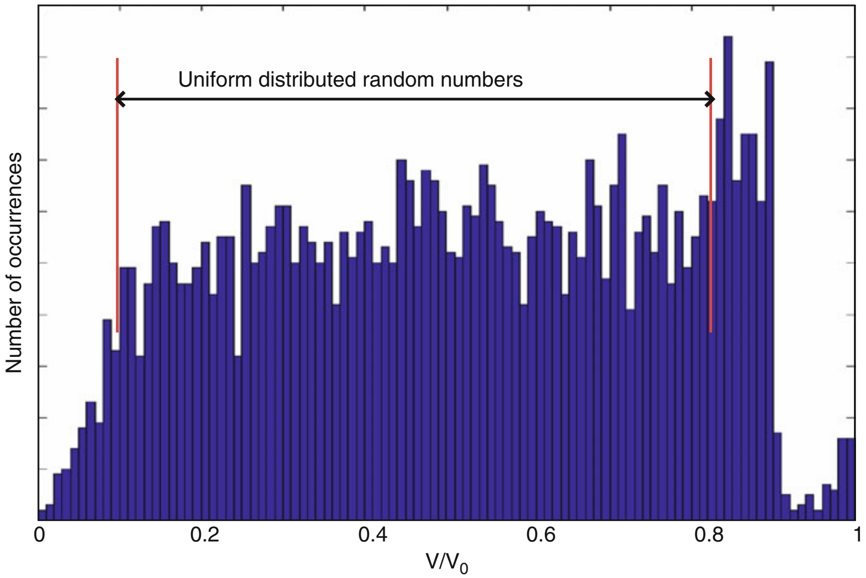

Figure 7.26: Histogram of binary numbers obtained using a TRNG-E with values $R = 1$ kΩ, $C = 1$ nF, and $\lambda = 20{,}000$ Hz. Here, the transformation in (7.64) was done in Matlab

The main limitation of this method is the need for the design of a hardware that implements (7.64). The values of $\lambda$ drifts for times comparable to the half-life of the radioisotope used and would result in a non-uniform random number output. The implementation of TRNG-U overcomes these limitations as the uniform TRNG is independent of the value of $\lambda$.

### 7.6.3 True Random Number Generator TRNG-U

The values of the arrival times of events of a radioactive process can be measured in units of clock cycles for a clock of frequency $f_c$. If we use a clock with $f_c \gg \lambda$, the ordered set of arrival times (as measured in real-time) would be uniformly distributed. Further, if the clock counts up an $N$-bit counter, the value of the counter at the instant of arrival of each event would represent a uniform $N$-bit random number. Using the detector used for our measurement, we can obtain a maximum output rate

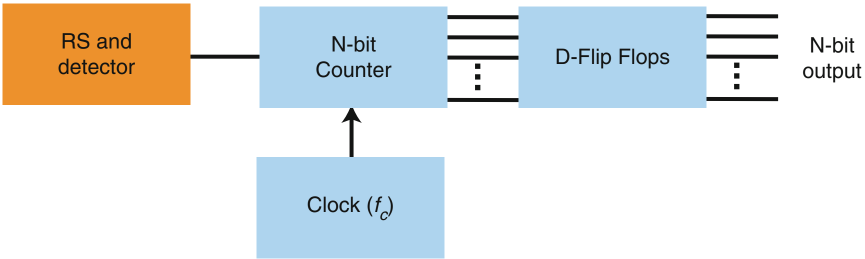

Figure 7.27: Schematic diagram showing the implementation of TRNG-U using an $N$-bit counter. The D-flip flops log the $N$-bit random number generated by the previous pulse until the next pulse arrives

of $1/T_{dead} = 1/5\,\mu\text{s} = 200\,\text{kHz}$. Thus to obtain uniform random numbers, the clock speed must satisfy the condition,

$$f_c \gg \frac{2^N}{T_{dead}} \tag{7.65}$$

The block diagram in Fig. 7.27 shows the implementation of a TRNG-U to generate a 3-bit random number. The data at the output of the D-flip flops are obtained using a 4-channel high-speed oscilloscope using Labview. Using this setup, one can only obtain a 3-bit output as the fourth channel is needed to record when a pulse occurs, as it is impossible to distinguish between two subsequent random numbers of the same value.

Figure 7.28 shows the histogram of a 3-bit TRNG-U implemented as described above. The histogram shows uniform distribution of 8 binary random numbers. The output rate in this case is 2 kHz or $2^3 \times 2 = 16$ kbps.

### 7.6.4 Conclusions and Future Directions

Two methods of generating truly random binary numbers for applications in cryptology were described and implemented. Both the methods are scalable in that they can each generate 1 $N$-bit random number per radioactive decay event. TRNG-E uses the exponential distribution of inter-arrival times to make to

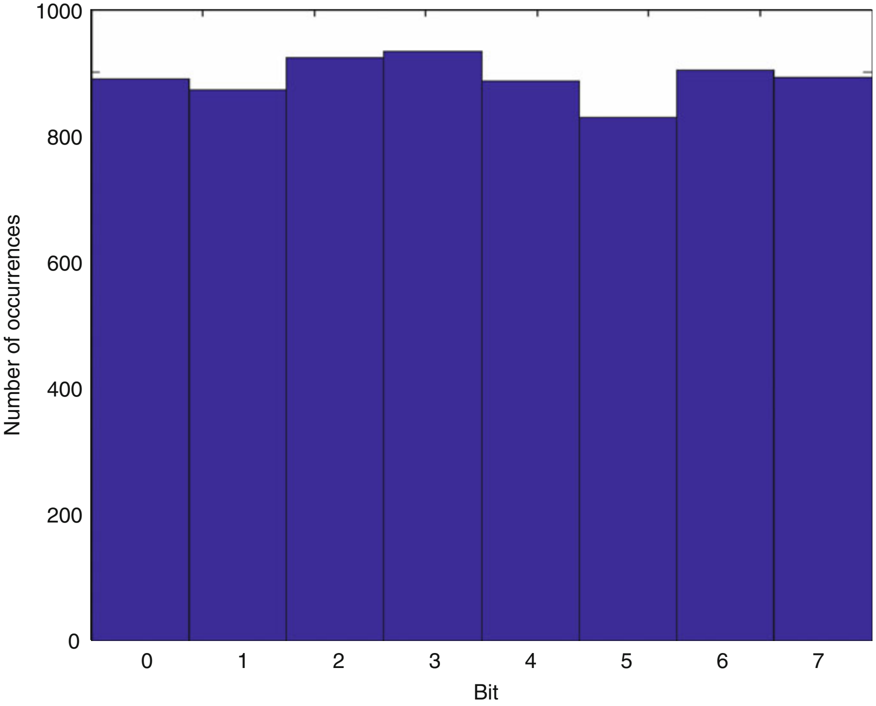

Figure 7.28: Histogram of 3-bit binary numbers obtained using a TRNG-U with a clock speed of 16 MHz

generated uniform random numbers using a hardware transformation. It suffers from the disadvantage that drift in the values of $\lambda$, $R$ or $C$ can cause the necessary equality in (7.64) to be invalid and hence would suffer from aging (long-term variations in these values). TRNG-U, on the other hand is independent of these values and directly generates the $N$-bit random numbers. We have demonstrated a 3-bit TRNG-U due to limitations in the measurement setup.

Future work in this regard should focus on implementing a single-chip version of the above bread-board implementation. Such a chip would consume very low power ($\sim$mW) and would be potentially useful for data encryption in secure communication applications.

## 7.7 Conclusions

This chapter successfully demonstrated the use of stable radioactive beta emissions from $\mathrm{Ni}^{63}$ radioisotope to produce a long-term stable frequency source. The rate of emissions was locked to a local oscillator with a (relatively) good short-term stability in a control loop realizes a short-term and a long-term stable clock – the short-term stability limited by the LO and the long-term stability limited by the Poisson noise in the radioactive source.

This approach of generating a frequency addresses the power-stability tradeoff inherent to frequency references in that the physics package (the radioactive source) consists of the radioactive source and consumes very little power. The current implementation of the RCCs are limited by the drift in the threshold of the beta detector, which after drift-correction shows excellent agreement with the theoretical model and simulation results of the counting clock.

## 7.8 Future Directions

The limit to the long-term stability of the RCCs currently are two-fold – drift in detector amplifier and high power consumption in loop electronics. Future work in the direction of the design of an amplifier with very small values of drift is required. It is supposed that the drift in the detector amplifier is mainly in the drift in the threshold (i.e., the minimum energy level of a beta particle that is required to register). The design of amplifiers using band-gap reference provides a solution to this problem to a first order. For a given temperature, the band gap reference gives an absolute energy (voltage) reference on-chip and hence can output a stable rate of emissions.

It is also necessary to design a detector with a small response time (currently 5 μs for the detector in the evaluation board). Design of such high speed amplifiers with low power consumption would be possible by monolithic CMOS integration of the detector with the loop electronics. For example with a detector speed of 100 MHz, one can use generate stable frequency references with $\lambda \simeq 10^6$, while potentially consuming only a few mW of power for the entire clock with frequency stabilities of better than 1 ppm for week-to-month-long operations.

# Appendix A
# Thin Film $^3$H Actuated Reciprocating Piezoelectric Unimorph Converters

PZT-silicon unimorph cantilevers with dimensions of $l_{cant} = 10\,\mathrm{mm}$, $l_{piezo} = 2.5\,\mathrm{mm}$, $w_{cant} = w_{piezo} = 2\,\mathrm{mm}$, $t_{cant} = 22.5\,\mu\mathrm{m}$ and $t_{piezo} = 1\,\mu\mathrm{m}$ were tested with a $2\,\mathrm{cm} \times 1\,\mathrm{cm}$ tritiated scandium film (developed by Professor Kevin Chen at University of Pittsburgh) for power generation characteristics. The PZT unimorph cantilever fundamental resonance frequency $f_{res,uni}$ was measured to be 38 Hz, and from the measured piezoelectric film capacitance $C_{uni}$ of 46 nF, $R_{l,uni,opt}$ was calculated to be $90\,\mathrm{k\Omega}$. The $^3$H thin film source was then calibrated by measuring the net current output $I_r$ of the radioisotope source in moderate vacuum to be 135 pA, indicating a radioisotope activity of 23 millicurie, and a thermal power output $P_{out,{}^3\mathrm{H}}$ of 715 nW (3.25).

REMPG power generation was then characterized for the PZT unimorph cantilevers by assembling them with radioisotope thin film sources inside a test vacuum chamber with a glass view port (Fig. 3.11). Both the piezoelectric unimorph cantilever and the radioisotope source were mounted on linear motion feedthroughs to characterize the REMPG at different values of $g_0$. The glass view port served to monitor the motion of the unimorph cantilever tip through a microscope connected to a CCD camera. The radioisotope source was positioned at an initial gap $g_0$ from the tip of the unimorph cantilever, and the vacuum chamber was pumped down to minimize charge leakages in the air-gap due to build-up of high voltages. The unimorph cantilever tip position was monitored optically through the charge-discharge-oscillation cycle, and $V_{out,uni}$ was recorded at the end of every reciprocation cycle to further extract the unimorph peak power output $P_{out,uni,max}$, $E_{out,uni}$ and $\eta_{rempg}$. The reciprocation cycle was timed by calculating the interval between two consecutive

$V_{out,uni}$ pulses. This was done for various values of $g_0$, until $g_0$ was too large for the unimorph cantilever to pull-in into the radioisotope and completely discharge.

## A.1 $^3$H Actuation

The PZT unimorph cantilevers were initially tested at 9 µtorr, realized after 2 h of pumping of the vacuum chamber. The reciprocation period $T_{rec}$ was measured to be 8 s and 30 s at 75 µm and 125 µm gaps respectively (Fig. A.1), and the maximum $g_0$ at which the unimorph reciprocated was 125 µm. Subsequently, the unimorph cantilevers were tested again at 1 µtorr, realized after pumping the vacuum chamber overnight. The lower pressure is necessary to minimize charge leakages in the air-gap that reduce energy conversion efficiency. The reciprocation period $T_{rec}$ was measured to increase to 15 s and 50 s at 75 µm and 125 µm gaps respectively (Fig. A.1). This was attributed to the drop in $I_r$ caused by effusion of $^3$H from the scandium films at low pressures. The difference in the measured values of $T_{rec}$ at 9 µtorr and 1 µtorr

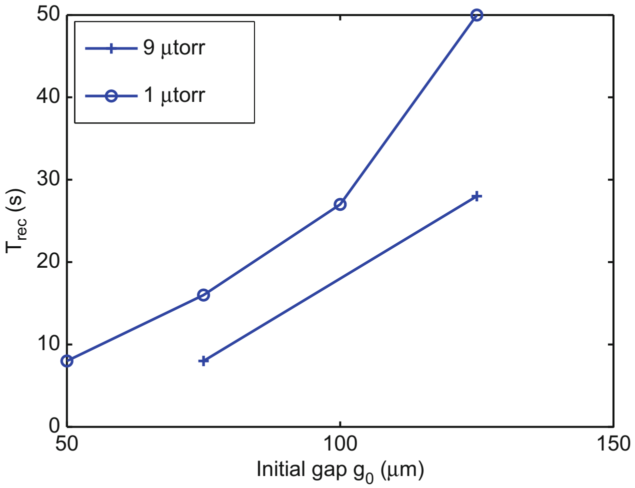

Figure A.1: Plot of measured increase in $^3$H actuated piezoelectric unimorph reciprocation period $T_{rec}$ with initial gap $g_0$ at two different pressures. The REMPG does not reciprocate for $g_0 > 125$ µm suggests a $I_r$ decrease of 40%. Unfortunately, this could not be verified by a measurement of $I_r$ after testing the REMPG. Once the vacuum chamber was opened after REMPG testing, a swab test showed that it was too contaminated to be safe for further testing.

## A.2 Power Generation Characteristics

Figures A.2(a) and A.2(b) plot the measured $V_{out,uni}$ at $g_0 = 75\,\mu\text{m}$ and $g_0 = 125\,\mu\text{m}$ respectively. The high specific activity of the $^3$H thin films results in very short reciprocation periods, which in turn leads to an almost continuous power output from the REMPG. The REMPG energy conversion efficiency $\eta_{rempg}$ was then calculated from the measured values of $T_{rec}$ and $V_{out,uni}$ to be 0.29% and 0.52% at $g_0 = 75\,\mu\text{m}$ and $g_0 = 125\,\mu\text{m}$ respectively. The measured values of $\eta_{rempg}$ were low because of the low values of $g_0$ at which the piezoelectric unimorph could reciprocate, which in turn led to low $\eta_{re-eme}$. In comparison, the same unimorph cantilever when actuated with 3 millicurie $^{63}$Ni source reciprocated even at $g_0 = 1.5\,\text{mm}$. The lower values of $g_0$ at which the $^3$H powered REMPGs could reciprocate can be attributed to the lower $E_{rad,avg}$ of $^3$H (5.7 keV) compared to $^{63}$Ni (17.3 keV), which in turn lowers the values of $V_{gap}$ that $^3$H can sustain.

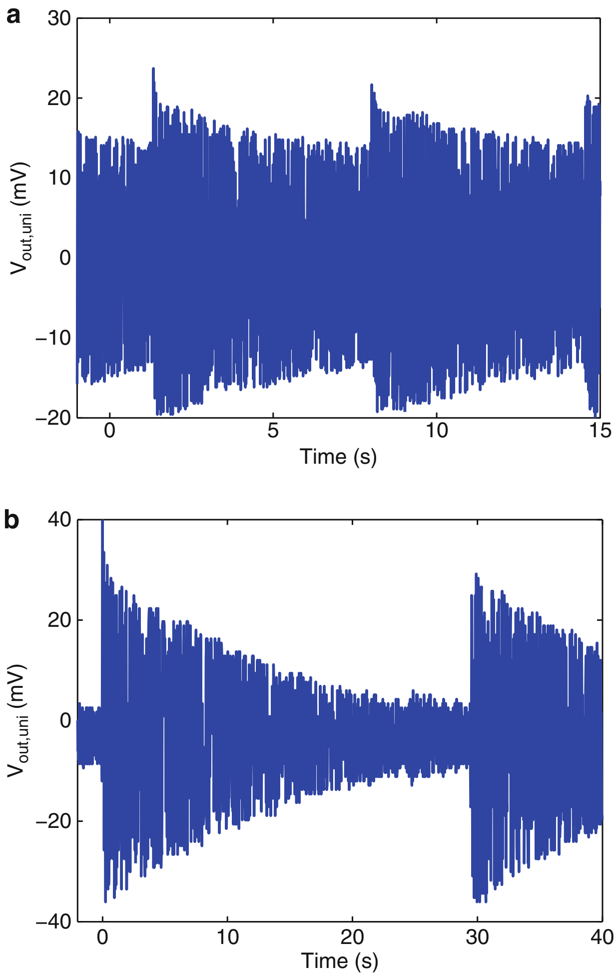

Figure A.2: Plot of measured $^3$H powered PZT REMPG piezoelectric unimorph voltage output $V_{out,uni}$ across $R_{l,uni,opt} = 90\,\mathrm{k\Omega}$ for (**a**) $g_0 = 70\,\mu\mathrm{m}$ and (**b**) $g_0 = 125\,\mu\mathrm{m}$ at 9 µtorr. The peak power outputs $P_{out,uni,max}$ for the two values of $g_0$ are 5.5 nW and 10 nW respectively

# Appendix B
# Macro-scale Hand Assembled Radioisotope actuated Electro-Mechanical Power Generator

## B.1 Assembly

The piezoelectric unimorph beam (Fig. B.1) was fabricated by epoxy bonding a laser cut 1.5 cm × 2.7 cm × 125 μm PZT-5H (lead-zirconate-titanate ceramic from Piezo Systems Inc.) sheet to the base of a laser cut 5 cm × 2.5 cm × 125 μm copper beam. A 4 cm × 8.5 mm × 125 μm copper sheet adhesively bonded to the tip of the copper beam served as the collector. The piezoelectric unimorph was then clamped between two ceramic plates for cantilever anchoring and electrical insulation.

The $^{63}$Ni radioisotope source comprised of four 1 cm × 1 cm× 100 μm nickel foils. Each nickel foil was electro-less coated with 3 milliCurie/cm$^2$ of $^{63}$Ni radioisotope (Isotope Products Laboratory, Los Angeles). The four $^{63}$Ni foils were also clamped between ceramic plates for anchoring and electrical isolation.

## B.2 Testing

The piezoelectric beam was first characterized for stiffness and resonant frequency. The stiffness of the unimorph cantilever $k_{uni}$ was measured by deflecting the beam tip by a known distance and measuring the generated blocking force using a force meter mounted on a micropositioner (Sutter Instruments Co., Model MP-285). The stiffness was calculated to be 24.6 N/m, which agreed well with the theoretical value of 25.2 N/m calculated using beam bending theory. The fundamental resonance frequency was measured by applying a mechanical impulse excitation to the tip

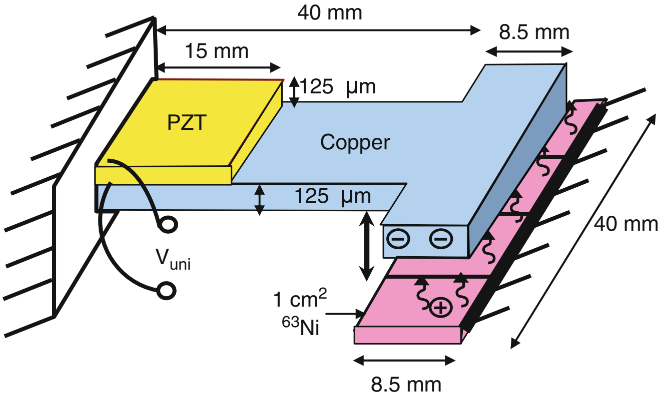

Figure B.1: Schematic illustrating the macro hand-assembled REMPG construction

and monitoring the ensuing natural vibrations via the piezoelectric leads. The resonant frequency was measured to be 32.4 Hz, which agreed well with the design value of 32.9 Hz calculated using the stiffness of the unimorph cantilever and mass loading of the betavoltaic at the tip. Subsequently, the radioisotope activity was characterized by measuring the net current output $I_r$ of the radioisotope source in vacuum to be 62.1 pA, indicating a $^{63}$Ni radioisotope activity of 10.54 millicurie and a power output $P_{out,^{63}\mathrm{Ni}}$ of 1.07 µW. The measured activity is 15% less than the expected activity because of the $\beta$-electron losses due to clamping.

REMPG power generation was then characterized by mounting the REMPG and the $^{63}$Ni source assembly on separate linear motion feedthrough stages inside a test vacuum chamber. The motion feedthroughs served to characterize the REMPG output at different initial gaps between the radioisotope sources and the betavoltaic collector. The vacuum chamber was pumped down to ≈1 µtorr to minimize charge leakages in the air-gap due to build-up of high voltages. The chamber was designed to have a glass view port on the top. A microscope connected to a CCD camera outside the chamber was used to monitor the motion of the unimorph cantilever tip. The radioisotope source was positioned at an initial gap $g_0$ from the collector at the tip of the unimorph cantilever, and $V_{out,uni}$ was monitored through the charge-discharge-oscillation cycle. $V_{out,uni}$ at the end of every reciprocation cycle

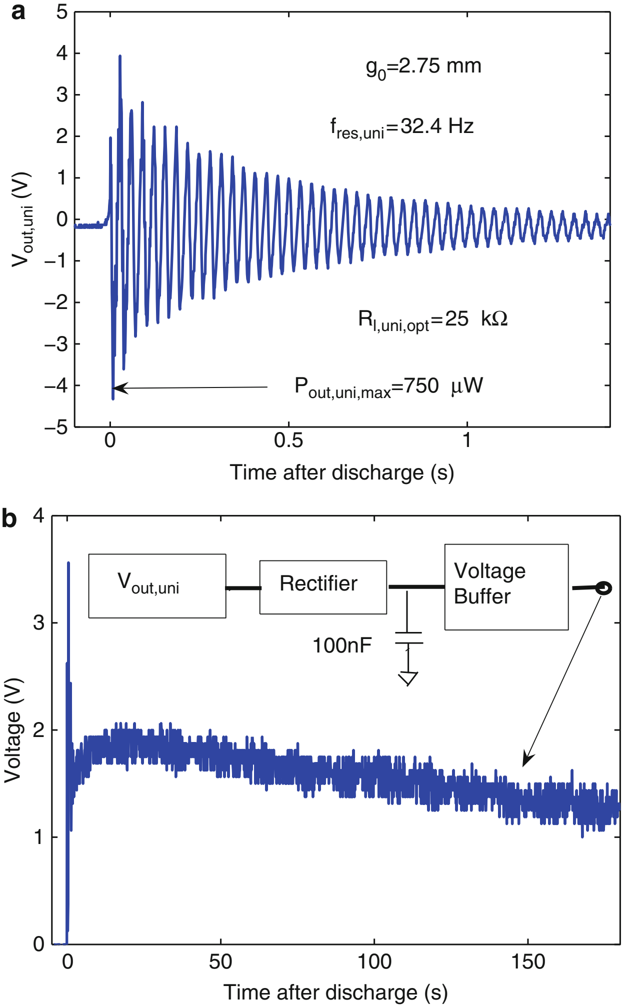

Figure B.2: Measured macro-scale hand assembled REMPG (**a**) unimorph output voltage $V_{out,uni}$ across a resistive load, reflecting the exponentially decaying sinusoidal nature of unimorph vibration after discharge, and (**b**) voltage of a storage capacitor charged by the rectified $V_{out,uni}$. The bridge rectifier employed commercial off-the-shelf silicon p–n diodes was recorded to further extract the unimorph peak power output $P_{out,uni,max}$, $E_{out,uni}$ and $\eta_{uni}$. The reciprocation cycle was timed by calculating the interval between two consecutive $V_{out,uni}$ pulses. This was done for various values of $g_0$, from 0.25 mm to 3.5 mm in increments of 0.5 mm, until $g_0$ was too large for the unimorph cantilever to pull-in into the radioisotope and completely discharge. The piezoelectric unimorph was found to reciprocate for initial gaps as high as 2.75 mm, and generate a maximum $P_{out,uni,max}$ of 750 µW (Fig. B.2(a)) across an optimal load impedance $R_{l,uni,opt}$ of 25 kΩ. The rectified voltage output of the REMPG was also demonstrated to charge up a storage capacitor to 2 V (Fig. B.2(b)).

Furthermore, $T_{rec}$ was measured to increase linearly and $P_{out,uni,max}$ was measured to increase quadratically (Fig. B.3) with $g_0$. Additionally, $\eta_{uni}$ was found to increase with $g_0$ (Fig. B.4(a)). This is primarily due to the increase in $\eta_{re-eme}$ (Fig. B.4(b)), which rises due to increasing $V_{Gap,avg}$ at larger values of $g_0$. Higher values of $V_{Gap,avg}$ lead to a larger portion of the $\beta$-particle kinetic energy getting converted into electromechanical energy. In contrast, $\eta_{me-e}$ remains fairly independent of $g_0$ (Fig. B.4(b)), until elastic non-linearity due to larger tip displacements starts

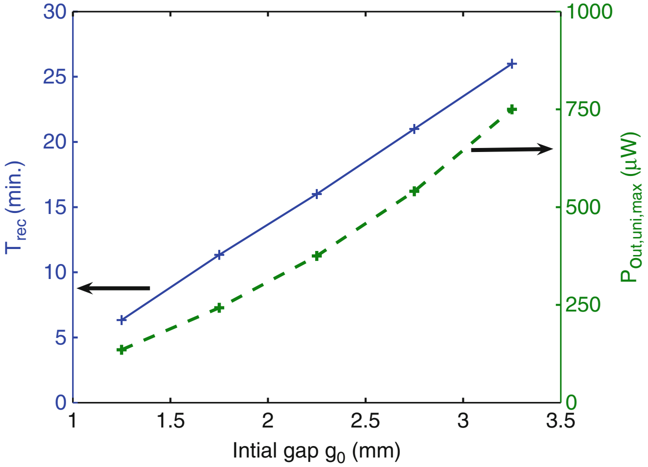

Figure B.3: Plots of measured macro-scale hand assembled piezoelectric unimorph reciprocation period $T_{rec}$ and peak power output $P_{out,uni,max}$ as a function of $g_0$

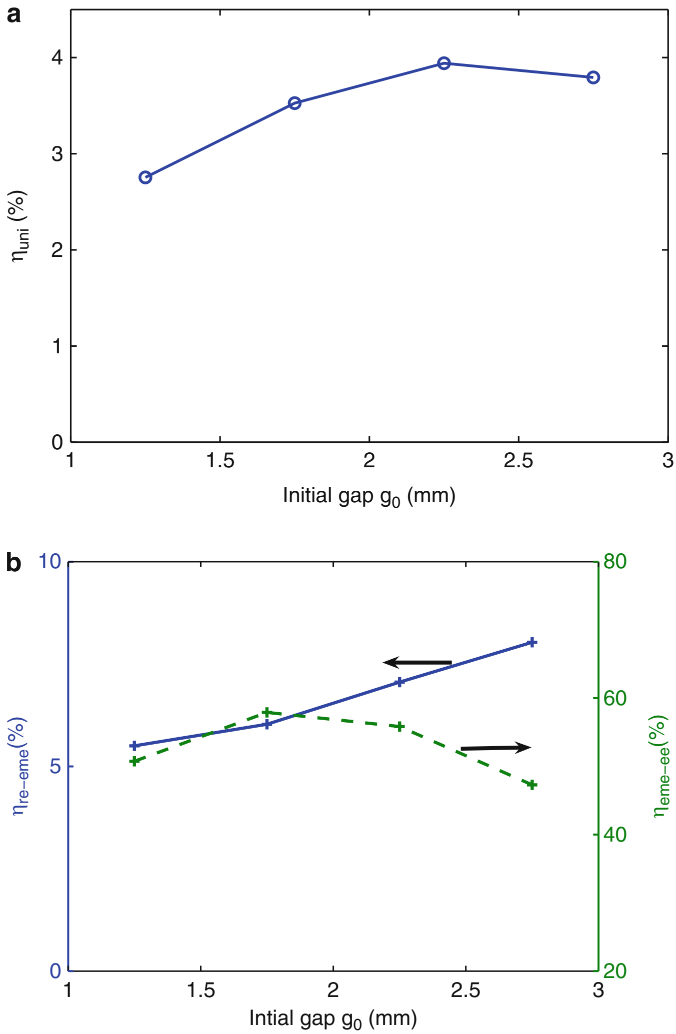

Figure B.4: Plots of measured macro-scale hand assembled REMPG (**a**) energy conversion efficiency $\eta_{uni}$, and (**b**) $\eta_{re-eme}$ and $\eta_{eme-ee}$ as a function of $g_0$

dominating, and reduces $\eta_{uni}$ for $g_0$ >2.25 mm. This is because $\eta_{me-e}$ depends solely on the mechanical losses in the unimorph cantilever system.

# Appendix C
# Modeling of Radioisotope Actuated Piezoelectric Unimorph Cantilever Dynamics Using Simulink

The non linear state equations describing the radioisotope actuation of piezoelectric unimorph cantilevers can be numerically integrated using a block-diagram model in the Simulink environment of MATLAB to predict the actuation dynamics for various geometries. The block diagram model (Fig. C.1) is developed from the three state equations describing the radioisotope actuation of piezoelectric unimorph cantilevers (3.6, 3.7, 3.11):

$$\frac{\partial Q_{gap}}{\partial t} = I_r - \frac{1}{R_{l,gap}} \frac{Q_{gap}}{(C_{gap} + C_p)} \tag{C.1}$$

$$\frac{\partial g}{\partial t} = v \tag{C.2}$$

$$\frac{\partial v}{\partial t} = -\frac{1}{m} \left( bv + k(g_0 - g) + \frac{\partial}{\partial g} \left( \frac{Q^2}{2\,(C_{gap} + C_p)} \right) \right) \tag{C.3}$$

The model has three integrators for integrating: (a) the current output of the radioisotope thin film source to calculate the accumulated charge on the radioisotope thin film source $Q_{gap}$; (b) the cantilever tip velocity $v$ to calculate the gap $g$ between the radioisotope source and the piezoelectric cantilever; and (c) the cantilever tip acceleration to calculate cantilever tip velocity $v$. Initial conditions of $Q_{gap} = 0$, $g = g_0$, and $v = 0$ are supplied to the integrators. The position integration is done using a saturation integrator to impose $2g_0 > g > g_{min} = g_0/100$. The limit of $g > g_{min}$ is necessary to avoid a singularity in the system when $g \to 0$. The velocity and charge integrators have reset inputs to model the pull-down and discharge of the cantilever respectively.

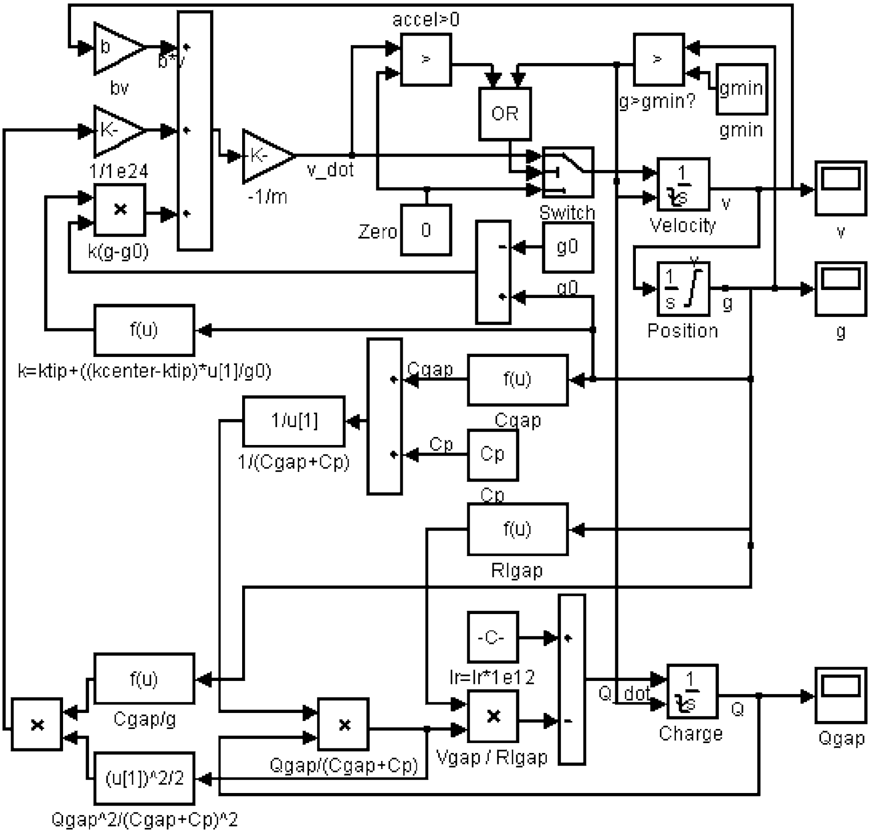

Figure C.1: Schematic of the Simulink block-diagram model of the REMPG

The reset input, driven by a comparator that compares $g$ with $g_{min}$, drives the output of the velocity integrator and charge integrator to zero when $g \leq g_{min}$. The release event is modeled by testing for the sign of the net force on the cantilever, which turns negative with the disappearance of the electrostatic force upon discharge, and enabling the input to the velocity integrator, so the cantilever can move upward. The inputs to the integrators are derived from the various REMPG geometrical and material property parameters defined using a MATLAB file. It is important to define the parameters so that the coefficients of the state variables in the state equations are all normalized to be of the same order of magnitude. In the model used in this dissertation, currents and charges were multiplied by $10^{12}$ for normalizing the coefficients of the state variables.

## C.1 MATLAB Input File for Defining Rempg Geometrical and Material Property Parameters

```
% Definition of constants for the modeling
% radioisotope actuation of piezoelectric unimorph
% cantilevers
% Universal constants
epsi0   =   8.85e-12;   % Permittivity of vacuum
% Silicon material properties
ESi     =   170e9;      % Youngs modulus of silicon
DensSi  =   2330;       % Density of silicon
% Piezoelectric unimorph cantilever dimensions
lcant   =   10e-3;
wcant   =   2e-3;
tcant   =   42.5e-6;
% Piezoelectric unimorph cantilever collector
% dimensions
lcoll   =   5e-3;
wcoll   =   5e-3;
tcoll   =   42.5e-6;
% Air gap parameters
g0      =   1.067e-3;   % Initial gap
gmin    =   g0/100;     % Minimum allowable g
rho     =   2.5e13;     % Resistivity of vacuum that
                        % results in simulated Trec
                        % agreeing with measured Trec
Cp      =   1.32e-12;   % Parasitic capacitance
                        % between radioisotope source
                        % and vacuum chamber that
                        % results in simulated Trec
                        % agreeing with measured Trec
b       =  2.4663e-005; % Damping constant of the
                        % system
% Radiation parameters
Ir      =  8.6e-12*1.7; % Radioisotope output current
                        % density 8.6 pA/cm^2 times
                        % exposed radioisotope source
                        % 1.7 cm^2. 0.3 cm^2 is lost
                        % due to clamping
```

```
% Stiffness of the piezoelectric cantilever
ktip    =   6.76;       % ANSYS simulated cantilever
                        % stiffness when equivalent
                        % point electrostatic force
                        % acts at the tip of
                        % cantilever
kcenter =   10.3;       % ANSYS simulated cantilever
                        % stiffness when equivalent
                        % point electrostatic force
                        % acts in the center
                        % of cantilever
```

# Appendix D
# MatLab Codes for Counting clock

## D.1 Simple Counting Clock

```
TI=-log(rand(N,1))/lambda;
AT=zeros(size(TI));
AT(1)=rand*TI(1);   % The counter starts randomly
                    % between two pulses
                    % (equilibrium process)
for i=2:N,
   AT(i)=AT(i-1)+TI(i);
end
while max(AT)<=Tau,     %In case N is not enough
   TIextend=-log(rand)/lambda;
   ATextend=max(AT)+TIextend;
   TI=[TI;TIextend];
   AT=[AT;ATextend];
end
i=1;                    % This will give AT(max)
                        % just > Tau
while AT(i)<=Tau,
    i=i+1;
end
AT=AT([1:i]);
i=i-1;      %i is the number of pulses in time Tau
```

## D.2 SR Codes

```
if Tdead > 0, %------------If Tdead is used,
              % do this-------
   registered=false; % This finds out the
                     % first pulse that is registered
                     % after Tdead
```

```
variation=(1+p*randn/100);
drift=1+pd*time;
Tdeadnow=Tdead*variation*drift;
i=0;
while registered==false,
    i=i+1;
    if AT(i)>Tdeadnow,
        registered=true;
    else
        deltaT=Tdeadnow-AT(i);
        probregistered=exp(-lambdadead*deltaT);
        if rand < probregistered,
            registered=true;
        end
    end
end
j=1;                      % this records counts
                          % for Tdead
ATdead=zeros(size(AT));   % for sake of memory
                          % allocation
TIdead=zeros(size(ATdead));
ATdead(j)=AT(i); %This is the first registered
                 %pulse for DT-D process
Tnow=AT(i);
dTnow=0;
drift=1+pd*(time+AT(i));
variation=(1+p*randn/100);
Tdeadnow=Tdead*variation*drift;
while Tnow<=Tau,
    dTnow=dTnow+TI(i+1);
    if dTnow>=Tdeadnow,
        ATdead(j+1)=ATdead(j)+dTnow;
        TIdead(j+1)=dTnow;
        j=j+1;
        dTnow=0;
        drift=1+pd*(time+AT(i));
        variation=(1+p*randn/100);
```

```
          Tdeadnow=Tdead*variation*drift;
      end
      i=i+1;
      Tnow=AT(i+1);
   end
   ATdead=[ATdead([1:j]);AT(length(AT))]; % is the
                                          % counts
                                          % from RS
   TIdead=[TIdead([1:j]);TI(length(TI))]; % j is the
                                          % counts
                                          % with
                                          % Tdead
else    %------------If Tdead is NOT used, do this---
   ATdead=AT;
   TIdead=TI;
   j=i;        %counts dead = counts Poisson
end     %------------End Tdead used/not used
        % if statement-------
```

# BIBLIOGRAPHY

[1] W. R. Corliss and D. G. Harvey, *Radioisotopic Power Generation.* Prentice- Hall, Englewood Cliffs, New Jersey, 1964.

[2] K. E. Bower, Y. A. Barbanel, Y. G. Shreter, and G. W. Bohnert, *Polymers, Phosphors, and Voltaics for Radioisotope Microbatteries.* CRC Press, 2002.

[3] H. Cember, *Introduction to Health Physics.* Pergamon Press, New York, 1983.

[4] S. Littleflower, B. Babu, R. Mukherjee, and B. Baliga, "Inner bremsstrahlung from $^{63}ni$," *Journal of Physics G (Nuclear and Particle Physics)*, vol. 16, no. 12, pp. 1873–1879, 1990.

[5] G. Harder, *Pocket Guide for Radiological Management.* Perma-Fix Environmental Services, 1999.

[6] B. Bowerman and C. Czajkowski, "Determination of the chemical form of tritium in self-luminous signs," Nuclear Regulatory Commission, Washington, DC (USA), and Brookhaven National Laboratory, Upton, NY (USA), Tech. Rep., 1990.

[7] W. Sun, "A three-dimensional porous silicon p-n diode for betavoltaics and photovoltaics," *Advanced Materials*, vol. 17, no. 10, pp. 1230–1233, May 2005.

[8] M. Kalinowski and L. Colschen, "International control of tritium to prevent horizontal proliferation and to foster nuclear disarmament," *Science and Global Security*, vol. 5, no. 2, p. 138, 1995.

[9] S. Shyamala, G. Udhayakumar, and A. Dash, "Preparation of $^{63}ni$ electrodeposited special custom-made sources," *BARC Newsletter*, no. 273, pp. 274–277, 2006.

[10] D. F. Williams, G. D. O'Kelley, J. B. Knauer, and J. T. Wiggins, "Recovery and purification of nickel-63 from hfir-irradiated targets," Oak Ridge National Laboratories, Tech. Rep., 1993.

[11] L. Olsen, "Beta voltaic energy conversion," *Energy Conversion*, vol. 13, no. 4, pp. 117–127, 1973.

[12] F. F. Knapp, R. A. Boll, and S. Mirzadeh, "Reactor production and purification of promethium-147," U.S. Patent US2008/0060998, Mar 13, 2008.

[13] R. Szewczyk, E. Osterweil, J. Polastre, M. Hamilton, A. Mainwaring, and D. Estrin, "Habitat monitoring with sensor networks," *Communications of the ACM*, vol. 47, no. 6, pp. 34–40, 2004.

[14] K. Martinez, J. Hart, and R. Ong, "Environmental sensor networks," *Computer*, vol. 37, no. 8, pp. 50–56, 2004.

[15] J. Lynch and K. Loh, "A summary review of wireless sensors and sensor networks for structural health monitoring," *Shock and Vibration Digest*, vol. 38, no. 2, pp. 91–128, 2006.

[16] G. Bloom, K. Murphy, and T. Cox, "An isotope-powered, indwelling intracranial pressure sensor," *Transactions of the American Nuclear Society*, vol. 13, no. 2, pp. 509–510, 1970.

[17] S. Roundy, D. Steingart, L. Frechette, P. Wright, and J. Rabaey, "Power sources for wireless sensor networks," in *First European Workshop on Wireless Sensor Networks, EWSN 2004.*, Berlin, Germany, pp. 1–17, 2004.

[18] D. Linden and T. B. Reddy, *Handbook of Batteries*. McGraw-Hill, 2002.

[19] I. E. T. Services and S. A. I. Corporation, *Fuel Cell Handbook*. U.S. Dept. of Energy, National Energy Technology Laboratory, 2002.

[20] H. G. H. Moseley, "The attainment of high potentials by the use of radium," *Proceedings of Royal Society A*, vol. 88, p. 471, 1913.

[21] P. E. Ohmart, "A method of producing an electric current from radioactivity," *Journal of Appllied Physics*, vol. 22, p. 1505, 1973.

[22] A. Thomas, "Nuclear batteries: Types and possible uses," *Nucleonics*, vol. 13, pp. 129–133, 1955.

[23] H. Guo and A. Lal, "Nanopower betavoltaic microbatteries," in *IEEE TRANSDUCERS 2003*, vol. 1, Boston, MA, USA, 2003, pp. 36–39.

[24] A. Lal, R. Duggirala, and H. Li, "Pervasive power: a radioisotope-powered piezoelectric generator," *IEEE Pervasive Computing*, vol. 4, no. 1, pp. 53–61, 2005.

[25] H. Li, A. Lal, J. Blanchard, and D. Henderson, "Self-reciprocating radioisotope-powered cantilever," *Journal of Applied Physics*, vol. 92, no. 2, pp. 1122–1127, 2002.

[26] H. Li, "Radioisotope-powered self-reciprocating cantilever for micro power generation," Ph.D. dissertation, Cornell University, 2005.

[27] H. Li and A. Lal, "Radioactively powered pressure transducer with rf pulse output," in *IEEE TRANSDUCERS 2003*, vol. 1, Boston, MA, USA, 2003, pp. 53–56.

[28] H. Flicker, J. Loferski, and T. Elleman, "Construction of a promethium-147 atomic battery," *IEEE Transactions on Electron Devices*, vol. ED-11, no. 1, pp. 2–8, 1964.

[29] J. Clarkson, W. Sun, K. Hirschman, L. Gadeken, and P. Fauchet, "Betavoltaic and photovoltaic energy conversion in three-dimensional macroporous silicon diodes," *Physica Status Solidi A*, vol. 204, no. 5, pp. 1536–1540, 2007.

[30] S. Tin, R. Duggirala, A. Lal, and C. Pollock, "Radioisotope-powered impulse radio frequency sensor node," in *Solid State Sensor and Actuator Workshop*, Hilton Head Island, SC, USA, 2008, pp. 336–339.

[31] S. D. Senturia, *Microsystem design.* Kluwer Academic Publishers, Boston, 2001.

[32] T. Sakurai and K. Tamaru, "Simple formulas for two- and three-dimensional capacitances," *IEEE Transactions on Electron Devices*, vol. ED-30, no. 2, pp. 183–185, 1983.

[33] J. Seeger and B. Boser, "Charge control of parallel-plate, electrostatic actuators and the tip-in instability," *Journal of Microelectromechanical Systems*, vol. 12, no. 5, pp. 656–671, 2003.

[34] F. Lu, H. Lee, and S. Lim, "Modeling and analysis of micro piezoelectric power generators for micro-electromechanical-systems applications," *Smart Materials and Structures*, vol. 13, no. 1, pp. 57–63, 2004.

[35] I. C. on Radiation Units and Measurements, *Stopping Powers for Electrons and Positrons.* Library of Congress Cataloging in Publication Data, 1984.

[36] M.-A. Dubois and P. Muralt, "Measurement of the effective transverse piezoelectric coefficient $e_{31,f}$ of aln and $pbzr_xti_{1-x}o_3$ thin films," *Sensors and Actuators A (Physical)*, vol. A77, no. 2, pp. 106–112, 1999.

[37] A. Kadish and W. B. Maier II., "Electromagnetic radiation from abrupt current changes in electrical discharges," *Applied Physics Letters*, vol. 70, no. 11, pp. 6700–6701, 1991.

[38] R. F. Pierret, *Semiconductor Device Fundamentals.* Addison Wesley, 1996.

[39] C. A. Klein, "Bandgap dependence and related features of radiation ionization energies in semiconductors," *Journal of Applied Physics*, vol. 39, no. 4, pp. 2029–2038, 1968.

[40] S. M. Sze, *Physics of Semiconductor Devices.* Wiley, 1981.

[41] M. A. Green, *High Efficiency Silicon Solar Cells.* Trans Tech Publications, 1990.

[42] S. Tin, R. Duggirala, R. Polcawich, M. Dubey, and A. Lal, "Self-powered discharge-based wireless transmitter," in *IEEE MEMS 2008*, Tucson, AZ, USA, pp. 988–991, January 2008.

[43] J. Kitching, S. Knappe, L. A. Liew, P. Schwindt, V. Shah, J. Moreland, and L. Hollberg, "Microfabricated atomic clocks," in *IEEE Micro Electro Mechanical Systems (MEMS'05)*, pp. 1–6, Jan. 2005.

[44] R. Boscaino, G. Concas, M. Lissia, and S. Serci, "Fluctuations in radioactive decays. i. nonequilibrium effects and noise," *Physical Review E*, vol. 49, no. 1, pp. 333–340, 1994.

[45] S. Radhakrishnan and A. Lal, "Radioactive counting clocks," in *IEEE Frequency Control Symposium '06*, July 2006.

[46] S. R. Stein, "Frequency and time - their measurement and characterization," in *Precision Frequency Control*, E. A. Gerber and A. Ballato, Eds. New York, NY: Academic Press, 1985, ch. 12, pp. 191–416.

[47] C. Audoin and J. Vanier, "Atomic frequency standards and clocks," *Journal of Physics E: Scientific Instruments*, vol. 9, no. 9, pp. 697–720, 1976. [Online]. Available: http://stacks.iop.org/0022-3735/9/697

[48] J. Kitching, S. Knappe, L. A. Liew, P. Schwindt, V. Shah, J. Moreland, and L. Hollberg, "Microfabricated atomic clocks," in *IEEE Micro Electro Mechanical Systems (MEMS'05)*, pp. 1–6, Jan. 2005.

[49] J. W. Muller, "Dead-time problems," *Nuclear Instruments and Methods in Physics Research Section A*, vol. 112, no. 1-2, pp. 47–57, Sept. 1991.

[50] G. Vannucci and M. C. Teich, "Effects of rate variation on the counting statistics of dead-time-modified poisson processes," *Optics Communications*, vol. 25, no. 2, pp. 267–272, May 1978.

[51] J. W. Muller, "Generalized dead times," *Nuclear Instruments and Methods in Physics Research Section A*, vol. A301, no. 3, pp. 543–551, Mar. 1991.

[52] M. Muselli, "Frequency analysis of binary oscillators triggered by a random noise," *Physica D: Nonlinear Phenomena*, vol. 188, pp. 119–133, Jan. 2004.

[53] J. W. Muller, "Some formulae for a dead-time-distorted poisson process," *Nuclear Instruments and Methods in Physics*, vol. 117, no. 2, pp. 401–404, Mar. 1974.

[54] C. H. Vincent, "The generation of truely random binary numbers," *Journal of Physics E Scientific Instruments*, vol. 3, pp. 594–598, Nov. 1970.

[55] M. Gude, *Ein quasi-idealer Gleichverteilungsgenerator basierend auf physikalischen Zufallsphanomenen (in German)*. A dissertation submitted RWTH Aachen, 1987.

[56] J. Walker. (2003, Jan.) Hotbits. [Online]. Available: http://www.fourmilab.ch/hotbits/

[57] A. Alkassar, T. Nicolay, and M. Rohe, “Obtaing true-random binary numbers from a weak radioactive source,” in *International Proceedings of the Computational Science and Its Applications Conference (ICCSA) 2005, Part II*, Singapore, May 2005, pp. 634–646.

# INDEX